Correlative cryo-bioimaging to study coronavirus replication organelles

Patrick Morley Phillips



Linacre College
Nuffield Department of Medicine
Division of Structural Biology
University of Oxford

A thesis submitted for the degree of Doctor of Philosophy

Hilary term 2025

Acknowledgement

I wish to thank all my supervisors for their support over the course of the project. Helena Maier and Philippa Hawes, alongside Sarah Keep and Nicole Doyle, were instrumental in driving the start of this project at The Pirbright Institute. Sarah and Nicole provided essential guidance and unwavering positivity especially beginning in the lab at the time of COVID-19 lockdowns. Helena has always been there to support me and I am also grateful for the support provided by other members of the Coronavirus and Coronavirus Cellular Biology lab groups, namely, Yana, Isobel, and Phoebe, as well as my other friends Lucy, Alex, Jed, Philie, and Mathilde for their good company outside the lab as well. I am exciting to see where our careers will take us. Moving over to Diamond Light Source, I would like to thank Maria Harkiolaki for her time working with me and sharing her invaluable scientific knowledge and advice. I have also learnt from Archana, Kamal, Tom and Chidinma at B24. At eBIC, firstly I must thank Dan Clare for his tireless support in helping me achieve the best from my project while always teaching me along the way. James Gilchrist and Parijat Majumder were also dedicated to teaching me, and I would not have been able to complete the work without their support. I have also been fortunate to get to know and make a home in the eBIC team and learn something new almost every day in the control room. This work could also could not have been completed without the support of lab technicians, goods handling teams, and student support teams from both institutes. The respect I see that is given to all my supervisors is admirable, inspirational, and I am lucky to have worked with you all. Now I am excited to continue in imaging field, test and expand the depth and width of my knowledge, and

hope to maintain these relationships as I really value them. A goal of mine is to help to keep developing the fields of *in situ* imaging so I can share knowledge back to everyone that has helped me up to this point.

This project was also supported by Jonathan Grimes and the Division of Structural Biology (STRUBI) in the Nuffield Department of Clinical Medicine (NDM), the Doctoral Training Programme in the Medical Sciences Division, Diamond Light Source (proposals nt26538 and bi34661), and the Pirbright Institute.

Finally, enormous thanks to my parents who provided me with every opportunity to succeed in life. Thank you to Raphi for sticking by my side, and to my sister Issy and my grandparents for all their encouragement along the way. I would like to dedicate this thesis to the memory of my grandpa, Morley, whose strength and dignity drive me to this day.

Declaration of Work

I hereby declare that the work described in this thesis is my own, except as described below.

Chapter 3: Modified nsp2 genes were designed and cloned into plasmids by Dr Helena Maier and Dr Sarah Keep (The Pirbright Institute). TDS to insert the modified nsp2 gene into the rVV vector, growth of selected rVV stocks, and partial purification of rVV DNA were also completed by Dr Sarah Keep. Subsequent steps, including phenol-chloroform DNA extraction and rIBV rescue, were completed by Patrick Phillips. CLEM samples were all prepared by Patrick Phillips but ultramicrotomy of resin sections was completed by Prof Philippa Hawes (The Pirbright Institute), and correlation and imaging of samples made at 18 h pi were completed by Dr Nicole Doyle (The Pirbright Institute). Anti-GFP western blot and IF labelling of BeauR-eGFP-nsp2 infected cells were completed by Dr Helena Maier. Colocalisation percentages were generated by Dr Joanna Wells.

Chapter 6: STA of ribosomes in electron tomograms was completed by Dr Daniel Clare (Diamond Light Source) to estimate the maximum achievable resolution.

Patrick Morley Phillips

Linacre College,

University of Oxford

The word count (exclusive of references, appendices, diagrams and tables) is 47067.

Abstract

All positive-sense single-stranded RNA (+RNA) viruses rearrange host cell membranes into platforms for replication called replication organelles (ROs). Elements of the coronavirus (CoV) RO have been studied, but the mechanisms driving their biogenesis and their functions are not fully established. In this thesis we examined the RO of the *Gammacoronavirus* infectious bronchitis virus (IBV), an important poultry pathogen. Using correlative cryo-imaging workflows with a fluorescent recombinant IBV (rIBV), the IBV RO has been revealed in unprecedented detail, under a near-native state, and within the context of the infected cell. Cryo-soft X-ray tomography (cryo-SXT) showed that the IBV RO fills a large volume of the cytoplasm of the infected cell and mainly consists of double membrane vesicles (DMVs) that are interspersed with discrete patches of zippered endoplasmic reticulum (zER) tethered with double membrane spherules (DMSs). Furthermore, using cryo-electron tomography (cryo-ET), the DMVs were shown to contain a double-membrane-spanning pore, as has been observed for *Betacoronaviruses*, suggesting a mechanism for RNA translocation. Moreover, populations of smaller DMVs, lacking RNA strands within their lumen but embedded with pores, contributed to hypotheses suggesting a mechanism for DMV biogenesis. Significantly, the zER and DMSs were shown to contain proteins spanning their double membranes for the first time, suggesting that they are separate structures to DMVs. Finally, by subtomogram averaging (STA), the DMSs were also shown to contain layered protein lattices, highlighting the uniformity of these structures, and appeared to form by zER wrapping around an ordered protein shell. These results provide important insights into the variety of the CoV RO, as

well as tools to facilitate further study of CoV DMSs and their function in viral replication. Consequently, this work contributes to a better understanding of CoV replication.

Table of Contents

Acknowledgement ..... ***I***

Declaration of Work ..... ***III***

Abstract ..... ***IV***

List of figures ..... ***XIII***

List of tables ..... ***XVIII***

Abbreviations ..... ***XIX***

Chapter 1. Introduction ***1***

1.1. **The *Coronaviridae Family*** **1**

1.1.1. *Alpha-*, *Beta-*, *Gamma-*, and *Deltacoronavirus* 1

1.1.2. The *Gammacoronavirus* Infectious Bronchitis Virus (IBV) 4

1.2 Virion and genome structure **5**

1.3. Viral proteins **7**

1.3.1. Non-structural proteins (nsps) 7

1.3.2. Structural proteins 16

1.4. IBV replication cycle **23**

1.5. Viral replication organelles (ROs) **27**

1.5.2. Invaginated spherule ROs 31

1.5.3. Vesicular network ROs 34

1.6. The coronavirus replication organelle **37**

1.6.1. Coronavirus double membrane vesicles (DMVs) 41

1.6.2. Coronavirus convoluted membranes (CM), zippered ER (zER), and double membrane spherules (DMSs) 47

1.6.3. Coronavirus RO biogenesis 51

1.6.3.1 Proteins involved in membrane rearrangements 51

1.6.3.2. Minimal SARS-CoV-2 nsp3-4 pore insights into membrane curvature....53

1.6.3.3. Insights into RO biogenesis from other +RNA viruses....57

1.6.3.4. Host factors involved in RO biogenesis 57

1.7. Cryo-correlative multi-scale imaging 59

1.7.2. Fluorescence microscopy, immuno-electron microscopy (IEM), and autoradiography EM 60

1.7.3. Cryo-soft X-ray tomography (cryo-SXT) 61

1.7.4. Cryo-focused ion beam milling (FIB) and cryo-electron tomography (ET)....62

1.7.5. Subtomogram averaging (STA) 65

1.8. Research aim 66

Chapter 2. Materials and Methods....68

2.1. Cells and Eggs....68

2.1.1. Primary chick kidney (CK) cells....68

2.1.2. Continuous cell lines 68

2.1.3. Embryonated Eggs 69

2.2. Cell culture medium....69

2.3. Viruses....71

2.3.1. IBV strains 71

2.3.2. Fowl pox Virus (FPV) 72

2.3.3. Vaccinia Viruses 73

2.4. Buffers and Solutions....73

2.5. Reverse Genetics to generate recombinant IBVs 75

2.5.1. Plasmid cloning to insert fluorescent tags 76

2.5.2. Transient Dominant Selection (TDS) 77

2.5.3. Growing ministocks of selected rVVs 80
2.5.4. Growing maxistocks of screened rVVs 81
2.5.5. Partial purification of rVV maxistocks 81
2.5.6. Phenol-Chloroform DNA extraction 81
2.5.7. Rescue of rIBV from rVV 82
2.6. RNA extraction 84
2.7. Reverse Transcription (RT) 85
2.8. Polymerase chain reaction (PCR) to detect virus 86
2.8.1. Agarose gel electrophoresis 87
2.8.2. Sanger sequencing 88
2.9. Quantitative Polymerase Chain Reaction (qPCR) to measure amounts of vRNA 88
2.10. Virus replication kinetics *in vitro* to characterise rIBV growth 89
2.11. rIBV genetic stability assay *in vitro* 90
2.12. Generating viral stocks 90
2.12.1. Generation of rIBV stocks in cells 91
2.12.2. Generation of virus stocks in embryonated eggs 91
2.12.3. Virus stock concentration 92
2.13. Viral titration by plaque assay 92
2.14. Immunoprecipitation 93
2.14.1. Cell lysis 93
2.14.2. SDS-PAGE electrophoresis 94
2.14.3. Western blot 94
2.15. Fluorescence microscopy 95
2.15.1. TC-ReAsH labelling 95
2.15.2. Sample preparation for immunofluorescence microscopy 96

2.15.3. Labelling of nascent viral RNA with bromouridine....99
2.15.4. Sample preparation for live cell fluorescence microscopy....99
2.16. Correlative Light and Electron Microscopy (CLEM) at room temperature....100
2.17. Cryopreservation of BeauR-eGFP-nsp2 infected cells on grids....102
2.17.1 Seeding cells on grids....103
2.17.2. Different plunge freezing protocols for cryo-SXT and cryo-FIB SEM....104
2.17.3. Infection and transfection of cells on grids....105
2.18. Fluorescence screening under cryogenic conditions....106
2.18.1. Cryo-structured illumination microscopy (SIM)....106
2.18.2. Leica cryoCLEM....107
2.19. Cryo-soft X-ray tomography (cryo-SXT)....108
2.20. Cryo-focused ion beam milling and cryo-electron tomography....109
2.20.1. Screening EM grids on Glacios....109
2.20.2. Cryo-focused ion beam milling and 3D correlation for lamella placement....109
2.20.3. Cryo-electron tomography using Krios....111
2.20.4. Cryo-electron tomography data processing....111
Chapter 3. Generation and characterisation of recombinant fluorescent viruses to visualise replication organelles....115
3.1. Introduction....115
3.2. Results....117
3.2.1. Multi-step replication kinetics of rescued IBV recombinants....117
3.2.2. Fluorescence microscopy of different IBV recombinants....121
3.2.3. Single step growth kinetics of BeauR-eGFP-nsp2....125
3.2.4. BeauR-eGFP-nsp2 recombinant stability by reverse-transcription polymerase chain reaction (RT-PCR)....127
3.2.5. Western blot to confirm presence of GFP in BeauR-eGFP-nsp2....128

3.2.6. Confirmation of presence of GFP by IF 130
3.2.7. Comparison of BeauR-eGFP-nsp2 fluorescence in different cell lines 132
3.2.8. BeauR-eGFP-nsp2 fluorescence in CK cells at early timepoints 135
3.2.9. BeauR-eGFP-nsp2 fluorescence correlation to intermediates in viral genome replication (dsRNA) and sites of nascent viral RNA synthesis (bromouridine labelling) 137
3.2.10. BeauR-eGFP-nsp2 correlation to dsRNA and BrU at early timepoints 142
3.2.11. BeauR-eGFP-nsp2 concentration to maximise infection observed by fluorescence microscopy 148
3.2.12. Correlative light and electron microscopy (CLEM) to confirm that BeauR-eGFP-nsp2 marks sites of replication organelles 153
3.2.13. Observation of replication organelles at early timepoints in infection 156

3.3. Discussion 161

3.4. Summary 175

Chapter 4. Cryo-correlative light and soft X-ray tomography to observe replication organelles in whole cells under near-native conditions 176

4.1. Introduction 176

4.2. Results 180

4.2.1. Cryo-preservation of infected cells on grids 180
4.2.2. Cryo-fluorescence microscopy of BeauR-eGFP-nsp2 infected cells on grids 184
4.2.3. Cryo-soft X-ray tomography of BeauR-eGFP-nsp2 infected in primary CK cells 185
4.2.4. Cryo-soft X-ray tomography of BeauR-eGFP-nsp2 infected DF1 cells at 6 h pi.....190
4.2.5. Cryo-soft X-ray tomography of IBV replication organelles in DF1 cells at 24 h pi.....192

4.3. Discussion 201

4.4. Summary 213

Chapter 5. Cryo-correlative light and electron tomography to observe IBV replication organelles in situ under near-native conditions 214

5.1. Introduction 214

5.2. Results 216

5.2.1. Cryo-preservation of infected cells on grids for electron microscopy 216

5.2.2. Cryo-fluorescence mapping of BeauR-eGFP-nsp2 infected DF1 cells 218

5.2.3. Fluorescence-guided cryo-focused ion beam (cryo-FIB) milling to generate lamella 220

5.2.4. Cryo-electron tomography of BeauR-eGFP-nsp2 fluorescence-guided lamella 223

5.2.4.1. Cryo-electron tomography of the IBV RO 223

5.2.4.2. Cryo-ET of zER and DMSs 228

5.2.4.3. The DMS 'spokes' 231

5.2.4.4. The DMS necks 234

5.2.4.5. Contents of the DMS and formation intermediates 235

5.2.4.6. Stacked membranes were observed in IBV nsp4-GFP transfected cells 237

5.2.4.7. Cryo-ET of the IBV DMV 239

5.2.4.8. Potential DMV precursors 242

5.2.4.9. DMVs with associated single membrane vesicles and invaginations 244

5.2.4.10. Cryo-ET of IBV virions 247

5.2.4.11. Partially degraded DMSs were also observed 248

5.2.5. Subvolume averaging from cryo-electron tomograms 249

5.3. Discussion 252

5.4. Summary 277

Chapter 6. Final Discussion 278

6.1. Novel insights into IBV DMVs 282

6.2. Novel insights into DMSs 283

6.3. Future work 286

6.4 Conclusion 292

Chapter 7. Bibliography 293

Chapter 8. Appendix 377

8.1 Tagged nsp2 viruses 377

8.2 Supplementary movies 379

List of figures

Figure 1. 1 Nidovirales Order Classification. 2

Figure 1. 2 IBV virion and genome structure. 6

Figure 1. 3 Proposed schematic model of the CoV replication transcription complex (RTC). 8

Figure 1. 4 Structure of SARS-CoV-2 nsp3 in minimal DMV pores. 12

Figure 1. 5 Structure of SARS-CoV-2 nsp4 in minimal DMV pores. 13

Figure 1. 6 Model of IBV nsp6. 15

Figure 1. 7 Pre-fusion structure of the IBV spike (S) protein. 17

Figure 1. 8 Structure of the CoV M protein. 19

Figure 1. 9 Structure of the IBV E protein. 20

Figure 1. 10 Structure of the IBV N protein. 22

Figure 1. 11 The IBV replication cycle and replication organelles. 24

Figure 1. 12 IBV genome replication and discontinuous transcription. 25

Figure 1. 13 Schematic of membrane rearrangements induced by +RNA virus infection. 28

Figure 1. 14 Universal coronavirus replication organelle structures observed by electron microscopy. 40

Figure 1. 15 Networks of double membrane vesicles (DMVs) induced by SARS-CoV. 43

Figure 1. 16 dsRNA and nascent viral RNA associate with DMVs but do not clearly associate with CM or DMSs. 44

Figure 1. 17 Zippered ER (zER) forming double membrane spherules (DMS). 48

Figure 1. 18 The double membrane spherules (DMS) first described in *Gammacoronavirus* IBV infected cells and observed in *Betacoronavirus* MERS-CoV infected cells by electron tomography at room temperature. 50

Figure 1. 19 Topology and interactions of nsp3 and nsp4 to curve membranes in the SARS-CoV-2 minimal pore from Huang *et al.*, 2024..... 55

Figure 2. 1 Recombinant IBV design..... 72

Figure 2. 2 cDNA copy of IBV genome within the thymidine kinase (TK) gene of a recombinant vaccinia virus (rVV) vector. 76

Figure 2. 3 Cloned pGPTNEB193 plasmid..... 77

Figure 2. 4 Transient dominant selection (TDS). 78

Figure 2. 5 Rescue system in CK cells used to generate rIBV virions from their rVV vector. 83

Figure 2. 6 Subtomogram averaging pipeline in RELION-5. 113

Figure 3. 1 Growth kinetics of BeauR-eGFP-nsp2 compared to WT BeauR in DF1 (A) and CK (B) cells..... 119

Figure 3. 2 Growth kinetics of BeauR-mCherry-nsp2 (A) and BeauR-TC-nsp2 (B) compared to WT BeauR in CK cells..... 120

Figure 3. 3 Comparison of BeauR-TC-nsp2, BeauR-mCherry-nsp2 and BeauR-eGFP-nsp2 by immunofluorescence microscopy. 124

Figure 3. 4 Characterisation of BeauR-eGFP-nsp2 replication by single step growth curve. 126

Figure 3. 5 BeauR-eGFP-nsp2 passaging in CK cells..... 128

Figure 3. 6 Western blot to confirm presence of GFP protein. 129

Figure 3. 7 Confirmation of GFP in BeauR-eGFP-nsp2 infected CK cells. 131

Figure 3. 8 BeauR-eGFP-nsp2 exhibits the strongest fluorescence signal at 6 h pi in CK cells. 135

Figure 3. 9 Immunofluorescence time course of BeauR-eGFP-nsp2 up to 6 h pi. 136

Figure 3. 10 Immunofluorescence of BeauR-eGFP-nsp2 with known markers of viral replication organelles. 141

Figure 3. 11 STED images of BeauR-eGFP-nsp2 association with dsRNA and nascent viral RNA. 148

Figure 3. 12 Virus concentration protocol. 150

Figure 3. 13 Confocal images showing the number of infected cells at different h pi following infection with different stocks of BeauR-eGFP-nsp2. 152

Figure 3. 14 BeauR-eGFP-nsp2 signal marks DMS and DMV structures in DF1 cells at 18h pi. 154

Figure 3. 15 Appearance of IBV replication organelles by electron microscopy is not affected by insertion of eGFP-nsp2. 155

Figure 3. 16 Correlative light and electron microscopy (CLEM) of BeauR-eGFP-nsp2 infected CK cell at 6 h pi reveals GFP-nsp2 signal marks infected cells and can direct imaging to specific RO membrane patches within the cell cytoplasm. 158

Figure 3. 17 Correlative light and electron microscopy (CLEM) of BeauR-eGFP-nsp2 infected CK cell at 4 h pi. 159

Figure 3. 18 Correlative light and electron microscopy (CLEM) of BeauR-eGFP-nsp2 infected CK cell at 4 h pi was able to identify DMVs. 160

Figure 4. 1 Artifacts in CK cell cryo-preservation. 182

Figure 4. 2 Cryopreservation of DF1 cells. 183

Figure 4. 3 Cryo-fluorescence images of cryopreserved BeauR-eGFP-nsp2 infected cells. 185

Figure 4. 4 Screening for replication organelle formation events at 6 h pi in CK cells. 187

Figure 4. 5 Potential DMS patch in CK cells at 18 h pi. 189

Figure 4. 6 Membrane observations in DF1 cells infected with BeauR-eGFP-nsp2 at 6 h pi. 191

Figure 4. 7 Replication organelles in DF1 cells infected with BeauR-eGFP-nsp2 at 24 h pi. 193

Figure 4. 8 Replication organelles in DF1 cells infected with BeauR-eGFP-nsp2 at 24 h pi. 195

Figure 4. 9 Segmented RO membranes in BeauR-eGFP-nsp2 infected DF1 cells at 24 h pi. 197

Figure 4. 10 Gallery of ROs taken from the tomograms in Figure 4.8. 198

Figure 4. 11 A large depth of field throughout the cells was imaged including ROs. 200

Figure 5. 1 Atlases of DF1 cells on grids. 217

Figure 5. 2 Cryo-fluorescence screening grids for correlative cryo-FIB-SEM. 219

Figure 5. 3 2D correlation of fluorescence data to FIB-SEM. 221

Figure 5. 4 3D correlation of fluorescence data to FIB-SEM. 222

Figure 5. 5 Cryo-ET overview of the IBV RO. 225

Figure 5. 6 Potential RO membrane connections. 227

Figure 5. 7 DMS and zER double membranes contain striation patterns and some zER branches. 229
Figure 5. 8 All DMSs are tethered to zER. 230
Figure 5. 9 The DMS ‘spokes’ extend into the DMS interior. 231
Figure 5. 10 Ordered arrangement of the DMS ‘spokes’. 233
Figure 5. 11 The DMS necks vary in width and length. 235
Figure 5. 12 Zippered ER is wrapped around layers of material to form the DMS. 236
Figure 5. 13 Contents surround the inner membrane of the DMS head. 237
Figure 5. 14 IBV GFP-nsp4 transfection-induced membrane stacking. 238
Figure 5. 15 Cryo-ET of the IBV DMV. 240
Figure 5. 16 Side views of the IBV DMV pore. 241
Figure 5. 17 Small DMVs with closely spaced pores. 243
Figure 5. 18 Membrane evaginations were observed attached to DMVs. 245
Figure 5. 19 DMVs with double membrane invaginations. 246
Figure 5. 20 BeauR-eGFP-nsp2 virions. 247
Figure 5. 21 Partially degraded DMS are observed inside single membrane vesicles in multiple tomograms. 248
Figure 5. 22 Particle picking strategy (oversampling the surface of spheres) and 3D classification. 250
Figure 5. 23 3D modelling of the DMS after STA. 251
Figure 5. 24 ER zippering mechanisms and DMS schematic. 256
Figure 5. 25 Fitting nsp4 into the model. 262
Figure 5. 26 Organisation of N in virions compared to the DMS model. 270
Figure 5. 27 The DMS interior lattices compared to the M lattice. 272

Figure 6. 1 Correlative imaging of the IBV RO over multiple scales with unprecedented detail. 281

List of tables

Table 1. 1 *Orthocoronavirinae* genera and species. 3

Table 1. 2 Morphologies of +RNA virus replication organelles (ROs) 29

Table 2. 1 Cell culture media. 70

Table 2. 2 Reaction mixture RT1 85

Table 2. 3 Reaction mixture RT2 85

Table 2. 4 SuperScript IV thermocycler program 86

Table 2. 5 PCR reaction mixture 86

Table 2. 6 PCR thermocycler program 87

Table 2. 7 qPCR reaction mixture 89

Table 2. 8 qPCR thermocycler program 89

Table 2. 9 Primary antibodies for Western blot 95

Table 2. 10 Secondary antibodies for Western blot 95

Table 2. 11 Primary antibodies for immunofluorescence microscopy 97

Table 2. 12 Secondary antibodies for immunofluorescence microscopy 97

Table 3. 1 Titration of stocks of successfully rescued recombinant viruses. 118

Abbreviations

aa Amino acid

ADRP ADP-ribose-1”-phosphate phosphatase

BES N, N-bis[2-hydroxethy1]-2-aminoethanesulfonic acid

BHK Baby hamster kidney cells

BME β-mercaptoethanol

BMV Brome Mosaic virus

bp Base pair

BSA Bovine serum albumin

BSMV Barley stripe mosaic virus

cDNA Complementary DNA

CEMOVIS Cryo-electro-microscopy of vitreous sections

CHIKV Chikungunya virus

CIRV Carnation Italian ringspot virus

CK Chick kidney

CLEM Corelative light electron microscopy

CM Convoluted membranes

CMV Cucumber mosaic virus

CNV Cucumber necrosis virus

CoV Coronavirus

CPE Cytopathic effect

Cryo-EM Cryo-electron microscopy

Cryo-ET Cryo-electron tomography

Cryo-FIB Cryo-focused-ion-beam

Cryo-FIB-SEM Cryo-focused-ion-beam/scanning electron microscope

Cryo-SIM Cryo-structured illumination microscopy

Cryo-SXT Cryo-soft-X-ray-tomography

CSF Classical Swine Fever

CTF Contrast Transfer function

CTD C-terminal domain

DAPI 4',6-diamidino-2-phenylindole

DENV Dengue virus

DMEM Dulbecco's minimum essential medium

DMS Double membrane spherule

DMSO Dimethyl sulfoxide

DMV Double membrane vesicle

DNA Deoxyribonucleic acid

dNTPs Deoxynucleotide triphosphates

dsRNA Double-stranded RNA

DTT Dithiothreitol

E Envelope protein

EAV Equine arteritis virus

E. coli *Escherichia coli*

Ecogpt *E. coli* guanine phosphoribosyl transferase

Ecto Ectodomain

EDTA Ethylenediaminetetraacetic acid

eGFP enhanced green fluorescent protein

EM Electron microscopy

EMEM Eagle's minimum essential medium

ER Endoplasmic reticulum

ERES ER exit sites

ERGIC ER-Golgi intermediate compartment

ET Electron tomography

FCS Fetal bovine serum

FHV Flock House virus

FP Fusion peptide

GFP Green fluorescent protein

GMEM Glasgow minimum essential medium

h Hour

H_20 Water

HCoV-229E Human CoV 229E

HCoV-NL63 Human CoV NL63

HCV Hepatitis C virus

HE Haemagglutinin esterase

HeLa Henrietta Lacks

HIV Human immunodeficiency virus

h pi Hours post infection

HδR Hepatitis delta antigenome ribozyme

IB Infectious bronchitis

IBV Infectious bronchitis virus

ICTV International Committee on Taxonomy of Viruses

IF Immunofluorescence

Ig Immunoglobulin

kDa Kilo Dalton

kb Kilobase

KIF Kinesin Family Member

LAC Linear absorption coefficient

LAMP1 Lysosomal-associated membrane protein 1

M Membrane protein

MDa Mega Dalton

MERS-CoV Middle East respiratory syndrome coronavirus

Mg Magnesium

mg Milligram

$MgCl_2$ Magnesium chloride

MHV Mouse hepatitis virus

min Minute

ml Millilitre

mm Millimetre

MNSV Melon necrotic spot virus

MOI Multiplicity of Infection

meGFP Monomeric enhanced green fluorescent protein

MPA Mycophenolic acid

M^{pro} Main protease

mRNA Messenger RNA

N Nucleocapsid protein

NaOH Sodium hydroxide

NBBS New-born calf serum

NMR Nuclear magnetic resonance

nsp Non-structural protein

nt Nucleotide

NTD N-terminal domain

ORF Open reading frame

P/S Penicillin/ Streptomycin

PAGE Polyacrylamide gel electrophoresis

PBS Phosphate buffered saline

PCR Polymerase chain reaction

PDB Protein data bank

PDCoV Porcine Deltacoronavirus

PEDV Porcine epidemic diarrhea virus

PFA Paraformaldehyde

PFU Plaque forming unit

PL^{pro} papain-like protease

PM Plasma membrane

pmol Picomole

pp Polyprotein

PRRSV Porcine reproductive and respiratory syndrome virus

PV Polio virus

qPCR Quantitative PCR

Rab Ras-related protein

RdRp RNA-dependent RNA polymerase

rFPV-T7 Recombinant Fowlpox-T7 virus

RFS Ribosome frameshift site

rIBV Recombinant IBV

RIPA Radioimmunoprecipitation assay

RIR Rhode Island Red

RNA Ribonucleic acid

RNaseOUT Ribonuclease inhibitor

RNP Ribonucleoprotein

RO Replication organelle

rpm Revolutions per minute

RT Reverse transcription

RTC Replication-transcription complex

RUBV Rubella virus

rVV Recombinant Vaccinia virus

s Second

S Spike protein

SARS-CoV Severe acute respiratory syndrome coronavirus

SARS-CoV-2 Severe acute respiratory syndrome coronavirus 2

SD Standard deviation

SDS Sodium dodecyl sulphate

SEM Standard error of the mean

SFV Semliki Forest Virus

sg Sub-genomic

sgRNA Sub-genomic RNA

SINV Sindbis virus

SMV Single membrane vesicle

SPA Single particle analysis

SPF Specific pathogen-free

SS Signal sequence

SSIV Super Script IV

STA Subtomogram averaging

TBE Tris borate EDTA

TBEV Tick-borne encephalitis virus

TBSV Tomato bushy stunt virus

TC Tetracysteine

TDS Transient dominant selection

TE Tris/ EDTA

TEM Transmission EM

TGEV Transmissible gastroenteritis virus

TM Transmembrane

TMD Transmembrane domain

TMH Transmembrane helix

TNV-A Tobacco necrosis virus A

TOC Tracheal organ culture

TPB Tryptose phosphate broth

TRIM25 Tripartite motif-containing protein 25

TRS Transcription regulatory sequence

TRS-B Body transcription regulatory sequence

TRS-L Leader transcription regulatory sequence

Ubl ubiquitin-like domains

TSWV Tomato spotted wilt virus

TYMV Turnip yellow mosaic virus

UTR Untranslated region

V Volts

VLP Virus-like particle

vRNA Viral RNA

WB Western blot

WNV West Nile virus

WT Wild type

zER Zippered endoplasmic reticulum

ZIKV Zika virus

Å Angstrom

°C Degrees Celsius

µg Microgram

µl Microlitre

µm Micrometre

µM Micromolar

+RNA Single-strand positive-sense RNA

2D 2-dimensional

3Cpro 3C protease

3D 3-dimensional

Chapter 1. Introduction

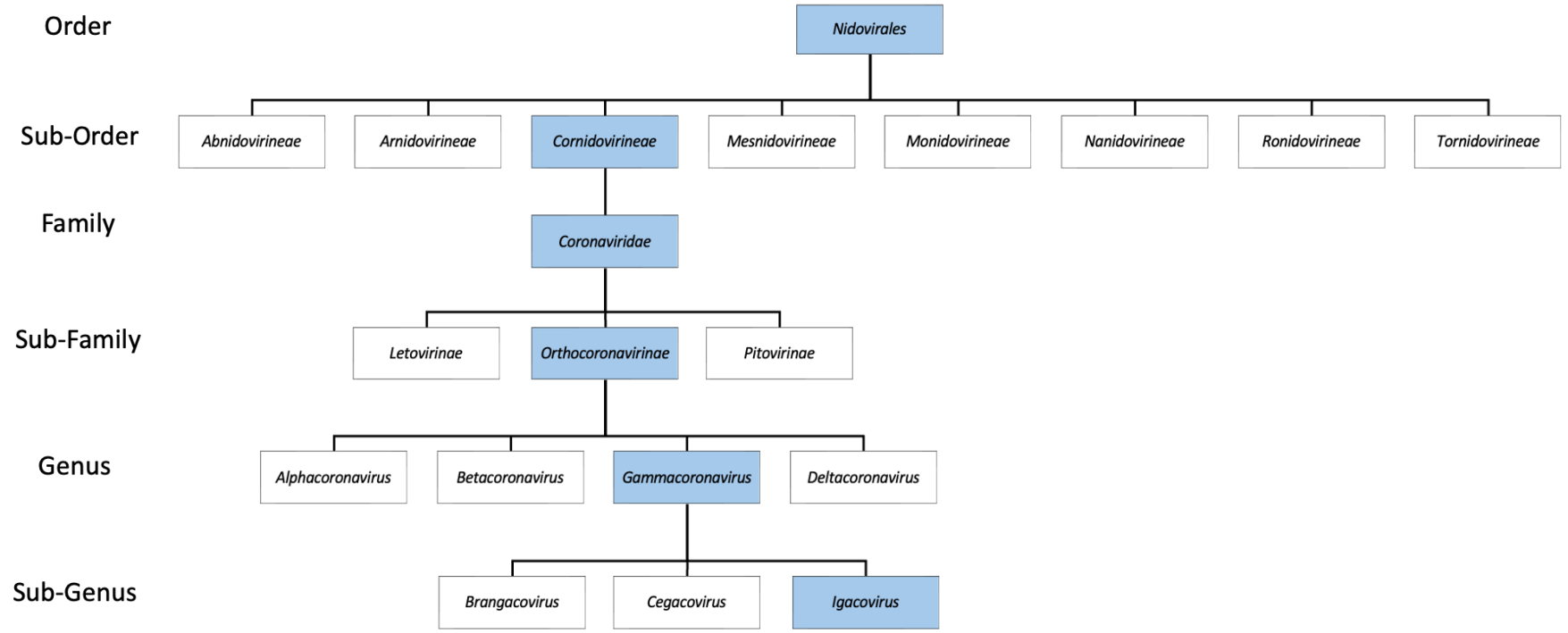
1.1. The *Coronaviridae Family*

1.1.1. Alpha-, Beta-, Gamma-, and *Deltacoronavirus*

The *Coronaviridae* (CoV) family are enveloped, positive-sense, single stand RNA viruses of the *Nidovirales* order. This family contains the *Orthocoronavirinae* subfamily which is divided into four genera: *Alphacoronavirus, Betacoronavirus, Gammacoronavirus, and Deltacoronavirus* (Figure 1.1). These viruses infect a variety of mammalian and avian hosts (Table 1.1).

CoV such as severe acute respiratory syndrome coronavirus (SARS-CoV), Middle East respiratory syndrome coronavirus (MERS-CoV), porcine epidemic diarrhoea virus (PEDV), and infectious bronchitis virus (IBV) pose significant threats to human and animal health and food security. This is evidenced by the pandemic of coronavirus disease (COVID-19), caused by *Betacoronavirus* SARS-CoV-2*,* and outbreaks of disease in livestock species (WHO, 2020; Cavanagh, 2007). Therefore, due to the current threats to human and animal health, and the potential threat of emerging CoV and zoonotic +RNA viruses, it is vitally important to understand CoV lifecycles in molecular detail.

Figure 1. 1 Nidovirales Order Classification.



Adapted from the International Committee on Taxonomy of Viruses (ICTV) website, as defined in 2024 (ictvonline.org). Blue boxes follow the lineage to infectious bronchitis virus (IBV) which is classified within the subgenus Igacovirus.

Table 1. 1 *Orthocoronavirinae* genera and species.

Genus	Subgenus	Species
Alphacoronavirus	*Amalacovirus*	Alphacoronavirus AMALF
	Colacovirus	Bat coronavirus CDPHE15
	Decacovirus	Alphacoronavirus CHB25
		Alphacoronavirus WA3607
		Bat coronavirus HKU10
		Rhinolophus ferrumequinum alphacoronavirus HuB-2013
	Duvinacovirus	Human coronavirus 229E
	Luchacovirus	Lucheng Rn rat coronavirus
	Minacovirus	Mink coronavirus 1
	Minuacovirus	Miniopterus bat coronavirus 1
		Miniopterus bat coronavirus HKU8
	Myotacovirus	Myotis ricketti alphacoronavirus Sax-2011
	Nyctacovirus	Alphacoronavirus HKU33
		Alphacoronavirus WA2028
		Nyctalus velutinus alphacoronavirus SC-2013
		Pipistrellus kuhlii coronavirus 3398
	Pedacovirus	Alphacoronavirus BT020
		Alphacoronavirus WA1087
		Porcine epidemic diarrhea virus
		Scotophilus bat coronavirus 512
	Rhinacovirus	Rhinolophus bat coronavirus HKU2
	Setracovirus	Human coronavirus NL63
		NL63-related bat coronavirus strain BtKYNL63-9b
	Soracovirus	Sorex araneus coronavirus T14
	Sunacovirus	Suncus murinus coronavirus X74
	Tegacovirus	Alphacoronavirus 1
Betacoronavirus	*Embecovirus*	Betacoronavirus 1
		China Rattus coronavirus HKU24
		Human coronavirus HKU1
		Murine coronavirus
		Myodes coronavirus 2JL14
	Hibecovirus	Bat Hp-betacoronavirus Zhejiang2013
	Merbecovirus	Hedgehog coronavirus 1
		Middle East respiratory syndrome-related coronavirus
		Pipistrellus bat coronavirus HKU5
		Tylonycteris bat coronavirus HKU4
	Nobecovirus	Eidolon bat coronavirus C704
		Rousettus bat coronavirus GCCDC1
		Rousettus bat coronavirus HKU9
	Sarbecovirus	Severe acute respiratory syndrome-related coronavirus
Gammacoronavirus	*Brangacovirus*	Goose coronavirus CB17
	Cegacovirus	Beluga whale coronavirus SW1
	Igacovirus	Avian Coronavirus
		Avian coronavirus 9203
		Duck coronavirus 2714
Deltacoronavirus	*Andecovirus*	Wigeon coronavirus HKU20
	Buldecovirus	Bulbul coronavirus HKU11
		Common moorhen coronavirus HKU21
		Coronavirus HKU15
	Herdecovirus	Night heron coronavirus HKU19

Adapted from International Committee for the Taxonomy of Viruses (ICTV) as in May 2024 (ictvonline.org). Notes: avian coronavirus is also known as infectious bronchitis virus, murine coronavirus is also known as mouse hepatitis virus (MHV), and coronavirus HKU15 is also referred to as porcine Deltacoronavirus (PDCoV).

1.1.2. The *Gammacoronavirus* Infectious Bronchitis Virus (IBV)

IBV is the prototypic *Gammacoronavirus* and was first identified in 1931 (Schalk *et al.*, 1931). Since then, high mutation rates and genome recombination events have resulted in the emergence of many serotypes and genotypes (Darbyshire *et al.*, 1979). Unlike other CoVs, multiple IBV strains and serotypes co-circulate (Cook *et al.,* 2012).

IBV infects domestic fowl (*Gallus gallus*) causing clinical disease ranging from mild respiratory symptoms to severe kidney and oviduct disease (Jackwood and de Wit, 2013; Cavanagh, 2007). Infectious Bronchitis (IB) disease results in the greatest economic losses to the poultry industry in the UK and is present worldwide (Bennett and IJpelaar, 2005; Cook *et al.,* 2012). In layers (chickens raised for egg production), oviduct epithelium infection reduces egg quality and production (Zhang *et al.*, 2020). In broilers (chickens raised for meat production), IB disease causes reduced weight gain and makes chicks susceptible to secondary bacterial infections (Matthijs *et al.*, 2003). IBV is highly contagious and is transmitted by inhalation of aerosolised droplets containing the virus (Jackwood and de Wit, 2013). The primary infection site is the epithelium of the respiratory tract, and some strains have further tissue tropisms. For example, IBV strain M41 predominantly infects the upper respiratory tract while strain QX is nephropathogenic (Meir *et al.*, 2004). Beaudette (BeauR) is a lab-adapted avirulent strain of IBV.

1.2 Virion and genome structure

There are four structural proteins in the IBV virion: spike (S), membrane (M), envelope (E), and nucleocapsid (N) (Figure 1.2 A). The spike protein is responsible for the characteristic appearance of coronavirus virions by electron microscopy which was used to name and identify this group of viruses in the 1960s (Figure 1.2 B). S, M, and E embed within single membranes of the ER-Golgi intermediate compartment (ERGIC) that form the viral envelope. Within the envelope, N coats the ss+RNA genome forming a ribonucleoprotein (RNP). Some *Betacoronaviruses* also contain a haemagglutinin esterase (HE) that may have been acquired via heterologous recombination with influenza C (Luytjes *et al.*, 1988).

The IBV single stranded positive sense RNA genome is 27.5 kb in length and has a 5′ cap and 3′ poly-A tail (Jackwood and de Wit, 2013). The 5′ two-thirds of the genome encode the replicase genes ORF1a and ORF1b which encode the nonstructural proteins (nsps) (Figure 1.2 C). ORF1a and ORF1b are translated into polyproteins pp1a and pp1ab, respectively. Pp1ab results from a -1 ribosomal frameshift site (RFS) at the short overlap of ORF1a and ORF1b. Ribosomal frameshifting enables the synthesis of multiple proteins from a single mRNA strand. Consequently, CoVs can maintain a compact genome while still encoding many proteins (Bhatt *et al.*, 2021). This is essential for efficient expression of the viral proteins in the correct stoichiometric ratios (Ramos *et al.*, 2004; Plant *et al.*, 2010). Frameshifting efficiency is regulated by an RNA pseudoknot, with a three-stemmed RNA secondary structure (Neupane *et al.*, 2021), and a heptanucleotide “slippery sequence” (e.g. UUUAAAC) which disturb the interactions of the transcript with the ribosome allowing the ribosome to slip back 1 nucleotide, resulting in the frame shift and translation in the new,

overlapping ORF (Brierley *et al.*, 1989; Brierley *et al.*, 1992). This was found to occur in 48-70% of translation events in MHV infected cells (Irigoyen *et al.*, 2016). Consequently, pp1a (nsp1-11) is expressed approximately 1.4-2.2 times more than pp1ab (nsp1-10, nsp12-16) (Finkel *et al.*, 2021). Downstream of the replicase there are genes encoding the four structural proteins and up to seven accessory genes named in relation to their location in the genome: 3a, 3b, 4b, 4c, 5a, 5b, and 7 (Keep *et al.*, 2020; Bentley *et al.*, 2013; Dinan *et al.*, 2019) (Figure 1.2 C).

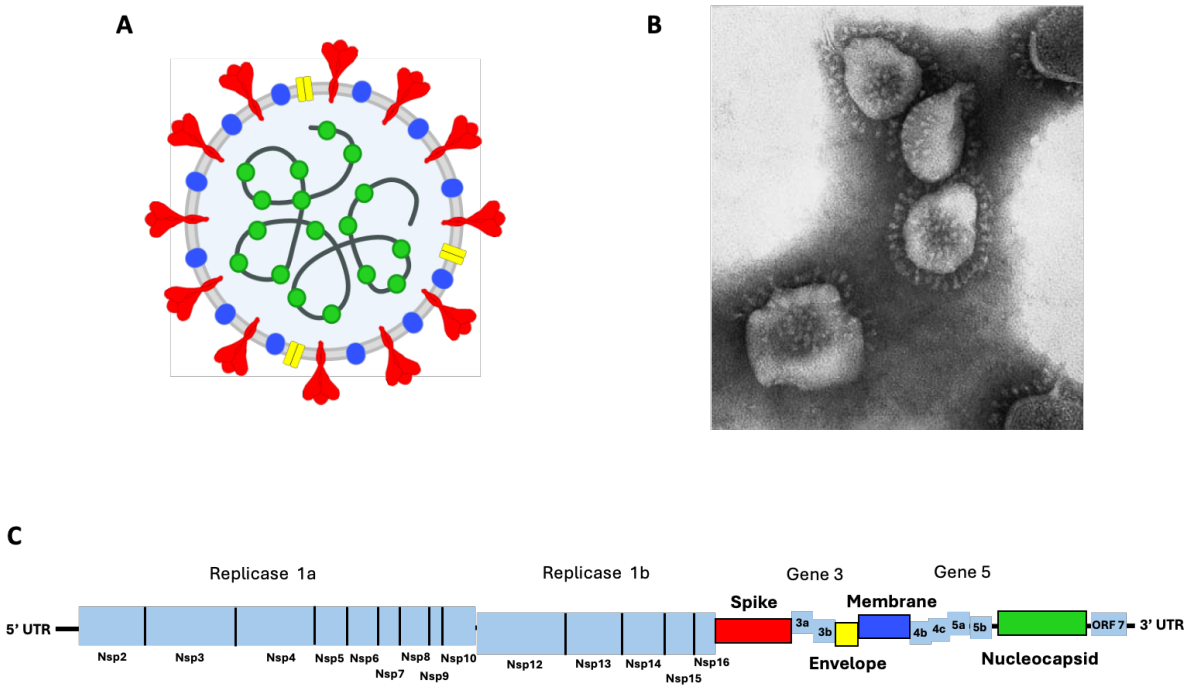


Figure 1. 2 IBV virion and genome structure.

In the schematic of the IBV virion (A) and genome (C), the structural proteins are labelled in red for spike (S), yellow for envelope (E), blue for membrane (M), and green for nucleocapsid (N). (B) IBV virions imaged by negative stain EM with visible spike proteins (Berry et al., 1964; Cavanagh, 1997). (C) Schematic depicting the organisation of the IBV genome based on the Beaudette strain; 1a and 1b overlap and nsp11 is a short 14 amino acid peptide.

1.3. Viral proteins

1.3.1. Non-structural proteins (nsps)

Here, the current knowledge of CoV non-structural proteins (nsps) has been collected and unique features of IBV nsps are highlighted. An atlas of the nsp structures across the CoV genera and their roles in replication organelles has been published (Neuman *et al.*, 2014; Neuman, 2016). The structural homology of SARS-CoV and SARS-CoV-2 proteins has also been reviewed by Gorkhali *et al.*, 2021 but some of the structures are yet to be elucidated. For IBV, only preliminary X-ray analysis of nsp2 has been published (Yu *et al.*, 2012) so predicted structures or comparative homology models of IBV nsps must currently be used to infer their functions. So far, all nsps tested localise to regions of virus induced membrane structures termed replication organelles (ROs) (V'kovski *et al.*, 2019). For IBV, the function of many nsps has not been directly confirmed with the current knowledge reviewed in Peng *et al.*, 2022. However, functions are inferred through homology with other members of the *Orthocoronavirinae* sub-family.

Following synthesis, the replicase polyproteins pp1a and pp1ab are self-cleaved by viral proteases nsp3 and nsp5 into the individual nsps. Pp1a produces nsps 1-11 and pp1ab produces nsps 1-16. The individual nsps then assemble, along with N, into the replication transcription complex (RTC), responsible for synthesising viral RNAs. The RTC is assumed to have a dynamic composition (Ziebuhr *et al.*, 2000; Ziebuhr *et al.*, 2001; V'kovski *et al.*, 2019) and a proposed model of the CoV RTC is shown in Figure 1.3 (Hartenian *et al.*, 2020).

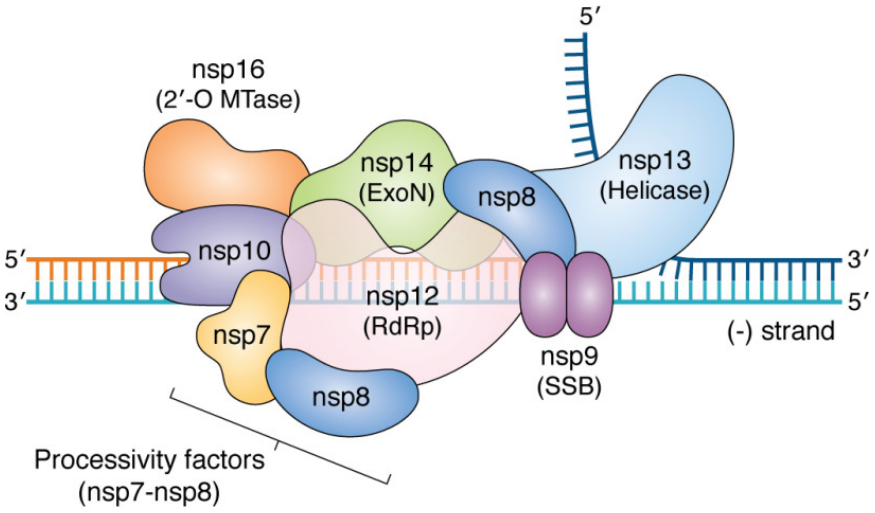


Figure 1. 3 Proposed schematic model of the CoV replication transcription complex (RTC).

Nsp7 and nsp8 act as cofactors for nsp12 RNA-dependent RNA polymerase (RdRp) activity in copying viral RNA templates. Nsp9 is a single-stranded RNA-binding (SSB) subunit. Nsp10, 13, 14, and 16 facilitate RNA capping. Also, nsp13 acts as a helicase and nsp14 is an exonuclease that proofreads nascent RNA. This figure is taken from Hartenian *et al.*, 2020.

In the *Alpha*- and *Beta*-CoV replicase polyprotein, there is a cleavage site between nsp1 and nsp2, which is lacking in the *Gamma*- and *Delta*-CoV replicase polyprotein. Therefore, cleavage of the IBV replicase produces 15 nsps (nsp2-16), where nsp2 is the first protein in the polyprotein and exists without a separate nsp1. The sequence homology within and across the genera is low but looking at the length of amino acids (aa), *Gammacoronavirus* IBV nsp2 consists of 673 amino acids (GenBank Accession No. NC_001451), while *Alphacoronavirus* HCoV-NL63 nsp2 is 639 amino acids and nsp1 is 111 amino acids (GenBank Accession No. NC_005831) and *Betacoronavirus* SARS-CoV-2 nsp2 is 635 amino acids (PDB 7MSW) and nsp1 is 180 amino acids (GenBank Accession No. NC_045512). It is not clear how the longer length of IBV nsp2 or the lack of a cleavage site to produce separate nsps translates into the functions of the protein. The name of the nsps then follows their order in the genome.

IBV nsp2 is a 75 kDa protein (Figure 1.4) and the crystal structure of an IBV nsp2 homodimer has been observed by X-ray diffraction (PDB 7F52; Ming *et al.*, 2021). Nsp2 has an unknown function and considerable sequence variation across different CoV species. This variation may indicate that nsp2 is a multifunctional protein that can rapidly mutate under host-specific selection pressures if it is involved in host interactions (Gupta *et al.*, 2021). For example, nsp2 may be involved in suppressing the host innate immune response by maintaining protein synthesis in infected cells that would otherwise stagnate as a defence mechanism (Yang *et al.*, 2009; Wang *et al.*, 2009; Cesaro and Michiels, 2021). Furthermore, SARS-CoV 2 nsp2 has more recently been proposed to associate with endosomes (Angeletti *et al.*, 2020), silence host gene expression (Zou *et al.*, 2022) and interact with several host proteins involved in translation (Gordon *et al*., 2020; Zheng *et al.*, 2021; Korneeva *et al.*, 2023). In MHV, mutations in the nsp1-2 or nsp2-3 cleavage sites and the protease domain of nsp3 have allowed replication (Denison *et al.*, 2004; Graham and Denison, 2006). Moreover, in MHV and SARS-CoV, nsp2 is dispensable for viral replication but growth and RNA synthesis are slightly attenuated (Graham *et al.*, 2005). Also, when nsp2 was deleted from MHV, expression of nsp2 from alternate locations did not complement the growth defects (Gadlage *et al.*, 2008). This suggested that the timing and the interactions resulting from nsp2 expression as part of the polyprotein between nsp1 and nsp3 were important for optimal replication. Using MHV with a tagged nsp2, it has been shown that the nsp2 C-terminus is essential for its recruitment to RTCs which are anchored at ROs including double membrane vesicles (DMVs) and convoluted membranes (CM) (Section 1.6). Therefore, nsp2 localises to ROs, and nsp2 appears to be associated with the cytoplasmic side of the DMVs (Hagemeijer *et al.*, 2010). In the same study, it was observed that once nsp2 is recruited to the RTC, it is not exchanged with nsp2 present in the cytoplasm or at other DMVs suggesting

it has stable interactions within the RTC (Hagemeijer *et al.*, 2010). For SARS-CoV nsp2, multiple interactions were also found with other viral proteins (Pan *et al.*, 2008; von Brunn *et al.*, 2007) and proteins involved with mitochondrial biogenesis and intracellular signalling (Cornillez-Ty *et al.*, 2009). Furthermore, MHV nsp2 has been tagged with a biotin ligase to label RTC-proximal proteins (within 10 nm) so they could be purified and analysed by mass spectrometry (V'kovski *et al.*, 2019). These experiments showed that all nsps, N, and over 500 host proteins interact at the RTC. MHV nsp2 has also been shown to tolerate fusion to GFP for studying RTC formation (Freeman *et al.*, 2014). Overall, these experiments suggest that tagging IBV nsp2 will be successful at localising the RTC and ROs.

IBV nsp3 is a 1592 residue, ~200 kDa, protein comprising up to 16 domains (Figure 1.4 A). Nsp3 is the largest protein encoded by the CoV genome and the nsp3 N-terminal cytosolic domain (NTD; ~160 kDa) varies among CoVs but the two transmembrane domains and C-terminal cytosolic domain (CTD; ~41 kDa) are highly conserved (Oostra *et al.*, 2008; Neuman, 2016; Lei *et al.*, 2018). Recently, the structure of SARS-CoV-2 nsp3 within minimal DMV pores was solved (Figure 1.4 A-D). There are conserved ubiquitin-like domains (Ubl1; 12.6 kDa) in the N-terminal domain that have been shown to bind to single-stranded RNA and N (Serrano *et al.*, 2007; Hurst *et al.*, 2013; Cong *et al.*, 2020). Nsp3 includes a papain-like protease (PL^{pro}) domain which can cleave pp1a nsp1-nsp2, nsp2-nsp3, and nsp3-nsp4 junctions (Ojha *et al.*, 2021). This can also remove ubiquitin modifications from proteins to delay the host's innate antiviral immune response (Yu *et al.*, 2017; Mielech *et al.*, 2014). The structure of nsp3 in DMV pores showed that nsp3 existed in 2 forms (nsp3L and nsp3S) with six copies of each form making up the cytoplasmic side of the pore complex (Huang *et al.* 2024). In this structure, the nsp3 NTDs make the cytosolic prongs, the ectodomain sits in the

intermembrane space, and the CTDs make a ring on the cytoplasmic side (Figure 1.4 A-D) (Huang *et al.*, 2024) (Section 1.6.1). Nsp3 also contains an ADP-ribose-1”-phosphate phosphatase (ADRP) domain, that acts as a virulence factor in the *Betacoronavirus* MHV (Eriksson *et al.*, 2008) but not in *Gammacoronavirus* IBV (Keep *et al.*, 2018). Moreover, in a comparison between pathogenic and attenuated strains of IBV of the same serotype, most attenuating amino acid differences occurred in nsp3 and so it was suggested that nsp3 might be important in viral replication (Phillips *et al.*, 2012). In SARS-CoV-2, nsp3 interactions with N have been shown to impact viral replication (Li *et al.*, 2023). Furthermore, nsp3 has extensive interactions with nsp4 and is involved in membrane rearrangements and DMVs as detailed in section 1.6.1. Indeed, the structure of nsp3 shown in Figure 1.4 B-D is from DMV pores (Huang *et al.*, 2024). Furthermore, prior to this structure, MHV with a deletion of nsp2 and expressing an enhanced green fluorescent protein (eGFP) in its place that fuses to the UBl1 domain of nsp3 has been used to visualise nsp3 as a component of the DMV pore complex (Wolff *et al.*, 2020).

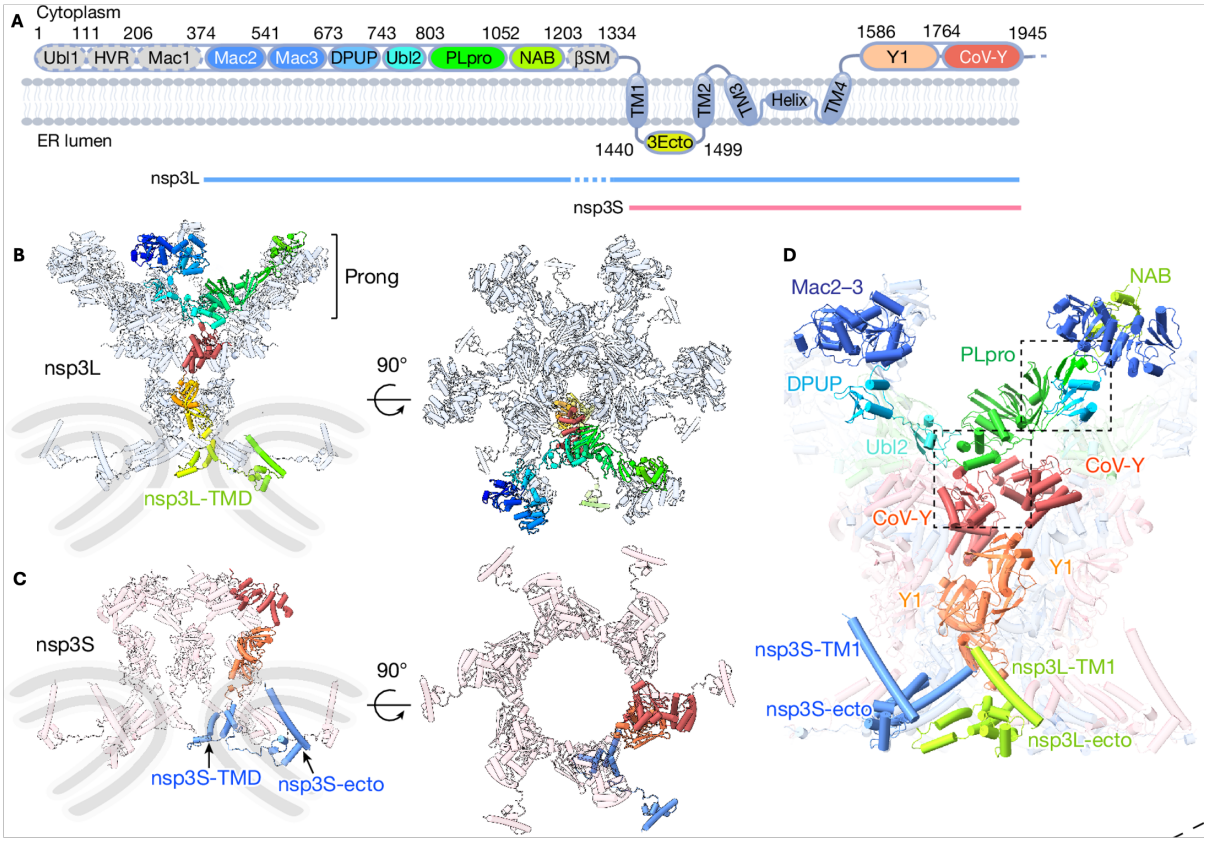


Figure 1. 4 Structure of SARS-CoV-2 nsp3 in minimal DMV pores.

Topology of nsp3 is labelled according to its structure in SARS-CoV-2 minimal DMV pores in which different forms of nsp3 were resolved (nsp3L and nsp3S; panel A). Grey ovals and dashed lines depict regions that were not resolved (panel A). The domain structure is as follows: ubiquitin-like domain (Ubl) 1, hypervariable region (HVR), macrodomains 1–3 (Mac1–3), a domain preceding Ubl2 and PLpro (DPUP), Ubl2, papain-like protease (PLpro), nucleic acid-binding (NAB) domain, β-coronavirus-specific marker (βSM) domain, a transmembrane (TM) domain, an ectodomain (3Ecto), Y1, and CoV-Y domains (panel A, D). The topology of the domains is also illustrated: the nsp3L N-terminal domains (NTDs) make the cytosolic prongs and the nsp3 ectodomain sits in the intermembrane space (panels A-C). The residue numbers for each domain are shown based on SARS-CoV-2 (panel A). This figure has been modified from Huang *et al.*, 2024.

IBV nsp4 is 514 residues and forms a ~60 kDa protein with 6 transmembrane helices (Figure 1.5 A). The topology of SARS-CoV-2 nsp4, according to its structure solved from within minimal DMV pore complexes, is shown in Figure 1.5 B-E (Huang *et al.* 2024). In this structure, two forms of nsp4 were resolved (nsp4L and nsp4S) with six copies of each form making up the base of the pore complex (Figure 1.5 A). The nsp3-nsp4 cleavage site is cleaved by the PL^{pro} domain of nsp3. Then, there is a helix after the nsp3-nsp4 cleavage site

(TM1), followed by a 240-residue soluble ectodomain before five transmembrane helices (TM2-6) and a 90-residue C-terminal domain (CTD). In the minimal SARS-CoV-2 DMV pore, TM2-6 put the ectodomain in the intermembrane space and the CTD in the DMV interior (Figure 1.5 B-C). In the lumen of the DMV the CTDs of each form of nsp4 interlock (Figure 1.5 D-E) (Huang *et al.*, 2024). Nsp4 has no known homologues, but it is involved in RO membrane rearrangements detailed in section 1.3.

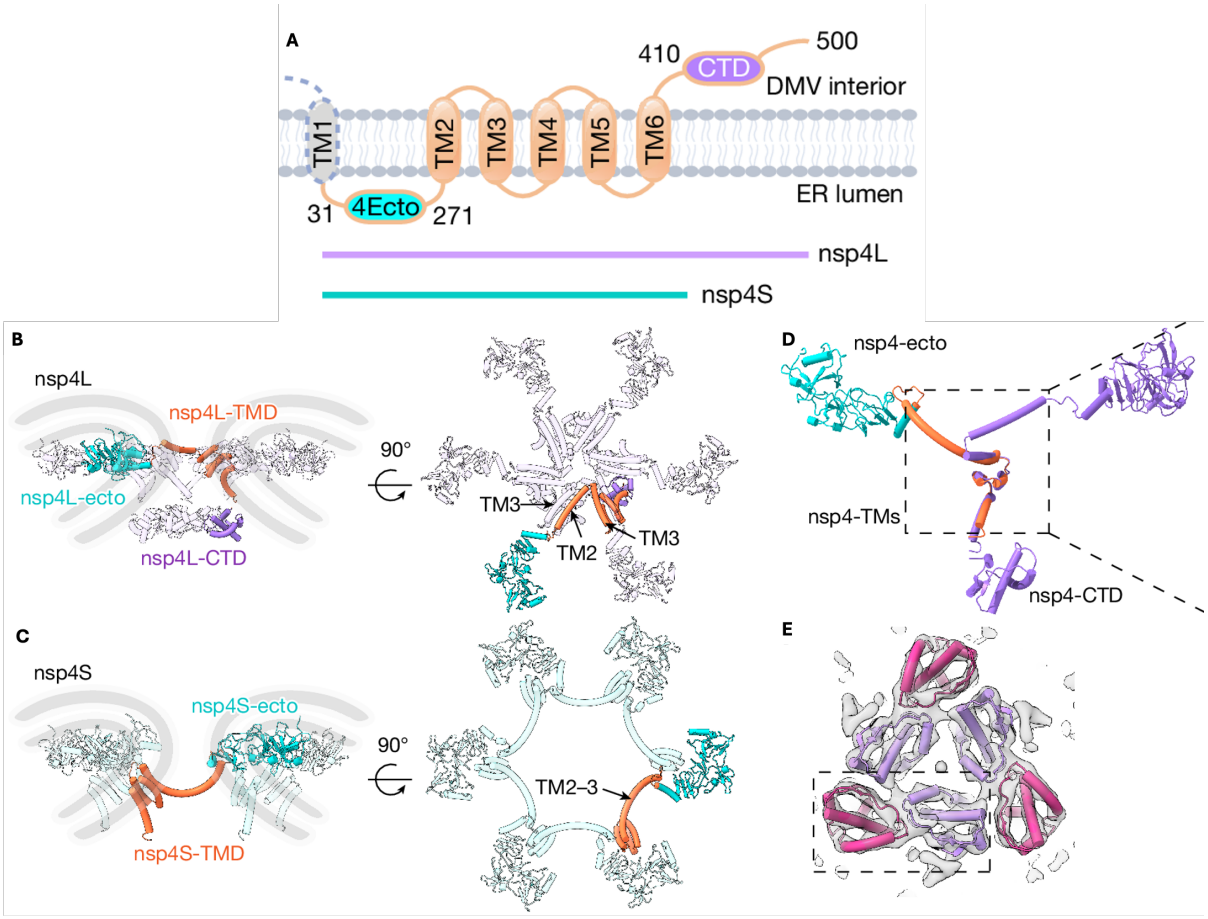


Figure 1. 5 Structure of SARS-CoV-2 nsp4 in minimal DMV pores.

Topology of nsp4 is labelled according to its structure from SARS-CoV-2 minimal DMV pores from which two forms of nsp4 were resolved (nsp4L and nsp4S) (panel A). Grey ovals and dashed lines depict regions that were not resolved (panel A). The nsp3-nsp4 cleavage site is cleaved by the nsp3 PL^{pro} domain, then the first transmembrane helix (TM1) is assumed to sit within a membrane, but this has not been observed yet. The 240 residue ectodomain (4Ecto) is a soluble domain that has been resolved within the DMV intermembrane space (panels B-C). Finally, five TM helices (TM2-6) place the C-terminal domain (CTD) on the opposite side of the membrane to the ectodomain. In the minimal DMV pore structure curvature of the membrane puts the nsp4 ectodomain in the intermembrane space and the CTD in the DMV interior where the domains interlock (panels D-E). This figure has been modified from Huang *et al.*, 2024.

Nsp5, also called the main protease (M^{pro}), is a 3-chymotrypsin like protease (3CLpro) and self-cleaves before cleaving the downstream nsps (Yang *et al.*, 2005). In IBV, nsp5 consists of 307 residues that make a ~33 kDa protein. Nsp5 is known to localise at the RTC (V'kovski *et al.*, 2019) and the crystal structure of the SARS-CoV-2 M^{pro} has been extensively studied due to is attractiveness as a drug target (Jin *et al.*, 2020) but its structure *in situ* within the RTC at ROs has not yet been observed.

IBV nsp6 is 293 amino acids, has a molecular weight of ~34 kDa, and has 6 transmembrane domains (Figure 1.6). IBV nsp6 alone has been shown to induce autophagy in some cell types (Cottam *et al.*, 2011; Maier *et al.*, 2013). Furthermore, the structure of cellular autophagosomes resembles viral DMVs so it has been suggested that autophagy may play a role in DMV formation (Liang *et al.*, 2022). Autophagosomes may also degrade factors in host immune response pathways but their connection to virus replication is unclear since dsRNA does not colocalise with key autophagosome proteins (Cottam *et al.*, 2011). Moreover, although it has been shown that DMVs lack conventional ER and Golgi markers, MHV DMVs do co-opt membranes coated with autophagy markers from EDEMosomes which regulate ER degradation (Reggiori *et al.*, 2010). Finally, nsp6 is proposed to be important for ROs as detailed in 1.6.3 (Lundin *et al.*, 2014).

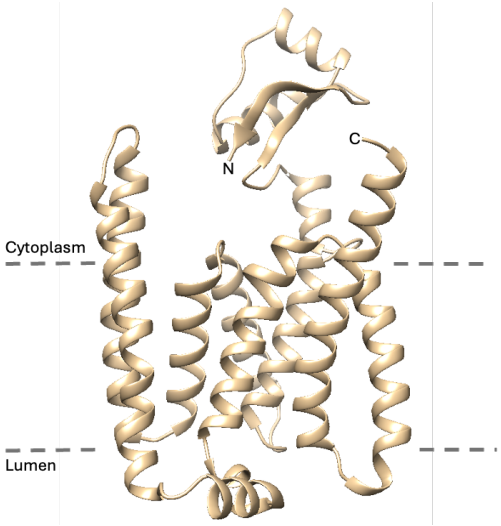


Figure 1. 6 Model of IBV nsp6.

Model of the IBV nsp6 protein generated in Alphafold2 from the P0C6Y2 sequence in UniProt (Casais *et al.*, 2001) with predicted membrane topology shown with dashed lines based on (Ricciardi *et al.*, 2022).

The remaining nsps include nsp7 (83 residues in IBV) and nsp8 (210 residues in IBV) that aid RNA binding to nsp12 (940 residues in IBV) which functions as the RNA-dependent RNA polymerase (RdRp) (Subissi *et al.*, 2014). Nsp9 (111 residues in IBV) also binds RNA and may stabilise nascent strands (Egloff *et al.*, 2004). Next, nsp10 (145 residues in IBV) is a cofactor for nsp14 and nsp16 (Bouvet *et al.*, 2010) while nsp11 is a short 14 amino acid peptide with a yet unassigned role. Nsp13 (600 residues in IBV) functions as a helicase (Xu *et al.*, 2011) while nsp14 (521 residues in IBV) supplies proof reading and, alongside nsp13 and nsp16 (302 residues in IBV), capping activities (Minskaia *et al.*, 2006; Chen *et al.*, 2009; Subissi *et al.*, 2014). Nsp15 (338 residues in IBV) acts as an endonuclease and has been shown to inhibit stress granule formation which promotes viral protein synthesis and reduces host response to infection (Zhao *et al.*, 2021; Gao *et al.*, 2021). Finally, nsp16 and nsp7 have been shown to inhibit cytokine production and antigen presentation (Zuo *et al.*, 2021).

All CoV nsps involved in the RTC are known to localise at RO membranes. First, SARS-CoV RTCs were shown to be membrane protected and require host factors for viral RNA synthesis (van Hemert *et al.*, 2008). Then, using MHV with a biotin ligase tagged nsp2, RTC proximal proteins were able to be biotinylated and purified for identification by mass spectrometry. Here, nsp2-10, nsp12-16 and N were detected, alongside 513 host proteins including proteins involved in vesicular trafficking and translation initiation factors (V'kovski *et al.*, 2019). Nsp1, when encoded as a separate nsp, is likely not an integral component of the RTC, and nsp11 is a short peptide (13 residues in SARS-CoV) with a yet unassigned role. Finally, immuno-EM (IEM) has been used to detect nsps including MHV ORF1a proteins (before they were classified into the nsps; van der Meer *et al.*, 1999), MHV nsp5, nsp12, and nsp13 (Gosert *et al.*, 2002), SARS-CoV nsp3, nsp5, and nsp8 (Knoops *et al.*, 2008), and MHV nsp2 (Hagemeijer *et al.*, 2010) at DMVs and convoluted membranes (CM). Furthermore, the MHV ORF1a proteins had been shown to colocalise with nascent viral RNA (Shi *et al.*, 1999) and nascent viral RNA was shown to localise to DMVs (Gosert *et al.*, 2002).

1.3.2. Structural proteins

Spike (S) is the viral attachment protein which binds to cellular receptors and allows fusion of the viral envelope with cellular membranes (Gallagher and Buchmeier, 2001). S is a class 1 virus fusion glycoprotein with a molecular weight of ~180 kDa that oligomerises into a homotrimer within host ER membranes (Saraste *et al.*, 2022). Homo-oligomerisation occurs via heptad repeats (HR-N and HR-C) and the homotrimeric S structure is shown in Figure 1.7 A-B (Shang *et al.*, 2018). S is translated as a single polypeptide and then cleaved by furin-like proteases within the Golgi apparatus to form two subunits: S1, creating the globular

head domain containing the receptor binding site, and S2 which anchors the protein to the virion envelope and contains the fusion machinery (de Haan *et al.*, 2004) (Figure 1.7 C). The IBV S receptor binding is dependent on N-linked glycosylation and the number of sequons and their positions in the S gene differ between strains of IBV with different pathogenicity and tropisms (Parsons *et al.*, 2019; Stevenson-Leggett *et al.*, 2021). Furthermore, in Beaudette IBV and SARS-CoV-2, an extra cleavage site, named S2′, aids fusion with host cells (Millet *et al.*, 2016; Yamada *et al.*, 2009).

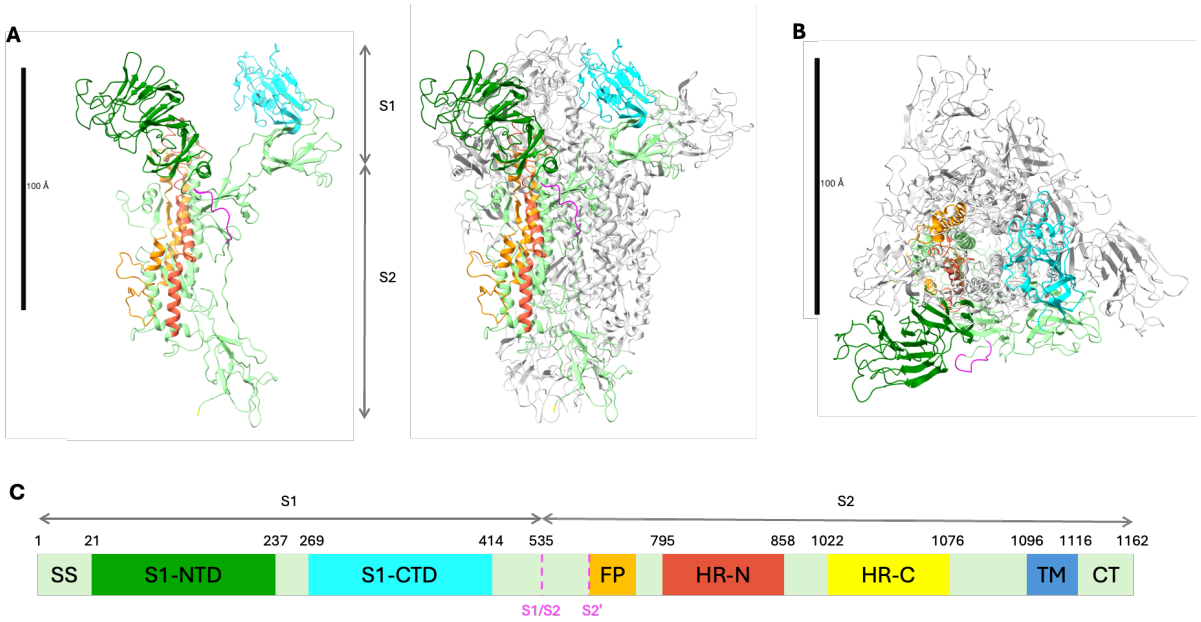


Figure 1. 7 Pre-fusion structure of the IBV spike (S) protein.

(A) Side view of the S protein (green) showing its 2 subunits (S1 and S2), domains coloured according to schematic in panel C, and homotrimer formation with 2 other copies of S in grey. (B) Top view of the S protein homotrimer. The structure in A and B has been resolved by cryo-EM (Shang *et al.*, 2018) and was visualised in ChimeraX with one protomer of the homotrimer highlighted in green and the domains coloured (RCSB PDB: 6CV0). (C) Schematic of the domains in the S gene with amino acid locations taken from Shang *et al.*, 2018. The location of the S2′ cleavage site is shown from the Beaudette sequence (Bickerton *et al.*, 2018). The S gene is flanked by a signal sequence (SS) and a cytoplasmic tail (CT). The S1 subunit contains two domains: the N-terminal domain (NTD; green), and C-terminal domain (CTD; cyan). The cleavage sites are represented with a dashed line (magenta). The S2 subunit contains three domains: the fusion peptide (FP; orange), heptad repeat domain (NTD in red) (CTD in yellow), and a transmembrane (TM) domain (blue).

The S1 NTD is used for binding to cellular receptors as was first shown for MHV S binding to carcinoembryonic antigen (CEA) family receptors (Kubo *et al.*, 1994). Binding then causes conformational changes to facilitate S2 fusion with cellular membranes (Matsuyama *et al.*, 2009). The fusion peptide (FP) in S2 fuses the viral and cellular membranes to release the IBV genome into the host cell cytoplasm and facilitates cell-cell fusion to make syncytia (Sainz *et al.*, 2005; Bickerton *et al.*, 2018). Syncytia formation also requires palmitoylation of the S protein and this cell-cell fusion mechanism is distinct to the virus-cell fusion mechanism used for entry (Rajah *et al.*, 2022; de Haan *et al.*, 2004). The IBV S1 C-terminal domain (CTD) has a distinct structure when compared to other CoVs so it may enable chicken-cell tropism for this virus (Bickerton *et al.*, 2018).

The membrane (M) protein ranges from 25-30 kDa depending on its N-glycosylation state, it has three transmembrane domains (TMDs) (Figure 1.8 A), and it is the most abundant protein in IBV virions (Masters, 2006; Binns *et al.*, 1986). Inhibiting M glycosylation allows viral assembly but abolishes infectivity of the virions (Stern and Sefton, 1982; Liang *et al.*, 2019). M also disrupts β-actin filaments and self-associates to drive envelope assembly and virion budding (Wang *et al.*, 2009; Corse and Machamer, 2003; Klumperman *et al.*, 1994). The SARS-CoV-2 M homodimer also resembles a viroporin which have rigid transmembrane domains, supporting the hypothesis that M support has a role in scaffolding virion assembly via interactions with the other structural proteins (Figure 1.8 B) (Dolan *et al.*, 2022; Corse and Machamer, 2003). Furthermore, the cytosolic side of M is positively charged so it may interact with N, S, and viral RNA. Moreover, M and E have been shown to interact via their cytoplasmic domains and are sufficient to produce virus-like particles (VLPs) (Vennema *et al.*, 1996; Baudoux *et al.*, 1998; Corse and Machamer, 2000; Godeke *et al.*, 2000) suggesting

that virus particle shape is primarily controlled by M. M has also been shown to have 'long' and 'compact' forms that create lattices lining the viral envelope (Neuman *et al.*, 2011). The relationship between M and E is also suggested to be important for virulence because for SARS-CoV mutants with E deletions, virulence could be recovered via a partly duplicated chimeric M protein (Jimenez-Guardeño *et al.*, 2015). This SARS-CoV chimeric M also had a growth defect that was partially recovered by complementation with E (Kuo *et al.*, 2016).

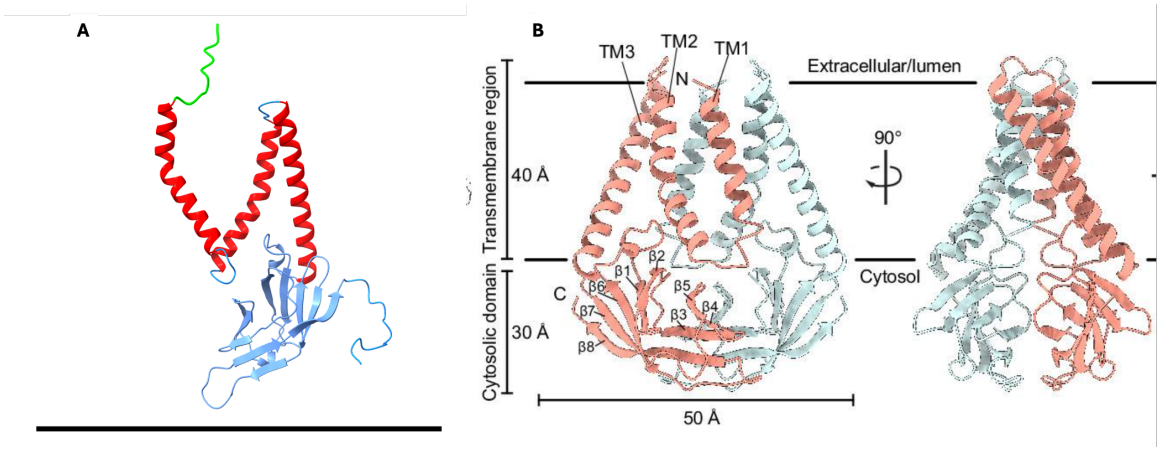


Figure 1. 8 Structure of the CoV M protein.

Model of the IBV M protein generated in Alphafold2 from the P05136 sequence in UniProt (A) (Binns *et al.*, 1986) with N-terminal domain labelled in green, transmembrane helices in red, and cytosolic domain in blue (scale bar is 100 Å). (B) Structure of SARS-CoV-2 M homodimer from lipid nanodisks (Dolan *et al.*, 2022).

The IBV envelope (E) protein is 12 kDa and exists in monomeric and pentameric forms (Figure 1.9 A-B) (Westerbeck and Machamer, 2015). E is a key virulence factor that is suggested to have roles in immune evasion (Nieto-Torres *et al.*, 2014; DeDiego *et al.*, 2007; Castaño-Rodriguez *et al.*, 2018; Li *et al.*, 2020) and its role in pathogenesis has been recently reviewed (Zhou *et al.*, 2023). IBV E has one transmembrane region leaving the N-terminus exposed to the lumen of the Golgi apparatus (surface of the virion) and the C-terminus

exposed to the cytoplasm (or intra-virion) (Yuan *et al.*, 2006). On the other hand, two membrane spanning regions are thought to exist in *Betacoronavirus* E (Yuan *et al.*, 2006; Maeda *et al.*, 2001). The CTD of E contains palmitoylation sites that have been shown to be important for viral assembly and stability of E in MHV but the function of palmitoylation in IBV is unknown (Boscarino *et al.*, 2008; Lopez *et al.*, 2008; Corse and Machamer, 2002). SARS-CoV E protein also has been shown to be glycosylated and ubiquitinated (Yuan *et al.*, 2006; Álvarez *et al.*, 2010). The cytoplasmic tail is also required for targeting E to the Golgi and interacting with M (Corse and Machamer, 2002; Cohen *et al.*, 2011; Corse and Machamer, 2003). Once E oligomerises into a pentamer, it forms a viroporin with ion channel activity which is essential for viral replication (Figure 1.9 B-C) (Liao *et al.*, 2004; Wilson *et al.*, 2006). The SARS-CoV E pentamer has been resolved by nuclear magnetic resonance (NMR) and, while IBV has a low sequence identity to *Betacoronavirus* E, the secondary structure is conserved, and purifying IBV E produces homo-pentamers (Surya *et al.*, 2018; Corse and Machamer, 2002; Torres *et al.*, 2005; Parthasarathy *et al.*, 2012).

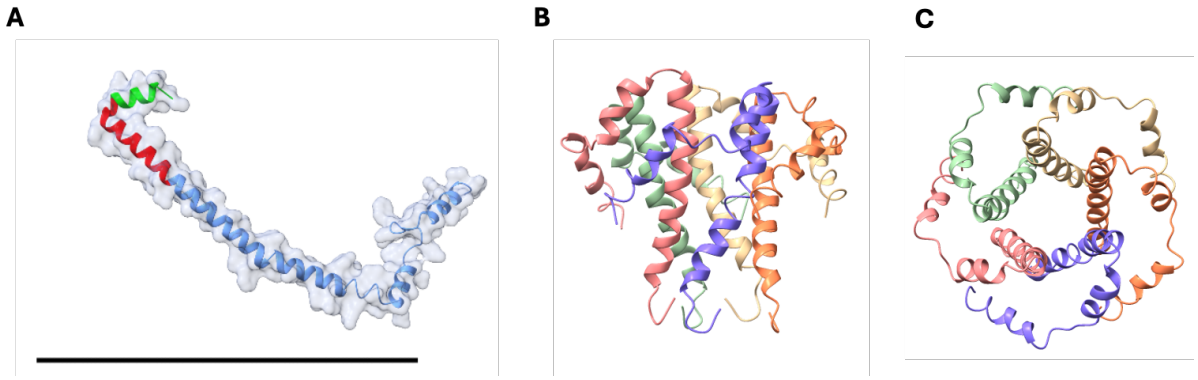


Figure 1. 9 Structure of the IBV E protein.

Model of the IBV E protein generated in Alphafold2 from the P05139 sequence un UniProt (A). with N-terminal domain at the virion surface labelled in green, transmembrane helices in red, and intravirion domain in blue (scale bar is 100 Å). (B-C) Structure of the IBV E pentamer in lipid micelles from nuclear magnetic resonance (NMR) spectroscopy (RCSB-PDB: 5X29) (Surya *et al.*, 2018). Structures were visualised in ChimeraX.

E plays a major role in viral assembly and is found embedded in the ER-Golgi intermediate compartment (ERGIC) membranes during infection (Hogue and Machamer, 2007; Stodola *et al.*, 2018). Here, E influences membrane curvature and scission for envelope formation and virion budding (Raamsman *et al.*, 2000; Fischer *et al.*, 1998). E and M together have been shown to be sufficient for the formation of VLPs and the cytoplasmic tail of E is essential for this function (Corse and Machamer, 2000). Moreover, the hydrophobic domain of E is essential for virion release and for Golgi pH neutralisation (Ruch and Machamer, 2011; Westerbeck and Machamer, 2019). This neutralisation affect causes Golgi diffusion that slows cargo trafficking and may allow the accumulation of virions, alter glycoprotein processing, and protect S from premature cleavage (Westerbeck and Machamer, 2019; Westerbeck and Machamer, 2015; Ruch and Machamer, 2012; Saraste and Prydz, 2021).

The nucleocapsid (N) protein plays a critical structural role in virions via interactions with genomic RNA, M, and other N molecules. N is ~45 kDa and coats the viral RNA genome to create a helical filamentous RNP within the IBV virion (Saikatendu *et al.*, 2007). N protein monomers can also dimerise and pack into helices in the presence or absence of RNA (Chen *et al.*, 2007; Barcena *et al.*, 2009; Saikatendu *et al.*, 2007) (Figure 1.10 B). The RNP has also been shown to create a membrane associated lattice in register with S and M and coiled shapes when disassociated from the viral envelope (Neuman *et al.*, 2006). Furthermore, *in situ* structures of SARS-CoV-2 have described the RNP arrangement in virions with a 'beads-on-a-string' model or with highly ordered packing like 'eggs-in-a-nest' or in 'tetrahedrons' (Klein *et al.*, 2020; Yao *et al.*, 2020). The interaction of N with RNA occurs via a positively charged cleft made by the N-terminal domains (Figure 1.10 A) (Fan *et al.*, 2005) and this

interaction aids RNA folding and enhances transcription efficiency (Zúñiga *et al.*, 2007; Zúñiga *et al.*, 2010). N also has a central disordered region that has been shown to interact with nsp3 in MHV (Keane and Giedroc, 2013). The CTD of N facilitates homodimerisation and interacts with M (Jayaram *et al.*, 2006) and this facilitates genome encapsulation during virion assembly (Kuo and Masters, 2002). Finally, N also mediates interactions with host G3BP1 (Emmott *et al.*, 2013) to limit sequestration of viral genomic RNA into stress granules and promote infection (Yang *et al.*, 2024).

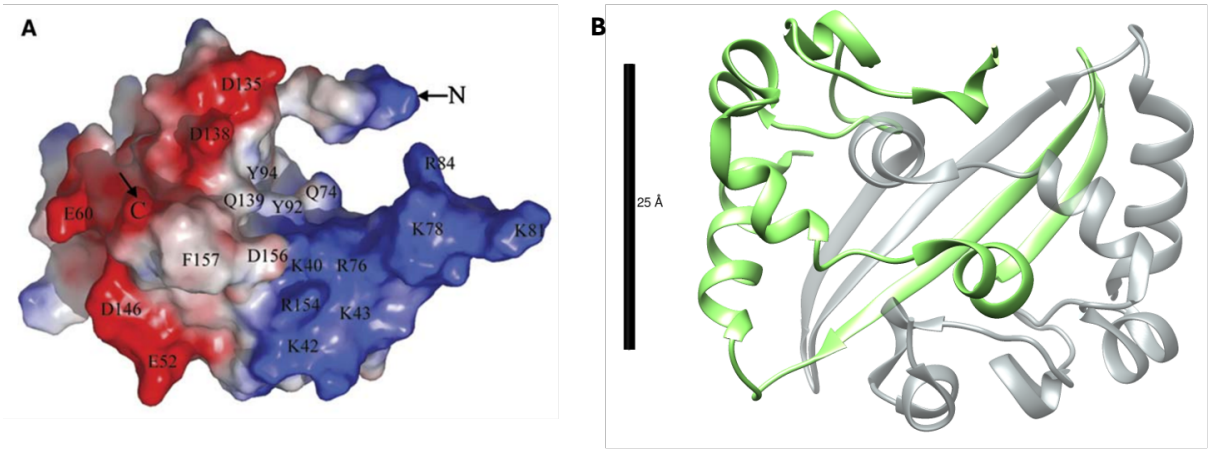


Figure 1. 10 Structure of the IBV N protein.

(A) The IBV N protein N-terminal domain (NTD). Panel A is taken from (Fan *et al.*, 2005) (RSCB-PBD: 2BTL) with the electrostatic charges labelled in blue (positive) and red (negative). The labelled residues are hypothesised to facilitate RNA binding and the N- and C- terminal ends of the NTD are labelled with arrows. (B) Structure of the homodimerised IBV N CTDs of the IBV N protein as solved by X-ray crystallography (RSCB-PBD: 2CA1, (Jayaram *et al.*, 2006)). The structure is rendered in ChimeraX with one domain labelled in green.

1.4. IBV replication cycle

The CoV lifecycle has been reviewed in detail and the IBV replication cycle is depicted in Figure 1.11 (Hartenien *et al.*, 2020; V'kovski *et al.*, 2021). While other CoVs have known entry receptors, IBV virions are endocytosed through the endo-lysosomal pathway via binding to an unknown receptor (Everest *et al.*, 2022). There are several putative IBV receptors and cellular attachment factors such as aminopeptidase N (APN) (Miguel *et al.,* 2002), sialic acids (Winter *et al.*, 2008; You *et al.*, 2023) and C-type lectins (Zhang *et al.*, 2012). Further studies are required to understand sialic acid binding by IBV as, for example, the S1-NTD of IBV S1 was shown to have a sugar binding sites (Shang *et al.*, 2018) and while the S1-NTD from IBV-M41 did bind sialic acid ligands (Promkuntod *et al*., 2014), the equivalent domain from the IBV-QX strain did not (Bouwman *et al*., 2020). Next, S protein binding induces a conformational change that allows the S fusion peptide (FP) to facilitate virus envelope and cell membrane fusion (Sainz *et al.*, 2005). IBV-Beaudette strain and SARS-CoV-2 S protein also have an additional cleavage site (S2') that aids fusion with host cells (Millet *et al.*, 2016; Yamada *et al.*, 2009). Consequently, the ss +RNA genome is released into the host cytoplasm to be translated by host ribosomes (Burkard *et al.*, 2014). Translation produces the replicase polyproteins pp1a and pp1ab that are cleaved into fifteen nsps and assemble, along with N, into the RTC (V'kovski *et al.*, 2019.) Expression of the nsps also triggers the rearrangement of host cell membranes into characteristic structures called replication organelles (ROs), described in more detail in section 1.6.

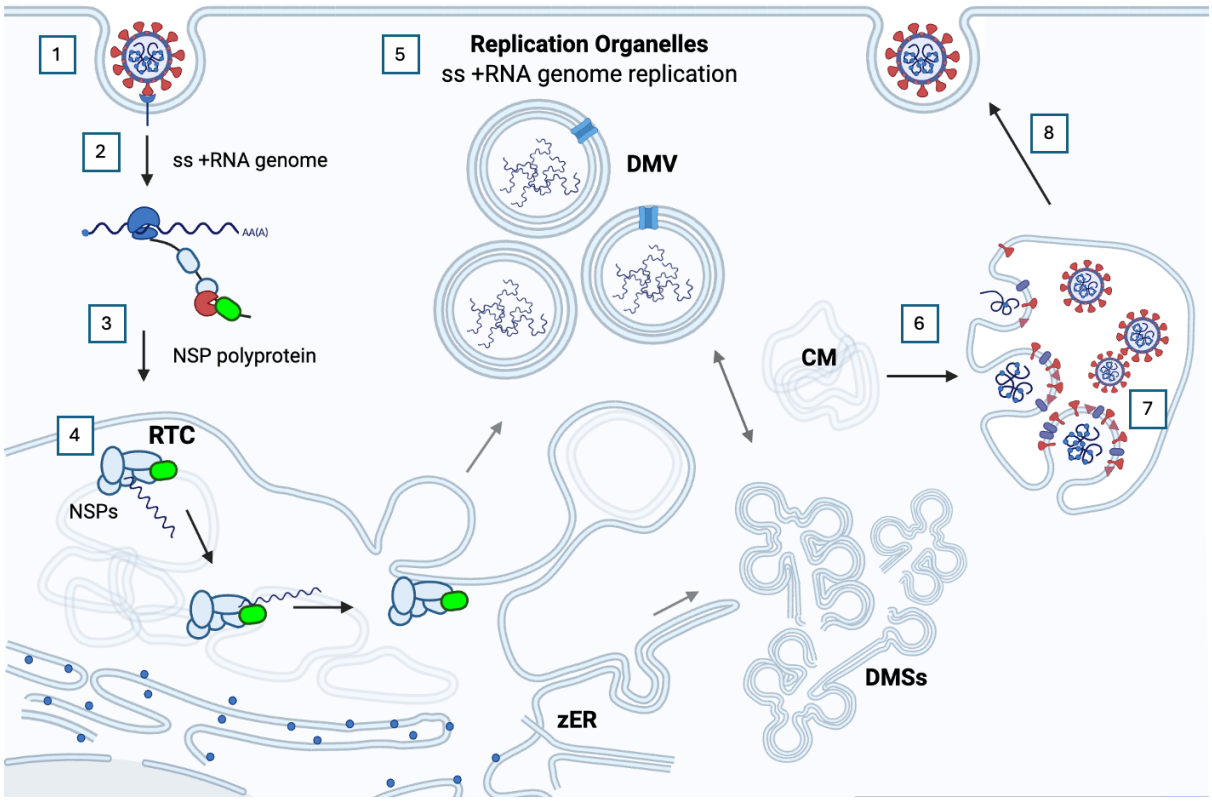


Figure 1. 11 The IBV replication cycle and replication organelles.

(1) IBV enters host cells via spike (S) protein attachment to an unknown receptor, membrane fusion, and endocytosis. (2-3) The IBV genome is released into the cellular cytoplasm and the non-structural proteins (nsps) are translated by the host. (4) The nsps assemble into the replication-transcription complex (RTC). The RTC generates genomic and sub-genomic (sg) RNA via negative-sense intermediates. (5) Nsp expression triggers membrane proliferation and membrane pairing that form replication organelles (ROs) where RNA synthesis takes place. The ROs provide platforms for RTC assembly and compartmentalise viral RNAs into protective microenvironments. ROs appear as convoluted membranes (CM), double membrane vesicles (DMVs), within which viral RNA synthesis occurs, and double membrane spherules (DMSs) tethered to sections of zippered endoplasmic reticulum (zER). (6) The viral structural proteins are translated on host ribosomes and the nucleocapsid (N) protein associates with nascent genomic RNA to form the ribonucleoprotein (RNP). (7) The other structural proteins, S, membrane (M), and envelope (E), embed within the ER-Golgi intermediate compartment and virions bud into the lumen encapsulating the RNP. (8) Progeny virions accumulate in vesicles that are transported to the plasma membrane for release via exocytosis. This figure was created using biorender.com.

The RTC replicates the genome via generation of a negative-sense copy of the genomic RNA that is used as a template for the synthesis of nascent positive-sense RNA genomes. During negative-strand synthesis, discontinuous transcription is used to transcribe the structural and accessory genes (Figure 1.12; Sawicki and Sawicki, 1995). At the 5′ end of the genome

exists the leader transcription-regulating sequence (TRS-L) and then complementary body TRSs (TRS-B) exist upstream of each gene. During negative-strand synthesis, each TRS can stall the RTC, which then template switches and, via complementary base-pairing, the 5′ TRS-L is added to each sgRNA (Perlman and Netland, 2009). The nested set of negative-sense sgRNA transcripts are then transcribed back to positive-sense to be translated into the viral proteins. CoV Transcription is regulated by the base-pairing interactions between positive and negative sense TRSs, viral and host proteins interacting with the transcripts, higher order RNA-RNA interactions, and unique RNA proofreading machinery to maintain the large genome size (Sola *et al.*, 2015).

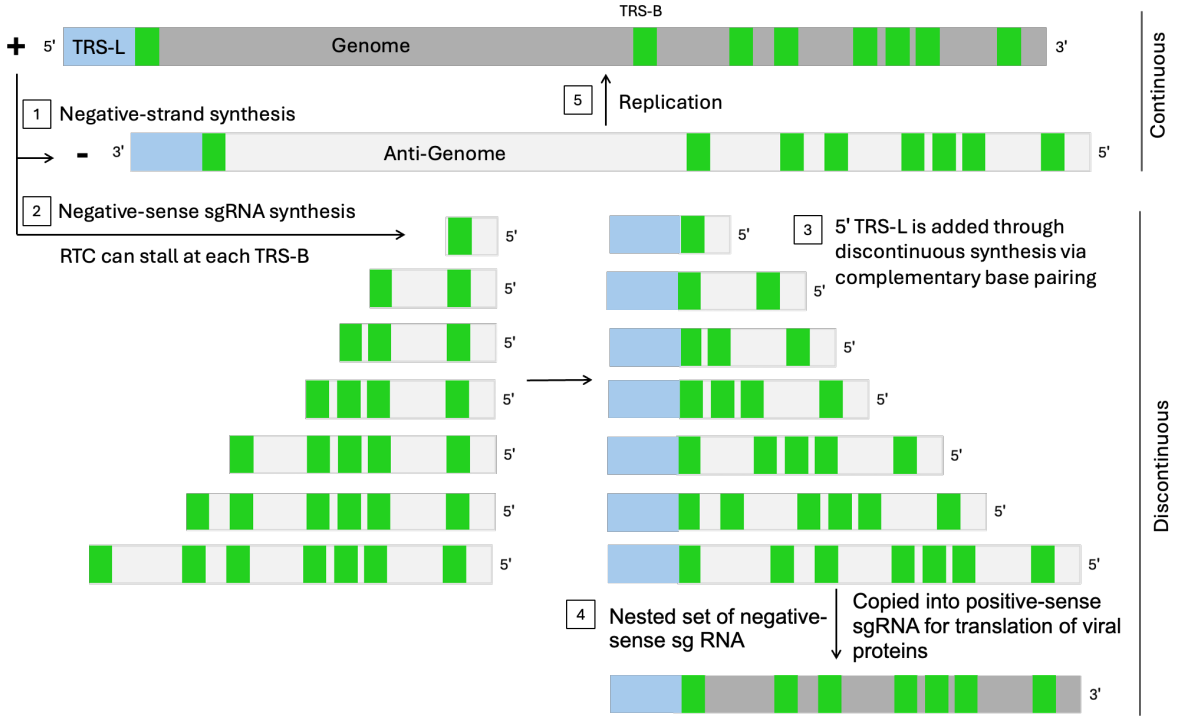


Figure 1. 12 IBV genome replication and discontinuous transcription.

The full-length positive sense genomic RNA is used as a template to produce (1) full length negative-sense copies, for genome replication (5), and (2) negative sense subgenomic RNA (-sg RNA) transcripts. At the 5′ end of the genome exists the leader (TRS-L; blue) and then complementary body TRSs (TRS-B; green) exist upstream of each gene. During -sg RNA synthesis, each TRS can stall the RTC and via complementary base-pairing, the 5′ TRS-L is added to each transcript (3). The nested set of -sg RNA transcripts are transcribed back to produce positive sense subgenomic mRNAs (sg mRNA) that is translated into the viral proteins (4).

The structural proteins are processed in the ERGIC and packaged in ER exit site (ERES) vesicles for virion assembly. For example, Golgi targeting signals have been found in the IBV E cytoplasmic tail and the M TMD (Corse and Machamer, 2002; Swift and Machamer, 1991). The S protein cytoplasmic tail does contain an ER retrieval signal, but S can also be translocated to the cell surface and facilitate syncytia formation (Lontok *et al.*, 2004; Rajah *et al.*, 2022). Furthermore, the N protein has been observed lining up on the cytosolic side of DMV pores in infected cells (Wolff *et al.*, 2020) so from this location it presumably coats the genomic RNA to form a helical RNP via an unknown mechanism. It is also unknown how the RNP is targeted to budding virions. The M protein is thought to scaffold virion assembly via interactions with the other structural proteins such that the structural proteins and RNA are concentrated at the ERGIC, the RNP is encapsulated within the envelope, and virions bud into the ERGIC lumen (Klumperman *et al.*, 1994). CoV viral assembly has been seen in EM of IBV infected cells since 1967 (Becker *et al.*, 1967) and MHV budding was observed at the ERGIC in smooth ER between rough ER and the *cis* side of the Golgi in 1984 (Tooze *et al.*, 1984). Viral assembly was then observed *in situ* under cryogenic conditions for SARS-CoV-2 where the RNP was shown to accumulate on the cytosolic ERGIC membrane and S accumulated on the luminal ERGIC membrane before budding (Klein *et al.*, 2020).

CoV egress may occur via the Golgi apparatus or via endo-lysosomal recycling; several egress pathways have been reviewed (Saraste and Prydz, 2021). Disrupting the structure of the Golgi has been shown to inhibit *Alphacoronavirus* TGEV release but the same was not seen for IBV (Salanueva *et al.*, 1999; Alonso-Caplen *et al.*, 1984). Moreover, IBV E neutralises the pH of the Golgi causing it to dilate and allowing the accumulation of numerous virions

(Westerbeck and Machamer, 2019). On the other hand, MHV has been shown to exit in endosomes directly from the ERGIC, thus bypassing the Golgi, using lysosomal-associated membrane protein 1 (LAMP1) which colocalises with the MHV M protein (Ghosh *et al.*, 2020). IBV M has also been shown to colocalise with Ras- related protein Rab-11 (Rab11) which is involved in endocytic recycling (Saraste *et al.*, 2022). Egress may also occur via a combination of Golgi transport and endosomal compartments to reach the plasma membrane (Luini *et al.*, 2008).

1.5. Viral replication organelles (ROs)

All single-stranded positive sense RNA (+RNA) viruses compartmentalise viral genome replication into replication organelles (ROs) that are derived from modified host membranes. Compartmentalisation is critical for viral replication because the membranes act as sites for the assembly of all components required for viral RNA synthesis. Also, the double stranded (ds)RNA replication intermediates can trigger the host antiviral response (Stok *et al.*, 2020; Rehwinkel and Gack, 2020). Therefore, compartmentalisation within ROs likely prevents or delays host recognition of viral RNAs (Scutigliani and Kikkert, 2017; Du *et al.*, 2018; Neufeldt *et al.*, 2016; Viktorova *et al.*, 2018; Boon and Ahlquist, 2010; Neufeldt and Cortese, 2022).

The +RNA viruses rearrange different host membranes into ROs with a variety of morphologies (Nguyen-Dinh and Herker, 2021; den Boon *et al.*, 2024). RO morphologies have been elucidated by EM for decades and a schematic of the different observations is shown in Figure 1.13. The different RO morphologies of the +RNA viruses are detailed in

Table 1.2 but can be roughly divided into two classes: invaginated spherules and vesicular networks.

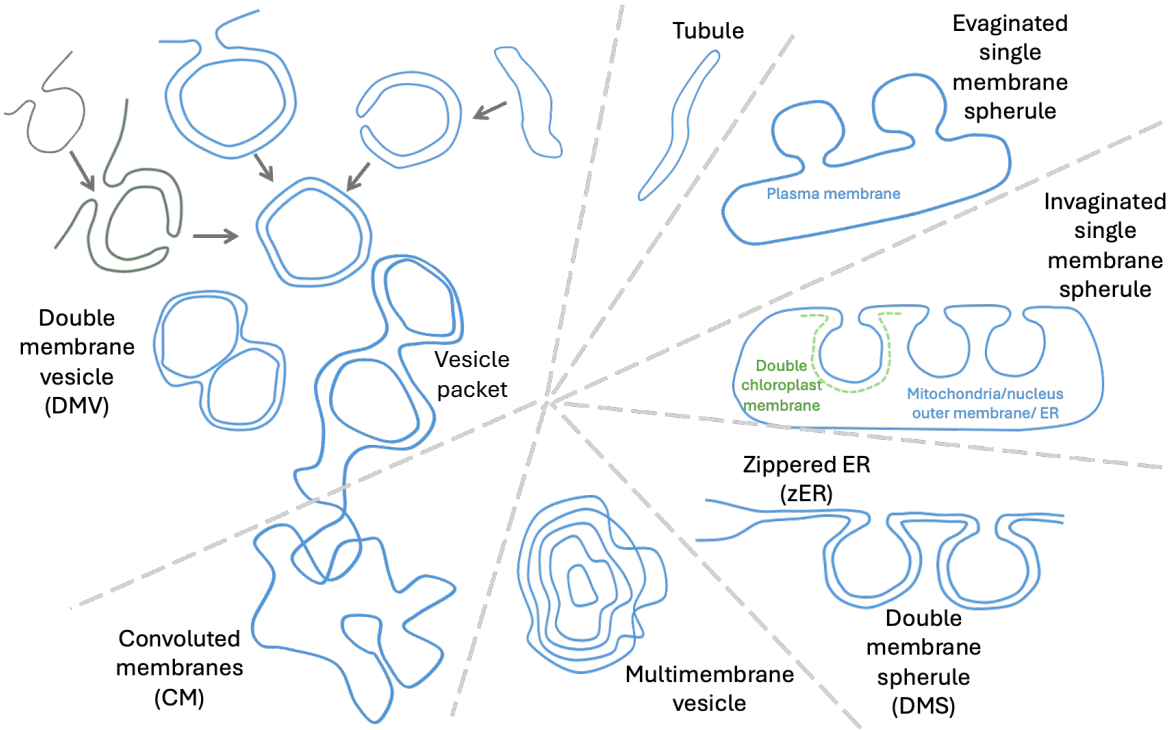


Figure 1. 13 Schematic of membrane rearrangements induced by +RNA virus infection.

Single lines represent sections of phospholipid bilayer, grey lines and arrows represent potential membrane dynamics. Membrane rearrangements are not drawn to scale, double membrane vesicles are typically larger than double and single membrane spherules. Some +RNA viruses induce multiple different membrane rearrangements and the paired membranes in double membrane vesicles appear under EM to be distinct from the DMS zippered membranes. The membrane rearrangements are discussed further in Harak and Lohmann, 2015 and Nguyen-Dinh and Herker, 2021. This figure was made in Microsoft PowerPoint.

Table 1. 2 Morphologies of +RNA virus replication organelles (ROs)

Host	Membrane	RO morphology	Virus	Virus Family	Reference
Plant	Endoplasmic reticulum	Single membrane spherule invagination into nucleus outer membrane/ER	Brome mosaic virus (BMV)	*Bromoviridae*	Schwartz *et al.*, 2002
			Beet black scorch virus (BBSV)	*Tombusviridae*	Cao *et al.*, 2015
		Double membrane-like vesicle with invaginated inner membrane	Turnip mosaic virus (TuMV)	*Potyviridae*	Wan *et al.*, 2015
		Convoluted membranes			
		Single membrane vesicles			
		Multi-membrane vesicle	Peanut clump virus (PCV)	*Virgaviridae*	Dunoyer *et al.*, 2002
		Convoluted membrane inclusion bodies	Wheat yellow mosaic virus (WYMV)	*Potyviridae*	Sun *et al.*, 2014
		Stacked double membranes	Brome mosaic virus (BMV)	*Bromoviridae*	Schwartz *et al.*, 2004
	Golgi	Dilated Golgi	Tomato spotted wilt virus (TSWV)	*Tospoviridae*	Kikkert *et al.*, 1999
	Peroxisome	Multi-membrane vesicle with spherule invaginations	Tomato bushy stunt virus (TBSV)	*Tombusviridae*	Fernandez de Castro *et al.*, 2017
			Cucumber necrosis virus (CNV)		Rochon *et al.*, 2014
	Mitochondria	Multi-membrane vesicle	Melon necrotic spot virus (MNSV)	*Tombusviridae*	Gómez-Aix *et al.*, 2015
			Carnation Italian ringspot virus (CIRV)		Heinze *et al.*, 2004
	Chloroplast	Double membrane spherule invaginations into chloroplast 'cytoplasmic invaginations'	Barley stripe mosaic virus (BSMV)	*Virgaviridae*	Jin *et al.*, 2018
			Turnip yellow mosaic virus (TYMV)	*Tymoviridae*	Li *et al.*, 2016
	Tonoplast	Single membrane spherule invagination into vacuole	Cucumber mosaic virus (CMV)	*Bromoviridae*	Wang *et al.*, 2021

				Tobacco necrosis virus A (TNV-A)	*Tombusviridae*	
Animal	Endoplasmic reticulum	Convoluted membranes		All CoV	*Coronaviridae*	Section 1.6
				Dengue virus (DENV)	*Flaviviridae*	Welsch *et al.*, 2009
				West Nile virus (WNV)		Gillespie *et al.*, 2010
				Zika virus (ZIKV)		Cortese *et al.*, 2017
				Tick-borne encephalitis (TBEV)		Miorin *et al.*, 2013
		Double membrane vesicle		All CoV	*Coronaviridae*	Section 1.6
				Hepatitis C virus (HCV)	*Flaviviridae*	Ferraris *et al.*, 2013
		Invaginated spherule	Single membrane invaginated into ER (~90 nm diameter)	Dengue virus (DENV)	*Flaviviridae*	Welsch *et al.*, 2009
				West Nile virus (WNV)		Gillespie *et al.*, 2010
				Zika virus (ZIKV)		Cortese *et al.*, 2017
				Tick borne encephalitis virus (TBEV)		Miorin *et al.*, 2013
			Tubules within ER	Tick-borne encephalitis (TBEV)	*Flaviviridae*	Bílý *et al.*, 2015
		Zippered ER in the cytoplasm		All CoV	*Coronaviridae*	Maier *et al.*, 2013; Section 1.3.6
				Zika virus (ZIKV)	*Flaviviridae*	Cortese *et al.*, 2017
		Double membrane spherules tethered to zippered ER in the cytoplasm		All CoV	*Coronaviridae*	Maier *et al.*, 2013; Section 1.6
	Mitochondria	Invaginated single membrane spherule (~50 nm diameter)		Flock house virus (FHV)	*Nodaviridae*	Kopek *et al.*, 2007; Ertel *et al.*, 2017
	Golgi	Single and double membrane vesicles		Polio virus (PV)	*Picornaviridae*	Belov *et al.*, 2012
	Lysosome	Cytopathic vacuole with single membrane invaginated spherule		Rubella virus (RUBV)	*Matonaviridae*	Fontana *et al.*, 2010

	Plasma membrane	Evaginated single membrane spherule (~60 nm diameter)	Sindbis virus (SINV)	*Togaviridae*	Frolova *et al.*, 2010
			Chikungunya virus (CHIKV)	*Togaviridae*	Laurent *et al.*, 2022
			Semliki Forest virus (SFV)	*Togaviridae*	Spuul *et al.*, 2010; Kallio *et al.*, 2013

1.5.2. Invaginated spherule ROs

The +RNA virus-induced spherules have been observed to invaginate into a variety of different membranes and organelles and it has been demonstrated that tombusviruses and nodaviruses can adapt to replicate in alternative host organelles (Xu and Nagy, 2014). Multiple observations of spherules from different viruses have been observed by EM and electron tomography (ET) to observe their 3D structure (Welsch *et al.*, 2009; Gillespie *et al.*, 2010; Cortese *et al.*, 2017). The overall architecture involves a spherular pocket, with a diameter between 50 and 150 nm, that is connected to the cytosol by a narrow, neck-like channel. Spherules have been shown to accommodate replication as nascent viral RNA has been observed in their interiors via immuno-EM and autoradiography (Grimley *et al*., 1968; Fernandez de Castro *et al.*, 2017). The architecture then suggested a model by which nucleotide import and export of +RNA for translation and encapsulation into virions would occur via the neck-like channel. Cryo-EM studies later revealed crown complexes at the spherule necks of flock house virus (FHV) and chikungunya virus (CHIKV) that coordinate molecular trafficking and RNA replication (Zhan *et al.*, 2023; Tan *et al.*, 2022).

The spherule crown complex was first observed via cryo-ET of purified mitochondria from cells infected with the nodavirus FHV (Ertel *et al.*, 2017). Using subtomogram averaging

(STA) (Section 1.4), the crown complex was resolved at increasing resolutions revealing a 24-mer of two stacked dodecameric rings with 12-fold symmetry (Unchaniwala *et al.*, 2020; Tan *et al.*, 2022). In FHV, a single protein, protein A, appears to be the sole component of the FHV crown complex (Zhan *et al.*, 2023). FHV protein A is the only protein required for viral RNA replication, and it contains RdRp, 5' RNA capping, membrane, and self-interaction domains (Nishikiori *et al*., 2022). In the STA structure, the C-proximal RdRp domains of protein A form the central neck of the crown and have the same orientation in the two stacked rings. On the other hand, the N-proximal protein A domains have distinct orientations in the basal and apical rings (Zhan *et al.*, 2023). In FHV infected cells, spherules can appear adjacent to virus budding sites so RO nsps may also coordinate viral assembly (Welsch *et al.*, 2009; Gillespie *et al.*, 2010; Barnard *et al.*, 2021).

The alphavirus CHIKV plasma membrane spherule crown complex has also been elucidated by cryo-ET and STA (Tan *et al.*, 2022; Laurent *et al.*, 2022). CHIKV encodes a replicase polyprotein that is cleaved into nonstructural proteins (nsp1-4). Cryo-EM and single-particle analysis (SPA) revealed that nsp1 forms a dodecameric ring (Jones *et al.*, 2021; Jones *et al.*, 2023; Zhang *et al.*, 2021). The nsp1 ring acts as the membrane-embedded scaffold for the nsp4 RdRp and nsp2 helicase/protease (Tan *et al.*, 2022). *In situ*, a larger complex was resolved by STA revealing an additional apical ring that may contain nsp3 and/or host factors (Laurent *et al.*, 2022). The organisation and functions of the alphavirus CHIKV RO are well understood and have been observed *in situ*: the RdRp nsp4 and the helicase/protease nsp2 coordinate and dock into the dodecameric nsp1 channel (Tan *et al.*, 2022). Incorporation of nsp4 into the channel also enhances polymerase activity so crown formation is probably important for the RdRp activity *in vivo.* For the nodavirus, where

protein A appears to be the sole protein of the crown complex, an additional protein A Pol domain that is actively synthesising RNA may sit in the centre of the stacked dodecameric rings (Zhan *et al.*, 2023). RNA capping may be performed by the floor domains of the crown complexes but coordination with virion assembly is not well understood.

Despite the large evolutionary distance between nodaviruses and alphaviruses, the architecture of the spherule neck complex is similar. Therefore, the dodecameric stacked rings may be a common feature of spherules induced by other +RNA viruses. Multiple other +RNA spherules have been observed by classical EM, but the resolving power of cryo-EM and SPA, and *in situ* cryo-ET and STA, are required to reveal the structure and identity of the RO-associated protein complexes in their native state.

Formation of the noda- and alpha-virus crown complexes and their spherule ROs appears concomitant. Proto-crowns (lacking the apical dodecameric rings) have been purified and imaged using SPA and also observed *in situ*. For FHV, if RNA replication is inhibited, proto-crowns appear in ordered arrays on mitochondrial membranes without spherule membrane invaginations (Zhan *et al.*, 2023; Kopek *et al.*, 2010). In CHIKV infected cells, proto-crowns without spherules have been observed alongside full crowns with spherules containing RNA (Tan *et al.*, 2022). Therefore, spherule generation for these viruses seems to be dependent on viral RNA synthesis (Kopek *et al.*, 2010; Spuul *et al.*, 2011). The presence of RNA templates may be the trigger for the formation of the full crown. In this case, the alphavirus proto-crown could recruit the +RNA template, nsp3, and host factors to produce the apical ring and the full complex (Tan *et al.*, 2022). For the nodaviruses, the +RNA template may be recruited by protein A domains on the apical side, the Pol activity could then synthesise -

RNA via dsRNA intermediates to fill a spherule membrane (Laurent *et al.*, 2022; Spuul *et al.*, 2011). This model is supported by the fact that the size of the replicating RNA dictates the volume of the spherule and the RNA content estimated by cryo-ET (Ertel *et al.*, 2017; Kallio *et al.*, 2013; Laurent *et al.*, 2022). Other +RNA viruses however do not require RNA synthesis for spherule formation as exhibited by Bromovirus BMV protein 1a and in Flavivirus DENV infection (Schwartz *et al.*, 2002; Cerikan *et al.*, 2020). Flavivirus spherule formation has also been shown to work by nonstructural (NS) protein-driven concentration of the host ER into a main replication compartment (Ci *et al.*, 2023) and the shape is regulated via interactions between vimentin and viral NS5A protein (Cheng *et al.*, 2023).

1.5.3. Vesicular network ROs

Examples of +RNA viruses that induce extensive vesicular networks include the picornaviruses (Limpens *et al.*, 2011; Belov *et al.*, 2012; Melia *et al.*, 2018), hepaciviruses (Romero-Brey *et al.*, 2012), noroviruses (Doerflinger *et al.*, 2017), and coronaviruses (see Section 1.6). Diverse membrane morphologies are created as described in Table 1.3 but a common structure is the double membrane vesicle (DMV). DMVs are observed as spherical vesicles with two paired membranes and diameters between 100 and 300 nm. Depending on the virus and stage of infection, DMVs may appear open or closed and can appear connected to each other and sections of ER or as distinct vesicles in the cytoplasm. DMVs also appear alongside further membrane arrangements including convoluted membranes (CM), single-membrane vesicles (SMVs) (and/or tubules), and multimembrane vesicles (MMVs) in picornaviruses, hepaciviruses, and noroviruses (Belov *et al.*, 2012; Romero-Brey *et al.*, 2012; Doerflinger *et al.*, 2017).

The picornaviruses encode a single polyprotein which is processed into the nsps and structural proteins. These viruses induce include single membrane structures (SMS) that can flatten into cisternae and then curve into open DMVs which eventually seal; only the viral membrane proteins 2BC and 3A are required for membrane rearrangement (Suhy *et al.*, 2000). Nascent viral RNA labelling shows diverse membrane structures are involved in RNA synthesis, but the single membrane structures were the predominant structures at the peak of RNA synthesis (Melia *et al.*, 2017; Limpens *et al.*, 2011). It is thought that the SMS-embedded picronavirus RdRp faces the cytosol like the RTC in spherules and nidovirus DMVs, but evidence suggests that RNA synthesis does not occur in a closed compartment but rather on the SMS RO surface (Bienz *et al.*, 1992; Lyle *et al.*, 2002). The viral RNAs may be shielded by the replicase complex (Du *et al.*, 2018). Cryo-ET most recently showed that capsid assembly also takes place on the surface of SMS and DMVs suggesting a direct link between RNA synthesis and encapsidation (Dahmane *et al.*, 2022; Nugent *et al.*, 1999). However, the organisation of the RTC and membrane proteins 2BC and 3A on RO membranes is unknown. Picornavirus DMVs also appear to engulf genome-loaded capsids ready for secretion (Dahmane *et al.*, 2022). Picornavirus RO biogenesis likely involves proteins 2BC and 3A, and the function of host COPI in ER-Golgi transport was thought to be required for RO formation and RNA replication but this has been shown to be only the case for poliovirus (Cuconati *et al.*, 1998) and not for encephalomyocarditis virus or parechovirus 1 (Gazina *et al.*, 2002).

Hepatitis C virus (HCV) also encodes a single polyprotein that is processed into 10 different proteins including nonstructural proteins that make up the replicase. The minimal HCV

replicase comprises the nonstructural proteins: NS3, NS4A, NS4B, NS5A and NS5B (Lohmann *et al.*, 1999). The HCV RO network has been modelled in 3D by electron tomography of high-pressure-frozen and freeze-substituted samples (HPF-FS; Section 1.7.2). HCV produces a network of single and double membrane vesicles, the appearance of DMVs correlates with the onset of RNA synthesis, and the network produces more complex arrangements over time including MMVs late in infection (Romero-Brey *et al.*, 2012). HCV replicase nonstructural protein NS4B alone was shown to induce single membrane vesicles, while the NS3-5A polyprotein and NS5A alone were able to produce DMVs (Romero-Brey *et al.*, 2012). These experiments suggest that concerted action of several nonstructural proteins is required for RO biogenesis. Overall, the organisation of the nonstructural proteins and the structure of the HCV RTC within the ROs in unknown.

The noroviruses also induce vesicular networks which harbour the viral replication sites. The norovirus genome contains three ORFs and ORF1 encodes a polyprotein that is autoprocessed into seven nonstructural proteins (NS1-7) involved in viral RNA synthesis. Electron tomography on HPF-FS sections has shown that expression of ORF1 can induce SMVs, DMVs and MMVs. When components of ORF1 were separated, NS1-2 was shown to induce membrane proliferation, NS3 induced convoluted membranes, and NS4 alone was able to induce convoluted membranes, SMVs, and DMVs (Doerflinger *et al.*, 2017). Therefore, the membrane rearrangements can be induced in the absence of viral RNA synthesis. All the nonstructural proteins colocalise with dsRNA in murine norovirus (MNV-1) infected cells (Hyde *et al*., 2009). In the same experiment, dsRNA and NS7 were shown to localise to single membrane vesicles via immunoelectron microscopy and COPI does not

appear to be recruited for RO formation (Hyde *et al*., 2009). However, the *in situ* structure of norovirus ROs is yet to be studied under cryogenic conditions.

1.6. The coronavirus replication organelle

Coronaviruses also induce a membranous network RO. The key conserved elements of the CoV RO are double membrane vesicles (DMVs), with convoluted membranes (CM) and zippered ER (zER). In addition, they induce formation of double membrane spherules (DMSs) (Figure 1.14) (Knoops *et al.*, 2008; Maier *et al.*, 2013; Cortese *et al.*, 2020; Snijder *et al.*, 2020). The DMVs are spherical with diameters of 250-300 nm and DMSs have diameters of 60-80 nm and appear as two membranes pinching from a paired membrane that is continuous with CM or zER. The CM appear as short and highly branched paired membranes and the zER appear as two ER membranes that are held together. All CoVs make these elements but there are differences in the abundance and appearance of the different structures induced by different viruses.

The knowledge of CoV ROs can be supported by studies of other viruses in the *Nidovirales* order, namely the arteriviruses and toroviruses. Like coronaviruses, the arteriviruses also encode nsps within a replicase gene that are autoprocessed to make up the RTC and generate a nested set of sgRNAs to express the structural and accessory proteins. The replicase genes have conserved RdRp and helicase activities and encode three transmembrane (TM) nsps (denoted TM1, TM2 and TM3) that have a range of sizes and numbers of (predicted) transmembrane domains (Gulyaeva and Gorbalenya, 2021). The arteriviruses also produce membranous networks including DMVs connected to ER but

without DMS (Knoops *et al.*, 2012; Zhang *et al.*, 2018). Torovirus infected cells also produce DMVs and regions of paired and curved membranes but DMSs have not been observed (Ávila-Pérez *et al.*, 2016; Ávila-Pérez *et al.*, 2022).

Comparisons so far have predominantly been based on RO structures as they appear in conventional electron micrographs. All CoVs induce DMVs, DMSs, zER, and CM as part of their RO. However, each virus seems to make a different balance of each RO structure (Figure 1.14 A-D). The first CoV RO studies completed with *Betacoronavirus* SARS-CoV and MHV infected cells suggested that DMVs and CM were the predominant and most distinct RO structures observed (Snijder *et al.*, 2006; Goldsmith *et al.*, 2004; Gosert *et al.*, 2002; Ulasli *et al.*, 2010). Then, for cells infected with the *Gammacoronavirus* IBV, DMVs were observed, but CM was rarely observed and rather, well-defined zER and DMSs, tethered to zER, were the predominant structures (Maier *et al.*, 2013) (Figure 1.14 C). Subsequently, *Betacoronavirus* MERS-CoV was also shown to induce abundant DMSs, however, the zER it was tethered to appeared shorter and highly branched (more like CM) compared to IBV zER (Snijder *et al.*, 2020) (Figure 1.14 B). MERS-CoV DMSs had previously been described as CM (de Wilde *et al.*, 2013). The *Alphacoronaviruses* PDEV and HCoV-229E have also been observed to predominantly induce DMVs and CM while DMSs appear scarce (Zhou *et al.*, 2017; Snijder *et al.*, 2020) (Figure 1.14 A). Finally, the porcine *Deltacoronavirus* RO was also shown to comprise all RO structures: DMVs, zER, and DMSs (Doyle *et al.*, 2019) (Figure 1.14 D). This highlights the variability of the CoV RO between and within the genera. The reason for CoV RO variability is unclear and the dynamics of the different RO structures, such as whether different structures form at different stages of infection, are not well understood. Furthermore, there is some understanding of the nsps involved in DMV formation for some

Betacoronaviruses (Angelini *et al.*, 2013). However, the complete RO has not been recapitulated outside of whole replicating virus infections. Therefore, there is still a gap in the knowledge surrounding the involvement of viral and host factors in RO biogenesis and the membrane curvature, budding, or wrapping mechanisms that may produce these structures. Understanding RO formation mechanics, which may be rapid events, is currently dependent on imaging intermediate structures within fixed samples so they have proved difficult to define. It must also be considered which ultrastructural imaging technique is used and how artifacts will affect the descriptions of different membranes (Romero-Brey and Bartenschlager, 2015).

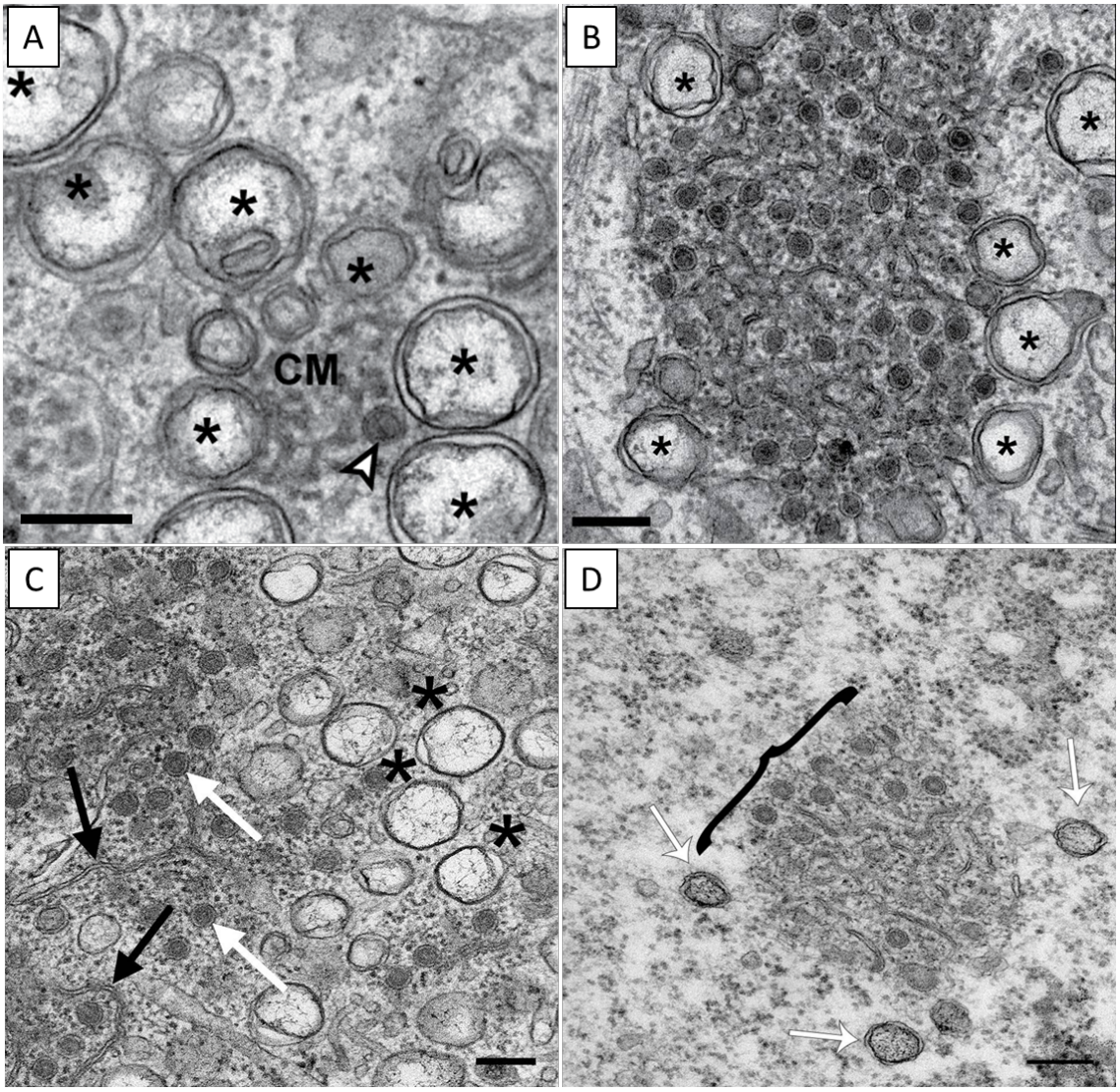


Figure 1. 14 Universal coronavirus replication organelle structures observed by electron microscopy.

In *Alphacoronavirus* human coronavirus 229E (HCoV-229E) infected cells (panel A, Snijder et al., 2020 (modified)), convoluted membranes (CM) and a single double membrane spherule (DMS) appeared interspersed with double membrane vesicles (DMVs) (B) In *Betacoronavirus* Middle East respiratory syndrome coronavirus (MERS-CoV) infected cells (Snijder et al., 2020 (modified)), the DMSs appeared alongside DMVs in an abundant cluster surrounded by CM which were more commonly imaged than long sections of zippered ER (zER) (C) In *Gammacoronavirus* infectious bronchitis virus (IBV) infected cells (Maier et al., 2013 (modified)), longer sections of zER were observed with multiple DMS curving the zippered double membrane sheet into equally- sized spheules (D) In *Deltacoronavirus* porcine deltacoronavirus (PDCoV) infected cells (Doyle et al., 2019 (modified)), DMVs, zER and DMSs were observed. DMVs are marked with asterisks (A-C) and white arrows (D). DMSs are marked with white arrowheads (A), white arrows (C), a black bracket (D) and a cluster is shown in B. Zippered ER is marked with black arrows (C). Scale bars, 250nm (A, B), 200nm (C), and 500nm (D).

In 2002, MHV nsps and viral RNA were localised to DMVs via IEM and EM in situ hybridization (EM-ISH), furthermore, BrU-labelling identified nascent RNA at DMVs (Gosert *et al.*, 2002). Next, IF showed that SARS-CoV nsp3, nsp5, nsp8, nsp9, nsp12 and nsp13 colocalise and IEM using the same antibodies showed that nsp3, nsp8, and nsp13 colocalise to the outside of DMVs but ER marker proteins do not (Snijder *et al.*, 2006). Stertz *et al.* (2007) also used IEM to show colocalisation of nsp3 to membrane rearrangements. In another IEM experiment, SARS-CoV nsp8 was shown to sparsely label the DMV interior and nsp3 and nsp5 were shown to sparsely label the DMV membrane but all three nsps were abundantly labelled in the CM (Knoops *et al.*, 2008). In the same study, dsRNA antibodies labelled the interior of SARS-CoV DMVs as well as CM (Knoops *et al.*, 2008). Fluorescent reporter fusions to MHV nsp2 and nsp3 have also proved to be tolerated and can be used to visualise these nsps without antibody labelling (Freeman *et al.*, 2014). The MHV GFP-nsp3 has since been used to decipher nsp3 as a component of the DMV pore (Wolff *et al.*, 2020). More recently, nsp7, nsp8, nsp9, nsp12, and nsp13 were shown to be located inside HCoV-229E DMVs (Chen *et al.*, 2024).

1.6.1. Coronavirus double membrane vesicles (DMVs)

DMVs appear as spherical vesicles with two membranes and diameters of 250-300 nm that are occasionally interconnected or connected to the ER via their outer membrane as part of a reticulovesicular network (Klein *et al.*, 2020; Snijder et al*.,* 2020, Wolff *et al.*, 2020). In chemically fixed and dehydrated samples the DMV double membrane appears loosely apposed but in fully hydrated cryo-preserved samples, the DMV double membrane is held at

an even distance around the surface area (Klein *et al.*, 2020). HPF-FS is an alternative technique that gives better preservation than chemical fixation. The effects of different sample preparation techniques for imaging IBV DMVs and HCV DMVs have been described (Maier *et al.*, 2013; Romero-Brey and Bartenschlager, 2015). In both dehydrated and hydrated samples, areas where the DMV double membrane joins have been observed.

For SARS-CoV, during the exponential phase of RNA synthesis, the number of DMVs expands into a large reticulovesicular network with a cluster of DMVs that are interconnected via their outer membrane which is also continuous with the ER and other virus induced membrane rearrangements (Figure 1.15 B-C) (Knoops *et al.*, 2008). It is not clear how the DMVs progress into a network. Moreover, these large DMV networks appear significantly less in EM of IBV infected cells where individual DMVs appear more common even at later hours post infection (Maier *et al.*, 2013). So far, only late stage IBV ROs have been imaged so the appearance of the IBV RO early in infection, and the progression of the IBV RO over time, is less clear. Interestingly, the inner membrane of DMVs was found to be completely sealed, with no visible connections to the cytoplasm.

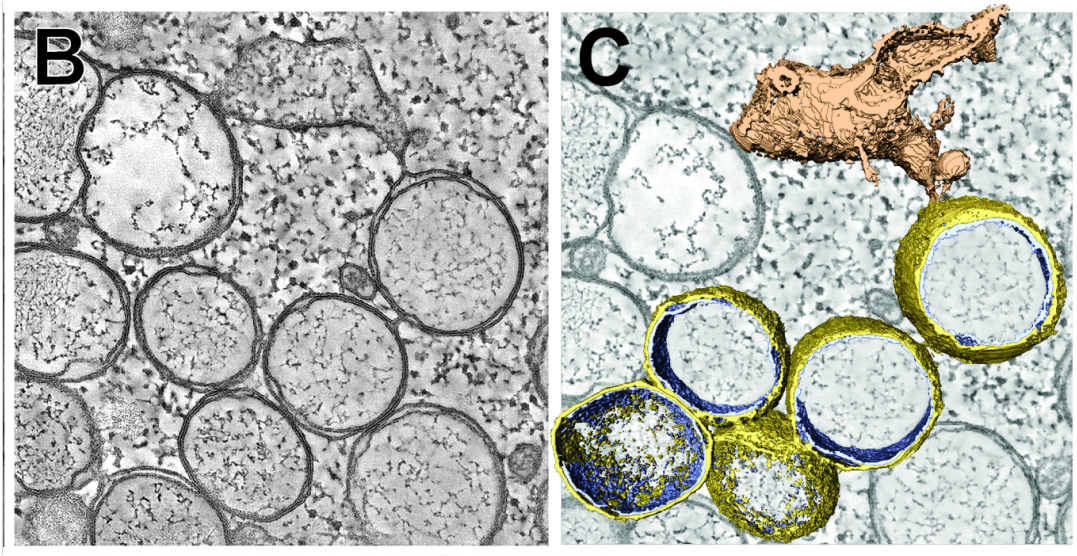


Figure 1. 15 Networks of double membrane vesicles (DMVs) induced by SARS-CoV.

(B-C) DMVs appear interconnected by their outer membrane and to sections of ER; modified from Knoops *et al.*, 2008.

DMVs are now known to be the primary sites of CoV RNA synthesis. Immunocytochemistry electron microscopy (IEM) had been used to show that nascent RNA localised to ROs (Gosert *et al.*, 2002) and colocalises with nsps (Hagemeijer *et al.*, 2012). IEM also showed that dsRNA labelling accumulated on SARS-CoV DMVs and, while distinct DMSs were not imaged, there was also labelling on regions of CM (Knoops *et al.*, 2008) (Figure 1.16 A). This was supported more recently by metabolic labelling of nascent viral RNA and visualisation by EM autoradiography which showed that nascent viral RNA was primarily associated with DMVs and did not appear to be associated with other virus-induced structures (Figure 1.16 B-C) (Snijder *et al.*, 2020). IEM experiments of arterivirus infected cells have also shown that viral replicase subunits and nascent viral RNA localise to DMVs (Pedersen *et al.*, 1999). Then, CoV viral RNA synthesis was confirmed to take place inside membrane bound compartments (Doyle *et al.*, 2021). This agreed with experiments that indicated that the viral RNA synthesis must be secluded from the cytoplasm in a membrane compartment (van Hemert *et al.*, 2008).

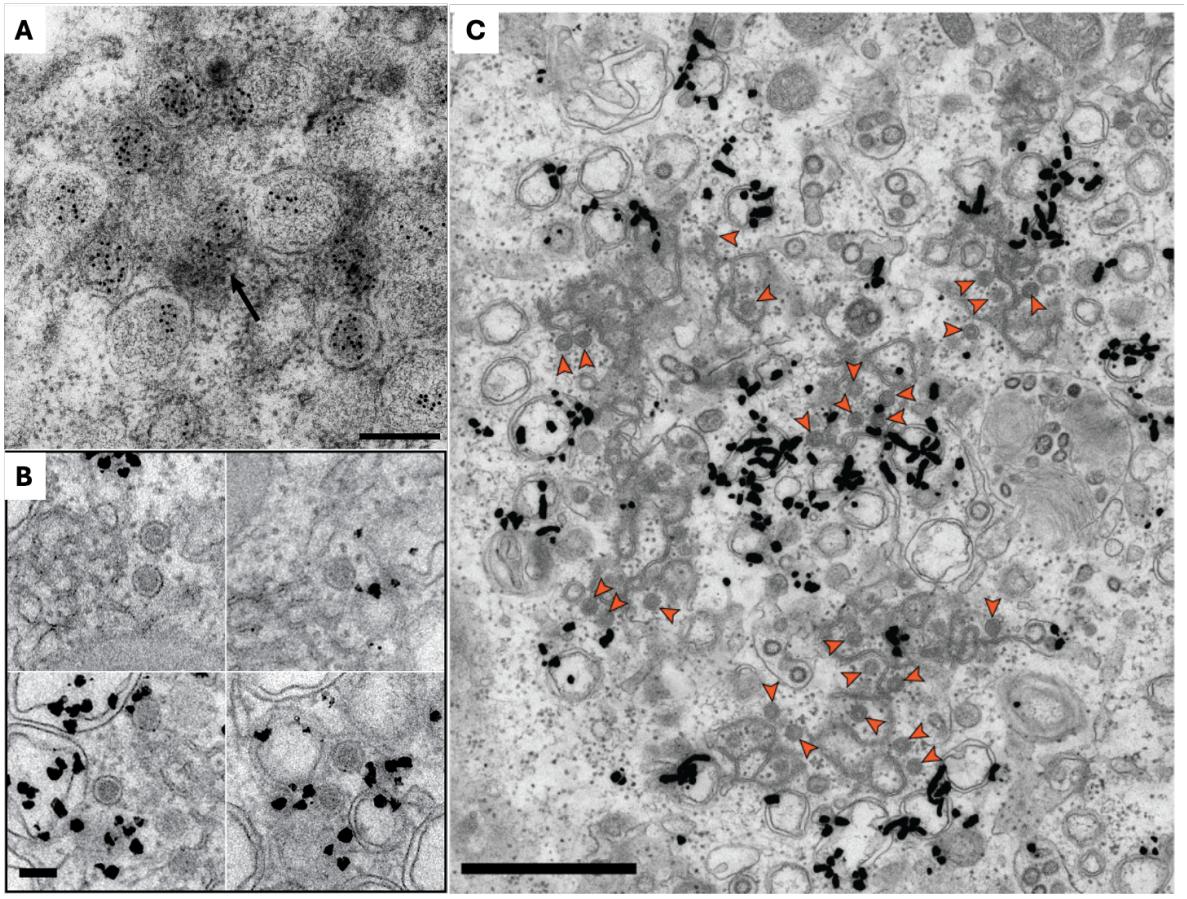


Figure 1. 16 dsRNA and nascent viral RNA associate with DMVs but do not clearly associate with CM or DMSs.

(A) Immunogold EM labelling of dsRNA (dark black densities) is primarily located in the interior of SARS-CoV DMVs; there is additional labelling in convoluted membranes labelled with a black arrow, scale bar is 250 nm; modified from Knoops *et al.*, 2008. (B) Nascent viral RNA of MERS-CoV labelled with tritiated uridine imaged by autoradiography electron microscopy, scale bar is 100 nm; modified from Snijder *et al*., 2020. DMVs are densely labelled with tritiated uridine autoradiography signal while CM and DMSs are relatively devoid of autoradiography signal. (C) Nascent viral RNA of IBV labelled with tritiated uridine imaged by autoradiography electron microscopy, scale bar is 1 μm; modified from Snijder *et al*., 2020. DMVs are densely labelled with tritiated uridine autoradiography signal while zippered ER and DMSs (orange arrowheads) are relatively devoid of autoradiography signal.

However, for translation and packaging into virions, the nascent sg RNAs and genomic RNA must be able to exit from the sealed DMV interior into the cytosol. Significantly, in 2020, using advances in cryo-focused ion beam milling, cryo-ET, and STA, double-membrane spanning, crown-shaped molecular pores were observed in CoV DMVs (Wolff *et al.*, 2020). The pore structure was estimated to have a mass of ~3 MDa and consist of a hexameric

crown on the DMV surface, a membrane region with 12-fold symmetry, and a central channel large enough for viral RNA transport. In the same study, using MHV with a GFP-tagged nsp3, the hexameric crown was determined to consist of 6 copies of nsp3 with their N-terminal domains making the prongs of the crown (Freeman *et al.*, 2014; Wolff *et al.*, 2020). This crown complex at the interface between the RO interior and the cytosol resembles the crown at the neck of the invaginated spherule RO seen in other +RNA viruses. However, the diameter of the cytoplasmic ring of the DMV pore is 9 nm and the CHIKV and FHV spherule crowns have diameters of 15.6 and 19 nm respectively (Huang *et al.*, 2024; Tan *et al.* 2022; Zhan *et al.*, 2023). The localisation of the cytoplasmic crown suggests that it may act as a gate to export +RNA transcripts and seclude -RNA transcripts and dsRNA intermediates. The location of the rest of the RTC is not known, although analysis of the MHV pore revealed additional electron densities that were not resolved but could correspond to other components of the RTC (Wolff *et al.*, 2020). Furthermore, nucleocapsids of PRRSV (another Nidovirus) have been observed associated to DMV pores suggesting that the RNP is formed at the cytosolic side of the pore as RNA exits (Wolff, 2022). As well as the crowns acting as a gate, the full complex may also be involved in RO formation and structural maintenance, scaffolding the RdRp complex, RNA capping, and RNP formation. Therefore, different conformations of the pores with additional electron densities may be expected to allow a dynamic RTC to perform several functions. Cryo-ET of ROs from virus-infected cells has only been completed so far for *Betacoronaviruses* MHV, SARS-CoV, and SARS-CoV-2 and only the MHV pore has been modelled via subtomogram averaging (Wolff *et al.*, 2020; Klein *et al.*, 2020; Mendonça *et al.*, 2021). Taken together, the evidence now demonstrates the DMV as a sealed replication compartment where RNA synthesis takes place with a mechanism for exchange of material with the cytoplasm.

RTCs involving structures confirmed to be the RdRp are yet to be observed in CoV-induced DMVs. This may be a difficult complex to resolve *in situ* since *in vitro* cryo-EM has resolved reconstituted RdRp complex with various nsp composition and stoichiometries, and molecular weights (between ~150 to 300 kDa) (Malone *et al.*, 2022; Lou and Rao, 2022; Yang and Rao, 2021). The structural heterogeneity of the CoV RdRp may be required *in vivo* to perform different functions (genome replication, sgRNA synthesis, RNA capping) thus making *in situ* structural determination by cryo-ET and STA difficult. However, recent proximity labelling STED microscopy, immunoprecipitation, immunoblotting, and mass spectrometry experiments on *Alphacoronavirus* HCoV-229E DMVs have shown that the active viral replicase involving nsp7, nsp8, nsp9, nsp12, and nsp13 is located inside DMVs (Chen *et al.*, 2024). Therefore, viral mRNA synthesis occurs inside the DMV lumen and the nascent transcripts then exit via the nsp4-lined pore. For gRNA encapsidation, densities consistent with the helical CoV RNP (~15 nm diameter) have been observed associated to the cytosolic side of DMV pores (Gui *et al.*, 2017; Wolff, 2022); the same has been observed in arterivirus infection (another nidovirus) (Wolff, 2022). Supporting this, the CoV nsp3 NTD which make the DMV crown prongs has been shown to interact with single stranded RNA and N (Serrano *et al.*, 2007; Hurst *et al.*, 2013; Bessa *et al.*, 2022). Previously, the nsp3-N interaction has been shown to be critical for optimal viral RNA synthesis and it may also be involved in gRNA encapsidation (Cong *et al.*, 2020). Once more, multiple conformations may be required for different functions as the sgRNAs make up 90 % of the viral RNA species made and these do not need packaging into particles (de Beijer *et al.*, 2024). This may function via different RNA signals, and RdRp and pore conformations reacting to increasing

concentrations of N in the cytosol that eventually trigger a switch from translation to encapsidation.

1.6.2. Coronavirus convoluted membranes (CM), zippered ER (zER), and double membrane spherules (DMSs)

Convoluted membranes (CM), highly branched and overlapping networks of paired membranes, were first described as prominent elements of the *Betacoronavirus* RO alongside DMVs in SARS-CoV and MHV infected cells, CoV from other genera were yet to be studied (Knoops *et al.*, 2008; Ulasli *et al.*, 2010). Then, double membrane spherules (DMSs) tethered to zippered ER (zER) were described for the first time in *Gammacoronavirus* IBV infected cells (Maier *et al.*, 2013) (Figure 1.17 A). These DMSs were described as uniformly sized, spherular paired membranes pinching from sections of zER in which two ER membranes become tightly apposed together (Figure 1.17 B). The pinched region of double membrane is referred to as the DMS neck, and the spherular region is referred to the DMS head. While straight sections of zER are observed, zER also curves into DMSs and individual DMS can appear along a section of zER, or clusters of multiple DMSs in proximity appear tethered to zER/CM like a bunch of grapes (Figure 1.17 A-B). The DMSs were then further observed in *Deltacoronavirus* PDCoV infected cells tethered to short stretches of zER (Doyle *et al.*, 2019). After the DMSs were described for IBV and PDCoV, *Betacoronavirus* MERS-CoV was also shown to induce extensive networks of DMSs tethered to short and highly branched zER/CM, while other *Betacoronaviruses* SARS-CoV and MHV, plus *Alphacoronavirus* HCoV 229E, were shown to induce DMS that were scarcer and integrated with CM without long or defined zER (Snijder *et al.*, 2020). Therefore, a unified model of the

CoV RO across the genera involving DMVs, CM/zER and DMSs has now been described (Snijder *et al.*, 2020) (Figure 1.4). Although always present, the abundance and precise appearance of CM/zER and DMSs shows variation among CoVs. In addition, although nsps have been shown to localise to CM, only DMVs were found to play a role in CoV RNA synthesis (Snijder *et al.*, 2020). Therefore, the role of these other elements of the RO during CoV replication is unclear. Fully understanding the variation of the DMS/CM/zER phenotype within the family will require the study of more viruses. So far, cryo-ET experiments have focused on *Betacoronavirus* infection (MHV, Wolff *et al.*; SARS-CoV-2, Klein *et al.*, 2020 and Mendonça *et al.*, 2021), where DMV membrane networks have been defined, but the DMSs have not been observed in their native-hydrated state.

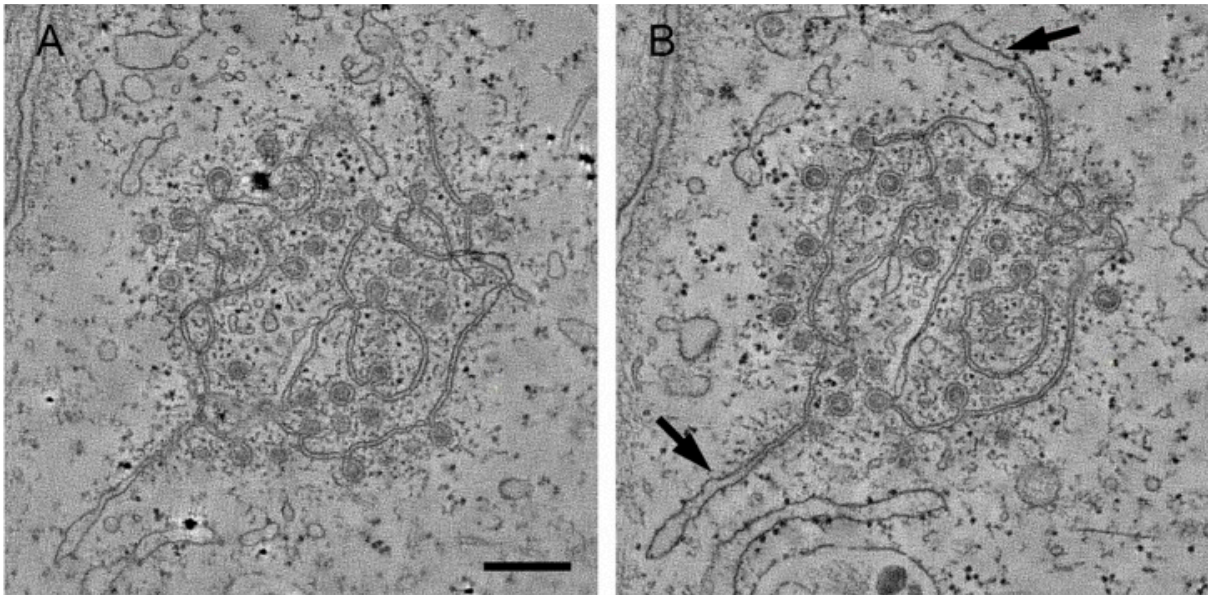


Figure 1. 17 Zippered ER (zER) forming double membrane spherules (DMS).

Zippering ER is marked with black arrows in panel B. Double membrane spherules are tethered to the zER and appear to form via zER curvature. Scale bar in panel A indicates 50nm. Modified from Maier *et al.*, 2013.

From EM of chemically fixed, resin embedded, and heavy metal-stained sections, the double membrane of DMSs is held at an even distance around the DMS head and along sections of zER. DMSs have also been observed to have electron dense material surrounding the double

membrane and lining the inner membrane in the interior of the spherule heads; this makes the DMSs appear much darker in electron micrographs compared to the double membrane of DMVs. Furthermore, the DMV membranes stay together in cells fixed by HPF but separate in chemically fixed cells, while for DMSs and zER, the membranes are always held together in chemically fixed or HPF samples. The average diameter of the DMSs has been shown to be 80.3 nm in chemically fixed samples, and 62.3 nm in HPF-FS samples (Maier *et al.*, 2013).

CoV DMSs are distinct from the spherules of other +RNA viruses because they are not evaginated or invaginated into other compartments but instead exist from zER/CM in the cytoplasm. Also, it is rare for spherules to have a double membrane as all other +RNA virus spherules are single membranes except for those that invaginate into chloroplasts (which have a double membrane) (Barley stripe mosaic virus (BSMV), Jin *et al.*, 2018; Turnip yellow mosaic virus (TYMV), Li *et al.*, 2016). Interestingly, although mitochondria also have double membranes, +RNA viruses that use mitochondrial membranes to produce spherules only invaginate into the outer mitochondrial membrane (Flock house virus (FHV), Kopek *et al.*, 2007).

The mechanism of DMS formation is unknown and the presence of a channel connecting the spherule to the cytoplasm remains unclear. The neck was originally found to remain open to the cytoplasm with the inner and outer membranes continuous with the zER and other DMS (Maier *et al.*, 2013) (Figure 1.18 A-C). Later work suggested that the inner membrane may seal and define a closed compartment while the outer membrane remains continuous with CM or zER and adjacent DMSs (Snijder *et al.*, 2020) (Figure 1.18 D). The neck domains have a

variety of widths which may depict different stages in formation or functions. It is unknown whether a complex exists at the DMS neck to stabilise the highly curved double membrane similar to the crown complexes of single membrane invaginated spherules, or whether another mechanism is employed to create the DMS structure.

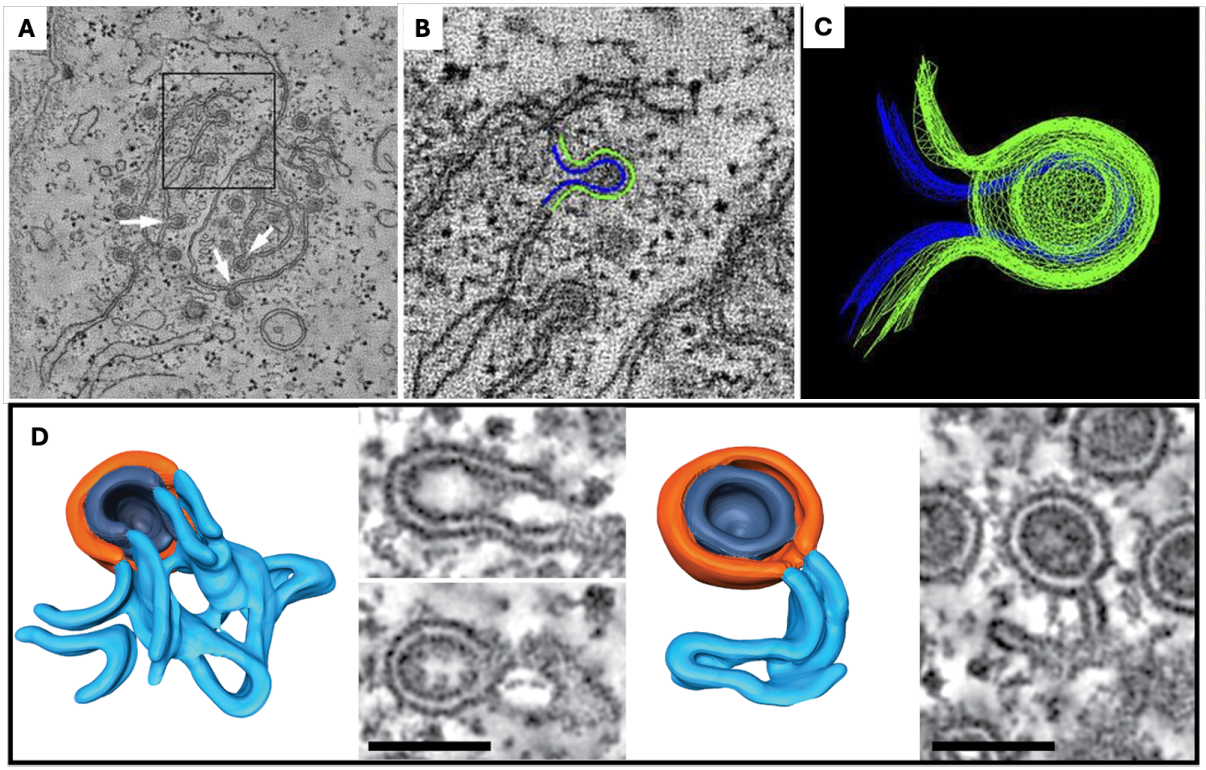


Figure 1. 18 The double membrane spherules (DMS) first described in *Gammacoronavirus* IBV infected cells and observed in *Betacoronavirus* MERS-CoV infected cells by electron tomography at room temperature.

(A) The spherules do not appear invaginated into a membranous compartment but zippered ER membranes fold and curve to form individual spherules with a clear channel connecting the cytoplasm and double membrane spherule (DMS) interior (white arrows). The DMS highlighted in panel A was segmented in panel B with the outer membrane in green and inner membrane in blue. (C) The three-dimensional mesh model of the segmented spherule shows the open channel between the cell cytoplasm and the interior of the double membrane spherule. (A-C) Modified from Maier *et al.*, 2013. Panel C was segmented in Imod. (D) Segmented DMSs of *Betacoronavirus* MERS-CoV (Modified from Snijder *et al.*, 2020), scale bars are 100nm.

The function of DMSs is unknown, although they do not play a role in RNA synthesis (Snijder *et al.*, 2020). If the DMSs do not function in RNA synthesis, analogies cannot be drawn from the single membrane spherular ROs for which the crown complexes shave been shown to perform viral RNA synthesis, so it is difficult to hypothesise their function. The size of DMSs

is uniform, material is observed in the DMS interior, and they are always present in CoV infected cells, albeit to varying extents. This suggests that the DMSs form in a controlled manner which is likely to require a high energy burden since two membranes are curved and held in opposing directions, thus supporting the hypothesis that the DMSs are likely to serve some function.

1.6.3. Coronavirus RO biogenesis

1.6.3.1 Proteins involved in membrane rearrangements

The mechanism of DMV formation has been studied over the last 20 years. First it was shown that SARS-CoV nsp3, nsp4 and nsp6 (the TM1, TM2, and TM3 nsps) can induce DMVs in the absence of viral RNA synthesis (Angelini *et al.*, 2013). Then, it was shown that co-expression of MERS-CoV and SARS-CoV nsp3 and nsp4 alone is sufficient to form DMVs (Oudshoorn *et al.*, 2017). Several experiments also highlighted the importance of nsp4 in *Betacoronavirus* membrane rearrangements. Gadlage *et al.* (2010), Beachboard *et al.* (2014) and Clementz *et al.* (2008) showed that mutations in MHV nsp4 alter the induced membrane rearrangements. The interaction between nsp3 and nsp4 was also shown to be important for DMV biogenesis (Hagemeijer *et al.*, 2014; Sakai *et al.*, 2017; Huang *et al.*, 2024). In particular, the nsp3 C-terminal domain (including the TMD-ectodomain-Y1 domain) was shown to be required for interaction with nsp4 and membrane rearrangement (Hagemeijer *et al.*, 2011; Hagemeijer *et al.*, 2014). Further transfections using cleavage-deficient nsp3-nsp4 produced multi-layer vesicles with paired membranes but no DMVs or nsp complexes were observed (Oudshoorn *et al.*, 2017; Zimmerman *et al.*, 2023; Huang *et*

al., 2024). Therefore, DMV formation is dependent on nsp3-nsp4 cleavage, and this suggests that the DMV and pore form together.

Additional expression of SARS-CoV-2 nsp6 alongside the nsp3 and nsp4 was shown to reconstitute DMVs with a size and uniformity that more closely resembled those observed during infection (Ricciardi *et al.*, 2022). In the same paper, connectors to DMVs were shown to be tracts of nsp6-zippered ER that restrict ER protein transport into DMVs but allow lipid flow. The ER connectors are zippered via nsp6 homodimerisation and amphipathic helix interactions. Plus, SARS-CoV nsp6 was shown to establish contact with lipid droplets (LDs) via the LD-tethering complex DFCP1-RAB18 (Ricciardi *et al.*, 2022). These interactions suggest that nsp6 is important for regulating lipid transport and the spatial organisation of DMV clusters. Moreover, the small molecule inhibitor K22 has been shown to inhibit HCoV-229E DMV formation, while mutations in nsp6 conferred resistance to K22, so nsp6 is likely to play an important role in DMV formation (Lundin *et al.,* 2014). For MHV, just the nsp3 transmembrane and C-terminal domains alongside nsp4 are required to recruit nsp6 as well as nsp2 (Hagemeijer *et al.*, 2014).

It is important to note that the transfection cassettes lack other components known to interact in the viral RTC and which localise inside DMVs (Chen *et al.*, 2024). For RNA synthesis, the other nsps would also be involved so the spatiotemporal polyprotein processing of nsp release into the RTC may be linked to DMV and pore formation. Examples of open DMVs have been observed in cells infected with the nidoviruses EAV and SARS-CoV-2 but these structures are rarely captured so they may represent short-lived intermediates

of DMVs that are typically closed and use pores for controlled molecular trafficking (van der Hoeven *et al.*, 2016; Cortese *et al.*, 2020).

CoV nsps 3, 4, and 6 are accepted as functional homologues with conserved domain and secondary structure. However, their amino acid sequence homology ranges from just 13.4 to 25.9 % between *Gammacoronavirus* IBV (BeauR) and *Betacoronavirus* MHV (A59). Significantly, IBV nsp3, nsp4, and nsp6, when expressed singly or in combination, were not sufficient for recapitulating DMVs (Doyle *et al.*, 2018). The only membrane rearrangement observed was with IBV nsp4 alone which was able to induce membrane pairing (Doyle *et al.*, 2018); this has not been observed for nsp4 alone from other CoV. For example, MERS-CoV nsp4 membrane rearrangements have been described as clusters of modified single membranes (Oudshoorn *et al.*, 2017) and SARS-CoV nsp4 alone is not reported to modify host membranes (Angelini *et al.*, 2013). Evidently, there are differences in the functions of nsps between the CoV genera that impact RO formation.

1.6.3.2. Minimal SARS-CoV-2 nsp3-4 pore insights into membrane curvature

In later experiments, using cryo-ET, expression of SARS-CoV-2 nsp3-nsp4 constructs proved to be sufficient to reconstitute DMV-spanning pores which is dependent on nsp3-4 proteolytic cleavage (Zimmerman *et al.*, 2023; Pahmeier *et al.*, 2023). The minimal SARS-CoV-2 nsp3-4 DMV-spanning pore has now been resolved to 4.2 Å (Huang *et al.*, 2024). Here, the pore consisted of twelve copies of nsp3 and twelve copies of nsp4 each with six long (L) and six short (S) forms. Each hexamer then stacked to make four concentric rings with a central ring of positively charged arginine residues suggesting a mechanism for RNA

translocation (Huang *et al.*, 2024). The protomers of nsp3 and nsp4 have different conformations depending on which hexameric ring they are in. This is important because it highlights the conformational variability of these nsps in multiple copies in the same complex. Although these minimal SARS-CoV-2 nsp3-4 pores resemble the MHV DMV pore observed *in situ* (Wolff *et al.*, 2020), the RNA synthesis machinery is not present in the minimal expression system so there are likely additional viral and/or host components included in the functional pore which may be responsible for some of the unassigned densities in the Wolff *et al.* (2020) structure.

In the 4.2 Å resolution model, the topology of the nsp3 and nsp4 domains within the minimal pore were resolved (Figure 1.19) (Huang *et al.*, 2024). The two N-terminal domains (NTDs) of nsp3 were not visible and they have been shown to be dispensable for DMV formation (Zimmerman *et al.*, 2023). Therefore, it was suggested that the rest of the nsp3 NTDs including the PL^{pro} domain make up the prongs of the DMV cytosolic crown. As well, the nsp3 C-terminal domain (CTD) and nsp4 were shown to be sufficient to form zippered and curved membranes (Hagemeijer *et al.*, 2014). Interestingly, the nsp3 CTD is highly conserved across the nidoviruses while the nsp3 NTD crown and prongs are highly variable (Neuman, 2016). After the nsp3 NTD cytosolic prongs, the first transmembrane helix (TMH; TM1) puts a small ectodomain (59 residues) within the intermembrane space, before two TMHs (TM2 and TM3), a short horizontal helix, and TM4, put the C-terminal domains (CTDs) in the cytosol. Continuing along the polypeptide, after the nsp3 CTD is the nsp3-nsp4 cleavage site. Next, at the N-terminus of nsp4 exists its first TMH which, interestingly, was unable to be resolved at the periphery of the minimal pore structure, but the large 240 residue nsp4 ectodomain was observed in the intermembrane space (Huang *et al.*, 2024).

Finally, 5 TMHs (TM2-6) put the nsp4 CTD into the lumen of the DMV. One nsp4 hexamer lines the central pore on the DMV luminal side. Then, the second nsp4 hexamer combines TM2 and TM3 of each protomer into a long, continuous, and curved helix that rotates the angle of the ectodomains and CTDs. This nsp4 organisation resembled the Feline CoV nsp4 crystal structure (Manolaridis *et al.*, 2009). Once more, this emphasises that these nsps can have multiple complementary conformations within the same complex.

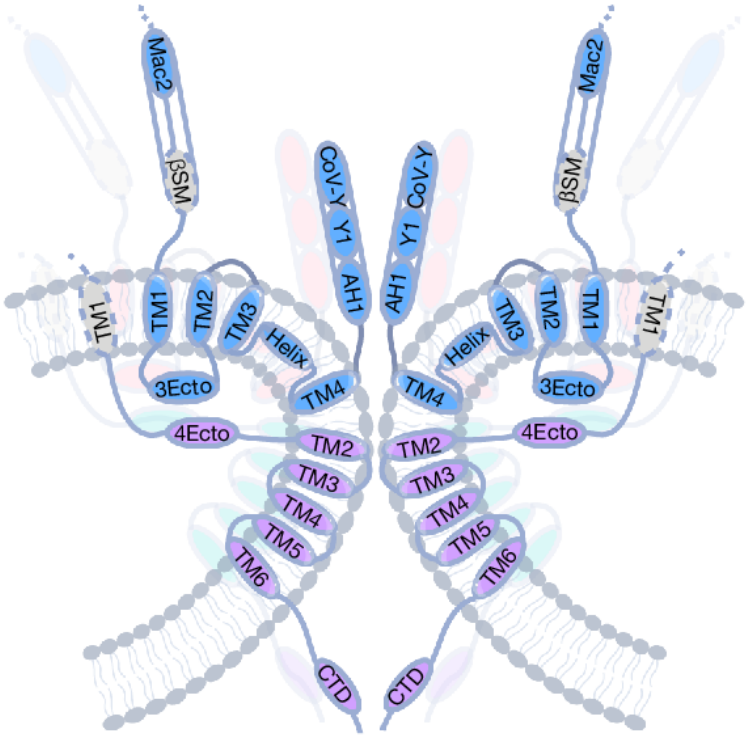


Figure 1. 19 Topology and interactions of nsp3 and nsp4 to curve membranes in the SARS-CoV-2 minimal pore from Huang *et al.*, 2024.

Two copies of nsp3 (blue) and two copies of nsp4 (lilac) are shown. Grey ovals and dashed lines depict regions that were not resolved by STA. The ectodomains of each nsp (3Ecto and 4Ecto) interact within the intermembrane space and the interactions are repeated between the two hexameric rings. The nsp3 N-terminal domain (NTD; macrodomain (Mac) 2 and β-coronavirus-specific marker (βSM)) form the cytosolic prongs, and the C-terminal domain (CTD; Y1 and CoV-Y) sit in the centre of the pore on the cytosolic side. The nsp4 N-terminal transmembrane (TM) helix 1 is unresolved by may embed in the outer membrane (grey ovals with dashed lines). TM2-6 place the CTDs in the DMV interior at the centre of the pore. Two nsp3 proteins of the nsp3L hexamer on opposite sides of the pore are shown in blue. Two nsp3 proteins of the nsp3S hexamer on opposite sides of the pore are shown in the background in faint red depicting the different angles of the cytosolic domains. Two nsp4 proteins of the nsp4L hexamer on opposite sides of the pore are shown in lilac. Two nsp4 proteins of the nsp4S hexamer on opposite sides of the pore are shown in the background in faint cyan depicting the different angles of the lumenal domains. This figure has been taken from Huang *et al.*, 2024.

Furthermore, interactions that may give clues to DMV biogenesis were observed. The nsp3 ectodomain interacts via hydrophobic and hydrophilic residues with the upper surface of the nsp4 ectodomain in the intermembrane space (Huang *et al.*, 2024). Also, 120 transmembrane helices (TMH) were included in the structure which interlock within the concentric hexamers to induce concave membrane curvature which has a highly negative charge that may be stabilised by the positively charged base of nsp3 TM1 (Huang *et al.*, 2024). These interactions suggested that a membrane reorganisation pathway to produce highly curved membranes: after the nsp3-nsp4 is embedded in a membrane, nsp3-nsp4 cleavage might separate the proteins to allow oligomerisation into the hexamers, interlocking of TMH, and interactions of the nsp3 and nsp4 ectodomains in the intermembrane space, together these interactions bend the membrane back onto itself to make the double membrane. Multiple occurrences could then produce a paired membrane sheet held together by the pores as observed in Zimmerman *et al.* (2023). In the nsp3-4 cleavage deficient mutant, the nsp3 CTD appears close to the membrane so it may be unable to oligomerise and instead remains conjugated to nsp4 within the bilayer and makes *trans* interactions with the ectodomains of nsp3-nsp4 in adjacent membrane sheets to produce the zippered membranes and multi-membrane vesicle phenotype (Zimmerman *et al.*, 2023; Huang *et al.*, 2023).

1.6.3.3. Insights into RO biogenesis from other +RNA viruses

The minimal constituents of arterivirus DMVs have also been studied. Coexpression of the equine arteritis virus (EAV) nsp2-nsp3 (the TM1 and TM2 nsps, equivalent to coronavirusnsp3-nsp4) has also been found to be necessary and sufficient for DMV biogenesis and pore formation (Wolff, 2022). Plus, interaction of these nsps is critical to produce membrane rearrangements (Posthuma *et al.*, 2008). Additional observations of EAV nsp2-nsp3 induced DMVs alongside the EAV TM3 nsp, nsp5 (equivalent to coronavirus nsp6), resulted in the formation of more uniform DMVs that more closely resemble those formed upon EAV infection (van der Hoeven *et al.*, 2016); this is comparable to observations for CoV TM1, TM2, and TM3 nsp expression (Ricciardi *et al.*, 2022). Furthermore, the use of dodecameric stacked rings and crown complexes with cytosolic prongs in the CoV DMV pore is like the crown complexes of spherule ROs of FHV (Zhan *et al.*, 2023) and CHIKV (Tan *et al.*, 2022).

1.6.3.4. Host factors involved in RO biogenesis

Host factors are also known to play an important role in +RNA virus biogenesis and function (Harak and Lohmann, 2015). Host ER-remodelling proteins appear to play a critical role in BMV spherule formation (Diaz and Wang, 2014). Also, DENV uses ER atlastins and reticulons to form spherules (Aktepe *et al.*, 2017; Neufeldt *et al.*, 2019). In addition, using a CoV with a biotin ligase fused to nsp2, RTC-associated proteins could be biotinylated, purified and identified by mass spectrometry. This revealed over 500 host proteins constituting the RTC microenvironment, and several ER/Golgi and endosomal factors were shown to be

important for viral replication (e.g. Kif11, Snx9, Dnm11, Scfd1, Ykt6, Stx5a, Clint1, Aak11, and Vapa; V'kovski *et al.*, 2019). For CoV, COPB1/2, which are also involved in Golgi/ER transport, also influence CoV replication and COPI interacts with nsp4 and S (de Wilde *et al.*, 2018; Oostra *et al.*, 2007; McBride *et al.*, 2007). Cyclophilins that facilitate protein folding and formation of multidomain proteins have also been shown to be required for CoV replication and bind to N (Carbajo-Lozoya *et al.*, 2014; Luo *et al.*, 2004). The autophagy proteins ATG5/12 are also required for CoV replication (Prentice *et al.*, 2004). The importance of phosphatidylinositol 4-kinases (PI4Ks) has also been described for RO integrity (Reiss *et al.*, 2011). Recently, host proteins FAM149B1, CCAR2, and ZC3HAV1 were also identified as SARS-CoV-2 host dependency factors that interact with nsp3/4 and have roles membrane remodelling (Pahmeier *et al.*, 2023). To begin to understand the lipids driving RO biogenesis, SARS-CoV-2 nsp6 has been shown to regulates lipid transport from the ER and lipid droplets (LDs) (Ricciardi *et al.*, 2022). Moreover, phosphatidic acid (PA) is a host lipid that is critical for Hepatitis C Virus (HCV) and SARS-CoV-2 DMV formation (Tabata *et al.*, 2021). In addition, lysophospholipids are known to be important for DMV formation (Müller *et al.*, 2018). Finally, VMP1 and TMEM41B (phospholipid scramblases) have been shown to be important pan-coronavirus host factors involved at different steps in DMV formation (Schneider *et al.*, 2021; Li *et al.*, 2021). For example, in VMP1 knockout cells, SARS-CoV-2 nsp3-nsp4 have been able to zipper ER but not close into DMVs, while in TMEM41B knock out cells nsp3-nsp4 interactions are limited and DMV biogenesis is reduced (Ji *et al.*, 2022). Further studies are required to understand how these host factors might contribute to RO formation.

1.7. Cryo-correlative multi-scale imaging

Cryo-bioimaging techniques such as cryo-soft X-ray tomography (cryo-SXT) and cryo-electron tomography (cryo-ET) have significantly improved the understanding of virus biology in cells and +RNA virus RO structure and function (Jadhav and Kounatidis, 2023; de Beijer *et al.*, 2024). These techniques are well suited to visualising CoV ROs *in situ* because they preserve the infected cells in a near-native state and can image large volumes in three dimensions. In addition, cryo-fluorescence microscopy can provide localisation information of the object of interest within the relatively large and complicated intracellular environment. Finally, subtomogram averaging (STA) can be applied to enhance the resolution achievable from cryo-ET and provide a more detailed structure of object of interest. Cryo-SXT can be correlated with fluorescence microscopy (correlative light and X-ray microscopy (CLXM)) for near-native state, high throughput, and high spatial resolution ultrastructural imaging throughout the depth of whole cells. This technique provides a large volume overview of the cellular ultrastructure at the mesoscale and has been used to study virus-host interactions (Nahas *et al.*, 2022; Castro *et al.*, 2023). Correlative light and electron microscopy (CLEM) has also been used to study virus-host interactions as reviewed by Bykov *et al.* (2016). This technique can image smaller volumes of the cellular ultrastructure at higher resolution and cryo-ET is compatible with STA if there are repeating structures present in the tomograms.

1.7.2. Fluorescence microscopy, immuno-electron microscopy (IEM), and autoradiography EM

In fluorescence microscopy, fluorescent proteins and dyes can be used as markers for proteins and membranes of interest. Using genetic engineering, fluorescent proteins can be tethered to proteins of interest in the genome such that when the protein is expressed it has a fluorescent tag which will be used to observe its location in the cell. Or, different tags can be engineered into proteins, such as tetracysteine, split-GFP, or Halo and SNAP tags, that are then bound by complementary ligands for fluorescence expression (Hoffman *et al.*, 2010; Romei and Boxer, 2019; Los *et al.*, 2008; Gautier *et al.*, 2008). Dyes which bind to nucleotides or certain proteins on specific types of membranes can be used to observe the location of cellular organelles. These natively fluorescent recombinant proteins and live cell dyes are compatible with cryo-preservation methods. For chemically fixed and perforated or sectioned samples, primary antibodies can be engineered to be specific to a nucleotide or protein of interest, which are then bound by secondary antibodies possessing a fluorophore, such that when the fluorophore is excited, the location of the antibody-labelled object is observed (immunofluorescence (IF) microscopy). Colloidal gold nanoparticles (5-15 nm in diameter) can also be conjugated to antibodies such that under EM, they appear as electron dense dots and the labelled objects can be located within the ultrastructure of the cell (immuno-EM; IEM). This technique is compatible with chemical fixatives and high pressure freezing and freeze substitution (HPF-FS) (Winey *et al.*, 2014) but it is dependent on the antigenicity of the sample being preserved within the EM sections. HPF-FS works by rapidly freezing cells under high pressure to fix the cells (rather than using chemicals) and form vitreous ice (McDonald, 2007). The temperature is then gradually increased while an organic

solvent containing stains replaces the water in the sample. Finally, the samples are embedded in resin and sectioned. This technique better preserves the ultrastructure of the sample when compared to chemical fixation (Sosinsky *et al.*, 2008). IF and IEM can also be performed on cryosections such as via the Tokuyasu technique (Kandela *et al.*, 2008; Möbius and Posthuma, 2019). IEM can more precisely label molecules compared to fluorescent tags because localising fluorescent tags is limited by the resolution of the EM-compatible light microscopy techniques. EM autoradiography is another labelling technique in which radioisotopes of molecules can be incorporated into samples which, after fixing and sectioning, are subsequently enhanced with silver particles such that they can be observed as electron dense foci in EM, localising them to cellular ultrastructure. To directly label sites of nascent viral RNA synthesis, metabolic labelling can be completed. Here, host cell transcription is inhibited with actinomycin D and the cells are provided with a labelled RNA precursor (such as Bromouridine (BrU)-uridine triphosphate (UTP) or tritiated uridine) for a short time before fixing the cells to minimise migration of the molecules but allow incorporation of the labelled RNA precursor into the viral RNA. BrU can then be visualised via IF or IEM and tritiated uridine can be detected by autoradiography EM (Doyle *et al.*, 2021; Snijder *et al.*, 2020).

1.7.3. Cryo-soft X-ray tomography (cryo-SXT)

Cryo-soft X-ray tomography (cryo-SXT) is another ultrastructural imaging technique that has intermediate to high spatial resolution and allows relatively large intracellular areas to be imaged. In cryo-SXT, a transmission X-ray microscope (TXM) is used in which soft X-rays are passed through whole vitrified cells, and the natural absorption of soft X-rays at 500 eV

(within the water window) by carbon generates amplitude contrast. Consequently, carbon-dense structures in the cell, such as membranes and protein complexes, appear dark, and the vitrified aqueous cytosol allows soft X-rays to pass through, appears light. This is used for tomography in which a series of 2D projections through the cell are recorded at discrete angular increments and the tilt series are then aligned and reconstructed into tomograms (Harkiolaki *et al.*, 2018). The soft-X-rays can transmit through samples over 10 µm so a large depth of field can be imaged. Thus, this method has been used to observe ultrastructural changes in whole cells, including during virus infection, without the need for staining, sectioning, and milling (Garriga *et al.*, 2021). This potentially makes it a higher-throughput near-native state ultrastructural imaging technique compared when to cryo-ET but at the cost of resolution. Fresnel zone plates are used to focus the soft X-rays, and the maximum resolution achievable in the image depends on the outermost zone width (Gorelick *et al.*, 2011). At Diamond Light Source B24, the soft-X-rays are generated from a synchrotron source and zone plates with resolution limits of 25 nm or 40 nm can be used. This resolution is useful for imaging mesoscale structures such as membranes and organelles. The large field of view and depth of field relative to cryo-ET is advantageous when looking for rare events. Cryo-SXT can also use non-synchrotron sources of soft X-rays and is compatible with correlative techniques such as the cryo-fluorescence microscopy technique cryo-structured illumination microscopy (cryo-SIM) (Fahy *et al.*, 2021; Phillips *et al.*, 2020).

1.7.4. Cryo-focused ion beam milling (FIB) and cryo-electron tomography (ET)

Electron microscopy (EM) has been an important tool for observing cell ultrastructure for almost a century and was used to discover the membrane rearrangements induced by +RNA

viruses (Romero-Brey and Bartenschlager, 2014). For conventional room temperature transmission EM (TEM) samples must be fixed, dehydrated, resin-embedded, sectioned and stained, which alter the native-state of the samples, produce artifacts, and limit the attainable resolution of images. These limitations were overcome using cryo-EM, in which samples are rapidly frozen such that the liquid water in them becomes amorphous (vitreous) ice thus maintaining the sample in a fully hydrated state. This process is also called cryo-preservation or vitrification (Dubochet *et al.*, 1988; Mielanczyk *et al.*, 2014). Biological samples can be grown or deposited on carbon coated gold EM grids and vitrified using several techniques including plunge freezing, high pressure freezing, and slam freezing. In plunge freezing, the excess liquid is blotted away to leave a thin film of buffered water that will become vitreous ice once the grid is rapidly plunged into the cryogen (often liquid nitrogen-cooled liquid ethane); cryoprotectants such as glycerol can also be added to the buffer to aid with even vitrification. The sample is then maintained at cryogenic temperatures to prevent devitrification and the production of crystalline ice that will damage the ultrastructure of the sample and scatter the electron beam. No chemical fixation or staining is required.

TEM techniques are limited by the voltage of electrons used, the type of sample, and the sample thickness. Resin-embedded samples must be sectioned on an ultramicrotome and are usually 60 nm for serial sections on a grid or 300 nm for tomography. For cryogenic samples, cryo-focused ion beam (FIB) milling can be used to generate electron transparent 100 – 300 nm thick lamella within the samples which can then be used for cryo-electron tomography (ET). Cryo-ET on cellular lamellae allows visualisation of structures in their native cellular environment (*in situ*) (Chua *et al.*, 2022; Villa *et al.*, 2013; Berger *et al.*, 2023).

Cryo-FIB milling can also be used for slice and view scanning EM (SEM) techniques for large volumes or serial lift-out in which serial chunks of vitreous material are milled from a specimen and deposited onto grids for further thinning (Schiøtz *et al.*, 2024). Another method is cryo-EM of vitreous sections (CEMOVIS) in which a diamond knife on a cryo-microtome is used to cut sections of the frozen sample. However, one problem with CEMOVIS is that it can introduce artifacts including knife marks and compression in the sample (Al-Amoudi *et al.*, 2004). The compression artifacts observed in CEMOVIS are not present in cryo-FIB milling as the ions used to ablate the cells do not apply any mechanical force to the sample (Rigort *et al.*, 2010; Zhang, 2019). In addition, specific regions can be targeted using FIB milling allowing a greater chance that the object of interest will be contained within the area used for cryo-ET.

During cryo-ET, the lamella is tilted, and imaged at discrete angles creating a tilt series; the image is realigned and focused at each tilt angle. The tilt series can be collected via a dose-symmetric scheme in which the images at lower tilt angles are collected first, and subsequent images are then collected at alternating positive and negative tilts to increasingly high tilt angles (Hagen *et al.*, 2017). The scheme distributes the dose such that the lower tilt images contain the least amount of radiation damage and therefore retain high resolution information. This is important because the lower tilt images are usually the thinnest images collected in a tilt series which contain the most ultrastructural information and are the easiest to focus and realign to in a tilt series. The tilt series can then be aligned and reconstructed into a tomogram. Several programs can be used for motion correction, CTF correction, tilt series alignment, and tomogram reconstruction including: RELION (Scheres, 2012), WARP (Tegunov and Cramer, 2019) and IMOD (Kremer *et al.*, 1996). ROs of

+RNA viruses have been studied *in situ* by cryo-FIB milling and cryo-ET as described above (de Beijer *et al.*, 2024).

Phase contrast is the primary source of contrast in a cryoEM image. However, biological specimens only contain light atoms so only scatter electrons weakly. As such, when the sample is imaged at focus, the interference between the scattered and unscattered electrons, corresponding to spatial frequencies that allow your object to be seen in the images, is weak. To increase the phase contrast, the objective lens is defocused, and this acts to increase the relative phase difference between the scattered electrons and unscattered electrons, thus increasing the transfer of spatial frequencies that allow your object to be seen. The Contrast Transfer Function (CTF) describes the way that the frequencies are transferred by the objective lens of the microscope (Erickson and Klug, 1971). The CTF estimation and correction must therefore be completed for each image in the tilt series to generate the correct phase contrast image.

1.7.5. Subtomogram averaging (STA)

From cryo-electron tomograms, repeating objects of interest can be computationally extracted, aligned, and averaged. This process is known as subtomogram averaging (STA) and as multiple subtomograms of the same particle at different angles are combined and averaged, the signal-to-noise ratio is enhanced so the noise in the image is reduced and the resolution is increased. This is in principle the same as single-particle analysis (SPA) where 2D projections of an object at different orientations are used to obtain an average high resolution 3D structures from purified proteins (Bäuerlein and Baumeister, 2021). In

practice, it is easier to get a larger number of particles for averaging in SPA when compared to STA from cellular lamella, as such, 3D structures from SPA typically have a higher resolution than structures from STA. However, in STA the *in situ* structure showing the native state(s) of the object, for example with interacting partners, can be revealed, alongside its cellular location. To be able to identify complexes in noisy cryo tomograms it helps if they are in high abundance, larger in size (~>400 kDa), and have a distinctive shape or spatial arrangement. None of these may apply to the target, especially if it has multiple conformations and interaction partners. Identifying complexes can be made easier using correlative techniques and STA pipelines are being continuously developed (Burt *et al.*, 2024). STA has been used to identify the proteins of macromolecular complexes involved in ROs and has subsequently provided information about their formation and functions as described above (Tan *et al.*, 2022; Zhan *et al.*, 2023; Huang *et al.*, 2024).

1.8. Research aim

CoV ROs are known to exist as a complex network of membranes with a range of elements produced that are hypothesised to be supported by a framework of proteins. The identity of the proteins involved in CoV ROs, in particular DMSs, remain to be elucidated. Furthermore, the mechanisms of RO formation and interactions between different elements of the RO and their roles in viral replication are unknown. Therefore, to test the hypothesis that the DMSs play a role in CoV replication, so may be formed of combinations of viral and/or host proteins, and are separate entities to DMVs, so may form via different mechanisms, the IBV RO will be investigated at unprecedented detail using correlative cryo-bioimaging. The first aim of this project was to characterise the complete RO network *in situ*, using correlative

imaging techniques, and search for RO biogenesis intermediates to help understand RO formation. Furthermore, due to the uniform structure of DMSs, their consistent presence in CoV infected cells, and the likely high energy cost of manipulating and holding the host cell membranes in extensive DMSs networks, it was hypothesised that the DMSs have a yet unknown function in CoV replication. Therefore, the second aim was to identify the proteins associated with DMSs to help determine their function. Consequently, a more complete understanding of how CoVs can manipulate cells will be achieved and specific components of ROs in infected cells will be observed. This will be important for rational vaccine design to improve IBV vaccines and understanding replication of CoVs as a whole, in particular those producing seemingly more abundant DMSs which include further animal and human pathogens (e.g. PDCoV and MERS-CoV).

1. The first objective of this project was to generate and characterise fluorescent recombinant viruses that would act as tools to localise replication organelle membranes.
2. The second objective was to observe the RO network in whole vitrified cells using cryo-SXT to look for RO formation events and interactions between DMV and DMS networks.
3. The third objective was to observe the ROs at higher resolution using cryo-ET to identify membrane and protein structures that may reveal new insights into RO structure and formation; particularly focusing on DMSs.

Chapter 2. Materials and Methods

2.1. Cells and Eggs

The Central Services Unit at The Pirbright Institute provided all the cells used in this thesis. Routine screening for mycoplasma was carried out using the LookOut Mycoplasma PCR Detection Kit (Merck, MP0035). Cells were maintained at 37°C and 5% CO_2. Eggs were maintained at 37°C and 30% humidity in a tilting incubator. All live cell and egg work was completed inside a microbiological safety cabinet (MSC) to maintain a sterile environment and prevent contamination from the air.

2.1.1. Primary chick kidney (CK) cells

Chick kidney (CK) cells were prepared from 2-3-week-old specific pathogen-free (SPF) Rhode Island Red (RIR) chickens by the Central Service Unit at The Pirbright Institute. CK cells are prepared from whole kidneys via manual and trypsin disaggregation (Lokhman *et al.*, 2020). CK cells were grown in CK growth media (Table 2.1). Cells were plated at $0.8x10^6$cells/ml and incubated for 72 hours (h) to settle at 37 °C and 5% CO_2. After infection, CK cells were maintained with 1 x N, N-bis[2-hydroxethy1]-2-aminoethanesulfonic acid (BES) (Table 2.1).

2.1.2. Continuous cell lines

Avian DF1 cells (LGC Standards Ltd., Teddington, UK) are a cell line of chicken embryo fibroblasts derived from 10-day-old East Lansing eggs (Himly *et al.*, 1998). DF1 cells were

maintained in Dulbecco's Modified Eagle's Medium (DMEM, Sigma Aldrich) supplemented with 10% FBS (Sigma Aldrich) at 37 °C and 5% CO_2. Post-infection, DF1 cells were maintained in 1 x BES (Table 2.1).

Mammalian Vero cells are derived from kidney epithelial cells of the African Green Monkey. Vero cells were maintained in DMEM (Sigma Aldrich) supplemented with 10% FBS (Sigma Aldrich) at 37 °C and 5% CO_2. Post-infection, Vero cells were maintained in 1 x BES (Table 2.1).

Chicken lung epithelial cells (CLEC) are derived from lungs of 5-7-week-old SPF Leghorn chickens (Esnault *et al.*, 2011). CLEC cells were maintained in DMEM (Sigma Aldrich) supplemented with 10% FBS (Sigma Aldrich) at 37 °C and 5% CO_2. Post-infection, CLEC cells were maintained in 1 x BES (Table 2.1).

2.1.3. Embryonated Eggs

SPF embryonated hens' eggs were ordered from VALO BioMedia GmbH and were set by the Animal Services Unit at The Pirbright Institute.

2.2. Cell culture medium

The details of cell culture media used in this thesis are shown in Table 2.1

Table 2. 1 Cell culture media.

	1 x BES	2 x BES	1 x EMEM	2 x EMEM	1 x GMEM	BHK-21 growth	CKC growth	DF1 growth	Vero growth	CLEC growth	Supplier and Catalogue Number
10 x EMEM	50 ml	100 ml		100 ml							Merck, M0275
GMEM					500 ml	500 ml					Merck, G5154
EMEM			500 ml				500 ml				Merck, M2279
DMEM								500 ml	500 ml	500 ml	Merck, D5796
TPB	50 ml	100 ml			55 ml	55 ml	55 ml				Merck, T8159
FBS				50 ml	5.5 ml	5.5 ml		55 ml	55ml	55ml	Fisher Scientific, 10099141
NBBS							55 ml				Merck, N4762
10% BSA	10 ml	20 ml									Merck, A7906
1M BES pH 7	10 ml	20 ml									Merck, B4554
7.5% $NaHCO_3$	14 ml	28 ml		23 ml							Merck, S8761
L-Glutamine	5 ml	10 ml	5 ml	10 ml	5 ml		5 ml				Merck, G7513
1M HEPES, pH 7-7.6							5.5 ml				Merck, H0887
P/S	0.5 ml	1 ml		1 ml	0.55 ml		0.55 ml				Fisher Scientific, 11548876
Nystatin	2.5 ml	2.5 ml		2.5 ml	2.5 ml		2.5 ml				Merck, N1638
H_2O	355 ml	218 ml		311 ml							Sterile water

Eagle's minimum essential medium (EMEM) is composed of Earle's salts, essential amino acids, and vitamins. Tryptose Phosphate Broth (TPB) is composed of tryptose (20g/L), dextrose (2g/L), NaCl (5g/L), and disodium phosphate (2.5g/L) adjusted to pH 7.3. FBS: fetal bovine serum, NBBS: new-born bovine serum, BSA: bovine serum albumin, BES: N, N-bis[2- hydroxethy1]-2-aminoethanesulfonic acid, P/S: penicillin/streptomycin. FBS was heat inactivated for 1 h at 50 °C before use.

2.3. Viruses

2.3.1. IBV strains

The IBV strain Beau-R is a molecular clone of Beau-CK (GenBank Accession number AJ311317; Casais *et al.*, 2001). Beau-CK is a non-pathogenic laboratory strain of IBV generated via serial passage through embryonated eggs resulting in a non-pathogenic phenotype and an extended tropism allowing replication in CK cells, DF1 cells, and Vero cells (Keep *et al.*, 2020; Bickerton *et al.*, 2018; Hodgeson *et al.*, 2004; Casais *et al.*, 2003). All IBV stocks were stored at -80 °C.

Recombinant IBVs (rIBVS) with inserts at the 5′ end of nonstructural protein 2 (nsp2) were generated for use in fluorescence microscopy to label RO membranes. The tags were added downstream of the native viral start codon for ORF1a and contained a 3′ alanine spacer region. Inserts included: monomeric enhanced green fluorescent protein (meGFP), mCherry, tetracysteine (TC) and SNAP (Figure 2.1 A-D). The corresponding rIBVs are named: BeauR-eGFP-nsp2, BeauR-mCherry-nsp2, BeauR-TC-nsp2, BeauR-SNAP-nsp2. rIBVs were generated as described in 2.5. If rescued, BeauR-eGFP-nsp2 and BeauR-mCherry-nsp2 would exhibit native fluorescence, while BeauR-TC-nsp2 and BeauR-SNAP-nsp2 would require additional fluorescent labels that targeted TC and SNAP respectively.

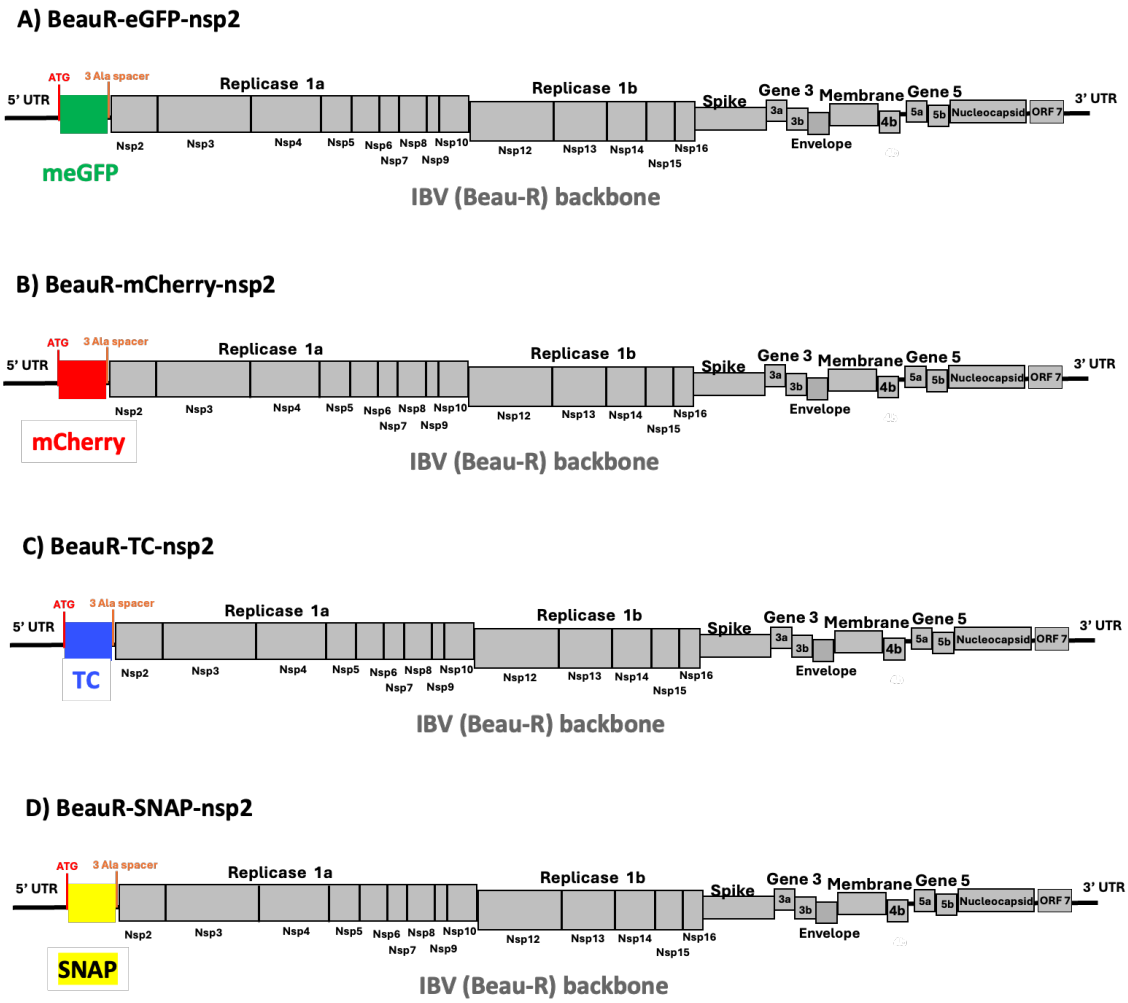


Figure 2. 1 Recombinant IBV design.

Inserts were added downstream of the native viral start codon (ATG) for ORF1a and contained a 3′ alanine spacer region. Inserts included: monomeric enhanced green fluorescent protein (meGFP; A), mCherry (B), tetracysteine (TC; C), and SNAP (D).

2.3.2. Fowlpox virus (FPV)

Recombinant Fowlpox-T7 virus (rFPV-T7) was used in the rescue system and expresses the bacteriophage T7 RNA polymerase required to transcribe the rIBV genome and pCi-Nuc-BeauR-N (Britton *et al.*, 1996). FPV stocks were stored at -80 °C.

2.3.3. Vaccinia Viruses

Recombinant vaccinia virus (rVV) was generated containing a complementary DNA (cDNA) copy of the Beau-R genome (rVV Beau-R) to be used in the reverse genetics system. Before use, all vaccinia viruses were sonicated using a Branson Digital Cup Horn Sonifier 450 with a continuous pulse at 70 % output for 2 minutes. Vaccinia viruses were stored at -20 °C.

2.4. Buffers and Solutions

Xanthine: 10 mg/ml Xanthine (Merck, X3627) in 0.1N Sodium Hydroxide (NaOH; Merck, S5881); 40 X concentrated

Mycophenolic Acid (MPA): 10 mg/ml MPA (Merck, M3536) in Sodium Hydroxide (NaOH; Merck, S5881); 400 X concentrated

Hypoxanthine: 10 mg/ml hypoxanthine (Merck, H9636) in 0.1M Sodium Hydroxide (NaOH; Merck, S5881); 667 X concentrated

Phosphate Buffered Saline (PBSa) pH 7.2: Prepared by the Central Services Unit at The Pirbright Institute. PBSa powder (Merck, P38135) was reconstituted in type 1 endotoxin-free water and sterilised by autoclaving a 115°C for 20 min.

Tris-EDTA (TE) buffer, pH 9: 10 mM Tris/HCl pH 9.0 (Merck, T2819), 1 mM Ethylenediaminetetraacetic acid pH 9.0 (EDTA; E9884) in Molecular-Grade water (Merck, W4502)

SDS-PAGE running buffer (10X): 50 ml 20 % SDS (Merck, 05030), 30 g Tris (Merck, M6250), 144 g glycine (VWR, 101194M). Topped up to 1 litre with Molecular- Grade water (Merck, W4502).

DNA loading buffer: 2 ml Glycerol (VWR, 24388.26), 50 mg Ficoll 400 (Merck, F2637), 25 mg Bromophenol blue (Merck, 114391) and 3 ml Molecular-Grade water (Merck, W4502).

3.3 % formaldehyde: 50 ml formaldehyde solution (VWR, 20909.29) made up to 500 ml in PBSa

2 x Proteinase K digestion buffer: 200 mM Tris/HCl pH 7.5 (Merck, T2319) , 10 mM EDTA (Merck, E9884), 0.4 % SDS (Merck, 05030), 400 mM NaCl (S3014)

Proteinase K: 20 mg proteinase K powder (Merck, P2308) in Molecular Grade water (Merck, W4502)

30 % Sucrose solution: 75 g sucrose (Merck, 16104), 250 µl 1M Tris HCl pH 9 (Merck, T2819) and 250 ml of Molecular-Grade water (Merck, W4502)

0.1 % crystal violet: 100ml 1 % crystal violet (Merck, C6158) in 900 ml of Molecular-Grade water (Merck, W4502)

PBS-T: 0.1 % Tween-20 (Merck, T2700) in PBSa

Blocking solution: 0.5 % BSA (Merck, A7906) in sterile PBS

2.5. Reverse Genetics to generate recombinant IBVs

Recombinant IBVs (rIBVs) were generated using a reverse genetics system based on a recombinant vaccinia virus (rVV) containing a complementary DNA (cDNA) copy of the complete IBV genome (Figure 2.2) (Casias *et al.*, 2001; Keep *et al.*, 2015; Britton *et al.*, 2005). The IBV cDNA within the rVV is modified through homologous recombination with a pGPT-NEB193 plasmid containing the modified sequence and flanking regions. The modified IBV genome is rescued from the rVV vector to generate infectious virions with the desired mutation. All steps up to the partial purification of the rVV DNA were performed by Sarah Keep (The Pirbright Institute).

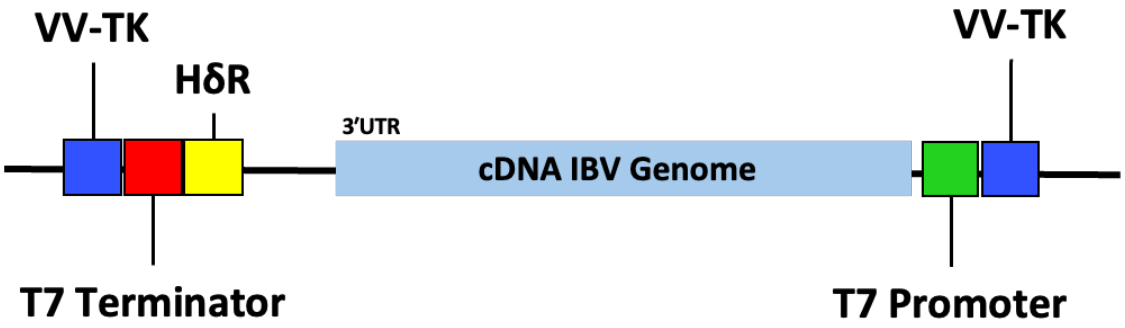


Figure 2. 2 cDNA copy of IBV genome within the thymidine kinase (TK) gene of a recombinant vaccinia virus (rVV) vector.

The cDNA copy was inserted into the VV TK gene using *Not I* restriction sites (Casais *et al*., 2003). The cDNA copy of the IBV sequence is flanked by a T7 RNA polymerase promoter at the 5' untranslated region (UTR). The hepatitis delta antigenome ribozyme (HδR) site was inserted at the 3' UTR of the IBV genome prior to the T7 RNA polymerase terminator sequence for self-cleavage of the IBV genome RNA. This schematic has been adapted from (Armesto *et al.* 2012).

2.5.1. Plasmid cloning to insert fluorescent tags

Modified nonstructural protein 2 (nsp2) genes flanked by 400 base pairs (bp) of adjacent sequence of the IBV genome were cloned into pGPT-NEB193 plasmids (Figure 2.3). The modified nsp2 genes contained different tags (with 3' alanine spacers) at the 3' end of the native start codon of ORF1a. Gene strings were designed in GeneArt by Dr Helena Maier (The Pirbright Institute) and cloned into pGPT-NEB193 *Sal I* restriction sites (5' G$^{\downarrow}$TCGAC 3'), which do not exist in the IBV genome, by Dr Sarah Keep (The Pirbright Institute). The *Escherichia coli* (*E. coli*) guanine phosphoribosyl transferase (*Ecogpt*) gene, which facilitates purine synthesis in the presence of xanthine and hypoxanthine, was used for selection.

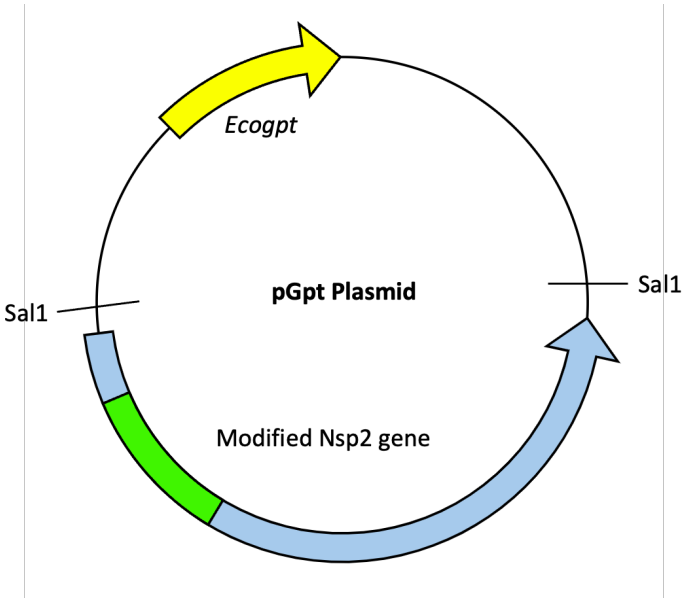


Figure 2. 3 Cloned pGPTNEB193 plasmid.

This plasmid was used as the recombination vector for modifying the cDNA IBV genome within the rVV Beau-R. The *Ecogpt* gene is under the control of a VV p7.5k promoter. *Sal I* restriction sites do not exist in the IBV genome so could be used to cloning in the modified nsp2 sequence (Keep *et al.*, 2015).

The plasmids were transformed in 50 μl of One-shot MAX efficiency DH5α-T1^{R} competent cells (Thermo Fisher, 12297016) to grow larger plasmid stocks (Completed by Dr Sarah Keep, The Pirbright Institute). Using the QIAGEN Plasmid Maxi kit (Qiagen, 12162), plasmid DNA was extracted following the manufacturer's protocol and screened by polymerase chain reaction (PCR) over the inserted region and Sanger sequencing (2.5.4).

2.5.2. Transient Dominant Selection (TDS)

TDS was used to modify the IBV cDNA within rVV Beau-R (Figure 2.4). In the first recombination event, the pGPTNEB193 plasmid recombined with the cDNA copy of the IBV genome in the rVV resulting in its incorporation into the rVV. Mycophenolic Acid (MPA) was used to inhibit the classical purine biosynthesis pathway so that rVVs that had

undergone the first recombination event, and thus contained the *Ecogpt* gene, were selected for in the presence of xanthine and hypoxanthine. The selected rVVs consist of unstable intermediates with duplicate sequences over the inserted region. As the selection agents were removed over three rounds of plaque purification, the second recombination event removes the duplicate sequences to produce either the original IBV receiver cDNA or the modified sequence.

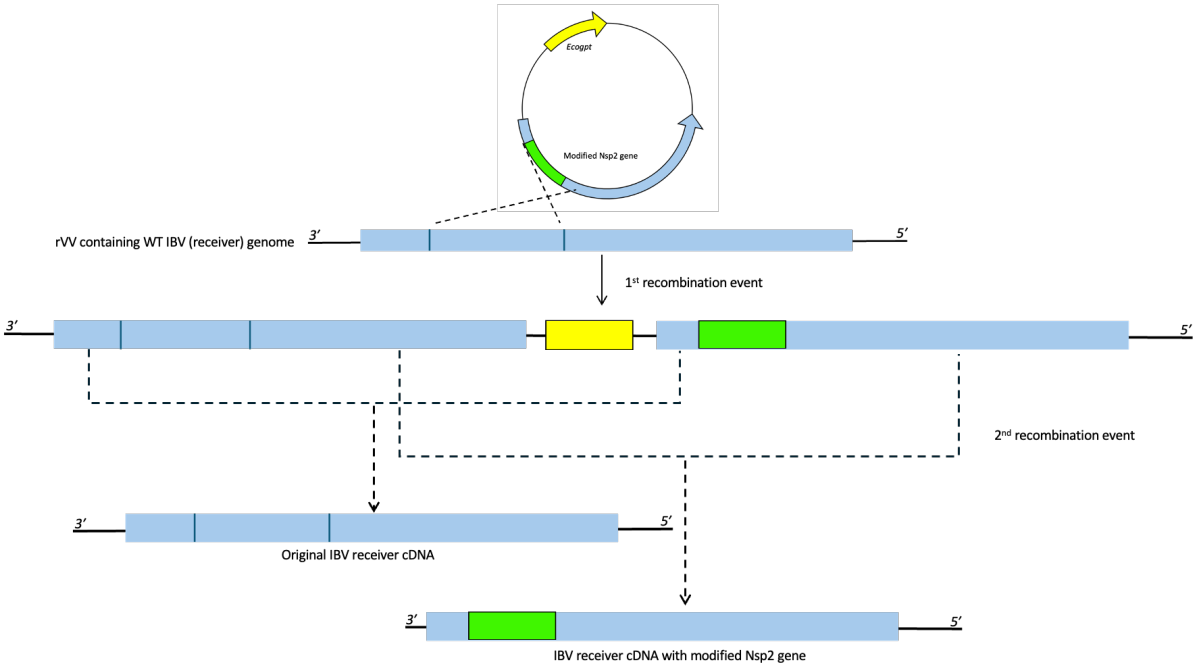


Figure 2. 4 Transient dominant selection (TDS).

TDS was used to generate IBV cDNA with a modified *nsp2* gene. The first recombination event forms an unstable intermediate with duplicate sequences. The second recombination event removes one of the duplicated sequences so that either the original IBV cDNA sequence or the modified sequence remains.

TDS was completed by Dr Sarah Keep (The Pirbright Institute). Vero cells seeded in 6 well plates at 50 % confluency were used for the first recombination. Wells were infected with 500 µl of rVV Beau-R at a multiplicity of infection (MOI) of 0.2 and incubated for 1 h at 37 °C. To transfect the plasmid into the cells, first, solution A (5 µg pGPTNEB193 in 1.5 ml

OPTIMEM (Fisher Scientific, 11524456)) and solution B (12 µl Lipofectin (Invitrogen, 18292037) in 1.5 ml OPTIMEM (Fisher Scientific, 11524456)) were prepared and incubated for 30 min at room temperature. Next, solutions A and B were combined and incubated for 15 min at room temperature. Next, the rVV inoculum was removed and cells were washed twice with 2 ml OPTIMEM (Fisher Scientific, 11524456). Next, 3 ml of the transfection solution AB was added to each well and incubated for 90 min at 37 °C. Then, the transfection solution AB was removed, 5 ml of 1 x BES media was added, and the cells were incubated overnight at 37 °C. At 24 h post rVV infection, the selection agents (12.5 µl MPA, 125 µl of Xanthine and 7.4 µl Hypoxanthine) were added and incubated at 37 °C for a further 2 days before cells were harvested.

Plaque purification and rVV selection were completed by Dr Sarah Keep (The Pirbright Institute). 6 well plates of confluent Vero cells were used for plaque purification of the rVVs. The rVV stocks were serially diluted (10^{-1} to 10^{-3}) in 1 x EMEM, cells were washed once with Phosphate Buffered Saline pH 7.2 (PBSa), 500 µl of inoculum was added per well, and cells were incubated for 2 h at 37 °C. Next, the inoculum was removed, and a solid overlay consisting equal volumes of 2 x EMEM and 2 % agar (Merck, 05040) was added to each well. To select for rVVs containing the *Ecogpt* gene, and thus the modified *nsp2* gene, over three rounds of plaque purification, selection agents (30 mM MPA, 66 mM xanthine and 73 mM hypoxanthine) were added into the overlay media. Plates were incubated for 4 days at 37 °C before adding agar overlays containing 0.01% neutral red (Merck, N4638) in Molecular-Grade water (Merck, W4502). For each rVV, three plaques were picked, added to 400 µl of 1 x EMEM, and stored at -20 °C. rVV growth, selection and picking was repeated three times to isolate those that had undergone the first

recombination. Next, the selection agents were removed in three further rounds of rVV plaque purification to remove the selection pressure and begin the second recombination.

2.5.3. Growing ministocks of selected rVVs

Ministocks were grown by Dr Sarah Keep (The Pirbright Institute). Ministocks of the purified rVVs were grown in 6 well plates of confluent Vero cells. The cells were washed once with PBSa, infected with 150 µl sonicated rVV in 350 µl 1 x BES per well, and incubated at 37 °C for 2 h. Next, the wells were topped up with 2.5 ml 1 x BES media and incubated at 37°C until extensive cytopathic effect (CPE) was observed. Then, the cells were scraped into 1.5 ml tubes and pelleted via low-speed centrifugation. The supernatant was discarded, and the cell pellet was resuspended in 400 µl 1 x BES. These ministocks were stored at -20 °C.

The QIAGEN QIAamp DNA mini kit (Qiagen, 51304) was used to extract the rVV DNA following the manufacturer's protocol into 200 µl of RNAse free water (provided by the manufacturer) to be stored at -20 °C. PCR was used to screen rVVs for the presence of the modified *nsp2* gene and the absence of the *Ecogpt* gene and these rVVs were Sanger sequenced to confirm that the modified sequence in the IBV cDNA was correct. These steps were completed by Patrick Phillips.

2.5.4. Growing maxistocks of screened rVVs

Maxistocks were grown by Dr Sarah Keep (The Pirbright Institute). Eleven confluent T175 flasks (Greiner Bio-One, 660175) of BHK-21 cells were used to grow larger stocks of rVVs with the correct sequence. Cells were infected with 2 ml of sonicated rVV diluted in 18 ml 1 x GMEM at an MOI of 0.1-1 and incubated at 37 °C until cells had completely detached (2-3 days). The cells were pooled into 50 ml Falcon tubes (VWR International, 734- 0448) and centrifuged for 15 min at 270 x *g* and 4 °C. The supernatant was discarded, and the cell pellet was resuspended in 2 ml Tris-EDTA (TE) buffer pH 9 and stored at -20 °C.

2.5.5. Partial purification of rVV maxistocks

Maxistocks were sonicated using a continuous pulse at 70 % output for 2 min to lyse the cells (Branson Digital Cup Horn Sonifier 450). The BHK-21 cell nuclei were separated by centrifugation at 500 x *g* for 10 min. Then, the supernatant was made up to a final volume of 13 ml with TE buffer and layered onto 16 ml of 30 % sucrose in a Beckman Coulter 38.5 ml ultracentrifuge tube (Fisher Scientific, 12706558). The tubes were centrifuged for 1 h at 36,000 x *g* and 4°C in a Surespin 630 rotor. The partially purified rVV DNA pellets were resuspended in 5 ml of 1 mM TE buffer for storage at -20 °C.

2.5.6. Phenol-Chloroform DNA extraction

To degrade any proteins binding the partially purified rVV DNA, 10 ml of the DNA was incubated for 2.5 h at 50 °C with 200 µl of 20 mg/ml solution of proteinase K (in an equal

volume of 2X proteinase K buffer pre-warmed to 50 °C). Next, 10 ml of Phenol-Chloroform (Life Technologies, 17909) was added, mixed by inverting the tube 10 times, and centrifuged at 1,100 x *g* for 15 min at 4 °C. Using a wide-pore pipette tip, the upper aqueous phase was transferred to a 50 ml Falcon tube (VWR International, 734-0448). This step was repeated once more using Phenol-Chloroform, and then once using Chloroform (Merck. 32211-M). The rVV DNA was then precipitated by adding 2.5 volumes of -20 °C absolute ethanol (VWR International, 20821.321) and 0.1 volumes of 3 M sodium acetate (Fisher Scientific, 11301618). Centrifugation at 1,200 × *g*, 4 °C for 75 min (Megafuge 16R Heraeus) produced a glassy pellet. The supernatant was discarded, and the DNA pellet was washed with 10 ml −20 °C 70 % ethanol (VWR International, 20821.321) to dissolve salts present in the sample. It was left on ice for 5 minutes and then centrifuged at 1,200 × *g* and 4 °C for 75 min (Megafuge 16R Heraeus). Next, the supernatant was discarded, and the inside of the tube was dried using a tissue to remove any ethanol (avoiding the pellet). Finally, the pellet was left to air-dry for 2 minutes and resuspended in 100 µl of Molecular-Grade water (Merck, W4502) without mixing to prevent shearing. The pellet was left to dissolve at 4 °C overnight before measuring the concentration using a Nanodrop.

2.5.7. Rescue of rIBV from rVV

A rescue system was used to release replicating rIBV virions with the desired modifications from the rVV (Figure 2.5). The rVV DNA containing a cDNA copy of the modified rIBV genome and a plasmid, pCi-Neo (which provides the BeauR N protein), were transfected into CK cells. Both the cDNA copy of the rIBV in the rVV and the pCi-Neo

plasmid are under the control of a T7 promoter which is activated by a recombinant Fowl pox encoding the T7 promoter (rFPV-T7) that is infected into the cells. Therefore, the T7 RNA polymerase transcribes the rIBV RNA genome from its cDNA copy in the rVV DNA.

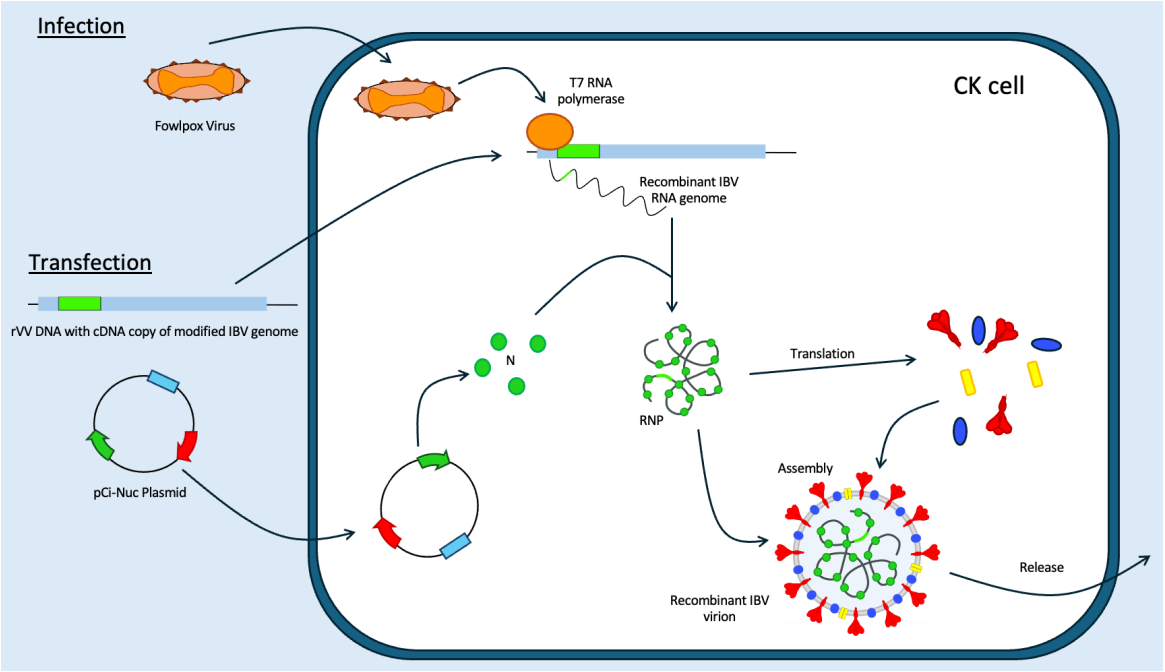


Figure 2. 5 Rescue system in CK cells used to generate rIBV virions from their rVV vector.

CK cells were transfected with rVV containing the rIBV cDNA and the pCi-Neo plasmid. The CK cells were also infected with rFPV-T7 which express the T7 RNA polymerase that will activate the T7 promoter controlling transcription of the rIBV cDNA within the rVV. The pCi-Neo plasmid transcribes Beau-R N protein to bind the rIBV RNA genome, form the ribonucleoprotein (RNP), and stimulate rIBV assembly, release, and replication.

CK cells were plated in six-well plates at $0.4x10^6$cells/ml to give 40 % confluency. They were washed once with PBSa, infected with rFPV-T7 (provided by Sarah Keep) at a MOI of 10 in 1 ml 1 x BES and incubated for 1 h at 37 °C and 5 % CO_2. Next, transfection solutions A (1.5 ml Opti-MEM (Fisher Scientific, 11524456), 10 µg rVV DNA, and 5 µg pCi-Neo (provided by Sarah Keep) per replicate) and B (1.5 ml Opti-MEM (Fisher Scientific, 11524456) and 30 µl Lipofectin (Invitrogen, 18292037) per replicate) were made and incubated at room temperature for 30 minutes. Then A and B were mixed producing

solution AB and left at room temperature for a further 15 minutes. The rFPV-T7 inoculum was removed, cells were washed twice with Opti-MEM (Fisher Scientific, 11524456), and 3 ml of solution AB was added per well. The transfected cells were incubated at 37 °C and 5 % CO_2 for 16–24 h. Next, the transfection medium was replaced with 5 ml 1 x BES and cells were incubated for 48 h until extensive CPE was observed.

The cell supernatant from CPE-positive wells was harvested and filtered through a 0.22 µm filter (Merck, SLGP033NS) attached to a 5 ml syringe (Industrial & Scientific, 302187) to remove the rFPV-T7 virus. The filtered supernatant, referred to as passage 0 (P_0 CKC), was stored at −80 °C and passaged twice more, to P_2, in CK cells. If the P_2 rIBV retained the modification, as seen via RNA extraction and RT-PCR screening and Sanger sequencing (2.6-2.8), larger stocks (P_3) were made in cells or eggs.

2.6. RNA extraction

RNA was extracted from infected cell supernatants, cell lysates and allantoic fluid using RNeasy Mini Kits (QIAGEN, 74104) following to the manufacturer's RNA clean-up protocol. Cells were lysed in buffer RLT (QIAgen) with 1:100 β-mercaptoethanol (Sigma). RNA was extracted using RNeasy columns and eluted into 35µl of RNAse free water (provided by manufacturer) for storage at -20 °C. On-column DNase treatment (Fisher Scientific, EN0521) following the manufacturer's animal cells spin protocol and animal tissues spin protocol was completed for cells and allantoic fluid respectively to prepare samples for quantitative PCR (qPCR). Total RNA was quantified, and 300 ng of RNA was used for each reverse transcription reaction.

2.7. Reverse Transcription (RT)

RT was performed to generate DNA from the viral RNA templates to use for PCR. The first step denatured the RNA strands using the reaction mixture RT1 (Table 2.2) which is incubated at 65 °C for 5 min and then on ice for 2 min. Random primer (5' GTTTCCCAGTCACGATCNNNNNNNNNNNNNN 3', stock concentration 100 µM, Sigma-Aldrich, Merck) was diluted to 50 µM before use.

Table 2. 2 Reaction mixture RT1

Reagent	Volume	Final concentration	Supplier
RNA	5 µl		
Nuclease free H_2O	6 µl		Merck, W4502
10 mM dNTPs	1 µl	0.5 mM / dNTP	Life Technologies, R0182
50 µM Random Primer	1 µl	2.5 µM	Merck

The second step used reverse transcriptase Super Script IV (SSIV) to transcribe RNA into cDNA using reaction mixture RT2 (Table 2.3). RNaseOUT inhibited ribonucleases and Dithiothreitol (DTT) is a reducing agent used to breakdown RNA secondary structures in preparation for PCR. The reaction mixture was incubated in a thermocycler as in Table 2.4.

Table 2. 3 Reaction mixture RT2

Reagent	Volume	Final concentration	Supplier
SSIV Buffer	4 µl	1 X	Life Technologies, 18090050
SSIV	1 µl	20 U/µl	Life Technologies, 18090050
RNaseOUT	1 µl	2 U/µl	Life Technologies, 10777019
DTT	1 µl	5 mM	Life Technologies, 18090050

Table 2. 4 SuperScript IV thermocycler program

Temperature	Time
23 °C	10 min
55 °C	10 min
80 °C	10 min
18 °C	Hold

2.8. Polymerase chain reaction (PCR) to detect virus

PCR was carried out using Taq DNA polymerase (Invitrogen, Thermo Fisher Scientific) or OneTaq Quick-Load DNA polymerase (New England Biosciences) according to the manufacturer's protocol. The reaction mixture is detailed in Table 2.5. Primers were ordered from Sigma Aldrich (Merck) used at 10mM. Primers targeting the IBV 3' UTR, BG56 (forward; 5' CAACAGCGCCCAAAGAAG 3') and 93/100 (reverse; 5' AGGCTAGTATAGAGTTAGAGC 3'), and the regions flanking the insert at nsp2, BG67 (forward; 5' GGCTGGTTCGAGTGCGAG 3') and BG78 (reverse; 5' GAATTACCACAGCGTATTGCA 3') or BG77 (reverse; 5' CCTCTTGAAGGGAGTTGACA 3'), were used. The thermocycler program used different annealing temperatures and extension times depending on the primer pairs and is detailed in table 2.6.

Table 2. 5 PCR reaction mixture

Reagent	Volume	Final concentration	Supplier
10X PCR Pxn Buffer	5 µl	1 X	Life Technologies, 110342046
$MgCl_2$	2 µl	2 mM	Life Technologies, 10342046
dNTPs	1 µl	0.2 mM	Life Technologies, R0182
Forward Primer	1 µl	0.2 pmol	Sigma Aldrich, Merck
Reverse Primer	1 µl	0.2 pmol	Sigma Aldrich, Merck
Taq DNA Polymerase	0.5 µl	2.5 U	Life Technologies, 10342046
Template DNA	5 µl		
Nuclease free H_2O	34.5 µl		Merck, W4502

Table 2. 6 PCR thermocycler program

Temperature	Time	Cycles
95 °C	3 min	1
95 °C	45 sec	25
Annealing Temperature (60-70 °C)	30 sec	
72 °C	Extension Time (sec per bp)	
72 °C	5 min	1
18 °C	Hold	1

PCR products were prepared for LIGHTrun sequencing (GATC Biotech) with 10 µM forward (BG67) and reverse (BG78) primers to check for mutations. The sequencing results were compared to the known BeauR sequence and the sequences coding for the inserts using SnapGene software (www.snapgene.com).

2.8.1. Agarose gel electrophoresis

Agarose gel electrophoresis was used to test for the maintenance of insertions in the rIBVs. Gels with 0.8% w/v agarose (Merck, A9539) were made in 0.5 X Tris Borate EDTA (TBE) buffer (Life Technologies, 15581044) containing SYBRTM Safe DNA Gel Stain (Invitrogen, S33102). Gels were added to a 9 x 11 horizontal submarine gel apparatus (Galileo Bioscience, 80-0911). 2 µl of DNA loading dye was added to 5µl of each PCR product which were added to the wells alongside a 1 kB DNA ladder (NEB, N3232L). Gels were run at 100 V for 40 minutes before imaging the DNA under a UV transilluminator (Biorad).

2.8.2. Sanger sequencing

Sequencing was completed by Eurofins GATC. Plasmids were sent at 100 ng/µl in 10 µl of Molecular-Grade water (Merck, W4502). PCR products (5 µl at 20-80 ng/µl)) were sent with primer (5 µl at 5 µM) in Molecular-Grade water (Merck, W4502). Sequences were compared in Staden.

2.9. Quantitative Polymerase Chain Reaction (qPCR) to measure amounts of vRNA

qPCR was completed using TaqMan ® Fast Advance Master Mix (Life Technologies, 4444557) on a 7500 Fast Real Time System (Applied Biosystems) with MicroAmp™ Fast Optical 96-Well Reaction Plates (Life Technologies, 4346907). The aim was to quantify the amount of viral genomic RNA (gRNA) using the IBV 5' UTR. The reaction mixture is detailed in Table 2.7 and the thermocycler program is in Table 2.8. RNA was extracted from infected cell supernatants and RT was completed as in 2.5 and 2.6. Each sample was normalised to contain approximately 50 ng/µl of cDNA to be used in the qPCR. Primer and probe sequences to detect the IBV 5' UTR were: IBV5'GU391 (forward), 5'-GCTTTTGAGCCTAGCGTT-3'; IBV5'GL533 (reverse), 5'-GCCATGTTGTCACTGTCTATTG-3'; and IBV 5' G probe, 5'-6-carboxyfluorescein (FAM)-CACCACCAGAACCTGTCACCTC-6-carboxytetramethylrhodamine (TAMRA)-3'. The primers and probes were designed in Snapgene and synthesised by Sigma-Aldrich (Merck). Primers were diluted to 10 µM and probes were diluted to 5 µM. qPCR standards were generated by PCR using the qPCR primers and made to $0.5x10^9$ molecules/µl in Molecular Grade water (Merck, W4502).

This was serially diluted, and Ct values were measured and plotted a standard curve. Sample Ct values were interpolated from the standard curve to measure the viral copies of the sequence present in the sample.

Table 2. 7 qPCR reaction mixture

Reagent	Volume	Final concentration	Supplier
TaqMan ® Fast Advance Master Mix	5 µl	1 X	Life Technologies, 4444557
Forward Primer	0.5 µl	0.1 µM	Sigma Aldrich, Merck
Reverse Primer	0.5 µl	0.1 µM	Sigma Aldrich, Merck
Probe	0.25 µl	0.1 µM	
cDNA	2 µl		
Nuclease free H_2O	1.75 µl		Merck, W4502

Table 2. 8 qPCR thermocycler program

Temperature	Time	Cycles
95 °C	20 sec	1
95 °C	1 sec	40
60 °C	20 sec	

2.10. Virus replication kinetics *in vitro* to characterise rIBV growth

Replication kinetics of rIBVs were measured in CK and DF1 cells. Confluent cells in 6 well plates were washed once with PBSa, infected with 500 µl virus diluted in 1 x BES to 1 x 10^5 (plaque forming units) PFU, and incubated for 1 h at 37 °C and 5 % CO_2. Next, the inoculum was removed, 3 ml 1 x BES was added to each well, and the plates were returned to 37 °C. Cell supernatants were harvested at specified timepoints, and the presence of progeny virus was assayed by plaque assay on CK cells (2.13). Supernatant was titrated in triplicate on CK cells to determine the quantity of progeny virus. Multi-step replication kinetics used supernatant harvested at 1-, 24-, 48-, 72- and 96-hours post

infection (h pi). Single-step replication kinetics used supernatant harvested at 1-, 2-, 4-, 6-, 8-, 10-, 12- and 24-h pi.

2.11. rIBV genetic stability assay *in vitro*

rIBVs were passaged in triplicate in 6 well plates of confluent CK cells. Cells were washed once with PBSa, infected with 500 µl of passaged virus per well (starting with the P_3 stock virus (2.12)), and incubated for 1 h at 37 °C and 5 % CO_2. Next, the inoculum was removed, 3 ml 1 x BES was added to each well, and the plates were returned to 37 °C. At 24 h pi, cell supernatants were harvested (P_4) to be used for the next repeat of infection, titration and RT-PCR screening. P_3 stocks were screened and passaged to P_6 where P_6 and P_5 were screened. Each passage included infection with the rIBV and WT Beau-R in parallel.

2.12. Generating viral stocks

Larger stocks of rIBVs were made in CK cells and embryonated eggs from P_2 rIBVs that successfully retained their modifications to be used for further characterisation and imaging.

2.12.1. Generation of rIBV stocks in cells

To generate cell stocks of virus, CK cells in 6 well plates were washed twice with PBS and infected with 500 µl of P_2 virus (that had been confirmed to retain the insert at P_3) diluted 1:100 in 1 x BES per well. Cells were incubated at 37 °C and 5 % CO_2 for 1 h. Inoculum was replaced with 3 ml 1 x BES per well and cells incubated for 24 h or until CPE was observed.

At 24 h pi, cell culture supernatant was harvested, aliquoted and stored at -80 °C. Alternatively, the plates were put at -80 °C for at least 6 hours before being thawed to extract the cell lysate. Then, the plates were scraped, the total cell supernatant and cell lysate were pooled into 50 ml Falcon tubes (VWR International, 734- 0448), centrifuged at low speed and 4 °C to pellet the cellular material, and the supernatant was aliquoted and stored at -80 °C.

2.12.2. Generation of virus stocks in embryonated eggs

Egg stocks of virus were generated by inoculating the allantoic cavities of 10-day old embryonated SPF VALO chicken eggs with P_2 virus (that had been confirmed to retain the insert at P_3) diluted 1:10 in PBS. The embryonated eggs were candled to mark the air sac membrane and ensure that the embryos were viable. The inoculation was injected into the allantoic cavity using a 25-gauge Microlance™ 3 Needle (BD, 300300) and a BD Plastipak™ syringe (BD, 303172) through a hole (made using a Dremel Electric Engraver) 1

cm from the air sac membrane. After rocking in incubator for 24 h, embryos were culled by refrigeration at 4 °C for a minimum of 4 h (Schedule 1 method).

To harvest the allantoic fluid, scissors were used to cut away the eggshell around the air sac. The shell membrane was pulled away and allantoic fluid was removed using 3 ml Pasteur pipettes avoiding the yolk and blood vessels. Allantoic fluid from eggs infected with the same virus was pooled into 50 ml Falcon tubes (VWR International, 734- 0448), clarified by centrifugation at 1000 × *g* and 4 °C for 5 minutes, aliquoted and stored at -80 °C.

2.12.3. Virus stock concentration

After generating virus stocks, before aliquoting, infected cell supernatant or allantoic fluid were added to Vivaspin20 100 kDa MWCO columns (Cytiva, 28932360) and centrifuged at 3200 x *g* for 30 minutes. Concentrated virus was then aliquoted and stored at -80 ^{o}C. Additional steps following Vivaspin20 concentration using an Optiprep (iodixanol; Stem Cell Technologies, 07820) cushion and gradient with ultracentrifugation were tested following manufacturer's instructions but ultimately not used.

2.13. Viral titration by plaque assay

Confluent CK cells in 12 well plates were washed twice with PBS and infected in triplicate with (tenfold) serial dilutions of P_2 or P_3 virus in 1 x BES (250 µl final volume). P_3 stocks of the virus were used for all subsequent replication kinetics and imaging experiments. After

incubation for 1h at 37 °C the inoculum was removed, and solid overlays were added to each well (2ml per well were made 1:1 with 2 x BES and 1 % agar (Merck, 05040)) and incubated for a further 72 h. Then, the cells were fixed with 3.3 % formaldehyde and stained with 0.1 % crystal violet. The number of plaques were counted in triplicate for each dilution and averaged giving the number of plaque forming units (PFU) per 250 µl. The titre in PFU/ml was calculated by multiplying the average number of plaques by four and then undoing the dilution from which the plaques were counted from.

2.14. Immunoprecipitation

2.14.1. Cell lysis

6 well plates of confluent CK cells were infected with BeauR-eGFP-nsp2 or WT Beau-R at an MOI of 0.8-1, incubated for 1 h at 37 °C and 5 % CO_2 (as were the conditions of all cell and infection incubation steps), the inoculum was removed, topped up with 3 ml of 1 x BES per well, and incubated for a further 24 h. Next, cells were washed with cold PBSa and left on ice for 20 min with 350 µl of radioimmunoprecipitation assay (RIPA) lysis buffer (Fisher Scientific, 10017003) and 1X Protein Inhibitor Cocktail (PIC, Fisher Scientific, 78442). The cells were scraped into Eppendorf tubes, centrifuged at 10,000 rpm for 3 min (Biofuge Pico, Heraeus) to pellet the cell debris, and the supernatant was stored at -20 °C.

2.14.2. SDS-PAGE electrophoresis

Cell lysates were mixed in 4X Laemmeli sample buffer (Biorad, 1610747) with β-mercaptoethanol (co, Merck, M6250), incubated at 80 °C for 10 min, then resolved by SDS-PAGE on a Mini TGX Protean 4-15 % gel (Biorad, 4561085) at 150 V for 1 h alongside a Precision Plus Protein™ Dual Color Standards molecular weight ladder (Biorad, 1610374).

Using a Trans-Blot Turbo Nitrocellulose kit (Biorad, 1704270) and the 1X Mini TGX gel (3 min) program on the TransBlot® Turbo™ Transfer System (Biorad, 1704150EDU), the proteins were transferred onto a nitrocellulose membrane.

2.14.3. Western blot

Nitrocellulose membranes containing resolved cell lysate proteins were blocked with 5 % milk solution in PBS-tween (PBS-T) for 1 h. Primary antibodies (Table 2.9) were diluted to 3 ml in 5 % milk solution and added to membranes that were left on an oribital shaker at 4 °C overnight. Unbound primary antibodies were removed by three 5 min washes with PBS-T. Secondary antibodies were diluted to 15 ml in the blocking solution (5 % milk solution in PBS-T) (Table 2.10) and incubated with membranes for 1 h rocking at room temperature. Unbound secondary antibodies were removed by three 5 min washes with PBS-T. Finally, the membranes were washed in Molecular-Grade water (Merck, W4502) before visualisation on a LICOR Odyssey CLx.

Table 2. 9 Primary antibodies for Western blot

Antibody	Supplier	Dilution	Reactivity
eGFP polyclonal	Thermo Fisher Scientific, CAB4211	1:1000	Rabbit IgG
Anti-IBV, chicken, IgY	Abcam, ab ab31671	1:1000	Chicken IgG
Anti-β-Actin monoclonal, BA3R	Thermo Fisher Scientific, MA5-15739	1:1000	Rabbit IgG

Table 2. 10 Secondary antibodies for Western blot

Antibody	Supplier	Dilution	IR Dye
Goat Anti-Rabbit	Abcam, ab216777	1:15,000	680 RD
Donkey Anti-Chicken	LI-COR, 926-32218	1:15,000	800 CW

2.15. Fluorescence microscopy

BeauR-TC-nsp2 required additional labelling to visualise the location of the insert so this was tested. Then, immunofluorescence (IF) microscopy was completed using antibodies to label sites of viral replication. This was done via double stranded RNA (dsRNA) labelling or bromouridine (BrU) labelling of rIBV-infected cells to confirm whether the rIBV fluorescence signal colocalised with sites of viral replication. This informed whether the rIBV would be suitable for downstream live cell, and eventually cryo-, fluorescence microscopy (without additional antibody labelling) to mark sites of RO membranes (which are the sites of viral replication) for ultrastructural interrogation.

2.15.1. TC-ReAsH labelling

BeauR-TC-nsp2 infected cells were labelled with 2.5 µM TC-ReAsH™ II In-Cell Tetracysteine Tag Detection Kit (Red Fluorescence; Invitrogen, Thermo Fisher Scientific,

T34562) for 30 min and then washed with 1 x BAL wash buffer diluted in Leibovitz's L-15 medium without phenol red (Thermo Fisher Scientific, 21083027). One-hour ReAsH incubation and two 1 x BAL washes were also tested. IF imaging was then completed as in 2.15.2. or live cell imaging as in 2.15.4).

2.15.2. Sample preparation for immunofluorescence microscopy

Cells were seeded to 80 % confluency on sterilised #1 glass thickness coverslips (TAAB Laboratories Equipment Ltd, M160/1.0) in 24 well plates (Scientific Laboratory, 353047), infected with 200 µl undiluted virus per well, and incubated for 1 h at 37 °C. Next, the inoculum was removed and replaced with 1 ml 1 x BES per well before further incubation until a specified timepoint when the cells were fixed for 15 minutes in 4% pfm (Agar Scientific, AGR1026) and washed twice with PBSa. Fixed coverslips were stored at 4 °C.

Cells were permeabilised in 0.1 % Triton X-100 (Merck, X100) in PBSa for 15 min. Next, the coverslips were washed with PBSa before incubation with blocking buffer for 1 h at room temperature. Blocking buffer was made as 0.5 % BSA (bovine serum albumin) in PBS, or 0.1 % fish gelatin (Sigma Aldrich, G7765).

Blocking buffer was removed from the coverslips and 200 µl of primary antibody diluted in the blocking buffer (Table 2.11) was added to each well for 1 h.

Table 2. 11 Primary antibodies for immunofluorescence microscopy

Antibody	Supplier	Dilution	Reactivity
Anti-BrU (Bromodeoxyuridine)	Roche, Sigma, 11170376001	1:50	Mouse IgG1
Anti- J2 dsRNA	Scions (English and Scientific Consulting, Budapest, Hungary) 10010200	1:1000	Mouse IgG2a
Anti-IBV N (Nucleocapsid)	Wageningen Bioveterinary Research, 7500891	1:1000	Mouse IgG1
Anti-eGFP	Thermo Fisher Scientific, CAB4211	1:350	Rabbit IgG

After washing for 5 min three times in PBSa, 200 µl of Alexa Fluor secondary antibody diluted in the blocking buffer (Table 2.12) was added to each well for 1 h.

Table 2. 12 Secondary antibodies for immunofluorescence microscopy

Antibody	Supplier	Dilution
Alexa Fluor 568 goat anti-mouse IgG1	Thermo Fisher Scientific, A-21124	1:500
Alexa Fluor 555 goat anti-mouse IgG2a	Thermo Fisher Scientific, A-21422	1:500
Alexa Fluor 568 goat anti-rabbit IgG	Thermo Fisher Scientific, A-11011	1:500
Alexa Fluor 488 goat anti-mouse IgG	Thermo Fisher Scientific, A-11001	1:500

Unbound secondary antibody was removed by three 5 min washes in PBSa and nuclei were labelled with 4',6-diamidino-2-phenylindole (DAPI; Sigma Aldrich, D9542) diluted 1:10,000 in Molecular-Grade water (Merck, W4502) for 4 min in the dark. Each coverslip was washed in H_2O and mounting onto glass slides with Vectashield® Anti-fade Mounting Medium (Vector Labs, H-1000-10). Coverslips were sealed with nail polish and stored at 4 °C.

Cells were visualised using a Stellaris 5 confocal microscope (Leica Microsystems) and images were collected in the Leica *LAS X* software using the sequential scanning function to remove any bleed-through artefact. Bleed-through (or crosstalk) is commonly seen

when imaging fluorophores that have a wide emission spectrum and it can be difficult to compensate for when using a standard fluorescence microscope with camera. However, using a confocal microscope with laser excitation and photo-multiplier tube (or similar) detectors to accurately collect emission windows means bleed-through can be completely removed.

When exciting a fluorophore with a laser, if multiple detectors collecting different wavelengths are on at the same time, positive signal could potentially be seen in all channels. For example, when DAPI (DNA stain) is excited with the 405 nm laser, emission occurs throughout a broad window of 400 – 600 nm; any active detector in this range will collect signal and present a positive result so nuclei will not only appear blue but also green and possibly red in the respective channels. To stop these false positives from interfering with interpretation of co-localisation, only the 405 nm laser and a single detector set to collect at the optimum emission for DAPI (approximately 440 – 480 nm) are turned on. Similarly, when AlexaFluor 488 is being excited with the 488 nm laser, only the 488 nm laser and a single detector collecting signal at the optimum emission for AlexaFluor 488 (approximately 510 – 530 nm) are active. This process is repeated for the relevant number of channels, creating a sequence of images which can be overlaid in the software to produce an image with no bleed-through artefact (Jonkman *et al.*, 2020). In short, for each channel imaged, only the relevant laser and detector are ever on at the same time. Line intensity profiles were generated in *LAS X* and Dr Joanna Wells (The Pirbright Institute) generated the colocalisation percentages between fluorophores using *Imaris*.

For super-resolution stimulated emission depletion (STED) microscopy, cells were instead seeded on sterilised #1.5 thickness glass coverslips (TAAB Laboratories Equipment Ltd, M160/1.5). Also, ToPro3 (Thermo Fisher Scientific, T3605) was used for nuclear staining (diluted 1:1000 in PBSa and incubated for 15 min in the dark) and ProLong Diamond (Thermo Fisher Scientific, P36965) was used for mounting. Mounting was completed overnight in the dark at room temperature before sealing with nail polish. Cells were imaged on a Leica SP8 gSTED 3X microscope with inverted stand. Images were collected in Leica LAS software and then deconvolved using Huygens Professional software 18.10 (Scientific Volume Imaging).

2.15.3. Labelling of nascent viral RNA with bromouridine

Cells seeded onto sterile glass #1 thickness coverslips were infected and, in a light-protected and RNase-free environment (MSC hood treated with RNaseZap (Fisher Scientific, 10708345)), treated with 2 mM bromouridine (BrU; Sigma Aldrich, 850187) and 15 µM actinomycin D (ActD; Sigma Aldrich, A9415) at 30 minutes prior to each timepoint. Cells were fixed in 4% RNase-free pfm at each timepoint and then labelled as in 2.15.2. IF labelling steps were carried out with RNasin ribonuclease inhibitor at 0.133 U/ml (Promega, N2111).

2.15.4. Sample preparation for live cell fluorescence microscopy

Unfixed cells without antibody labelling but exhibiting fluorescence from live cell labels or native fluorescent protein expression were videoed to visualise cell dynamics or imaged

prior to fixation for EM sample preparation. For videoing live cells, cells were prepared as in 2.5.1 and 2.5.2 in glass bottom chamber slides (Merck, 41122600) instead of glass coverslips, and without fixing, permeabilization and labelling. After infection and/or TC-ReAsH labelling at specified times, the nuclei were labelled with Hoechst 34580 (Thermo Fisher Scientific, H21486) at 5 µg/ml for 15 min and the media was replaced with Leibovitz's L-15 medium without phenol red (Thermo Fisher Scientific, 21083027). For live cell fluorescence imaging of samples to be prepared for room temperature CLEM, the above was repeated but using dishes containing gridded coverslips (Mattek, P35G-1.5-14-C-GRD) instead of the glass bottom chamber slides (Merck, 41122600).

2.16. Correlative Light and Electron Microscopy (CLEM) at room temperature

Fluorescence signal from rIBVs was used to find infected cells and the position of ROs within the cell cytoplasm. To confirm that the rIBV formed ROs that appeared the same as WT ROs, DF1 or CK cells were imaged and fixed at 18-24 h pi. To look for RO formation events, CK cells were imaged and fixed from 3-6 h pi. CLEM was completed as in Russell *et al*., 2017.

Cells seeded into dishes containing gridded coverslips (Mattek, P35G-1.5-14-C-GRD) were infected or mock infected and live cell fluorescence was imaged as in 2.15.4. Lower magnification images were captured including the nuclei within an entire grid coordinate square. Then, higher magnification images of the specific cell exhibiting fluorescent RO membranes were captured. After capturing rIBV fluorescence images from 1-3 areas, cells were fixed with 2 % glutaraldehyde for 1 h. There was up to 30 min between

fluorescence image collection and fixation. The fixed cells were incubated with 1 % osmium tetroxide for 1 h and dehydrated with 70 % ethanol for 30 min, 90 % ethanol for 15 min, and three 10 min washes with 100% ethanol. 36 g of Agar 100 epoxy resin (Agar Scientific, AGR1031), 24 g of dodecenyl succinic anhydride (DDSA; hardener; Agar Scientific), 15 g methyl nadic anhydride (MNA; hardener; Agar Scientific), and 2.25 g of benzyl dimethylamine (BDMA; accelerator; c. 3%; Agar Scientific) were mixed in a plastic bottle. The dishes were washed with propylene oxide for 10 min to remove the ethanol, then in a 50:50 mixture of propylene:resin for 45 min, and then infiltrated with resin alone for 1 h at room temperature. Finally, the resin was replaced with fresh resin and the resin was left to polymerise overnight at 60 °C.

A hacksaw and files were used to cut out the grid area embedded in the solid resin dish. Next, the coverslip stuck to the hardened resin was removed by scoring the coverslip with a razor blade and leveraging it under the coverslip, so it comes off, or by dipping the block in liquid nitrogen. This left the cells embedded at the hardened resin surface. Next, the specific individual grid coordinate square was cut out using the hacksaw and a razor blade, without damaging any other coordinate squares of interest. The resin block was trimmed into the shape like a frustum of a square pyramid but with a trapezium-shaped block face (Figure 2.6). The blocks were trimmed to approximately 2 mm tall with a block face of 500 μm^2 with the cell of interest in the centre. Then, 80 nm thick sections were cut using an ultramicrotome (completed by Philippa Hawes (The Pirbright Institute)), collected on hexagonal 200 thin bar copper grids, and stained with 2 % uranyl acetate and lead citrate (Leica EM stain).

Data were collected using a Talos L120C TEM (Themo Fisher Scientific) at 120 kV with a 4k × 4K Ceta CMOS camera. First, sections showing the nuclei at their widest diameter were found and lower magnification images were captured in the region of the cell of interest based on the shape of the section. These images were rescaled and overlayed with the lower magnification fluorescence images based on the size and pattern of the nuclei in PowerPoint with the nuclei labelled blue with Hoechst and the EM image in greyscale. Then, the nuclei of the infected cell could be identified in the EM and higher magnification EM images were collected all around the visible cell cytoplasm or in specific areas of the cytoplasm based on the higher magnification fluorescence images of the ROs. Again, the images were overlayed in PowerPoint based on the size and shape of the nuclei. Areas of cytoplasm overlapping with RO-fluorescence were captured at higher magnifications if the ROs were not already obvious in the electron micrographs. Where adjacent sections were available, correlation was repeated to find the same cell and capture the area of cytoplasm containing ROs at another Z height.

2.17. Cryopreservation of BeauR-eGFP-nsp2 infected cells on grids

EM grids were picked up with EM tweezers one at a time in a MSC, submerged in 70 % ethanol, submerged in sterile HBSS (Thermo Fisher Scientific, 14025092), placed into a 6 well plate containing filtered FBS (Fisher Scientific, 10099141) at a 45° angle, and released to the bottom of the well. The ethanol was used to sterilise the grids and the FBS was used to functionalise the grids for cell adherence. Up to 10 grids were placed in each well. Plates of grids were incubated at 37 °C for at least 8 h. Next, without disturbing the grids, the FBS was removed, the grids were washed once with cell culture medium to remove

excess FBS, 2 ml of cell culture media was added to each well, and cells were seeded on the grids. Once the cells had settled, occupied the grids, and been washed, they were treated by infection or transfection. Finally, the grids were plunge-frozen at -170 °C and 70 % humidity on a Leica GP2 plunge freezer (Leica Microsystems). Longer blot times were used for more confluent grids and for cryo-FIB sample preparation compared to cryo-SXT sample preparation. Cryopreserved grids were kept under liquid nitrogen.

2.17.1 Seeding cells on grids

For CK cells, cells were prepared from chick kidneys on Friday mornings at The Pirbright Institute, they were collected as soon as possible after preparation and driven on ice to B24 at Diamond Light Source. Here, cells were counted and 600,000 cells in 3 ml CKC media were added to each well of sterilised and functionalised grids to account for primary cell death, the plates were incubated at 37 °C for 72 h to allow the healthy cells to adhere and grow. Then, floating cells were washed away from the grids with two HBSS washes before infection.

For DF1 cells, cells were maintained in flasks at B24 readily available for seeding. 60,000 cells in 1 ml DF1 media were added to each well of sterilised and functionalised grids. The DF1 cells were incubated at 37 °C for 30 min to 1 h, and the number of settled cells adhered to each grid was observed under a brightfield microscope. If too few cells had settled onto the grids in a particular well, the top 1 ml of floating cells were removed and 30,000-60,000 more cells in DF1 media were added. Plates were incubated at 37 °C for 24

h to allow the cells to spread out and occupy the grid squares. Cells were washed once with HBSS before treatment.

2.17.2. Different plunge freezing protocols for cryo-SXT and cryo-FIB SEM

For cryo-SXT, R2/2 Au200F1 grids (Quantifoil) were used and for cryo-FIB SEM, R2/2 Au200F1, Au300, or Au200 grids (Quantifoil) were used.

For cryo-SXT, treated (or mock-treated) cells on grids were labelled with 500 nM MitoTracker Deep Red FM (Thermo Fisher Scientific, M22426) for 30 min at 37 °C before plunge freezing at specified timepoints (Leica GP2) with the addition of 2 µl of 250 nm gold colloid fiducials (BBI Solutions, EM.GC250) prepared as in Nahas *et al.*, 2022. The ethane temperature was -170 °C, the chamber humidity was 70 %, the chamber temperature was 25 °C , and the blot time varied between 0.5-2.5 s depending on the confluency of cells on the grid.

To prepare the 250 nm gold fiducials, 1 ml of the stock was centrifuged for 5 min at 12 x *g* and the pellet was resuspended in 50 µl of Hanks' Balanced Salt Solution (HBSS; Thermo Fisher, 14025092) and stored at 4 °C.

For cryo-ET, treated (or mock-treated) cells on grids were plunge frozen at 24 h pi using a Leica GP2 at -170 °C, 70 % humidity, chamber temperature at 25 °C, and blot time 8-10 s depending on cell confluency. Before attachment of the tweezers holding the grid to the plunge freezer, the tweezers were placed horizontally on the bench, grids were manually

blotted at the edge for 3 s to remove media (Whatman No.1 paper), 5 μl of PBS (Thermo Fisher Scientific, 14040117) was added as a drop on top of the grid for 3 s, PBS was blotted away from the grid edge, and then a 5 μl drop of 10 % glycerol (Merck, G2025) in PBS containing a 1:10 dilution of Dynabead myOne 1 μm diameter beads (Thermo Fisher Scientific, 65001) was added on top of the grid for 1 min. Then, the tweezers were added to the plunging arm without losing the drop of glycerol/beads and the in-chamber blotting and plunge freezing were completed. Grid clips were marked in pen with three dots so that the grid could be orientated in the Leica cryoCLEM and cryo-FIB-SEM and the grids were clipped.

The Dynabeads were prepared in glycerol as follows. The beads in the original vial were resuspended by vortexing, 50 μl were taken into 1 ml water, and spun in a microcentrifuge for 20 min. The supernatant was removed, and beads were spun again with water to remove sodium azide. PBS (Thermo Fisher Scientific, 14040117) was made with 10 % glycerol (Merck, G2025). The washed bead pellet was resuspended in 50 μl PBS/10% glycerol, 20 μl of resuspended beads was added to 180 μl of PBS/10% glycerol, and this 1:10 beads dilution was stored at 4 °C.

2.17.3. Infection and transfection of cells on grids

For WT BeauR or BeauR-eGFP-nsp2 infection of cells on grids, grids were prepared, and cells were seeded as in 2.17 and 2.17.1. 1 ml of undiluted virus stock (at 1.86×10^6 PFU/ml) was added to each well of a 6 well plate containing washed cells on grids giving an MOI of 0.8-1. The plate was incubated at 37 °C for 1 h, the viral inoculum was

removed, 3 ml 1 x BES was added to each well, and the plate was incubated at 37 °C until plunge -freezing as in 2.17.2.

For nsp4-GFP transfection, 125 μl Opti-MEM (Fisher Scientific, 11524456) was added to 1.25 μl of nsp4-GFP plasmid DNA, IBV nsp4 cloned into pEGFP-C1 (Clontech; Freeman *et al.*, 2014), plus 5 μl P3000 (Lipofectamine™ 3000 Transfection Reagent (Thermo Fisher Scientific, L3000001)). In a separate tube, 125 μl Opti-MEM (Fisher Scientific, 11524456) was added to 2.5 μl lipofectamine 3000 (Thermo Fisher Scientific, L3000001). Next, the plasmid mixture was added to the lipofectamine mixture and incubated for 10 min at room temperature. The DF1 media was removed from grids with DF1 cells and replaced with 2.5 ml of DMEM (Merck, D5796). Then, the transfection mixture was added dropwise to the well and the plate was rocked and incubated at 37 °C for 24 h until plunge-freezing as in 2.17.2.

2.18. Fluorescence screening under cryogenic conditions

2.18.1. Cryo-structured illumination microscopy (SIM)

Cryo-structured illumination microscopy (cryo-SIM, B24) was used to screen the grids for fluorescent foci indicating RO membranes. First a brightfield map of the whole grid was collected. Then, different grid squares containing cells as central as possible to the grid were individually images under the fluorescence lasers. SIM uses patterned light at three different angles that interact with the fluorophores. Images at each angle of patterned

light were captured every 0.5 µm throughout of a Z -stack encompassing the cell (8 – 10 µm). The images at each angle were reconstructed for each frame of the Z-stack giving a super-resolution 3D image (Phillips *et al.*, 2020). The 488 laser was used to collect GFP fluorescence, the 568 laser was used to collect MitoTracker fluorescence, and brightfield stacks were also collected to observe the shape of cells, fiducials and any grid features. The SIM brightfield grid map was matched onto the brightfield map of the grid taken by the in-line visible light microscope (VLM) once the grid was loaded into the transmission X-ray microscope (TXM) (2.19) using GridSnap (Thomas Fish, B24). X-ray mosaics of each grid square were overlayed with the maximum intensity projection of the SIM stack in PowerPoint or the shape of the cells were seen by eye. Tomogram areas were then placed on the x-ray mosaic covering the locations of the GFP fluorescence captured by SIM without being too closely adjacent in the x-axis and favouring areas where fiducials were evenly distributed (2.19).

2.18.2. Leica cryoCLEM

The cryoCLEM (Leica Microsystems) was also used for cryo-fluorescence screening of BeauR-eGFP-nsp2 infected cells on grids. The cryoCLEM is a widefield fluorescence microscope and was used to image grids under cryogenic conditions using a 50 x dry objective (with a numerical aperture of 0.9 and working distance of 0.28 mm). Images were further processed with Leica THUNDER deconvolution. Importantly, the grid clips were marked with three dots to indicate their orientation so that they could be loaded with the central dot pointing up in the holder to mark the ‘top’ of the grid. Brightfield maps of the whole grid were captured. Then, using the live mode at 488 to scan over the

entire grid, areas with GFP fluorescence of interest were marked. Next, at each area of interest, z-stacks were collected including 488, 568, and brightfield modes. The best areas of fluorescence that would be accessible in for FIB-SEM were marked on the brightfield map. If most of these areas were on the top half of the grid, for FIB-SEM, the grid was loaded with the three dots on the clip at the bottom of the sample holder because the images were 180° flipped in the FIB-SEM views. If the best areas were on the bottom half of the grid in the cryoCLEM, the grid was loaded with the three dots facing the top of the FIB-SEM cartridge and the fluorescence images were flipped for correlation.

2.19. Cryo-soft X-ray tomography (cryo-SXT)

The fluorescently screened grids, maintained at cryogenic temperatures, were transferred to the UltraXRM-S/L220c X-ray microscope (Carl Zeiss X-ray Microscopy) at beamline B24 at Diamond Light Source and X-ray tomograms were collected at the same areas as the fluorescent foci shown by SIM or Leica cryoCLEM screening. Grids were imaged in a liquid nitrogen-cooled vacuum chamber and samples were illuminated with 500 eV X-rays (λ = 2.48 nm) for 0.5 or 1 s per projection. The transmitted light was focused by diffraction using a Fresnel zone plate with an outermost zone width of 25 nm. Transmitted images were collected using a 1024B Pixis CCD camera (Princeton instruments) at 10 nm/pixel. Tilt series of regions of interest from the cryo-SIM screen were collected by rotating the sample around an axis normal to the incident X-ray beam in increments of 0.2° or 0.5° per image, with tilt angles of $\pm$60°. Reconstruction of the x-ray tilt series into tomograms was completed using *eTomo* in *IMOD* (version 4.9.2;

Mastronarde and Held, 2017). Tomograms were visualised in *ImageJ* (Schindelin *et al.*, 2012) and segmentations were completed using *3dmod* in *IMOD*.

2.20. Cryo-focused ion beam milling and cryo-electron tomography

2.20.1. Screening EM grids on Glacios

Clipped grids were loaded into a Glacios 2 transmission electron microscope (TEM) (Thermo Fisher Scientific). Atlas acquisitions were taken to determine blotting conditions that gave the best sample thickness and grids were discarded that were too thin or too thick for lamella preparation.

2.20.2. Cryo-focused ion beam milling and 3D correlation for lamella placement

Marked and clipped grids were loaded into the Scios DualBeam cryo-FIB-SEM system (Thermo Scientific) with a gallium ion beam. Using the map of fluorescent cells of interest, the grid was reoriented using the mark on the clip to ensure that most cells were accessible to the ion beam at the milling angle. Grids were sputter coated with a thin layer of conductive platinum (60 s) using a sputter coater (at 5 mA current and 240 V) within the transfer chamber before loading onto the stage. Next, a thicker protective layer of platinum was deposited on the grid for 5-10s using the in-chamber gas injection system (GIS) in which the process gas is 1 bar Argon (reaching 0.02 mbar in the chamber). The accessible cells of interest were found in the SEM and FIB view images were collected using a 30kV accelerating voltage at a tilt angle of 19°. Using 3D Correlative Toolbox

(3DCT, Arnold *et al.* 2016), a maximum intensity image of the fluorescence z-stack images of the infected cell (from the Leica cryoCLEM, 2.18.2) was generated, rescaled, and imported into the program alongside the tilted ion beam image of the same area on the grid. In 3DCT, 3 beads observable by their autofluorescence signal in the maximum fluorescence intensity image were manually matched to their positions in the tilted ion beam image, as they appear as bumps under the platinum coating. Next 5-10 more beads evenly distributed around the cell of interest were located in the fluorescence image and matched to their equivalent positions in the tilted ion beam image. 3DCT helps this process by showing the estimated bead position based on previously matched beads. Finally, the fluorescent puncta of interest were marked, and the correlation tool was used to put points on the tilted ion beam image predicting the x, y and z coordinates for lamella placement. The lamella boxes were accurately placed based on the 3D correlation and milling was performed using a 30kV Ga ion beam. Milling was performed in steps, starting with coarse milling of a 3 μm lamella at 300 pA, followed by a 1.5 μm lamella at 100 pA, and a 0.7 μm lamella at 50 pA. Finally, the lamella was polished to a thickness of approximately 150-200 nm using a 30 pA FIB current.

For non-fluorescent samples, serialFIB was used on the Scios to generate grids with lamella in an automated fashion (Klumpe *et al.*, 2021). FIB images of 25 cells were collected and milling boxes and lamella sites were placed onto the images in the serialFIB software. The software ran the coarse milling steps overnight using the same beam currents as above. The next day, the liquid nitrogen dewar was refilled and the polishing was done manually requiring around 15 minutes per surviving lamella.

2.20.3. Cryo-electron tomography using Krios

Lamella grids were loaded into an autoloader cassette at 90° relative to the milling direction so that the walls of the lamella were perpendicular to the microscope tilt axis giving the maximum tilt range during data collection. A Titan Krios electron microscope (Thermo Fisher Scientific) located at eBIC (Krios III) was used to collect tilt series at 300 keV with a selectris-X filter and falcon 4i camera. Tilt series were initially collected at different magnifications to optimise finding ROs with the tomograms. Samples were pre-tilted to 13° to compensate for the milling angle. Tilt series were collected at a magnification of 42K, with a defocus range of -5 μm to -2 μm, a tilt range of ±50° with 2° increment, and an electron dose of 2.06 $e^-/Å^2$/tilt. The resulting images had a pixel size of 3.05 Å/pixel.

2.20.4. Cryo-electron tomography data processing

On-the-fly processing of tomograms was done using the eBIC *Murfey* pipeline (Horstmann *et al*., 2024) to assess data collection quality. Tilt series were motion corrected using *MotionCor*2 (Zheng *et al.*, 2017), *CTFFind*4 (Rohou and Grigorieff, 2015) was used for CTF estimation, and *AreTomo* (Zheng *et al.*, 2022) was used for alignment and reconstruction via patch tracking. Automatic denoising is performed with *Topaz* (Bepler *et al.*, 2020) using a pre-trained model. The pipeline also uses *IMOD* (Kremer *et al.*, 1996) for basic micrograph manipulations.

For subtomogram averaging (STA), RELION-5 (Burt *et al.*, 2024) was used (Figure 2.6). In this pipeline, *MotionCor*2 (Zheng *et al.*, 2017), *CTFFind*4 (Rohou and Grigorieff, 2015), and *AreTomo* (Zheng *et al.*, 2022) were also used for reconstruction and *cryoCARE0.3.0* (Buchholz *et al*., 2018) was used for denoising. Particle picking was done using a Napari-based viewer (Gaifas *et al.*, 2023) and was completed within the pipeline and STA was completed on the extracted subvolumes as described for RELION-4 (Zivanov *et al.*, 2022). DMS structures were picked using the oversampling around a sphere technique as described in Scaramuzza and Castaño-Díez (2021), and Pyle *et al.* (2022). The centre of each DMS was marked and the radius was set at the inner DMS membrane. Particle spacing was set at 40 Å for the extraction of subtomograms around the spheres. The spherical picking also provided a prior angle for each of the particles so that the particles were orientated with their Z-axis normal to surface of the pseudo-spheres. Different extraction box sizes and masks were tested to reconstruct an initial model. The initial model was used for classification of the subvolumes at bin 4 (12.2 Å/pixel). The best class was selected and used to reconstruct a new reference model at bin 2 (6.1 Å/pixel) for further classification. The alignment of the particles was refined until the model reached the Nyquist frequency.

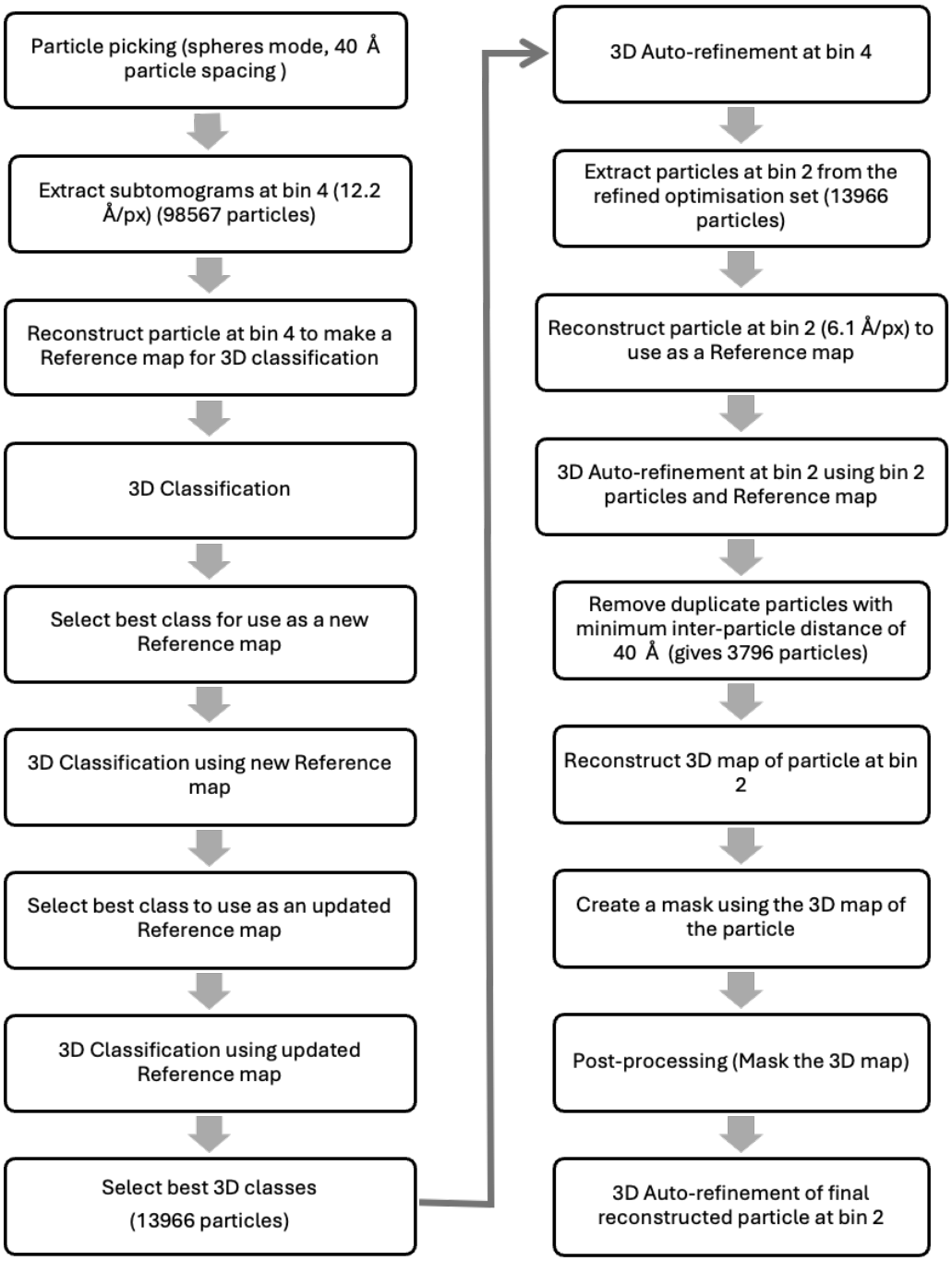


Figure 2. 6 Subtomogram averaging pipeline in RELION-5.

Tilt series from cryo-ET were imported into RELION-5 (Burt *et al.*, 2024) and motion corrected, aligned, and reconstructed. Each DMS was picked as a sphere and subtomograms were extracted at bin 4 (12.2 Å/px) around the surface of the spheres in sub-boxes including the DMS double membrane spaced 40 Å apart. The extracted particles (98567 particles) were used to reconstruct an initial model to use as a Reference map. Then, the particles were iteratively classified using the best class as a reference for the subsequent classification and refined. Next, the subset of refined particles (13966 particles) were extracted from the tomograms at bin 2 (6.1 Å/px) and used to reconstruct a Reference map at bin 2. The bin 2 particles were refined and duplicate particles were removed leaving 3796 particles. Finally, the subset of 3796 particles were reconstructed at bin 2, masked, and refined to test the resolution of the model.

For membrane segmentations, reconstructed tomograms were also denoised using *Isonet* (Liu *et al.*, 2022) in which the tomograms were binned to a pixel size of 9.15 Å/pixel and filtered with a deconvstrength = 1, an snrfalloff = 0.7, the density_percentage = 90 and the std_percentage = 50. For denoising, 30 iterations were run on a single tomogram with noise_start_iter range of 10,15,20,25 and a noise_level range of 0.05,0.1,0.15,0.2 to determine the best level of denoising for the tomograms, and a filter_base = 96. The membranes were then segmented by *Membrain-seg* using the model version MemBrain_seg_v10_alpha.ckpt (Lamm *et al.*, 2024; Lamm *et al.*, 2022). Other segmentations were also completed using *3dmod* in *IMOD* (version 4.9.2; Mastronarde and Held, 2017). *UCSF ChimeraX* (Pettersen *et al.*, 2021) was used to model reconstructed tomograms, membrane segmentations, subvolume averages, and AlphaFold and PDB structures.

Chapter 3. Generation and characterisation of recombinant fluorescent viruses to visualise replication organelles

3.1. Introduction

CoV have been visualised in cells via electron microscopy since 1984 (Dubois-Dalcq *et al.*, 1984) and CoV DMVs were described first (Gosert *et al.*, 2002) and DMSs described later (Maier *et al.*, 2013). To visualise these membrane rearrangements in a targeted manner, fluorescence markers for replication organelles can be combined with ultrastructural imaging techniques. This correlative approach circumvents labour-intensive, and potentially ambiguous, search for specific membranes within the ultrastructure of cells, especially for small, fast, time-sensitive, and rare events.

Fluorescence correlation guides the ultrastructural imaging at the level of finding the right cell holding the biology of interest as well as locating the interesting membranes within the cytoplasm of the specific cell. Plus, within the complex and interconnected membrane ultrastructures of the cytoplasm, a fluorescent marker for specific membranes (or proteins) of interest can be used for unambiguous identification so the structures are not confused for similar looking, but irrelevant, events.

Fluorescent labels and fluorescent imaging techniques must be compatible with the ultrastructural imaging techniques such that the integrity of the sample is maintained. Correlative techniques that best maintain the native-state of the cells include

endogenously expressed fluorescent tags or live-cell fluorescence labels (where no cell perforation or chemical fixing is required) combined with imaging under cryogenic conditions (ensuring no chemical dehydration or staining artifacts). Although protocols have been developed for pre-embedding antibody-labelling CLEM at room temperature, some ultrastructural elements are more sensitive to the process than others (Doyle *et al.*, 2024). For example, experiments combining IF labelling of markers for IBV replication with EM have shown that the DMSs and zER were retained but the DMVs were lost under the specific sample preparation conditions (Doyle *et al.*, 2024). Therefore, to efficiently image the CoV RO under near native conditions in vitrified samples, fluorescent recombinant viruses were generated as tools that will directly label the replication organelle membranes. The first aim of this chapter was to generate fluorescent viruses, characterise their growth, and find the recombinant virus which exhibited the most fluorescence signal.

Recombinant viruses were designed with fusions to nonstructural protein 2 (nsp2) by Dr Helena Maier (The Pirbright Institute). Nsp2 interacts at the replication transcription complex (RTC) and thus labelling it will mark sites of replication (V'kovski *et al*., 2019). Nsp2 is the first protein in the IBV replicase 1a polyprotein and the tags were inserted downstream of the native viral start codon of ORF1a followed by a 3-alanine spacer before the 5' terminus of nsp2. This location was tested as it should not interfere with polyprotein cleavage or risk the tag being cleaved. As the tag will be the first protein to be translated from the IBV genome, expression will be observed early in genome expression. Recombinant BeauR IBV cDNAs with four different tags were produced: SNAP-tag (543 nucleotides), tetracysteine (TC; 30 nucleotides), mCherry (236

nucleotides), monomeric enhanced green fluorescent protein (meGFP; 239 nucleotides) (Appendix 8.1). The TC-tag would only be fluorescent upon incubation with further labelling reagents. Recombinant Vaccinia viruses containing complementary DNA (cDNA) copies of the modified IBV genomes were produced and sequenced by Dr Sarah Keep (The Pirbright Institute). Finally, the rIBVs were rescued by Patrick Phillips. The rIBVs which rescued first, had stable incorporation of the tag, exhibited the most fluorescence signal upon infection, and the earliest appearance of fluorescence signal, were taken forward for stock production, virus characterisation and correlative imaging.

3.2. Results

3.2.1. Multi-step replication kinetics of rescued IBV recombinants

Recombinant IBVs with meGFP, mCherry, and TC tags were successfully rescued. PCR products encompassing the insert-region were sent for Sanger sequencing which confirmed the presence of the modification. Stocks of the rescued viruses were made in CK cells and embryonated eggs and named BeauR-eGFP-nsp2, BeauR-mCherry-nsp2, and BeauR-TC-nsp2. The stocks were titrated by plaque assay with plaque forming units (PFU) per ml calculated (Table 3.1). For infection experiments, the preferred titre was at least 1×10^6 PFU/ml. The titre of the BeauR-eGFP-nsp2 stock made in CK cells was five times lower than the stock made in the first batch of embryonated eggs. Using another batch of embryonated eggs, the titre reached 1.86×10^6 PFU/ml, almost fifteen times higher than the stock made from the first batch. All stocks of BeauR-mCherry-nsp2 and BeauR-TC-nsp2 were above 1×10^6 PFU/ml.

Table 3. 1 Titration of stocks of successfully rescued recombinant viruses.

Recombinant virus	Stock production host	Titre (PFU/ml)
BeauR-eGFP-nsp2	CK Cells	2.27×10^4
	Embryonated eggs batch 1	1.29×10^5
	Embryonated eggs batch 2	1.86×10^6
BeauR-mCherry-nsp2	CK Cells	2.50×10^6
	Embryonated eggs	5.71×10^6
BeauR-TC-nsp2	CK Cells	3.23×10^6
	Embryonated eggs	2.01×10^6

CK cells were infected with serial dilutions of rIBV stocks from CK cells or embryonated eggs and the titre in plaque forming units (PFU) / ml was calculated. The titres given are the average of three repeats of the plaque assay for each rIBV stock.

After the identity of the rIBVs had been characterised by PCR and sequencing, their growth kinetics were compared to those of the wild-type (WT) IBV BeauR. Initially, multistep growth curves were performed. CK and DF1 cells were infected with WT BeauR or BeauR-eGFP-nsp2 stocks made from cells. At 1, 8, 24, 48, 72, and 96 h pi, cell supernatant containing virus was harvested and titrated by plaque assay. In DF1 cells, the viral titres peaked at 48 h pi but the growth kinetics of BeauR-eGFP-nsp2 were delayed compared to WT and a lower peak titre was reached (Figure 3.1 A). In CK cells, the viral titres peaked at 24 h pi and although the peak titre of BeauR-eGFP-nsp2 was once again lower than WT, the growth kinetics of the viruses followed a more similar pattern (Figure 3.1 B). In both infections, it is unclear why the rIBV has a higher initial titre when cells were infected with 1×10^5 PFU/ml of each virus to give the same starting MOI. Overall, these results show that although the rIBV can still replicate, insertion of the eGFP tag attenuates replication.

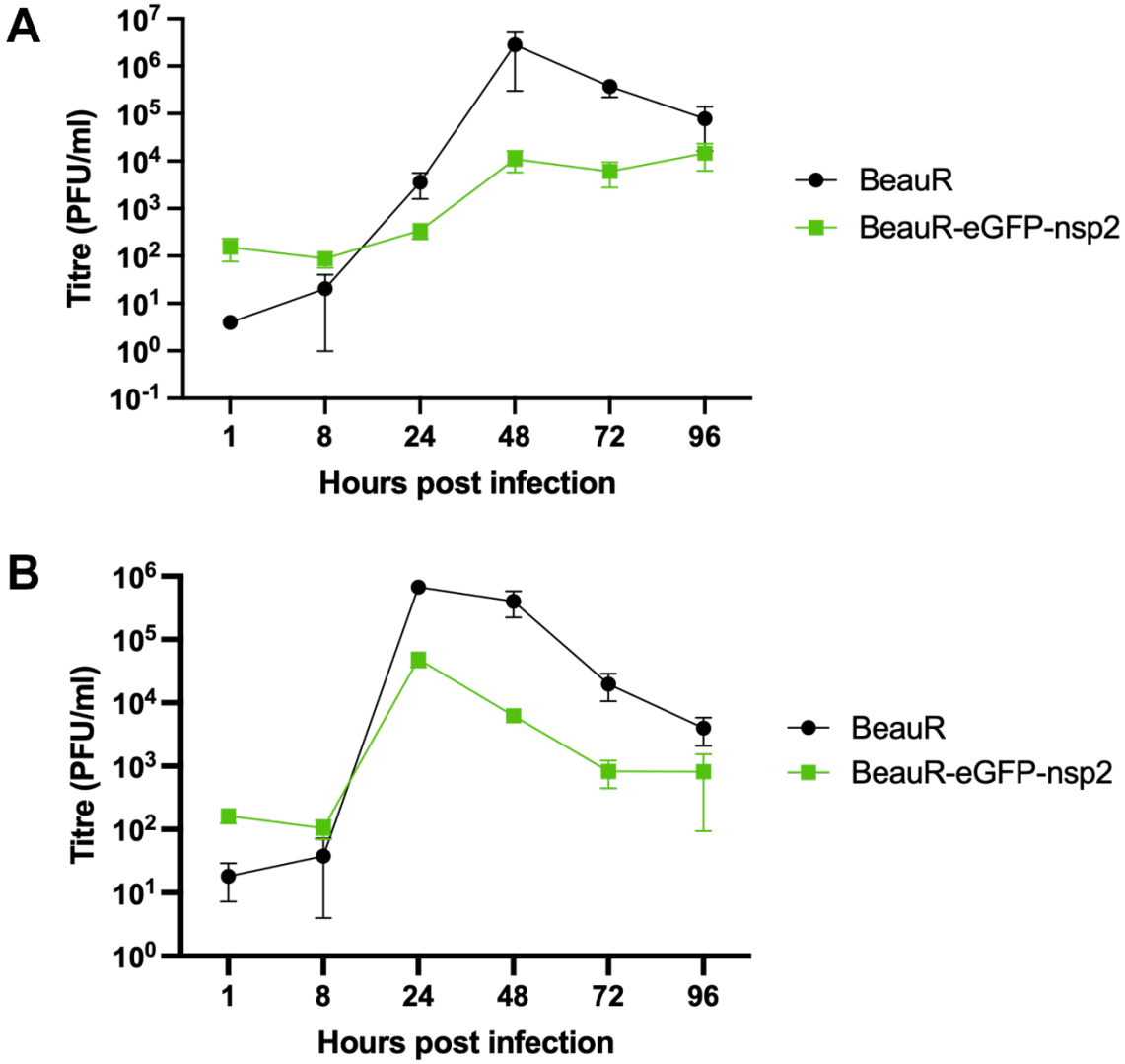


Figure 3. 1 Growth kinetics of BeauR-eGFP-nsp2 compared to WT BeauR in DF1 (A) and CK (B) cells.

DF1 (A) or CK (B) cells were infected at a titre of 1×10^5 PFU/ml (MOI~0.08) with cellular stocks of WT BeauR or BeauR-eGFP-nsp2. The supernatant was harvested at 1, 8, 24, 48, 72 and 96 h pi. Error bars represent ± standard error of the mean (SEM) of three independent experiments.

Since CK cells provided a better replication model, subsequently, growth kinetics of BeauR-TC-nsp2 and BeauR-mCherry-nsp2 compared to BeauR were determined only in CK cells. Here, both BeauR-mCherry-nsp2 and BeauR-TC-nsp2 reached peak titres at 48 h pi that were not significantly different to WT (Figure 3.2 A-B). Moreover, the pattern of the growth curves for the rIBV and WT IBV were similar. Overall, this confirmed that these tags did not significantly attenuate viral replication.

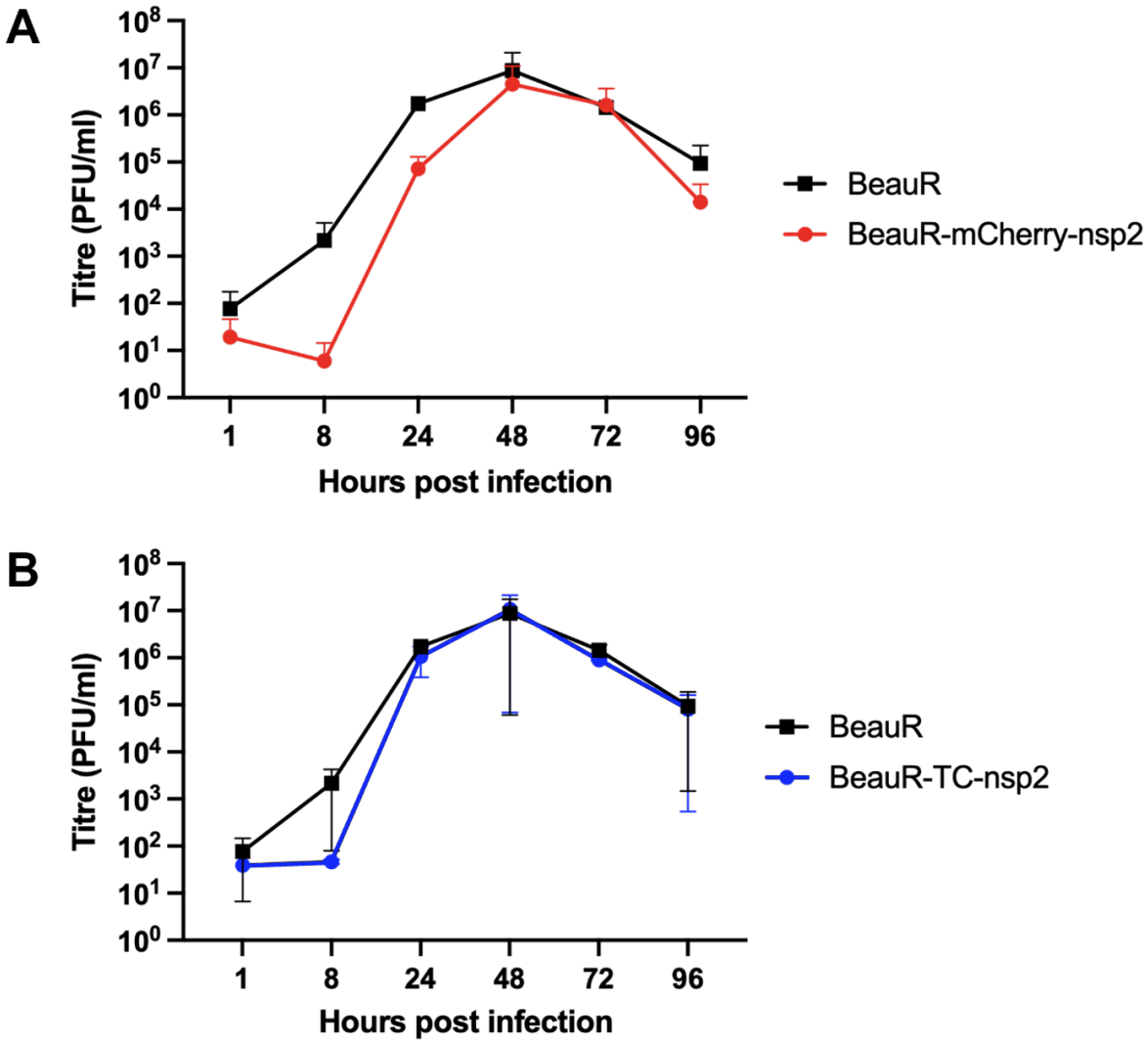


Figure 3. 2 Growth kinetics of BeauR-mCherry-nsp2 (A) and BeauR-TC-nsp2 (B) compared to WT BeauR in CK cells.

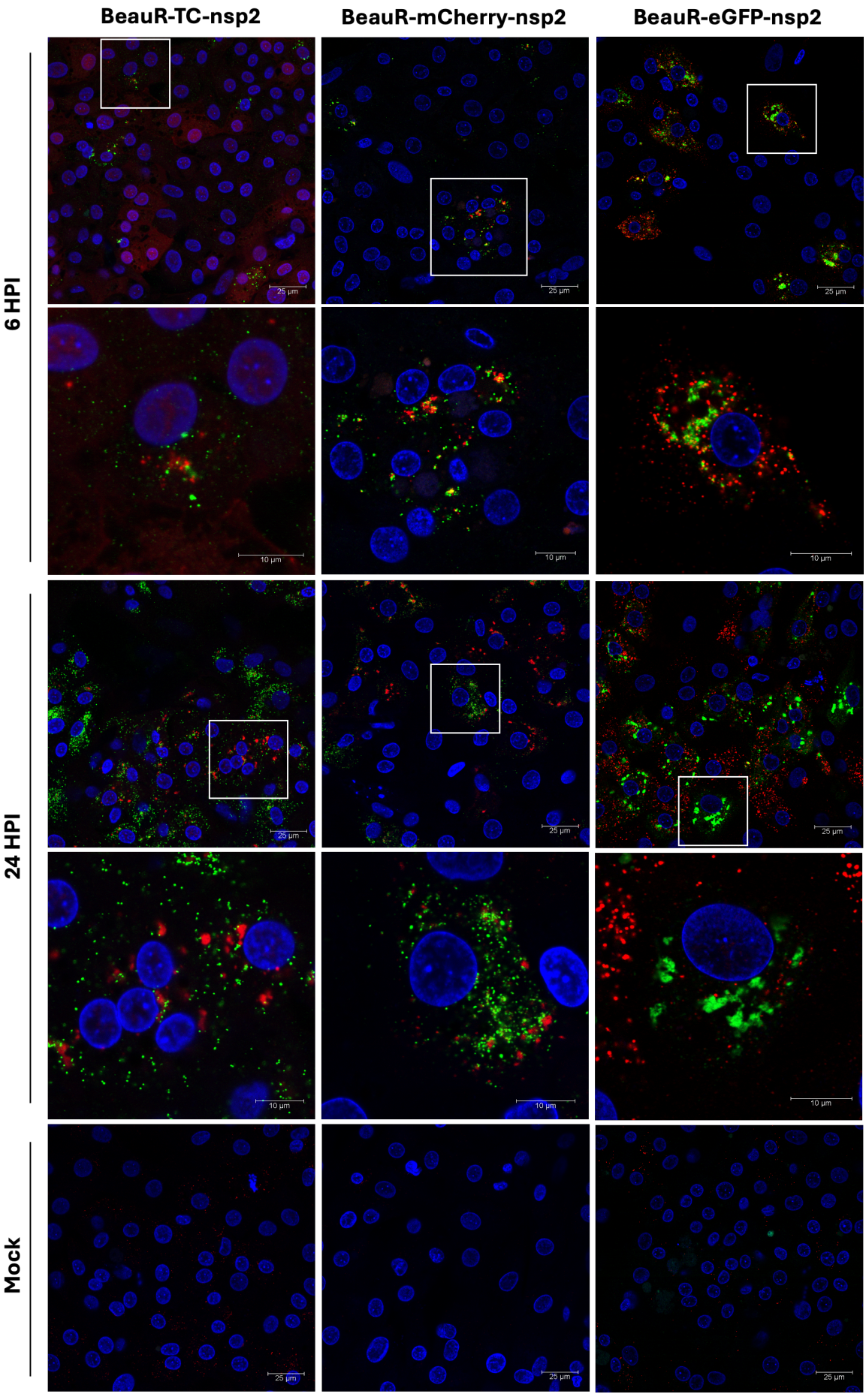
CK cells were infected at a titre of 1×10^5 PFU/ml (MOI~0.08) with WT BeauR, BeauR-mCherry-nsp2 (A) or BeauR-TC-nsp2 (B). The supernatant was harvested at 1, 8, 24, 48, 72 and 96 h pi. Supernatant was titrated on CK cells to determine the quantity of progeny virus. Error bars represent ± standard error of the mean (SEM) of three independent experiments.

3.2.2. Fluorescence microscopy of different IBV recombinants

Since the rIBVs could all replicate, to determine their suitability for the ultimate imaging experiments, ease of detection of fluorescence was tested. CK cells were infected with the undiluted rIBV stocks (MOI ~0.8-1) and at 6 and 24 h pi, cells were fixed and labelled with anti-dsRNA, which is a marker for viral RNA replication. Neat virus was used to infect the cells to give the highest MOI and maximise infection. BeauR-TC-nsp2 infected cells were labelled with TC-ReAsH before fixation.

Fluorescent-nsp2 puncta were observed in the cell cytoplasm and in perinuclear patches in the same cells as dsRNA puncta were observed (Figure 3.3). In some regions, the tag and the dsRNA signal were colocalised at 6 h pi (Figure 3.3 6 h pi magnified regions and line intensity plots). For example, over the magnified images of the rIBVs at 6 h pi, BeauR-TC-nsp2 signal colocalised with 0.45 % of dsRNA foci, BeauR-mCherry-nsp2 colocalised with 4.96 % of dsRNA foci, and BeauR-eGFP-nsp2 colocalised with 11.28 % of GFP foci. All rIBVs exhibited similar fluorescent foci patterns in similar locations suggesting that addition of the tags was not altering the location of nsp2. Interestingly, the rIBV and dsRNA signals appeared to colocalise more often at 6 h pi compared to 24 h pi. Despite all BeauR-eGFP-nsp2 stocks having a lower titre than BeauR-mCherry-nsp2 and BeauR-TC-nsp2 stocks, at both timepoints, more eGFP-nsp2 positive cells were observed compared with mCherry-nsp2 positive cells and TC-ReAsH positive cells (Figure 3.3). The ReAsH labelling agent gave some background signal in cells without dsRNA so the puncta were not easy to detect corresponding to BeauR-TC-nsp2. The background from the ReAsH dye was also greater at the higher laser powers used to look for smaller TC-ReAsH signals at

the earlier timepoint. Overall, BeauR-eGFP-nsp2 signal was the easiest to detect and was visible in the most cells at the earliest timepoint. Therefore, BeauR-eGFP-nsp2 was characterised further and stocks of this virus would be used as the tool for detecting RO membranes in the correlative imaging techniques.


BeauR-TC-nsp2
BeauR-mCherry-nsp2
BeauR-eGFP-nsp2
6 HPI
24 HPI
Mock
25 µm
10 µm

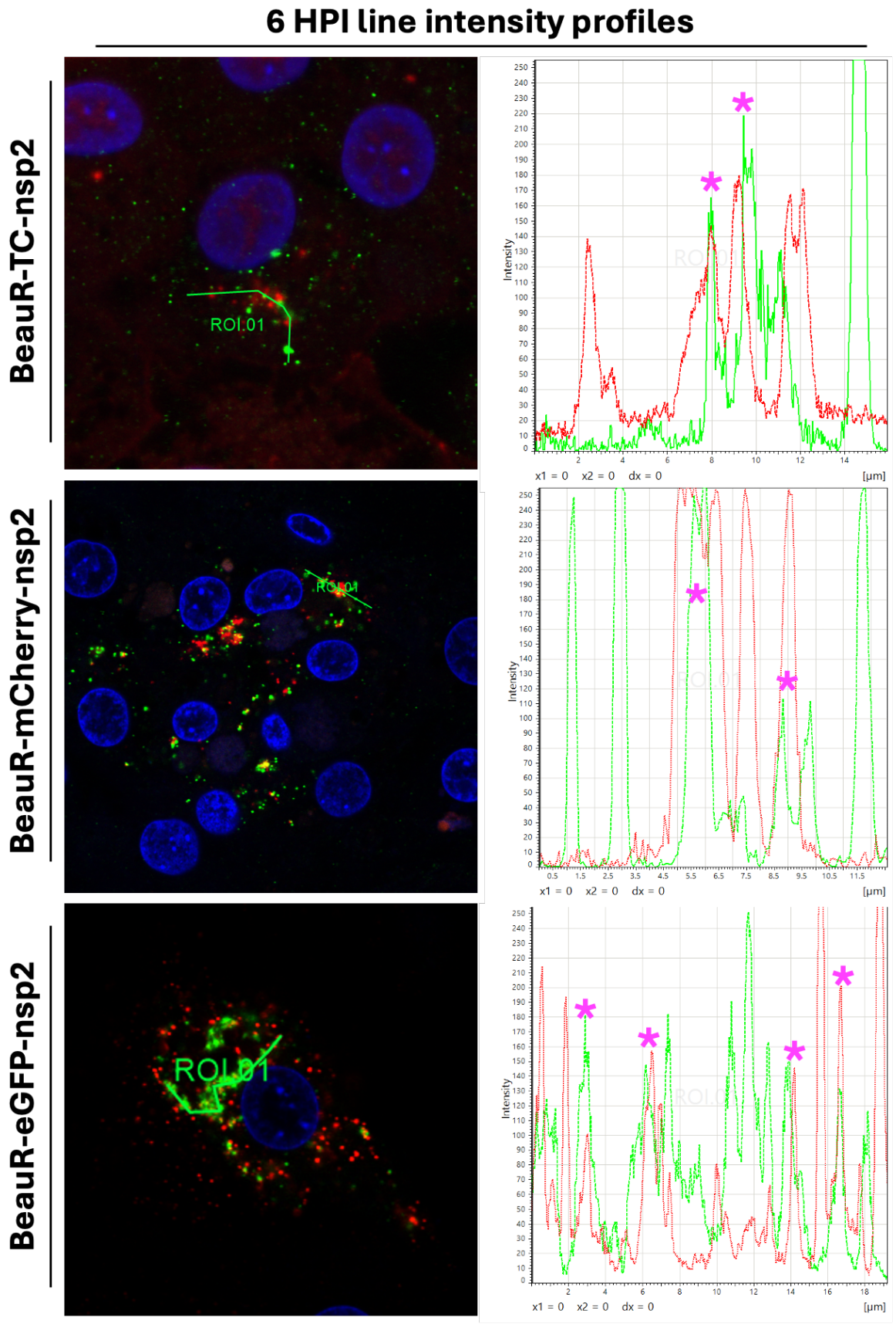


Figure 3. 3 Comparison of BeauR-TC-nsp2, BeauR-mCherry-nsp2 and BeauR-eGFP-nsp2 by immunofluorescence microscopy.

CK cells were infected with neat BeauR-TC-nsp2 (left), BeauR-mCherry-nsp2 (middle), or BeauR-eGFP-nsp2 (right). For BeauR-TC-nsp2, cells were labelled with TC-ReAsH (red), fixed at the stated timepoints and labelled with anti-dsRNA (green). For BeauR-mCherry-nsp2 (red), at the stated timepoints, cells were fixed and labelled with anti-dsRNA (green). For BeauR-GFP-nsp2 (green), at the stated timepoints, cells were fixed and labelled with anti-dsRNA (red). Nuclei were stained with DAPI (blue). Scale bars are given in the bottom right corner of each image. The degree of colocalisation between the fluorescence of the rIBV and the antibody labelling dsRNA is shown in the line intensity plots following the ROI in the righthand panels. Intensity peaks with colocalisation are labelled with magenta asterisks. Line intensity profiles from 6 H PI panels were made in Leica LAS X software.

3.2.3. Single step growth kinetics of BeauR-eGFP-nsp2

It was decided that BeauR-eGFP-nsp2 would be used for the correlative imaging to investigate RO membranes because it was easier to visualise. Therefore, the single-step replication kinetics from 0-12 h pi, the incubation time over which early RO formation events might be captured, were investigated (Figure 3.4 A-B). There were differences between WT and rIBV multistep replication kinetics, so it was important to see if there were also differences at earlier timepoints. Furthermore, by simultaneously analysing the gRNA levels, any impact of the tag on the function of the RO would be confirmed. At each timepoint, cell supernatant and RNA were harvested from infected cells to measure the titre of released progeny virus and the relative amount of viral genomic RNA, respectively. During infection with WT virus, new progeny virions were released from cells at 6-8 h pi with an increase through to 24 h pi. Whereas, in BeauR-eGFP-nsp2 infection, new progeny virions were released from 8-10 h pi with an increase through to 24 h pi (Figure 3.4 A). Consistent with results in Figure 3.1, a lower titre was reached by 24 h pi compared to wild type, although titres at 8-10 h pi were not significantly different. Interestingly, despite cells being infected at a titre of 1×10^5 PFU/ml of WT or recombinant virus, titres measured for BeauR-eGFP-nsp2 from 1-6 h pi are higher than

for WT, comparable to observations in Figure 3.1. The reason for this is unknown. The recombinant virus did show attenuated replication as is consistent with the multistep growth kinetics (Figure 3.1 A). However, it is important to note that the viral RNA levels within the infected cells were not significantly different up to 12 h pi (Figure 3.4 B). This indicates that the activity of the RTC is not impacted by the presence of the tag.

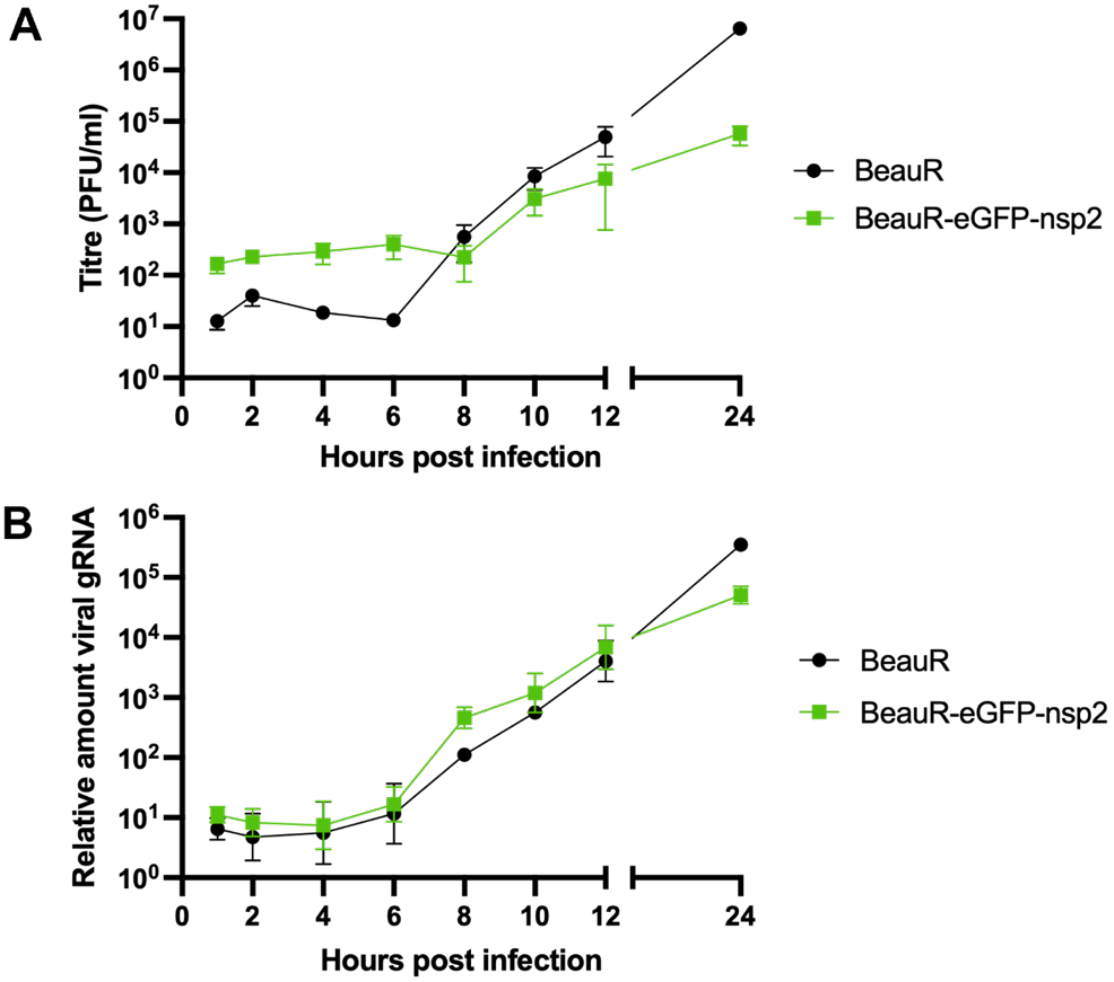


Figure 3. 4 Characterisation of BeauR-eGFP-nsp2 replication by single step growth curve.

CK cells were infected at a titre of 1×10^5 PFU/ml (MOI~0.08) with GFP-nsp2-IBV (green) or WT IBV (black) and cell supernatant was harvested, and total RNA was extracted at 1, 2, 4, 6, 8, 10, 12 and 24 h pi. (A) Supernatant was titrated in triplicate on CK cells to determine the quantity of progeny virus. (B) Levels of genomic RNA (gRNA) were measured by qRT-PCR with primers targeting the IBV 5′-UTR. Error bars represent ± standard error of the mean (SEM) of three independent experiments.

3.2.4. BeauR-eGFP-nsp2 recombinant stability by reverse-transcription polymerase chain reaction (RT-PCR)

It was confirmed that the insert at nsp2 did not impact RTC activity so next, the genetic stability of the insert was tested over several passages in CK cells. This would show whether the stock virus could revert to WT and would no longer be fluorescent. Each passage, CK cells were infected with the previous passage and cell supernatants were harvested at 24 h pi and used as the inoculum for the next passage. One isolate of BeauR-eGFP-nsp2 was independently passaged to P_6 in triplicate. As shown by PCR screening (Figure 3.5 A-B), by P_6, one replicate maintained the insert shown by the 1119 bp product (insert flanking regions (880 bp) plus eGFP insert (239 bp)), one replicate had partial loss of the insert with several products between 1119 bp and 880 bp, and the final replicate fully lost the insert shown by the 880 bp product (Figure 3.5 B). Therefore, at P_6, BeauR-eGFP-nsp2 showed some loss of the insert. Earlier analysis at P_3 showed that the insert was maintained so following experiments were completed with a maximum P_3 stock.

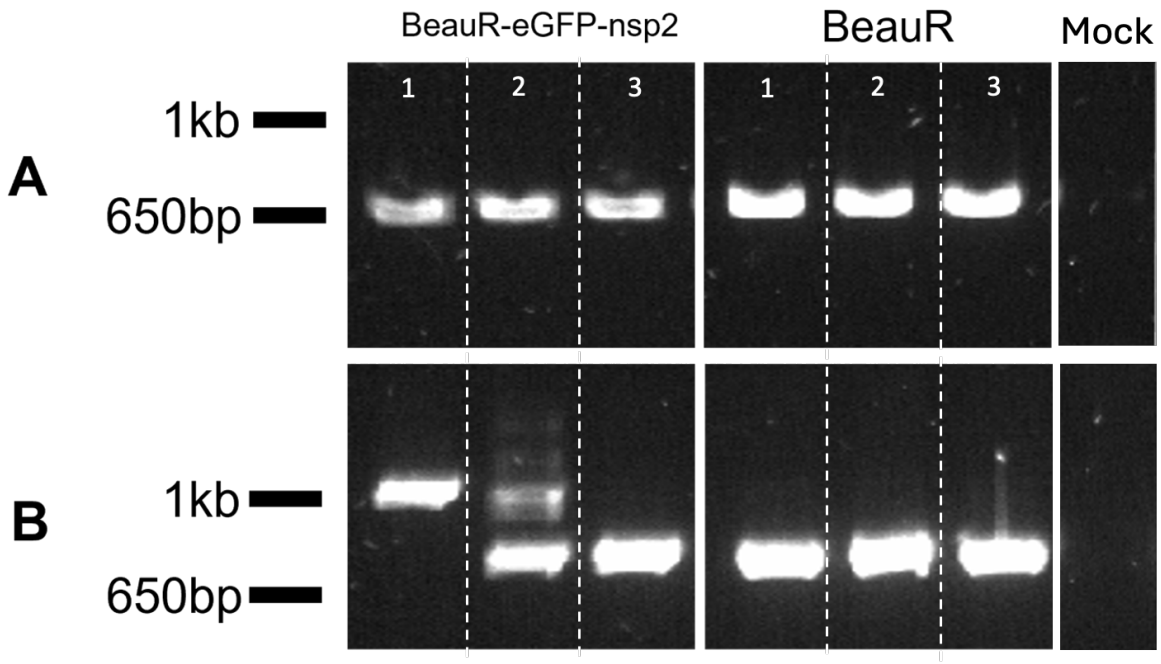


Figure 3. 5 BeauR-eGFP-nsp2 passaging in CK cells.

CK cells were infected with P_5 BeauR-eGFP-nsp2 or BeauR for 24 h to give P_6. RT-PCR screens of P_6, with 3 wells for each of BeauR-eGFP-nsp2 and WT BeauR infected cells, are shown. (A) Screen for IBV 3' UTR to confirm presence of virus. (B) Screen for eGFP insert at nsp2. Presence of the 3' UTR was determined by a 660 base pair (bp) product. Presence of the insert was determined by a 1119 bp product (insert flanking regions (880 bp) plus eGFPinsert (239 bp) gives 1119 bp product).

3.2.5. Western blot to confirm presence of GFP in BeauR-eGFP-nsp2

The eGFP insert in BeauR-eGFP-nsp2 stocks was shown to have sufficient stability for the imaging experiments. Therefore, western blot was used to confirm that the GFP signal observed in confocal microscopy was GFP fused to nsp2 in BeauR-eGFP-nsp2 and that GFP had not been cleaved off. Cells were infected in three biological repeats and at 24 h pi protein lysates were harvested. Proteins were separated by SDS-PAGE, transferred to a nitrocellulose membrane, and then detected by western blot. A band corresponding to GFP-nsp2 at 102 kDa was observed for BeauR-eGFP-nsp2 that was not present in mock or WT infected cells (Figure 3.6 A). Moreover, there was no band at the expected molecular

weight for GFP alone (27 kDa) inferring there was no cleavage of GFP from nsp2. Bands were also observed for IBV M from WT and BeauR-eGFP-nsp2 to confirm cells were infected (Figure 3.6 B). IBV M was expected at 24.5 kDa but it has two predicted N-linked glycosylation sequons so could be estimated to have a size of up to 28.5 kDa (Liang *et al*., 2019).

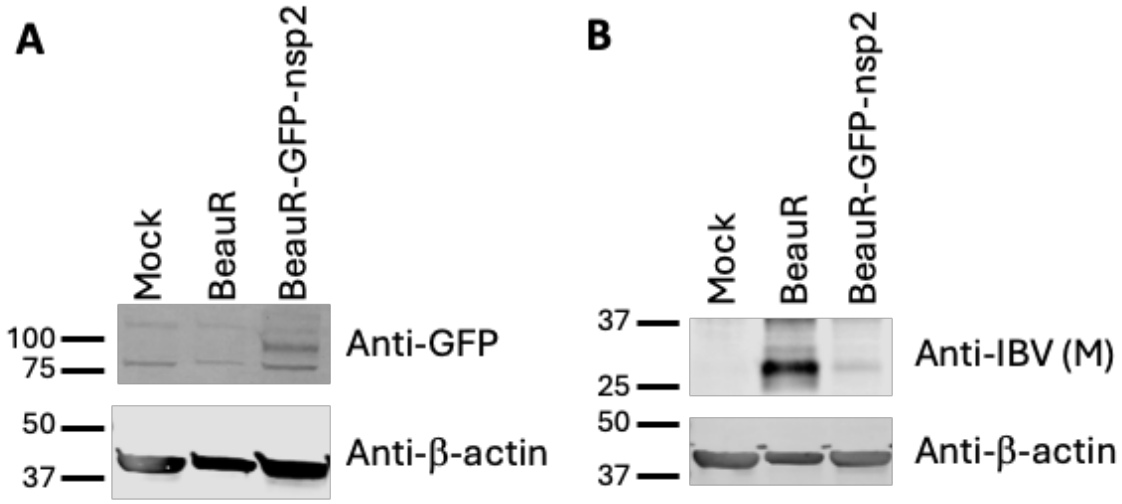


Figure 3. 6 Western blot to confirm presence of GFP protein.

CK cells were mock infected or infected with BeauR or BeauR-eGFP-nsp2. Cells were lysed and the lysate was resolved by SDS-PAGE and transferred onto a nitrocellulose membrane which were labelled with primary antibodies targeting GFP (panel A), IBV (which labels IBV S, M and N; panel B) and actin as a control. Then, the membranes were labelled with secondary antibodies for visualisation. One repeat out of three biological repeats is shown. The M band is shown to represent IBV infection (panel B). Western blots were completed by Dr Helena Maier (The Pirbright Institute).

3.2.6. Confirmation of presence of GFP by IF

Following confirmation of eGFP size in BeauR-eGFP-nsp2, fluorescence signal was also confirmed by IF microscopy using anti-GFP antibodies (Figure 3.7 A-F). Cells were infected with BeauR-eGFP-nsp2, fixed at 24 h pi, and labelled with anti-GFP. All eGFP-nsp2 signal correlated to anti-GFP antibody signal (Figure 3.7 E-F). This validates the fluorescence signal and confirms that it is unlikely that any cells infected with BeauR-eGFP-nsp2 are undetectable when imaging endogenous GFP signal.

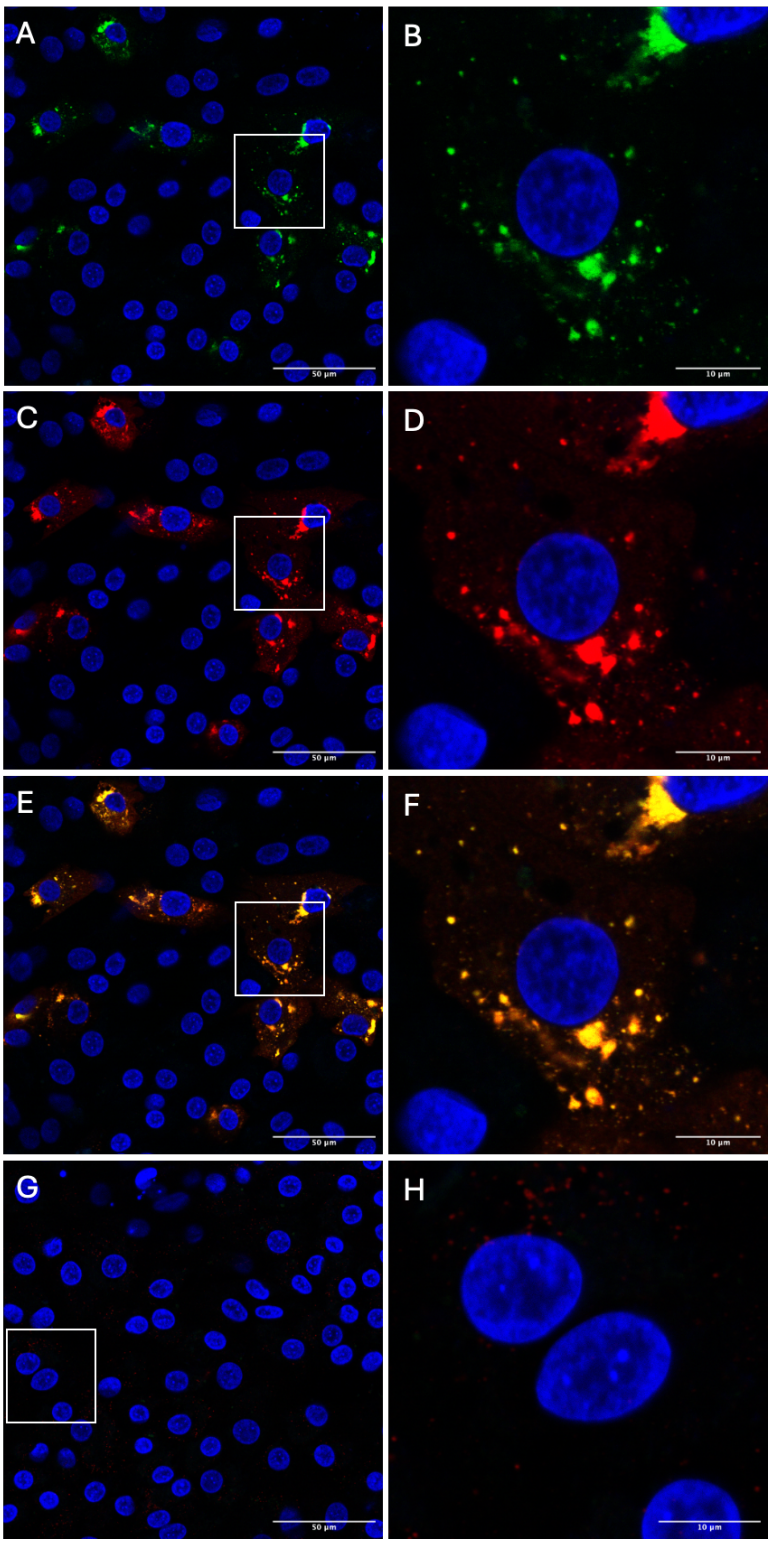


Figure 3. 7 Confirmation of GFP in BeauR-eGFP-nsp2 infected CK cells.

CK cells were infected with BeauR-eGFP-nsp2 (A-F) or mock infected (G-H). At 24 h pi, cells were fixed and labelled with anti-GFP primary antibodies and then Alexa Fluor 568 secondary antibodies. BeauR-eGFP-nsp2 native fluorescence was imaged in green (A-B) and anti-GFP antibody was imaged in red (C-D). The composite is shown in panels E-F. Right hand panels are magnified areas of the images in the left hand panels (indicated by boxes). Composite images of mock infected cells are shown in panels G-H. IF of BeauR-eGFP-nsp2 and anti-GFP was completed by Dr Helena Maier (The Pirbright Institute).

3.2.7. Comparison of BeauR-eGFP-nsp2 fluorescence in different cell lines

The identity of the eGFP insert had been confirmed and fluorescence imaging of BeauR-eGFP-nsp2 was preferred over the other rIBVs since it was the easiest to detect. Therefore, cell lines that supported the highest level of infection and most abundant eGFP-nsp2 fluorescence were investigated. Several cell lines known to support IBV replication were tested to see if the number of infected cells, as observed by the fluorescence signal from BeauR-eGFP-nsp2, could be maximised. Continuous avian cell lines from chick embryo fibroblasts (DF1 cells) and chicken lung epithelial cells (CLEC) were tested alongside a continuous mammalian cell line (Vero) and primary chick kidney (CK) cells. The cell line that exhibited the most and earliest eGFP-nsp2 fluorescence would be the easiest to use for finding early RO formation events during the correlative imaging.

Cells were infected, fixed 6 h pi and eGFP-nsp2 signal was imaged. BeauR-eGFP-nsp2 exhibited the highest number of cells with GFP foci, the highest number of GFP foci per cell, and the largest GFP foci in CK cells when compared to DF1, Vero and CLEC cells at 6 h pi (Figure 3.8). This implies that the CK cells will presumably have the highest concentration of RO membranes, making it more straightforward to identify them at the earlier timepoints.

CK cells are primary cell line made from tissue trypsinisation so there were some faint areas of GFP autofluorescence, that appear like clouds rather than puncta, from cell debris (Figure 3.8). Moreover, the stock of BeauR-eGFP-nsp2 used, since it had a higher

titre (Table 3.1), was generated in embryonated eggs and was harvested in the egg allantoic fluid. Therefore, the mock-infected cells were exposed to allantoic fluid from uninfected eggs to check for further autofluorescent debris. Small areas of autofluorescence were again observed whether from CK cell preparation from tissue or allantoic fluid from the stock. In any case, the autofluorescent foci were rare and often had a fainter cloud-pattern compared to the bright puncta induced by the rIBV, examples are shown in the mock-infected allantoic fluid samples (Figure 3.8 magnified insets). In Figures 3.3 and 3.7, the virus stocks made in cells were used and mock infected with 1 x BES, these mock coverslips exhibited no GFP autofluorescence.

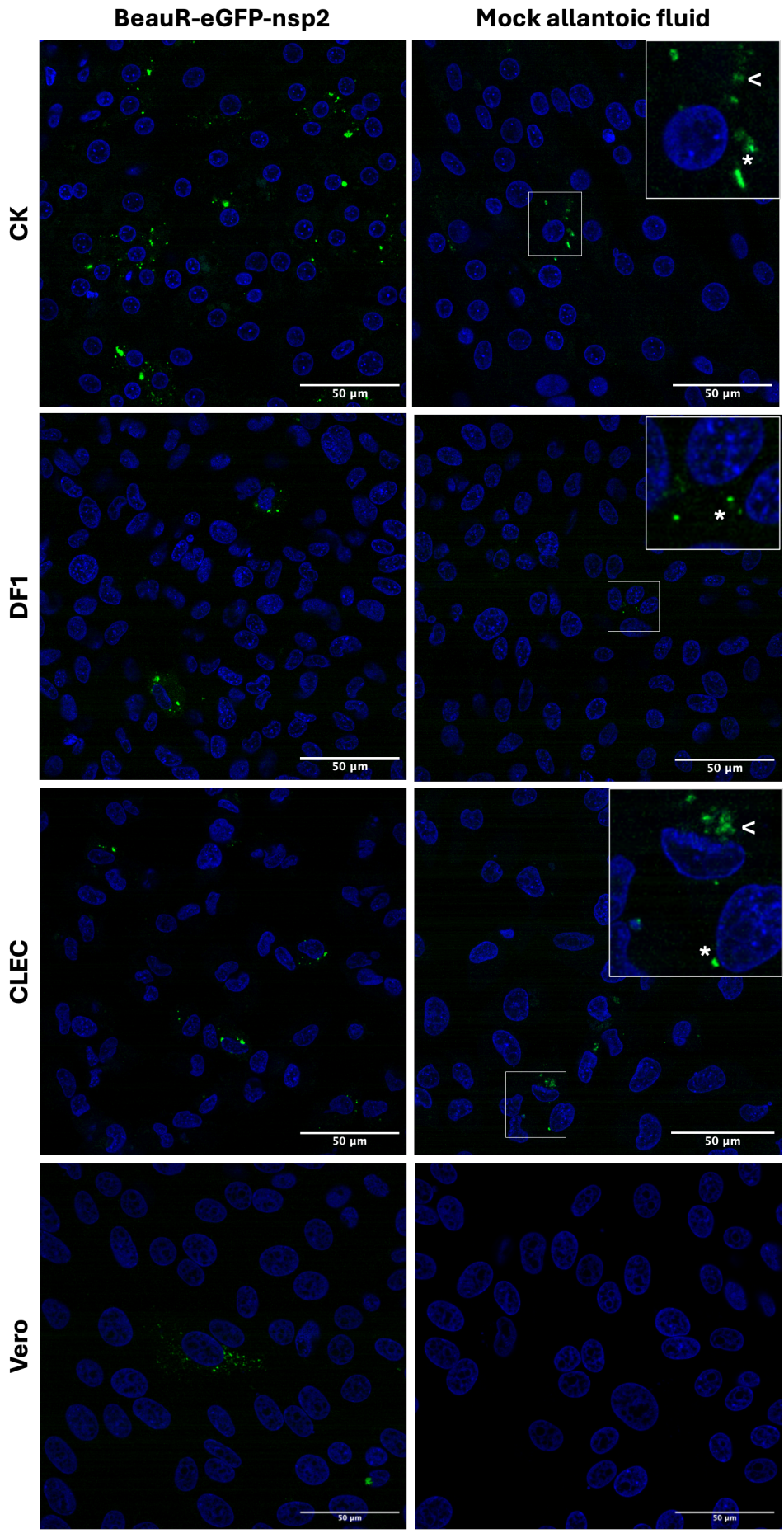

BeauR-eGFP-nsp2
Mock allantoic fluid
CK
DF1
CLEC
Vero
50 μm

Figure 3. 8 BeauR-eGFP-nsp2 exhibits the strongest fluorescence signal at 6 h pi in CK cells.

Chicken Kidney (CK), DF1, Vero and Chicken Lung Epithelial Cells (CLEC) were infected or mock-infected with undiluted BeauR-eGFP-nsp2 (green), cells were fixed, and nuclei were stained with DAPI (blue). There was some 488 signal observed in the mocks as shown in the magnified insets and described like clouds (arrowheads) or puncta (asterisks), which were likely autofluorescence signals from cell debris or allantoic fluid that the stocks were made in.

3.2.8. BeauR-eGFP-nsp2 fluorescence in CK cells at early timepoints

Following confirmation that eGFP-nsp2 signal could be detected both earliest in CK cells and with the most infected cells visible, the earliest time at which fluorescence could be detected was investigated. This was useful because one aim of the ultrastructural interrogations was to image RO formation events before they were indistinguishable from fully formed ROs.

CK cells were infected with BeauR-eGFP-nsp2 and fixed at 2-6 h pi. The earliest eGFP-nsp2 fluorescence could be detected was 2 h pi where it appeared as small individual puncta in cells (Figure 3.9). At 3 h pi, the number of puncta increased, and some puncta had combined into larger foci. At 4 h pi, multiple perinuclear foci existed in several cells in the same field of view. At 5 h pi, some larger foci migrated from perinuclear regions further out into the cytoplasm. At 6 h pi, large perinuclear and cytoplasmic fluorescent patches were visible in several cells in the same field of view. The mock-infected coverslip shows an example of the autofluorescence pattern caused by the CK cells and allantoic fluid.

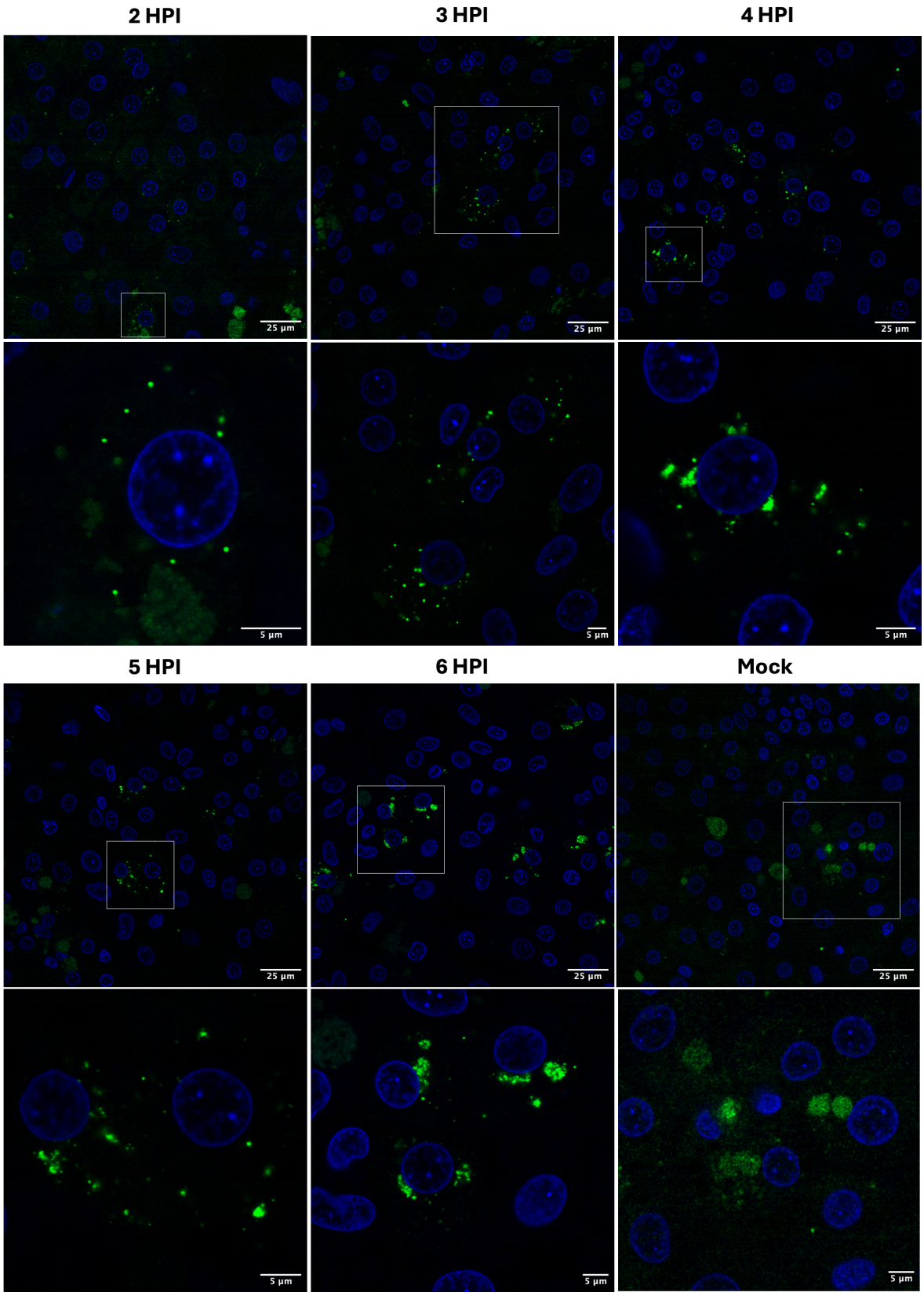


Figure 3. 9 Immunofluorescence time course of BeauR-eGFP-nsp2 up to 6 h pi.

CK cells were infected or mock-infected with egg stocks of BeauR-eGFP-nsp2 (green), cells were fixed at the specified times and imaged. Nuclei were stained with DAPI (blue). Magnified areas, indicated by white boxes, are shown below the images at each time point.

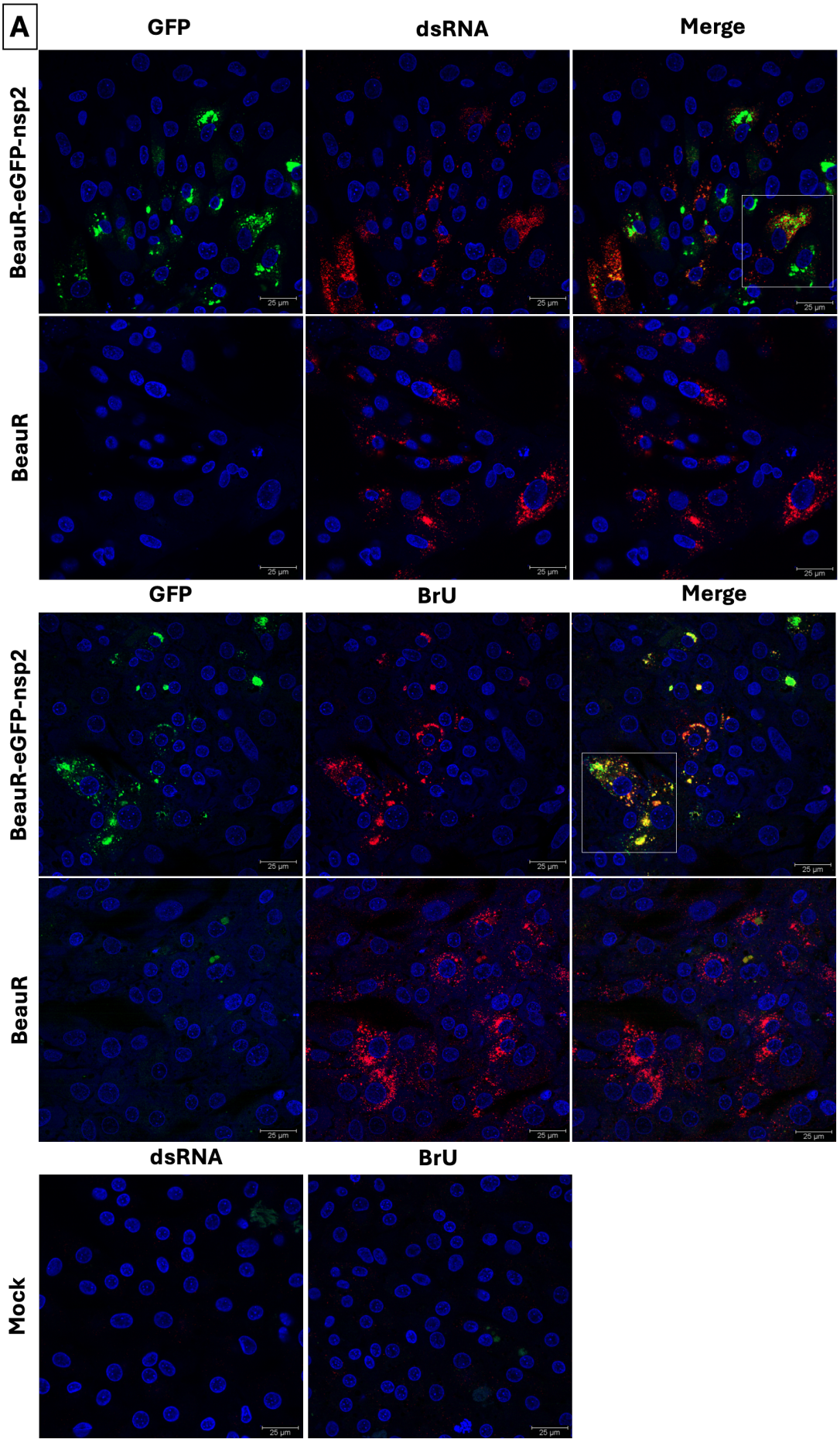
3.2.9. BeauR-eGFP-nsp2 fluorescence correlation to intermediates in viral genome replication (dsRNA) and sites of nascent viral RNA synthesis (bromouridine labelling)

Following confirmation that BeauR-eGFP-nsp2 fluorescence was visible prior to 6 h pi, colocalisation of GFP with known markers for ROs was investigated. Double stranded RNA (dsRNA) can be used as a marker for infected cells since it is a presumed intermediate in viral RNA synthesis. The presence of nascent viral RNA can be directly detected using bromouridine (BrU) labelling as optimised in Doyle *et al.*, 2021. BrU is a uridine analogue that will be incorporated into synthesising RNA. By simultaneously inhibiting host cell RNA synthesis by adding actinomycin D (ActD), BrU will only be incorporated into nascent viral RNA. Subsequently, BrU can be labelled with antibodies, allowing sites of nascent viral RNA to be identified via IF microscopy.

CK cells were infected with BeauR-eGFP-nsp2, and either fixed at 24 h pi and labelled with anti-dsRNA antibodies or treated with BrU and ActD 30 min prior to fixation, kept in an RNase-free environment, and labelled with anti-BrU antibodies. All cells with GFP signal also contained dsRNA or BrU signal showing that BeauR-eGFP can mark cells containing ROs (Figure 3.10 A). Moreover, in several infected cells, regions of GFP and dsRNA colocalise (3.10 B). However, there were also cytoplasmic puncta of dsRNA alone. BrU-labelling more specifically labels sites of nascent viral RNA synthesis and had a greater level of colocalisation to GFP signal compared to dsRNA-labelling (Figure 3.10 B). This showed that BeauR-eGFP-nsp2 marks sites of nascent viral RNA synthesis. Using the sequential scanning function it was confirmed that the GFP fluorophore was not detected

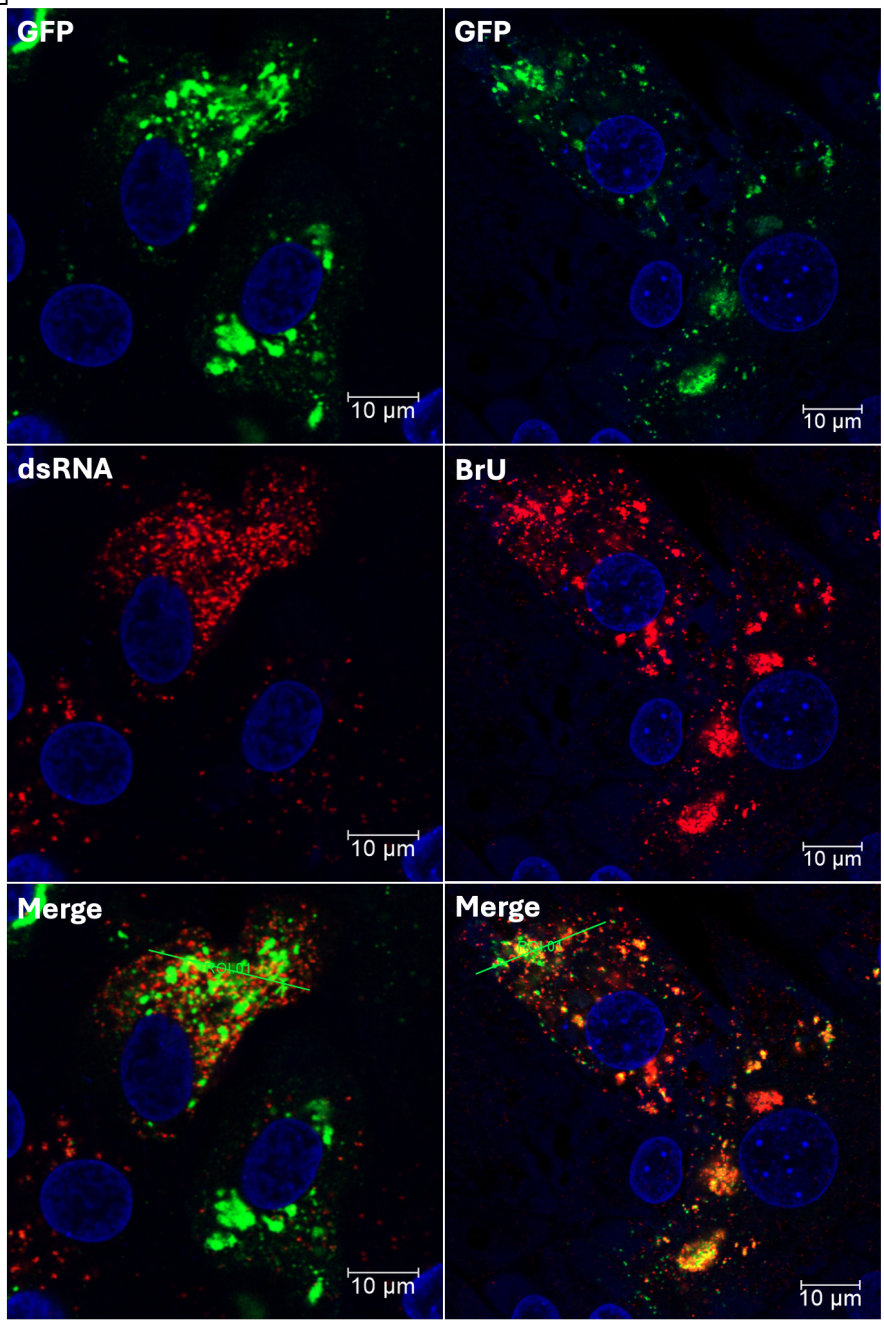
by the red channel and the AlexaFluor 568 was not recorded in the green channel (Figure 3.10 C; Chapter 2.15.2; Jonkman *et al*., 2020).

The patterns of dsRNA and BrU labelling were similar in BeauR-eGFP-nsp2 infected and WT BeauR infected cells (Figure 3.10 A). This suggests that the location of markers of viral replication has not been altered by incorporation of the eGFP tag. Interestingly, some cells that did not contain BeauR-eGFP-nsp2 signal did label for dsRNA (Figure 3.10 A).

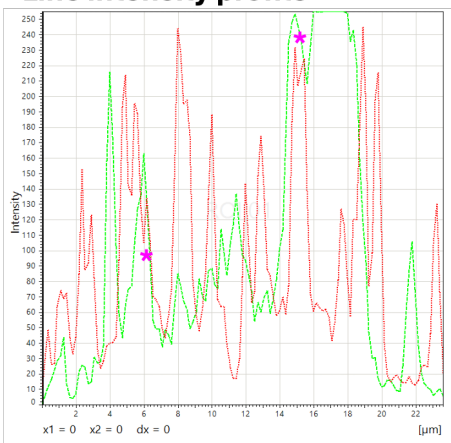

A
GFP
dsRNA
Merge
BeauR-eGFP-nsp2
BeauR
GFP
BrU
Merge
BeauR-eGFP-nsp2
BeauR
dsRNA
BrU
Mock

B

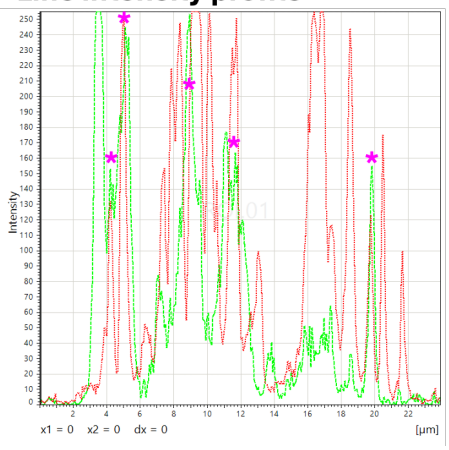
BeauR-eGFP-nsp2 infected cells



Line intensity profile



Line intensity profile



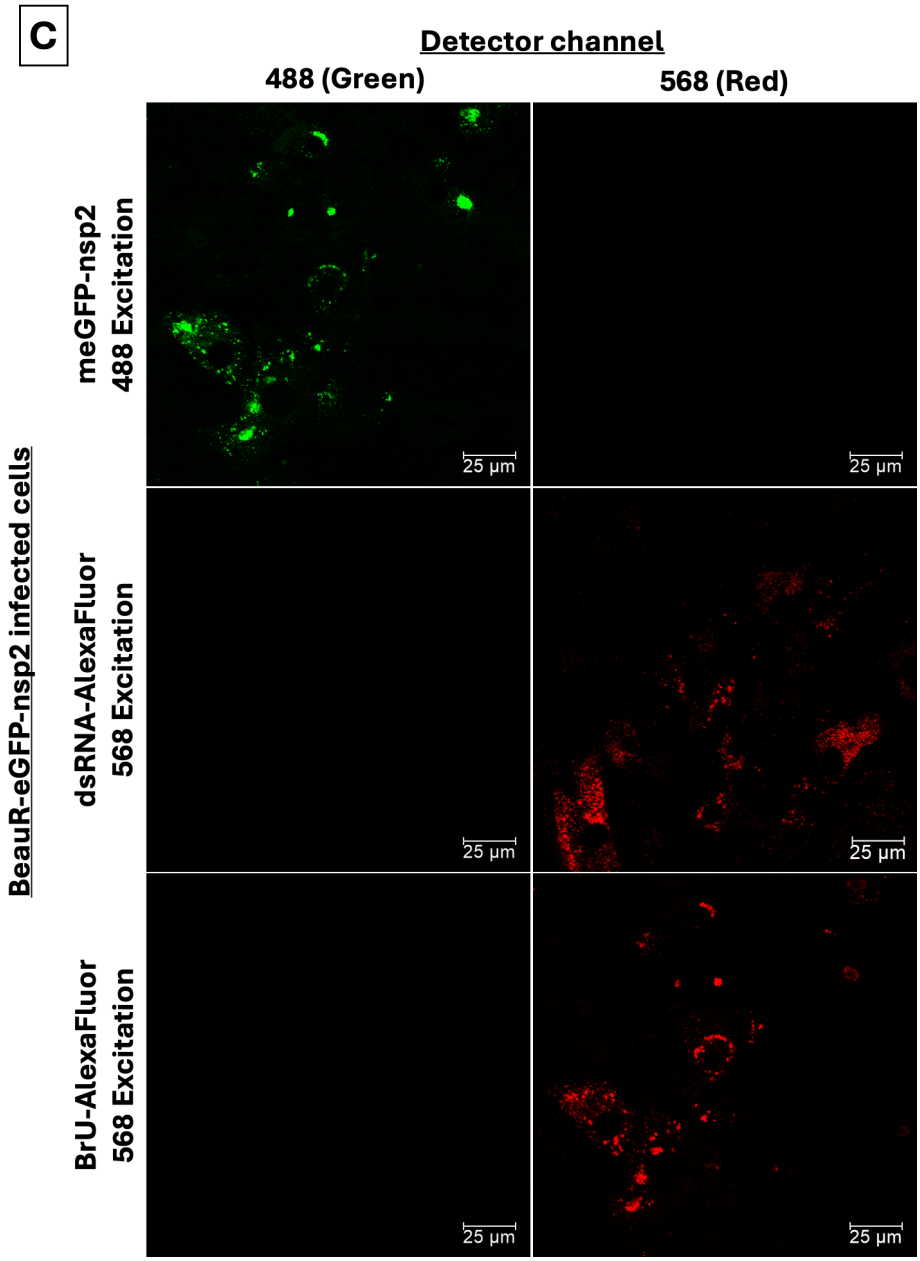


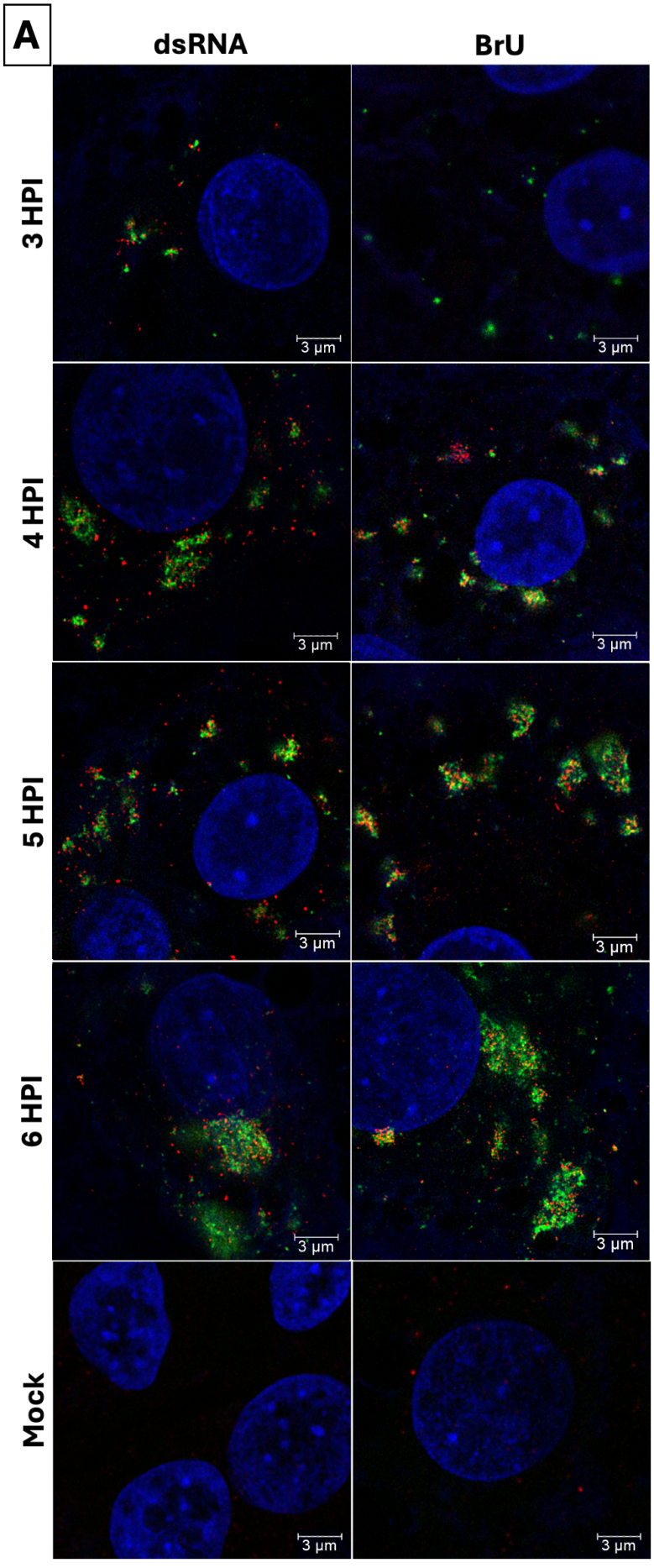
Figure 3. 10 Immunofluorescence of BeauR-eGFP-nsp2 with known markers of viral replication organelles.

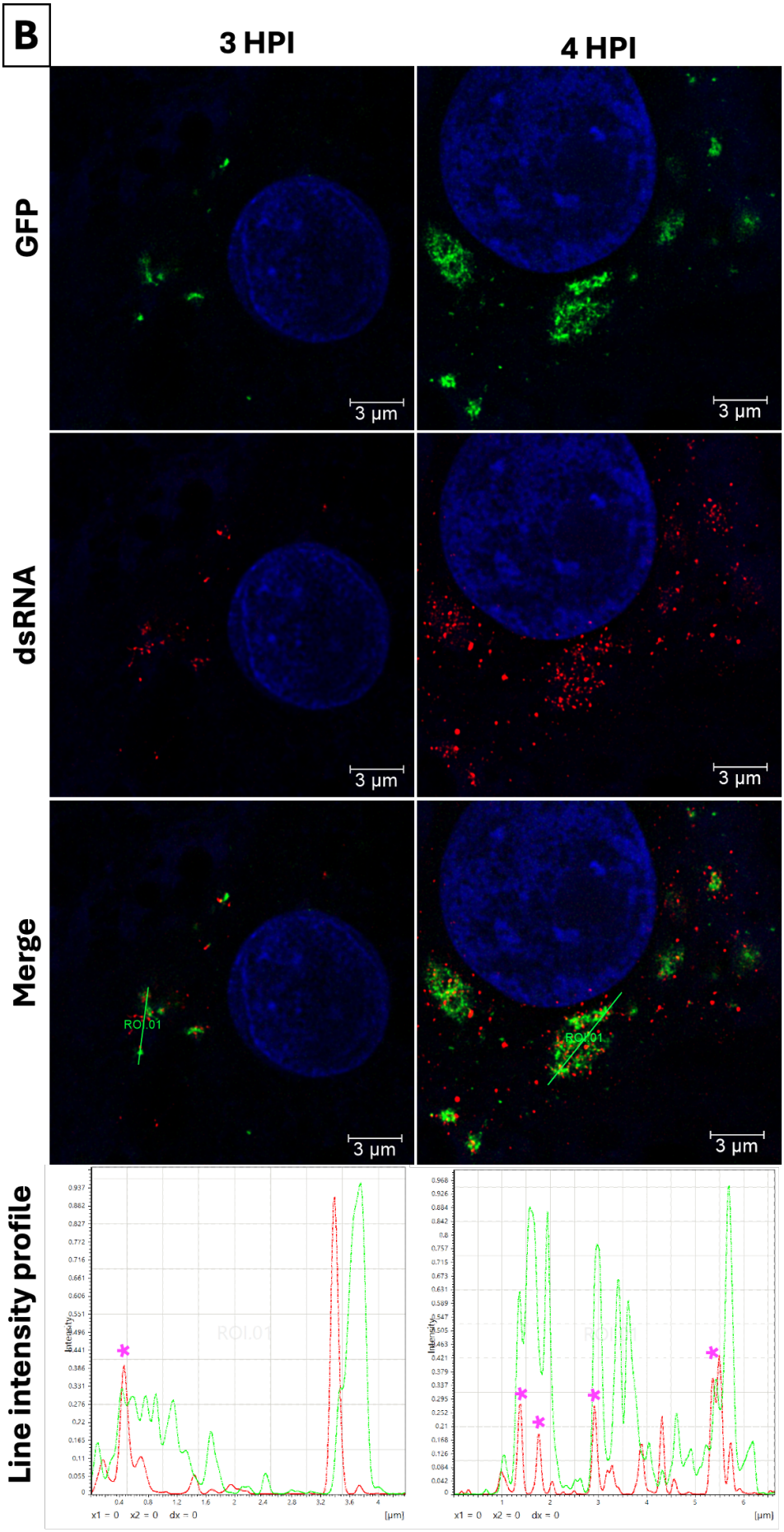
CK cells were infected or mock-infected with BeauR-eGFP-nsp2 (green), cells were fixed at 24 h pi and labelled with anti-dsRNA (red) or anti-BrU (red) (panel A). For BrU labelling, cells were treated with BrU and ActD 30 minutes prior to fixation and kept in an RNase-free environment. Nuclei were stained with DAPI (blue). Scale bars are 25 µm in panel A. In panel B, boxed out regions from panel A were examined in more detail to analyse the line intensity profiles (generated in *LAS X*) and determine areas of colocalisation compared to association of the different labels in the same cells (magenta asterisks). Panel C shows the results of the sequential scanning function in the Leica Sterllaris 5 using *LAS* X software to eliminate crosstalk (Chapter 2.15.2; Jonkman *et al*., 2020). The meGFP-nsp2 excitation image and the BrU-AlexaFluor 568 excitation image examples are taken from the BrU labelled BeauR-eGFP-nsp2 infected cells in panel A. The dsRNA-AlexaFluor 568 excitation image is taken from the dsRNA labelled BeauR-eGFP-nsp2 infected cells in panel A.

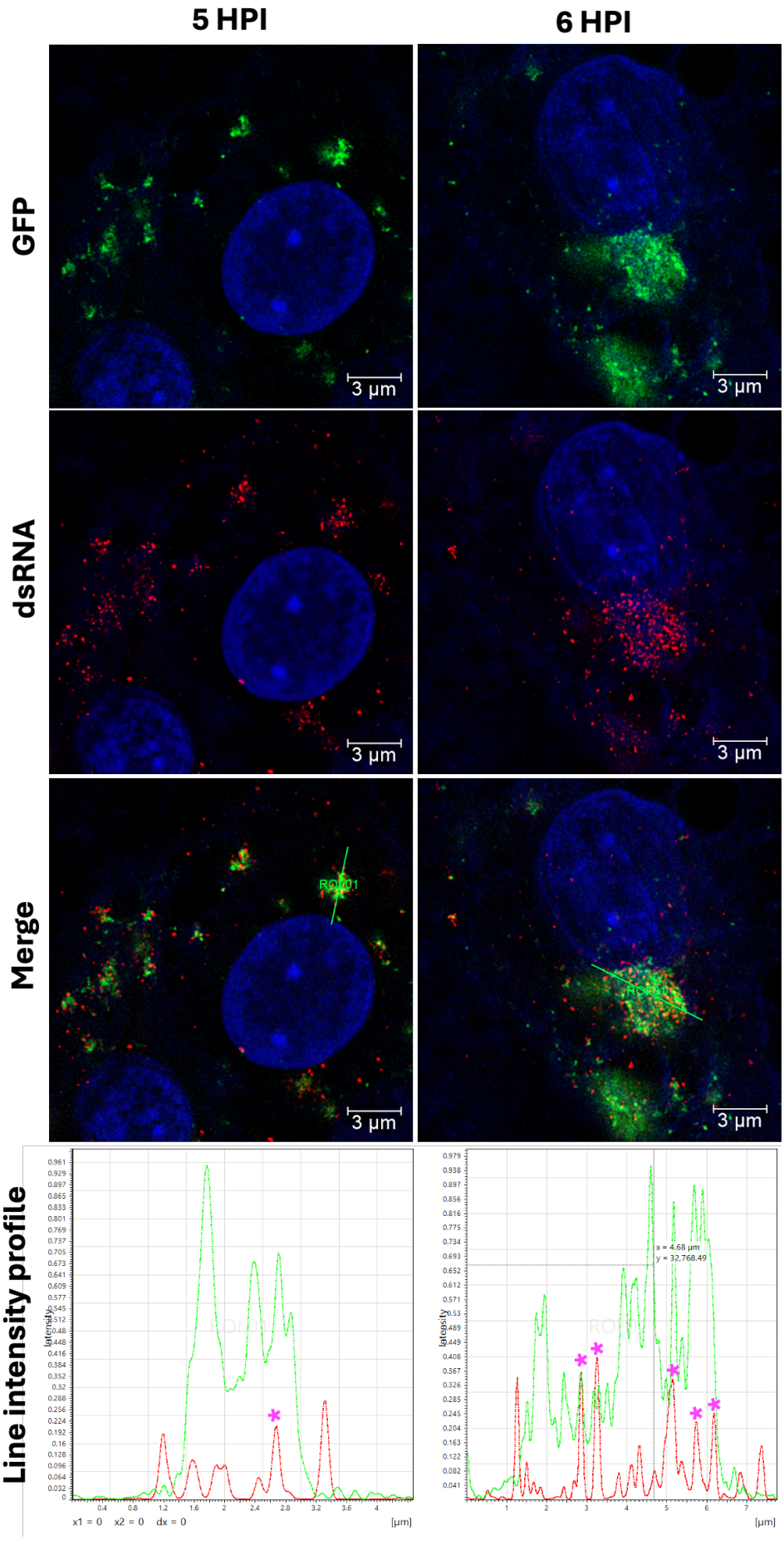
3.2.10. BeauR-eGFP-nsp2 correlation to dsRNA and BrU at early timepoints

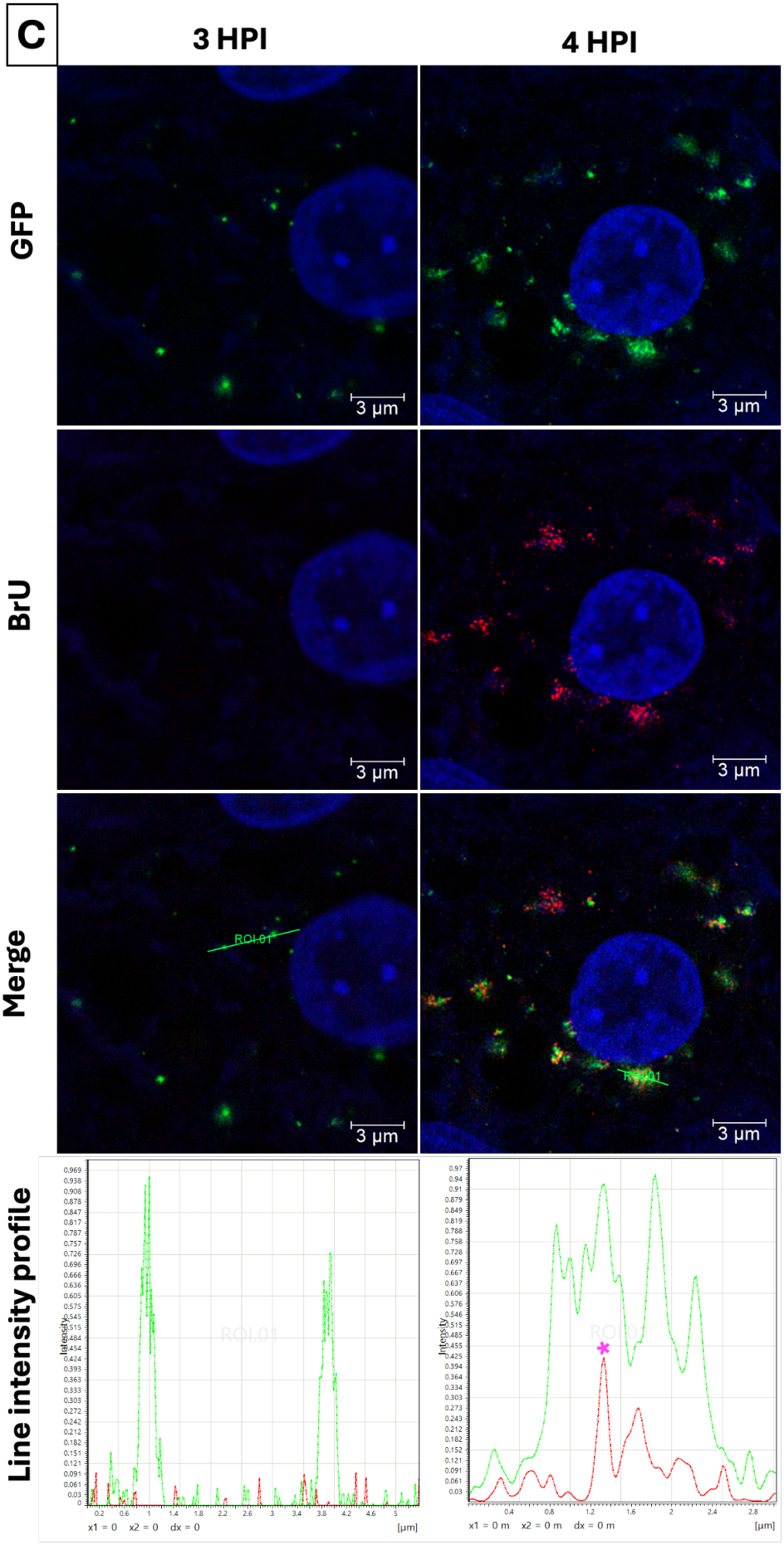
To determine the degree of colocalization to markers of ROs in more detail and at early timepoints, coverslips were prepared for stimulated emission depletion (STED) microscopy. The Leica SP8 gSTED could achieve a maximum lateral resolution of 50 nm and a maximum axial resolution of 130 nm. CK cells were infected with BeauR-eGFP-nsp2 and fixed at the specified timepoints and labelled with anti-dsRNA antibodies or treated with BrU and ActD before fixing at the specified timepoints and labelling with anti-BrU antibodies.

In agreement with figure 3.10, although BrU and dsRNA associate with eGFP-nsp2, the pattern of BrU and dsRNA labelling is slightly different. There was no cross-talk recorded between AlexaFluor 568-labelled BrU and dsRNA and viral eGFP-nsp2 when using the sequential image recording in the confocal microscope (Chapter 2.15.2; Jonkman *et al*., 2020). Labelling dsRNA gave small puncta that increase in number throughout infection while BrU-labelling began as puncta which developed into larger foci; this BrU pattern better matches the GFP-nsp2 pattern throughout infection. Plus, dsRNA signals are distributed further throughout the cytoplasm whereas BrU signals tend to remain in larger perinuclear foci (Figure 3.11). At 3 h pi, in some cells, eGFP-nsp2 signal was visible in cells without dsRNA or BrU signal so it may be expressed before viral RNA replication has begun. Overall, BeauR-eGFP-nsp2 was associated with dsRNA from 3 h pi and BrU from 4 h pi, and BrU was not detected at 3 h pi. This highlights that BeauR-eGFP-nsp2 marks sites of viral RNA synthesis at the earliest stages of the virus lifecycle.


A
dsRNA
BrU
3 HPI
4 HPI
5 HPI
6 HPI
Mock
3 µm


B
3 HPI
4 HPI
GFP
dsRNA
Merge
Line intensity profile
3 µm
ROI.01
Intensity
[µm]


5 HPI
6 HPI
GFP
dsRNA
Merge
Line intensity profile
3 µm
ROI 01
Intensity
x1 = 0 x2 = 0 dx = 0
[µm]
x = 4.68 µm
y = 32,768.49


C
3 HPI
4 HPI
GFP
BrU
Merge
Line intensity profile
3 µm
ROI:01
Intensity
x1 = 0 x2 = 0 dx = 0
[µm]
x1 = 0 m x2 = 0 m dx = 0 m
[µm]

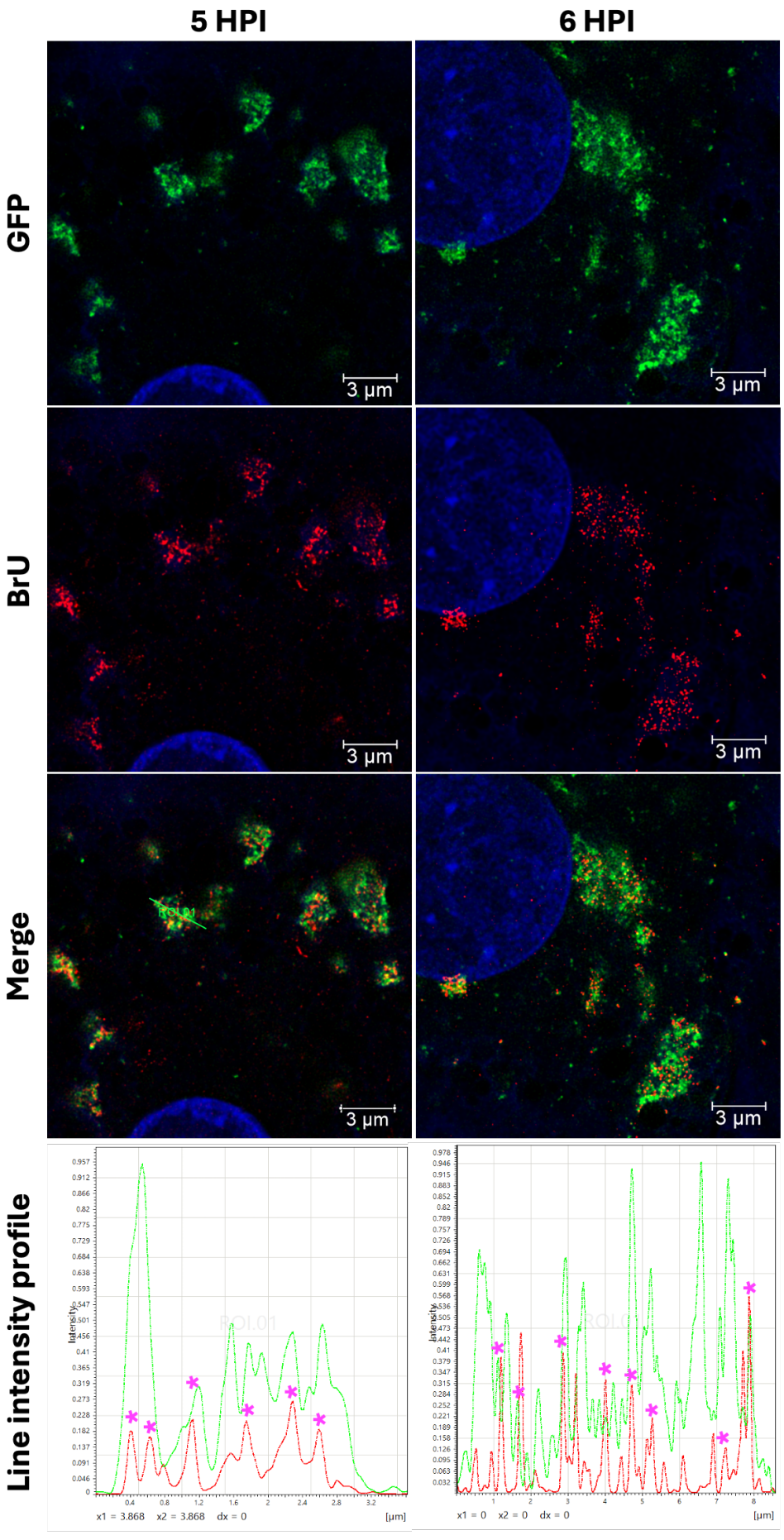

5 HPI
6 HPI
GFP
BrU
Merge
Line intensity profile
3 µm
ROI.01
Intensity
x1 = 3.868 x2 = 3.868 dx = 0
x1 = 0 x2 = 0 dx = 0
[µm]

Figure 3. 11 STED images of BeauR-eGFP-nsp2 association with dsRNA and nascent viral RNA.

CK cells were infected or mock-infected with BeauR-eGFP-nsp2 (green), cells were fixed at the specified times and labelled with anti-dsRNA (Panel A left column; red) or anti-BrU (Panel A right column; red). For BrU labelling, cells were treated with BrU and ActD 30 minutes prior to fixation and kept in an RNase-free environment. Nuclei (blue) were labelled with Topro3. Panel B shows the separated channels and composite images for BeauR-eGFP-nsp2 infected cells labelled with anti-dsRNA antibodies from 3-6 h pi with the line intensity profile over an area of associated signals from each fluorophore. Panel C shows the separated channels and composite images for BeauR-eGFP-nsp2 infected cells labelled with anti-BrU antibodies from 3-6 h pi with the line intensity profile over an area of associated signal. Line intensity profiles were generated in *LAS X* software and positions where the eGFP-nsp2 and antibody signal colocalise are marked with a magenta asterisk.

3.2.11. BeauR-eGFP-nsp2 concentration to maximise infection observed by fluorescence microscopy

Although the infection rate was highest in CK cells, at the earliest time points eGFP fluorescence was detected, only two to five cells per coverslip were eGFP-nsp2-positive. This was following infection with the undiluted viral inoculum at 1.86×10^6 PFU/ml (MOI ~0.8-1). Therefore, to maximise the number of eGFP-nsp2-positive cells observed and increase the throughput of the correlative imaging, particularly at early timepoints during infection, several concentration protocols were tested. Furthermore, to remove the autofluorescence caused by allantoic fluid stocks, it was tested whether concentration of virus grown in CK cells could achieve a similar or higher level of infection.

Coronavirus concentration and purification methods for visualising infected cells via confocal microscopy have been published by Milewska *et al.*, 2020. Following this protocol, CK cells were infected with BeauR-eGFP-nsp2 for 24 h pi in T75 flasks, the cells were lysed by freeze thawing, and the lysates were centrifuged to remove cell debris. Next, the supernatant was concentrated using 10,000 kDa cut off Vivaspin columns and a

sample was taken for titration by plaque assay on CK cells (Figure 3.12). Then, the virus concentrate was ultracentrifuged at 170000 x *g* through a 15 % iodixanol cushion and 11 fractions were taken and titrated (Figure 3.12, bars 1.1-1.11). Finally, the bottom fraction (fraction 1.11) was added on top of a 10-20 % iodixanol gradient, ultracentrifuged at 170000 x *g*, and 10 fractions were taken and titrated (Figure 3.12, bars 2.1-2.10).

Titrations showed that Vivaspin purification alone was sufficient to increase the titre of the BeauR-eGFP-nsp2 stock made in cells from 10^4 PFU/ml to 10^6 PFU/ml. This titre was comparable to the stock made from the second batch of embryonated eggs (Table 3.1) which had produced the highest titre of BeauR-eGFP-nsp2 so far (at 1.86×10^6 PFU/ml) and thus had been the preferred stock for the imaging experiments. However, the subsequent iodixanol cushion and gradient-sedimentation ultracentrifugation steps did not increase the titre further (Figure 3.12). The cushion produced virus in the final 6 fractions so conditions could have been optimised to ensure the virus was purified to the final fraction. The gradient was unsuccessful in concentrating the virus to a single fraction so the gradient may have failed, and the virus was diluted across the fractions.

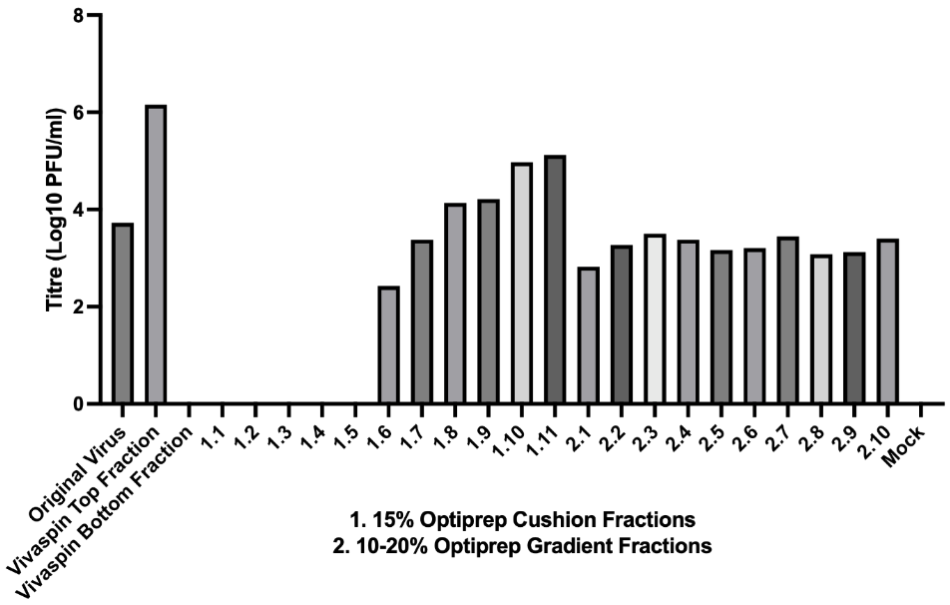


Figure 3. 12 Virus concentration protocol.

SPF VALO embryonated chicken eggs were infected with BeauR-eGFP-nsp2 or mock infected. The allantoic fluid was harvested, and a sample taken for titration as the 'original virus'. The allantoic fluid was pooled and concentrated on Vivaspin columns giving concentrated virus in the top fraction above the PES membrane. The Vivaspin top fraction was added on top of a 15% Optiprep cushion centrifuged at 67000 x *g* for 2.5 h and 11 fractions collected. Viral titre in each fraction was determined by plaque assay. The final fractions containing virus were pooled and then ultracentrifuged through an Optiprep gradient (10-20%) at 260000 x *g* for 2.5 h, 10 fractions were taken and titrated (2.1-2.10). Titration was completed on CK cells to determine the quantity of progeny virus in plaque-forming units (PFU) per ml.

The Vivaspin column alone was able to increase the titre of cell grown stocks of BeauR-eGFP-nsp2 by 2 $\log_{10}$. Therefore, this concentration protocol was used on stocks made in embryonated eggs to see if the number of visibly infected cells was improved. Subsequently, to find the stock which provided the most abundant BeauR-eGFP-nsp2 signal prior to 6 h pi, CK cells were infected with the highest titre stock from embryonated eggs, the CK cell stock concentrated on Vivaspin columns, and an embryonated egg stock concentrated on Vivaspin columns. The cells were fixed at the specified timepoints and imaged.

At 4h pi, the embryonated egg stock still showed more infected cells than the CK stock that had been concentrated on the Vivaspin columns, even though they both had titres at 10^6 PFU/ml (Figure 3.13). Interestingly, the Vivaspin-concentrated stock from embryonated eggs did provide a higher level of infection at 4 h pi than the embryonated egg stock that was not concentrated. Therefore, this virus preparation was used for CLEM experiments described below to look for ultrastructural changes at the earliest possible timepoints. By 6 h pi, the Vivaspin-concentrated egg stock did not seem to produce more visibly infected cells compared to the egg stock (from batch 2 of eggs). However, both egg stocks appeared to produce marginally more infected cells than the Vivaspin-concentrated CK cell stock at 6 h pi, although the difference may not be significant (Figure 3.13). At 24 h pi, the number of infected cells appeared the same for all stocks no matter how they were prepared (Figure 3.13).

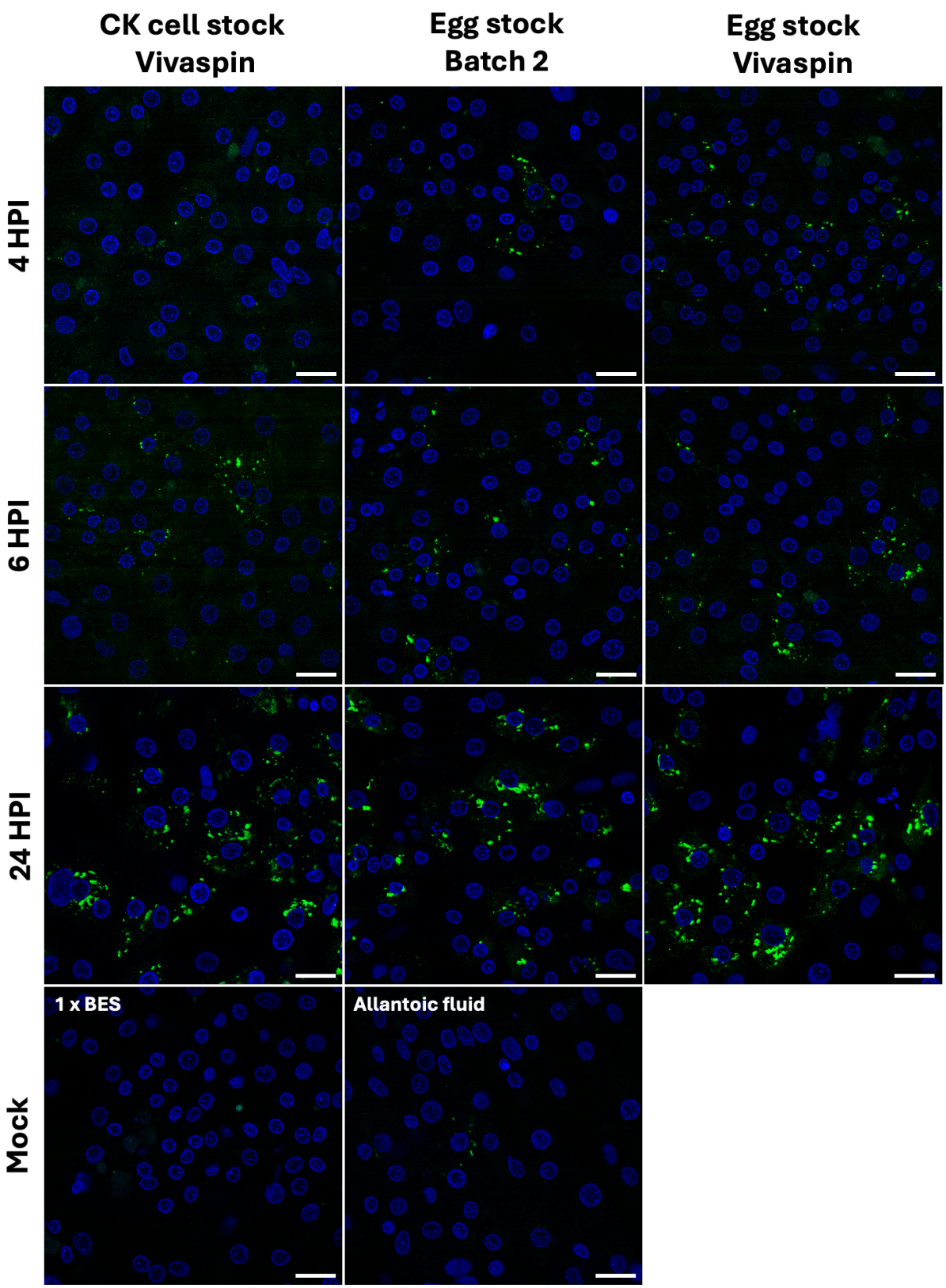


Figure 3. 13 Confocal images showing the number of infected cells at different h pi following infection with different stocks of BeauR-eGFP-nsp2.

CK cells were infected with Vivaspin-concentrated CK cell stock, the highest titre embryonated egg stock (Egg stock Batch 2), or a Vivaspin-concentrated embryonated egg stock. Nuclei were stained with DAPI (blue). Scale bars are 25 µm.

3.2.12. Correlative light and electron microscopy (CLEM) to confirm that BeauR-eGFP-nsp2 marks sites of replication organelles

BeauR-eGFP-nsp2 fluorescence signal was shown to mark sites of nascent viral RNA synthesis and the virus was concentrated to maximise the number of eGFP-nsp2-positive cells detectable. Therefore, the next step was to confirm that the tag did not interfere with RO formation and that the RO structures were equivalent to WT. The first ultrastructural interrogation of BeauR-eGFP-nsp2 infected cells was completed using CLEM with resin-embedded samples.

Cells were infected on gridded coverslips in dishes, infected with Vivaspin-concentrated stocks of BeauR-eGFP-nsp2, and labelled with Hoechst at 30 min prior to imaging in L-15 media using a confocal microscope at 37 °C and 5 % CO_2. The nuclei needed to be visible in the fluorescence images so that they could be used as fiducials for correlation to the electron micrographs. Brightfield images of entire grid coordinates containing infected cells were imaged alongside higher magnification images of the GFP foci. Cells were then fixed and embedded in resin up to 30 min post-fluorescence imaging, and EM sections were prepared and stained. In the electron microscope, the shape of the section and the nuclei pattern were used to the identify infected cells. Consequently, the membrane structures which colocalise with eGFP-nsp2 were identified.

In an initial experiment, cells were infected with BeauR-eGFP-nsp2 and processed at 18 h pi. Following imaging and correlation, eGFP-nsp2 fluorescence was found to colocalise

with zER, DMSs and DMVs (Figure 3.14). Importantly, the zER, DMSs, and DMVs visualised in these cells was found to be indistinguishable from those found in cells infected with WT virus (Maier *et al.*, 2013). This confirmed that the fluorescent tag does not interfere with the formation of RO structures (Figure 3.15 A-B). Consequently, BeauR-eGFP-nsp2 could also be used to look for ROs earlier in infection with the aim to detect the earliest stages of RO formation. In addition, these results validate BeauR-eGFP-nsp2 for further correlative ultrastructural imaging to be completed under cryogenic conditions where their structures will be resolved in 3D and under near-native conditions.

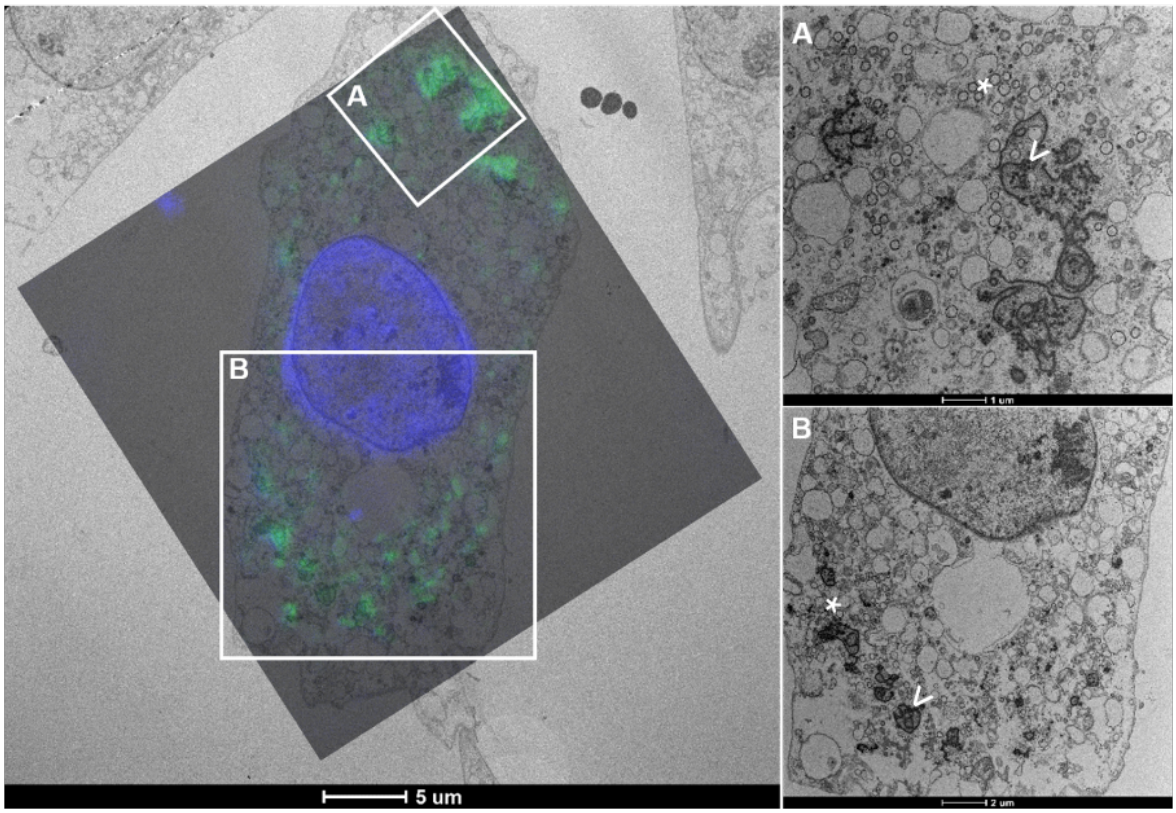


Figure 3. 14 BeauR-eGFP-nsp2 signal marks DMS and DMV structures in DF1 cells at 18h pi.

DF1 cells were infected with BeauR-eGFP-nsp2 (green), nuclei were labelled with Hoechst (blue) and live cells were imaged to identify cells with eGFP-nsp2 signal. Fluorescence information was captured before fixing cells at 18 h pi, staining, dehydration, resin embedding and sectioning. The pattern of the nuclei from the live cell fluorescence images is correlated to the pattern of nuclei on the electron micrographs to identify the infected cell for which the patterns of eGFP-nsp2 signal were captured. Electron micrographs of this cell were collected at higher magnification to observe the RO structures. Fluorescence data and the electron micrographs can then be overlayed to see the membranes which correlate to the eGFP-nsp2 signal. Darkest membranes

represent zippered ER (zER) with double membrane spherules (DMSs) tethered along its length (arrowheads), dark rings represent double membrane vesicles (DMVs) (asterisks). Electron micrographs were captured and correlated by Dr Nicole Doyle (The Pirbright Institute).

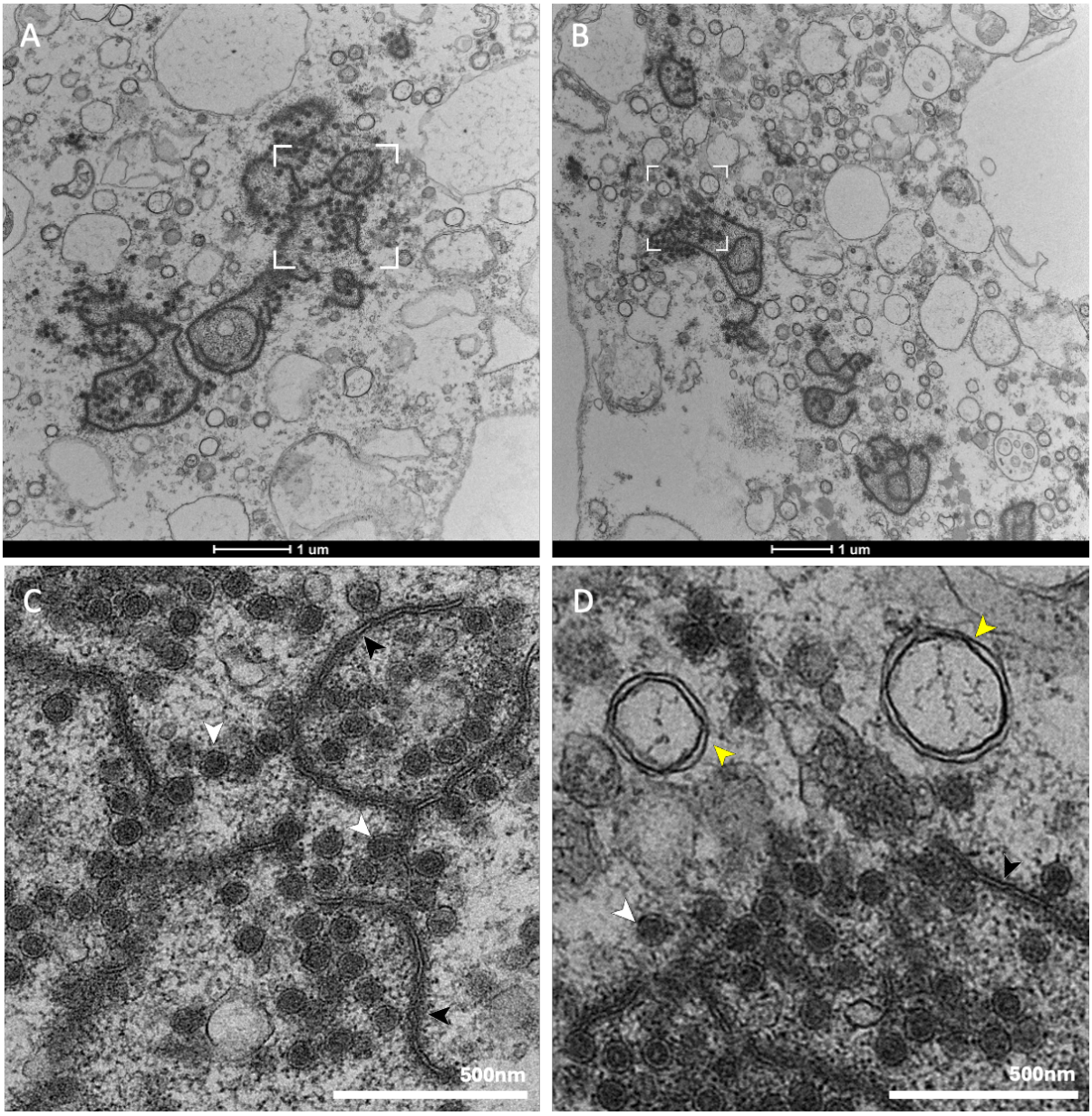


Figure 3. 15 Appearance of IBV replication organelles by electron microscopy is not affected by insertion of eGFP-nsp2.

DF1 cells were infected with BeauR-eGFP-nsp2, fluorescence screened and prepared for electron microscopy. Electron micrographs of cells identified to contain rIBV fluorescence signal (Figure 3.15) were collected at higher magnification to observe the RO structures. Panel A shows a boxed area shown in panel C and panel B shows a boxed area shown in panel D. Zippered ER (zER) is labelled with black arrowheads, double membrane spherules (DMSs) are labelled with white arrowheads, and double membrane vesicles (DMVs) are labelled with yellow arrowheads pointing to regions where the double membrane joins. Electron micrographs were captured and correlated by Dr Nicole Doyle (The Pirbright Institute).

3.2.13. Observation of replication organelles at early timepoints in infection

After it was proven that the rIBV could form WT-like ROs, the Vivaspin-concentrated virus stock was used to look for RO formation events as early as possible post infection. Live BeauR-eGFP-nsp2 infected cells were visualised under a confocal microscope, fluorescent Z-stacks of infected cells were captured, and cells were fixed 6 h pi and processed for EM. In these cells, eGFP-nsp2 signal highlighted already fully formed DMV clusters and small sections of zER beside partially visualised DMSs (Figure 3.16 A-D). DMV patches were the predominant structures and DMVs were observed with a range of diameters from 200 to 300 nm (Figure 3.16 A-B). However, by looking at the same area through serial sections, the apparently smaller DMVs were just orthogonal views of a larger DMV as would be observed in 3D (Figure 3.16 D z1-z2). In Figure 3.16 C, zER is marked with a white arrowhead and DMS heads are marked with black arrowheads. DMSs and zER were captured less often at 6 h pi than 18 h pi and were more difficult to identify than DMVs using this technique at this timepoint. These 6 h pi-fixed DMSs appear associated with shorter strands of zER (100 nm in length) and appear less densely labelled, rather than the extensive, distinct, and densely labelled DMSs tethered to long sections of zER observed at later h pi which can appear over 500 nm in length (Figure 3.15 C).

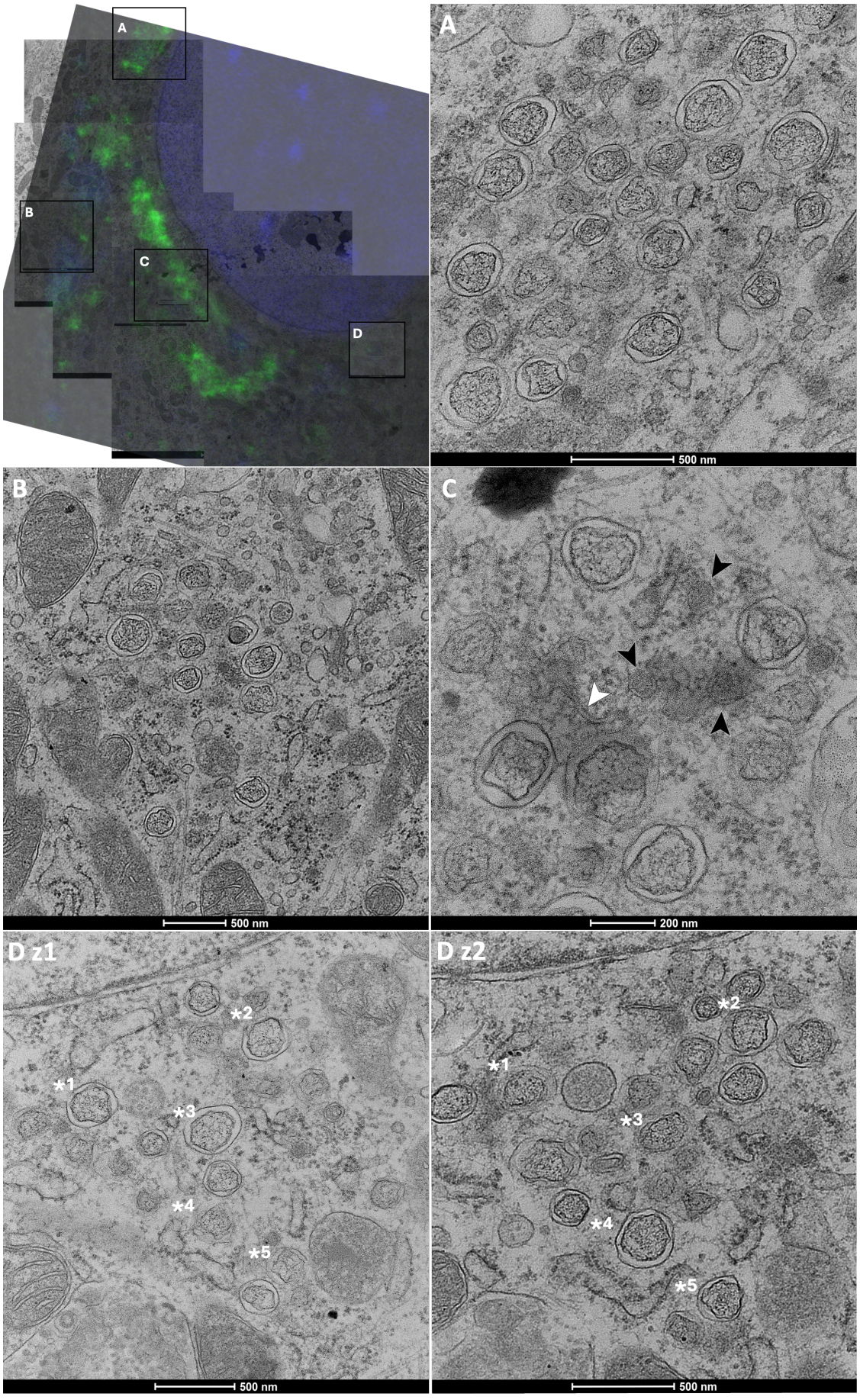

A
B
C
D
A
500 nm
B
500 nm
C
200 nm
D z1
*1
*2
*3
*4
*5
500 nm
D z2
*1
*2
*3
*4
*5
500 nm

Figure 3. 16 Correlative light and electron microscopy (CLEM) of BeauR-eGFP-nsp2 infected CK cell at 6 h pi reveals GFP-nsp2 signal marks infected cells and can direct imaging to specific RO membrane patches within the cell cytoplasm.

CK cells were infected with BeauR-eGFP-nsp2 (green), nuclei were labelled with Hoechst (blue) and live cells were imaged to identify cells with eGFP-nsp2 signal. Fluorescence information was captured before fixing cells at 6 h pi, staining, dehydration, resin embedding and sectioning. The pattern of the nuclei from the live cell fluorescence images was correlated to the pattern of nuclei on the electron micrographs to identify the infected cell for which the patterns of eGFP-nsp2 signal were captured. Electron micrographs of this cell were then collected at higher magnification to observe the RO structures. The same cell can be found in other sections on the grid to give information from different z-depths. Fluorescence data and the electron micrographs can then be overlayed to see the membranes which correlate to the eGFP-nsp2 signal. Darkest membranes represent zER and DMSs, dark rings represent DMVs. Nuclei (blue) labelled with Hoechst. The top left panel shows the correlation between fluorescence and electron microscopy with RO patches in boxes A-D. Partial DMSs and zER can be seen in C. The DMV patch captured in box D was observed in two separate microtomy slices (sections) of the same sample 160nm apart in z, the same DMV in each z-slice is labelled with an asterisk with the same number.

As rIBV DMVs appeared fully formed at 6 h pi, samples were fixed at earlier timepoints to try and capture formation events. Overall, although cells were fixed as early as possible after fluorescence data collection, no obvious RO formation intermediates could be defined. At 4 h pi, the correlation accuracy was very low since it was limited by the resolution of the live cell fluorescence microscopy and still only small puncta were visible (Figure 3.17 A-C). Although, the small puncta at 4 h pi could not be correlated to specific regions in the cytoplasm, it was enough to find infected cells whose cytoplasm could then be explored by eye in a less-directed manner. This technique was successful at identifying DMVs at 4 h pi and this is the earliest that ROs have been observed in IBV infected cells to date (Figure 3.17 D-F; Figure 3.18 A-F). At 4 h pi, single DMVs were detected, rather than in clusters as seen at 6 h pi. However, these individual DMVs may be connected to ER or exist alongside other DMVs in 3D. The 4 h pi DMVs have diameters of approximately 200 nm, appear to be a similar size to the 6 h pi DMVs, and had areas around their diameter at which the two membranes are tightly apposed (Figure 3.18 E; white arrowheads). No

signs of membranes appearing like zER or DMS could be described from the 4 h pi-fixed samples.

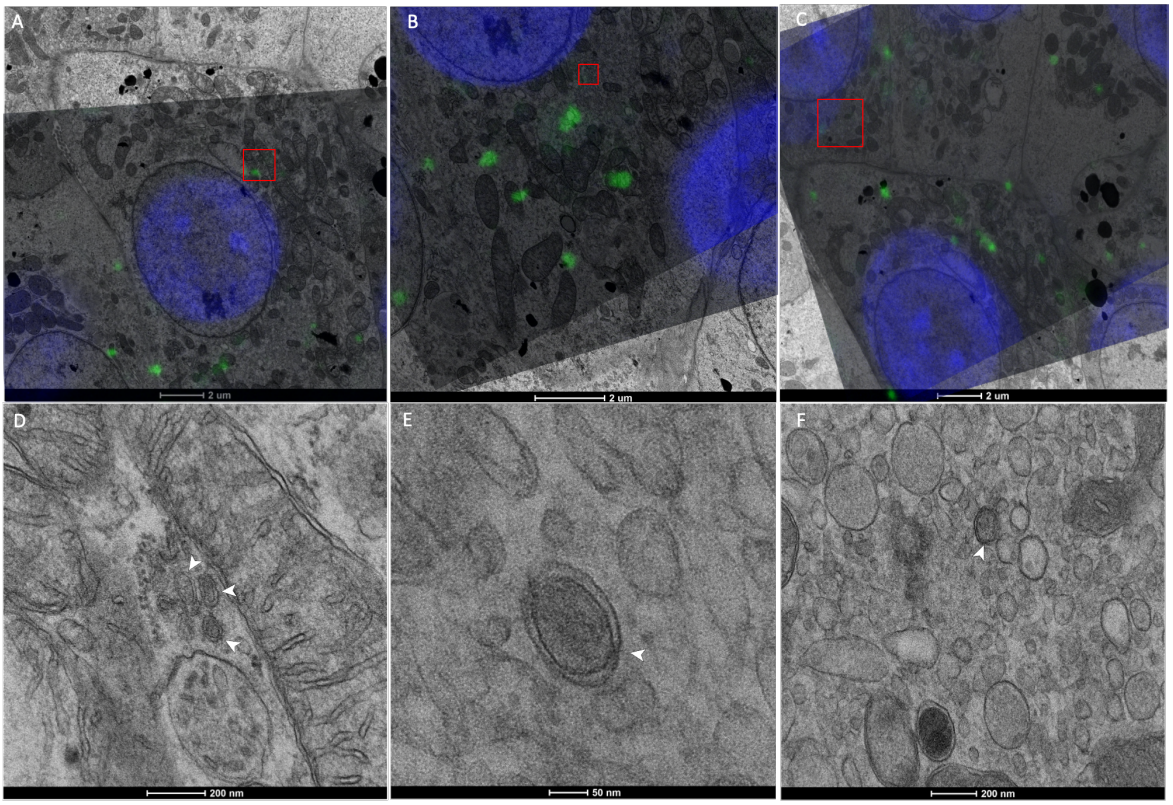


Figure 3. 17 Correlative light and electron microscopy (CLEM) of BeauR-eGFP-nsp2 infected CK cell at 4 h pi.

CK cells were infected with BeauR-eGFP-nsp2 (green), nuclei were labelled with Hoechst (blue) and live cells were imaged to identify cells with eGFP-nsp2 signal. Fluorescence information was captured before fixing cells at 4 h pi, staining, dehydration, resin embedding and sectioning. The pattern of the nuclei from the live cell fluorescence images was roughly correlated to the pattern of nuclei on the electron micrographs to identify the infected cell for which the patterns of eGFP-nsp2 signal were captured. Electron micrographs of this cell were then collected at higher magnification to observe the RO structures. Fluorescence data and the electron micrographs were overlayed but the small fluorescence puncta at this timepoint was difficult to link to membrane structures that could definitively be recognised as replication organelles or their precursors. Double membrane vesicle-like structures are labelled with white arrowheads. The red box in panel A corresponds to panel D, the red box in panel B corresponds to panel E, and the red box in panel C corresponds to panel F. Scale bars are shown at the bottom of each panel. Several electron micrographs at different magnifications were stitched together to search a large area of the cells and zoom into regions of interest (panels D-F).

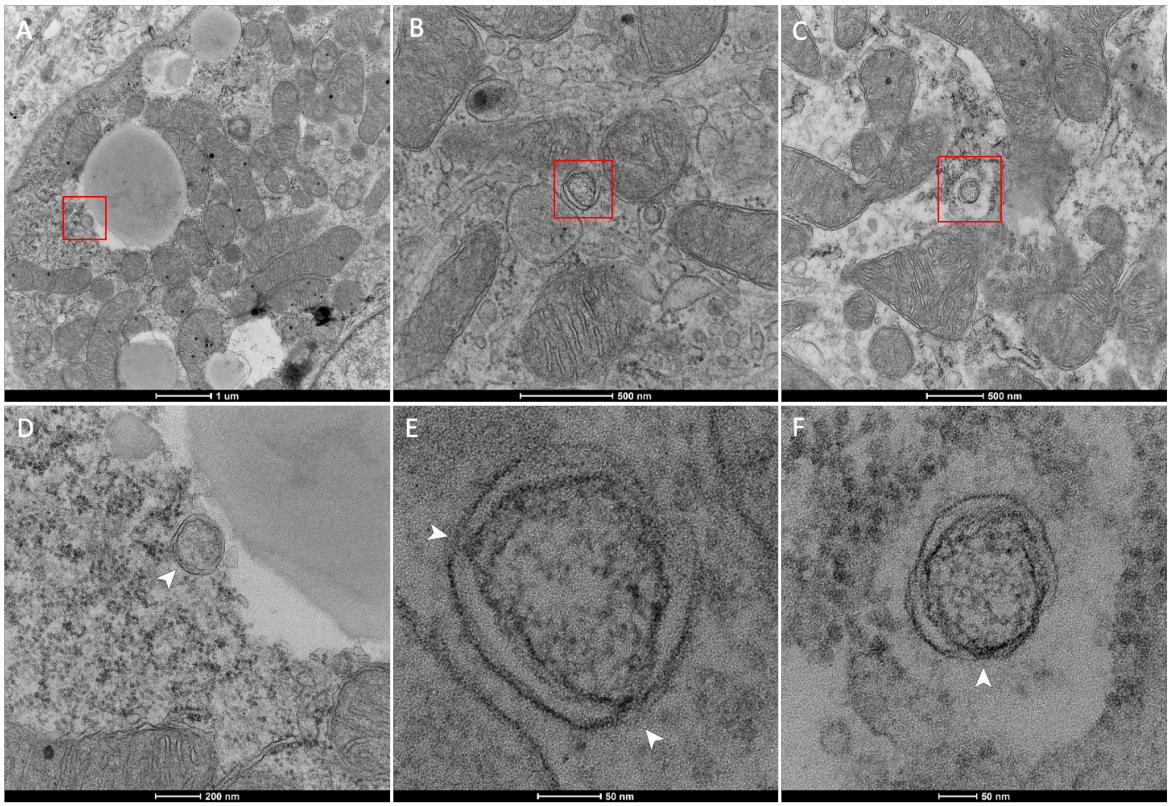


Figure 3. 18 Correlative light and electron microscopy (CLEM) of BeauR-eGFP-nsp2 infected CK cell at 4 h pi was able to identify DMVs.

Cells from the same resin sections as in Figure 3.17 were explored with less-direct fluorescence correlation. Electron micrographs were collected in these cells at higher magnification and double membrane vesicles (DMVs) with regions where the membranes connect (white arrowheads) were observed. The red box in panel A corresponds to panel D, the red box in panel B corresponds to panel E, and the red box in panel C corresponds to panel F.

3.3. Discussion

In this chapter, several IBV recombinants were generated with tags fused to nsp2 and their growth kinetics were characterised to confirm that the formation of the RTC was not affected by the tag. The ease of fluorescence detection for each recombinant was assessed and their ability to label sites of nascent viral RNA synthesis was confirmed. Finally, the ability of the recombinant virus to induce replication organelles equivalent to those induced by WT IBV was confirmed. Overall, these experiments fulfilled the first aim of the project: to generate a tool that would label replication organelles for ultrastructural investigation. The tool, BeauR-eGFP-nsp2, can label sites of nascent viral RNA synthesis as early as 3 h pi and was used to locate DMVs as early as 4 h pi. This is a unique tool for labelling RO membranes in live cells that will allow high-resolution *in situ* studies under cryogenic conditions.

The rIBV rescue system, based on Britton *et al.* (2005), had previously been used to create rIBV with reporters like GFP and luciferase (Bentley *et al.*, 2013). However, these tags were inserted in place of IBV Gene 5 or ORFs 3a and 3b, which are not part of the RTC so would not label ROs. Therefore, using a fluorescent-nsp2 recombinant virus would allow RO membranes to be labelled such that they could be directly targeted for ultrastructural investigation *in situ*, and in a near-native state, in cryo-preserved cells.

The transmembrane nsps (nsp3, nsp4, and nsp6) have been extensively studied in *Betacoronaviruses* for their roles in RO formation. For example, these nsps from MHV, MERS-CoV and SARS-CoV, when expressed from plasmids in transfected cells, have been

able to recapitulate DMVs and paired membranes (Angelini *et al.*, 2013; Hagemeijer *et al.*, 2014; Oudshoorn *et al.* 2017; Ricciardi *et al.*, 2022). However, expression of IBV nsp3, nsp4, or nsp6 from plasmids did not reproduce DMVs or any RO structure, and only nsp4 alone was shown to induce membrane pairing (Doyle et al., 2018). To study ROs from whole virus, although nsp3 has been tagged in MHV, and used to show that nsp3 is a part of DMV pores (Wolff et al., 2020), previous work in the group had shown tagging IBV nsp3 was unsuccessful. Here, rescue attempts for rIBVs with FLAG-tagged nsp3, nsp6, and nsp12 failed and while IBV with nsp14-FLAG was rescued, the tag was not detectable by western blot or IF (H Maier, personal communication). Furthermore, nsp4 and nsp6 have not yet been tagged within any coronavirus. Although nsp12 (the RdRp) is expected to label sites of RNA synthesis, anti-nsp12 antibodies have not been shown to not colocalise with dsRNA or BrU, suggesting that the antibody can only bind to some of the nsp12 present but not nsp12 in the RTC (Doyle *et al.*, 2021). Therefore, although nsp12 would be a good marker for ROs it may be difficult to tag due to its functions and complexes in the RTC. Therefore, tagging nsp2 seemed like a good target.

Nsp2 was also a promising nsp to tag because previous work in MHV showed that nsp2 deletion mutants with GFP or luciferase tags were tolerated (Graham *et al.*, 2005; Freeman *et al.*, 2014). Moreover, in MHV the N-terminus of nsp2 has been tagged with a biotin ligase or APEX2, which labelled RTC-proximal proteins and DMVs and CM respectively (V'kovski *et al*., 2019). This confirmed that nsp2 fusion proteins localise to replication sites. Subsequently, rIBVs with N-terminally tagged nsp2 were successfully rescued here. The rIBVs generated in this project all colocalised with dsRNA (data not shown) suggesting that they all label sites of viral RNA synthesis. BeauR-eGFP-nsp2 was

further shown to target dsRNA, sites of nascent viral RNA, via BrU labelling, and ROs, via CLEM. At 18 h pi, all elements of the IBV RO (DMVs, zER, DMSs) were all labelled by eGFP signal so nsp2 may be present. This is comparable to the observations of MHV DMV and CM labelling via APEX2-nsp2-MHV (V'kovski *et al.*, 2019).

The panel of rIBVs generated with different tags fused to nsp2 had varied replication kinetics. Replication kinetics of the BeauR-eGFP-nsp2 were more comparable to WT BeauR in the primary CK cells compared to the DF1 cells, and different titres were reached in stocks generated in cells or in embryonated eggs. This was expected as IBV mutants have been shown to have cell-type dependent replication kinetics (Webb *et al.*, 2022) and it is known that embryonated eggs support the growth of most IBV strains while cultured cells do not (Bickerton *et al.*, 2017). Different batches of CK cells and embryonated eggs produced different titre viruses due to differences in the animals that could not be controlled. However, the embryonated eggs were able to support production of higher titre BeauR-eGFP-nsp2 stocks. The growth kinetics may have been slower and reached a lower peak titre in DF1 cells as recent experiments have shown that wild IBV strains are able to assemble in primary cells but not in immortalised DF1 cells (Yang *et al.*, 2024). Although, in CK cells both BeauR-eGFP-nsp2 and BeauR reached their peak titres at 24 h pi, the tagged virus had reached a significantly lower titre. This could be due to the additional metabolic burden of expressing an extra protein, genome packaging constraints, or downstream regulatory pathways effecting virion assembly.

BeauR-eGFP-nsp2 showed a greater replication defect compared to WT BeauR than BeauR-mCherry-nsp2 and BeauR-TC-nsp2 in multi-step growth curves. However, the

single-step replication kinetics and gRNA levels of BeauR-eGFP-nsp2 were comparable to WT up to 12 h pi. Importantly, this suggests that RNA synthesis was successful despite fewer progeny viruses being produced. Therefore, the RTC was not affected by the tag so the rIBV should be suitable for investigating ROs. Indeed, BrU labelled nascent viral RNA was indistinguishable between WT and BeauR-eGFP-nsp2 infected cells. Interestingly, the similar levels of viral gRNA up to 12 h pi are likely to cover the first round of viral replication. Then, at 24 h pi, less gRNA is measured for the rIBV compared to WT IBV. This could be explained if, upon the second round of infection at this time, rIBV progeny release was attenuated compared to WT IBV.

The attenuated growth of BeauR-eGFP-nsp2 could be explained if tagging nsp2 altered its function. Nsp2 has predicted functions in suppressing the host innate immune response and maintaining protein synthesis in infected cells (Yang *et al.*, 2009; Wang *et al.*, 2009; Cesaro and Michiels, 2021). If these functions were correct and the tag was detrimental, the host cells may be able to reach a defence state with stagnated protein synthesis to stop progeny release. To confirm whether progeny production was affected, the amount of infectious virus could be determined by looking at the number of cells in an antiviral state by translation levels of antiviral proteins. Additionally, the PFU and viral RNA in cell lysates compare to cell supernatants could be compared to measure the amount of assembled virus compared to the amount of released virus and determine whether any released virus is non-infectious.

The slower growth of BeauR-eGFP-nsp2 compared to BeauR-mCherry-nsp2 in multi-step growth curves was unexpected since the tags are similar sizes, 239 nucleotides and 236

nucleotides respectively. However, the stability of the BeauR-mCherry-nsp2 stock was not tested past P_3, so some of the population may have reverted to WT during the multi-step growth curve. BeauR-TC-nsp2 showed replication kinetics most like WT, as was expected since the tag was small (30 nucleotides). However, this virus required an extra labelling step to generate fluorescence and there was high background signal from the ReAsH dye impacting detection of smaller foci at early timepoints. Furthermore, the performance of the ReAsH dye under cryogenic conditions was unknown. Overall, BeauR-eGFP-nsp2 fluorescence was the easiest to detect, especially at early timepoints post infection, its attenuated replication kinetics at 24 h pi were accepted. By eye it was obvious that BeauR-eGFP-nsp2 infection gave more eGFP-nsp2 positive cells at 6 h pi. Then, at 24 h pi, all the rIBVs produced comparable and abundant numbers of fluorescence-positive cells. Therefore, to label early replication events (6 h pi and earlier), BeauR-eGFP-nsp2 was preferred, but any rIBV could be used to label replication sites later in infection.

There may be several reasons for the difference in the ease of fluorescence detection from cells infected with the different rIBVs. BeauR-eGFP-nsp2 infection could be easier to detect than BeauR-mCherry-nsp2 infection because monomeric enhanced GFP (FPbase ID QKFJN) does have a greater molecular brightness than mCherry (FPbase ID ZERB6) (33.6 and 15.84 respectively, as published in FPbase (Lambert, 2019)). The brightness is also dependent on protein folding which may be affected by its relation to other structures. GFP variants exist including mNeonGreen (Shaner *et al.*, 2013), which is one of the brightest monomeric fluorescent proteins available, and StayGold, which is a highly photostable variant (Hirano *et al.*, 2022). These could be used as alternative tags that

may be able to label ROs earlier in infection. Split-GFP is another option for labelling proteins in which two GFP fragments (GFP1-10 and GFP11) are expressed separately (e.g. one in the virus and one in the host cell) and only when they assemble does the full GFP emit fluorescence (Cabantous *et al.*, 2005). Split-GFP has been used in other viral replication studies (Schaar *et al.,* 2016) and could be useful to study CoV RTC assembly and how these interactions may coincide with RO membrane formation. Plus, the GFP11 fragment is only 16 amino acids so it should cause minimal disturbance to the native folding and function of the protein, and the larger fragment can be introduced somewhere less sensitive. Therefore, the small fragment could be useful for tagging small multifunctional nsps with several conformations.

It was unclear why lower titre stocks of BeauR-eGFP-nsp2 produced more visibly infected cells at 6 h pi than higher titre stocks of BeauR-mCherry-nsp2 and BeauR-TC-nsp2. There may be a maximum MOI for the cells reached where using a higher titre stock does not increase the number of infected cells or even attenuates virus production or has cytotoxic effects. For example, quantification of individual SARS-CoV-2 gRNA molecules, using single molecule fluorescence in situ hybridisation (smFISH), has shown that, upon infection, intracellular gRNA levels were widely variable in cells and tissues (Lee *et al.*, 2022). In this experiment, across three cell lines, only a small cell population (~3-5 %) were displayed a high burden of viral RNA. Moreover, 60 % of one cell line appeared to be infected with incoming virions but there was no increase in the number of gRNA copies over the period of active replication from 4-8 h pi (Lee *et al.*, 2022). Also, even at 24 h pi, 40 % of the cells did not support a high viral RNA burden. Furthermore, in the minor population of highly permissive cells, the number of gRNA copies remained the

same up over the time course suggesting that there was an upper limit of gRNA copies in the cells (Lee *et al.*, 2022). This wide variation in cell susceptibility to CoV replication may also be the case for IBV in CK and DF1 cells so it may explain why even if a maximum MOI was reached, replication (as indicated by nsp2 fluorescence in the rIBV) would only be seen in a small proportion of the population. In the case of the mixed preparation of primary CK cells from different animals each week, the number of susceptible cells could also vary, and once all susceptible cells had been infected, increasing the viral load would not further increase the number of infected cells.

Additionally, stocks with mixed populations of rIBVs and WT-revertant virus might have influenced results. The stability of the cell grown stock virus was tested by passaging in CK cells and complete loss of the tag was only detected at P_6. Furthermore, the P_3 cell and egg grown viral stocks were shown to have stable incorporation of the tag when the PCR product was sent for sequencing. Therefore, to minimise reversion to WT, only P_3 cell or egg grown stocks were used for imaging experiments. However, the stability of the P_3 stocks made in embryonated eggs was not tested past P_3, so they could contain mixed populations of virus, and these were the preferred stocks to use for imaging experiments as they produced higher numbers of infected cells. This might explain the example of a dsRNA positive cell that did not exhibit eGFP-nsp2 signal (Figure 3.10). IF microscopy with the anti-GFP antibody also infers that revertant-WT IBV exists. Because all anti-GFP antibody signal correlated to native GFP signal, it is likely that dsRNA positive cells that lack GFP signal do represent revertant-WT virus rather than stable recombinant virus in which the GFP signal was undetectable. Although revertant-WT virus may exist,

potentially limiting the number of visibly infected cells, this was a minor population and the eGFP-nsp2 signal was still useful to label ROs for correlative imaging.

Association of eGFP-nsp2 with dsRNA and BrU supported the aim of the rIBV to label RO membranes. For example, dsRNA is known to associate with DMVs and CM in SARS-CoV infected cells (Knoops *et al.*, 2008) and RNA filaments observed inside SARS-CoV-2 DMVs are consistent with the size of dsRNA (Cortese *et al.*, 2020). Snijder *et al.* (2020) also showed that dsRNA accumulated on DMVs in MERS-CoV infected cells and nascent viral RNA correlated to DMVs and some DMSs, zER, and CM in MERS-CoV and IBV infected cells. Furthermore, it was shown that dsRNA and BrU and are located within membrane-bound compartments (Doyle *et al.*, 2021) and the APEX2-tagged nsp2 in MHV labelled DMVs and CM (V'kovski *et al.*, 2019). Therefore, it was likely that BeauR-eGFP-nsp2 would label ROs.

BrU appeared to show greater colocalisation with BeauR-eGFP-nsp2 than dsRNA as the pattern of fluorescence is more similar. Line intensity profiles were generated but the degree of colocalisation could be quantified further for example using *Imaris* and measuring intensity colocalisation over several specific regions of interest within the images. Using the sequential scanning function to record the images in the confocal microscope with laser excitation and photo-multiplier tube detectors it was possible to accurately collect specific emission windows for each fluorophore in turn such that bleed-through was completely removed (Figure 3.10 C; Chapter 2.15.2; Jonkman *et al.*, 2020). Some differences in the appearance of BrU and dsRNA labelling were expected because the BrU-RNA observed is viral RNA made 30 minutes prior to fixing while dsRNA labelling

shows all dsRNA at the time of fixation. The different patterns of dsRNA and BrU following IBV infection have also been shown previously (Doyle *et al.*, 2021). Studies on SARS-CoV-2 RNA have also shown that the J2 dsRNA antibody underestimates infection rates (Lee et al., 2022) so it may appear less accurate than BrU labelling.

Ease of fluorescence detection was also tested in a range of cell lines susceptible to BeauR infection. Several reasons may explain why the different cell lines exhibited varying infectivity. CK cells are a heterogenous primary cell line made weekly at The Pirbright Institute from chick kidney disaggregation. In comparison, DF1, CLEC and Vero are more homogenous continuous cell lines. CK cells were the most relevant for characterising IBV since they are primary cells from the natural host. Although they are not from the primary site of infection in the bird, kidneys can be infected by some strains of IBV in the field, resulting in significant kidney pathology (Winterfield and Albassam, 1984). The CK cells did allow faster growth of BeauR-eGFP-nsp2 and exhibited more fluorescence-positive cells at earlier timepoints than the either avian DF1 or CLEC cells. This would be especially important for the cryo-bioimaging, where fewer cells can be visualised on smaller EM grids. Moreover, IBV ROs have also previously been imaged in CK cells and the observations are equivalent in *ex vivo* tracheal organ cultures (TOCs) showing that they are an appropriate model for imaging ROs (Maier *et al.*, 2013). In addition, although Vero cells been used for imaging mammalian CoV ROs (Knoops *et al.*, 2008; Klein *et al.*, 2020), they are less relevant hosts as the cells are derived from the African green monkey and the infection rate with IBV was not high.

The CK cells also supported the earliest detection of virus prior to 6 h pi which was important to image early replication events such as RO biogenesis. BeauR-eGFP-nsp2 was detected in CK cells at 2 h pi, with association to dsRNA at 3 h pi and colocalisation with BrU at 4 h pi. In DF1 cells, dsRNA and BrU have also been shown to be closely associated in IBV infected cells from 4 h pi onwards (Doyle *et al.*, 2021). For SARS-CoV-2, smFISH has been used to detect gRNA molecules in cells as early as 2 h pi which were determined to originate from incoming virions upon infection (Lee et al., 2022). Then, the number of gRNA molecules was varied but significantly increased from 4- 6 h pi, which were a result of active replication (Lee et al., 2022). BeauR-eGFP-nsp2 RNA synthesis in CK cells also significantly increased from 6 h pi, so to look for formation events and avoid abundant fully formed ROs, CLEM samples were fixed prior to 6 h pi. The timings may be different for IBV but the appearance of BeauR-eGFP-nsp2 fluorescence from 2 h pi in small puncta, and larger foci at 6 h pi, plus the single DMVs at 4 h pi and DMV clusters at 6 h pi observed by CLEM, match this trend, especially as DMVs are the primary, if not only, sites of RNA synthesis relative to CM/DMSs (Snijder *et al.*, 2020).

For choosing optimal cell models for CLEM, producing the highest number of visibly infected cells was the most important factor for selecting the cell line and virus because this would provide the most chances of imaging ultrastructural events. Questions that would not benefit from samples fixed at early timepoints could use CK or DF1 cells infected with any of the recombinant viruses. DF1 cells are also known to produce equivalent ROs to CK cells (and therefore TOCs) following IBV infection so they are suitable for RO analysis (Doyle *et al.*, 2018).

To maximise the number of infected cells available for ultrastructural interrogation, various steps were used to concentrate the virus and produce higher titre stocks. In initial experiments, pelleting virus through a sucrose cushion was tested for 2 h at 120000 x *g* (data not shown). However, this appeared to inactivate the virus, as has been shown previously (Gias *et al.*, 2008). Next, the Vivaspin-Optiprep (iodixanol) protocol was performed as described in Milewska *et al.* (2020) for purification of OC43, NL63, and CRCoV for confocal imaging. Interestingly, while Vivaspin concentration did improve viral titre of cell grown virus, iodixanol ultracentrifugation steps did not further concentrate the virus (Milewska *et al.*, 2020). It could be that the iodixanol gradient failed as the virus became diluted across all fractions and not concentrated in a single fraction. Therefore, Vivaspin-concentration alone increased the titre of the cell grown stock (Figure 3.12), and it reached a similar titre to the highest titre egg stock (Table 3.1). However, the number of visibly infected cells prior to 6 h pi was not improved. Then, Vivaspin-concentration of an egg stock may have slightly increased the number of visibly infected cells pre-6 h pi, but the numbers of infected cells from 6 h pi onwards were similar for all stocks (Figure 3.13). The percentage of infected cells following infection with each stock could also be calculated as any increase in the number of visibly infected cells pre-6h pi was helpful for the CLEM experiments looking at RO formation events. Perhaps the cells had an inherent and widely variable permissibility to infection and a maximum limit for the number of gRNA copies within each cell (Lee *et al.*, 2022). Therefore, concentrating the virus would not significantly improve the number of infected cells.

Significantly, in the CLEM experiments, the BeauR-eGFP-nsp2 ROs were equivalent to WT (Maier *et al.*, 2013), validating that the tool could be used to answer questions about

ROs. There was extensive eGFP-nsp2 signal throughout the cytoplasm of infected cells at 18 h pi correlating to a combination of DMVs, zER, and DMSs. This shows that nsp2 may be involved in both structures, highlighting the heterogenous nature of the nsps. In addition, this result is supported by experiments showing that nsp2 is proximal to all nsps (V'kovski *et al.*, 2019), SARS-CoV and MHV nsps accumulate at CM (Knoops *et al.*, 2008; Ulasli *et al.*, 2010), and MERS-CoV nsp3 accumulates at DMSs and CM (Snijder *et al.*, 2020).

Correlation between fluorescence and EM images was done manually, using the pattern of nuclei reported by the Hoechst stain and the pattern of nuclei on the EM section. Although the correct coordinate could be sectioned from the resin block following published protocols (Russell *et al.*, 2017), the nuclei patterns were difficult to correlate. Correlation could have been improved using tools in ImageJ such as *Landmark Correspondences* (Saalfeld and Tomancák, 2008). Another approach would be to also image each EM section under fluorescence and check for retention of the eGFP-nsp2 signal. This would be able to more accurately correlate each section compared to trying to correlate fluorescence from the volume of the live cell. A different embedding approach such as HPF-FS would be more likely to preserve the signal than the dehydration and resin-embedding used here (Johnson *et al.*, 2015). Furthermore, a separate fiducial visible between the two modalities like a fluorescent nanoparticle could have been added to assist correlation (Fokkema *et al.*, 2018).

Correlation of larger foci of eGFP-nsp2 signal at 6 h pi was successful and clusters of DMVs were observed alongside small sections of zER and small patches of partially

observed DMSs. The DMSs fixed at 6 h pi were associated with shorter strands of zER and appeared less distinct and densely labelled compared to zER and DMSs observed at later h pi (Figure 3.16 C; black arrowheads). These early DMSs appeared like some descriptions of convoluted membranes described in previous CoV RO EM studies (Snijder *et al.*, 2020). Moreover, these short zER sections have been observed in IBV infected cells fixed late in infection too (Maier *et al.*, 2013). To draw conclusions about the formation of zER and DMS from early to late in infection, many more examples need to be imaged.

ROs were also imaged earlier in infection. It was thought that RO formation events would be easier to identify at earlier timepoints, when fluorescence signals were more discrete, rather than at later timepoints when any formation events would be difficult to distinguish from already extensive patches of reorganised membranes. 4 h pi was the earliest that samples were fixed and single fully formed DMVs were already observed at this time. Due to the manual correlation, only a few cells were investigated, and RO formation intermediates could not be described. For SARS-CoV, DMVs have been imaged as early as 2 h pi, with CM appearing from 3 h pi onwards, and then the ROs increased following the onset of RNA replication from 4-6 h pi, as was observed here, but RO formation intermediates also remained elusive (Knoops *et al.*, 2008). Interestingly, no signs of membranes appearing like zER or DMSs could be described from the 4 h pi-fixed samples. Therefore, it is likely that the DMVs form first before CM/zER/DMSs, and this is also what has been reported for *Betacoronaviruses* SARS-CoV (Knoops *et al.*, 2008), MERS-CoV (de Wilde *et al.*, 2013), and MHV (Ulasli *et al.*, 2010).

To better understand RO formation mechanisms, minimal nsp expression cassettes have been transfected into cells to determine the membrane rearrangements imposed by nsp3, nsp4 and nsp6 of different CoVs (Angelini *et al.*, 2013; Oudshoorn *et al.*, 2017; Doyle *et al.*, 2018; Ricciardi *et al.*, 2022). To understand mechanisms of RO formation from whole viruses, small interfering RNA (siRNA) molecules have been used to inhibit translation of RTC-proximal host factors and impair viral replication (V'kovski *et al.*, 2019). Moreover, knock out cell lines have been made lacking host factors important for RO biogenesis and visualised by EM following infection (Ji *et al.*, 2022; Prentice *et al.*, 2021). Although these questions are being investigated, the focus has been MHV, SARS-CoV-2, and DMVs so there is a gap in the knowledge surrounding DMSs. Therefore, these same targets could also be tested for IBV infected cells.

Using larger volume imaging techniques would also be advantageous for studying RO formation. For example, serial block-face SEM (SBF-SEM) or tomography on thicker resin sections could have provided 3D data, HPF-FS methods could reduce dehydration artifacts (Russel *et al.*, 2017), and these methods have been used to study ROs previously (Knoops *et al.*, 2008; Maier *et al.*, 2013; Melia *et al.*, 2019). Moreover, cryo-ET on 100-300 nm lamella also provides a greater depth of field than 70 nm room temperature EM sections, alongside the sample being preserved to a near-native state, so it has been used for studying ROs (Wolff *et al.*, 2020; Ricciardi *et al.*, 2022; Zimmermann *et al.*, 2023; de Beijer *et al.*, 2024). Alternatively, cryo-SXT is a large-volume near-native state imaging technique in which the whole depth of the cell ultrastructure (up to 10 μm) can be explored so it has been used to image rare events during infection (Nahas *et al.*, 2022).

The DMVs observed at 4 and 6 h pi were similar sizes so there was no sign of smaller DMVs at earlier timepoints expanding into larger DMVs. The size of DMVs has been described as consistent for several other coronaviruses as well (Knoops *et al.*, 2008; Ulasli *et al.*, 2010). Interestingly, the IBV DMVs observed here, and in Maier *et al.* (2013), do not appear to be interconnected like those reported in SARS-CoV infected cells (Knoops *et al.*, 2008). Moreover, consistent with the likely site of DMV pores, some areas around the IBV DMV double membranes were compressed together. Indeed, these sites where the DMV membrane contacts have been seen in many chemically fixed DMVs previously, prior to the identification of the pore structure (Knoops *et al.*, 2008; Maier *et al.*, 2013; Doyle *et al.*, 2019; Snijder *et al.*, 2020). Using *in situ* cryo-tomography techniques to elucidate the components of the DMSs, or recapitulating these structures in minimal expression systems, will help provide insight into their functions and biogenesis.

3.4. Summary

1. *Recombinant IBVs have been generated and characterised with fusions to non-structural protein 2 (nsp2).*
2. *BeauR-eGFP-nsp2 exhibited the greatest number of infected cells at the earliest timepoints in primary CK cells*
3. *BeauR-eGFP-nsp2 colocalised with sites of nascent viral RNA synthesis, DMVs and DMSs.*
4. *IBV ROs have been imaged at, 4h pi, the earliest timepoint to date*

Chapter 4. Cryo-correlative light and soft X-ray tomography to observe replication organelles in whole cells under near-native conditions

4.1. Introduction

Following confirmation that BeauR-eGFP-nsp2 marked sites of known RO structures, the next step was to observe these structures under near-native conditions and in three dimensions (3D). The first experiments on cryo-preserved samples were completed using cryo-soft X-ray tomography (cryo-SXT) at beamline B24 at Diamond Light Source. Cryo-SXT is a technique that can image relatively large volumes of cryo-preserved cells at the mesoscale, which bridges micron-sized cellular structures and nanometre-sized molecular structures and can achieve resolutions of 10 to 50 nm depending on the X-ray optics available (Harkiolaki *et al.*, 2018). This method has been used to observe 3D ultrastructural changes in whole cells and cells infected with viruses (Jadhav and Kounatidis, 2023). At B24, tomograms with XY dimensions of 10 μm^2 were collected throughout the depth of whole cells without thinning or sectioning. The soft X-rays at 500 eV have a wavelength of ~2.48 nm, while the wavelengths of electrons in 200 kV and 300 kV electron microscopes are ~2.5 pm and ~2 pm respectively. The longer wavelength of the soft X-rays means that they can penetrate through thicker samples, such as whole cells. Therefore, mechanical stresses to cells caused by sectioning and potentially time-consuming milling techniques are avoided. Moreover, cryo-SXT is an absorption contrast technique so chemical labelling is not required. To generate contrast, soft X-rays used at

the ‘water window’ of the electromagnetic spectrum pass through the aqueous cytosol but are absorbed by carbon dense structures such as lipids in cell membranes. The ‘water window’ is the range between the K-shell absorption edges of oxygen and carbon and spans 284 eV to 543 eV (or wavelengths from 4.4 nm to 2.3 nm) (Wolter, 1952). Therefore, cryo-SXT images the cellular ultrastructure in a near-native and fully hydrated state, without labelling artifacts, and throughout the depth of the whole cell. The depth of field which is in focus and has good contrast depends on the size of the zone plate. For example, a 25 nm zone plate provided a depth of field of 1 – 2 µm and experiments using a 40 nm zone plate have achieved an in-focus z-range of 8 µm from three tilt series (Otón *et al.*, 2017). Since a large volume of the cell is imaged, there is a greater chance that rare events, such as RO biogenesis intermediates, will be included in the tomograms. However, imaging these intermediates is dependent on fixing the sample during these events and the ultrastructural changes being visible at the mesoscale or the resolution limit of the zone plate (25 nm in these experiments). Since the advent of SARS-CoV-2, morphological changes to cells infected with this virus have been visualised by cryo-SXT. This has been completed in cells on grids via limited-angle tomography (Mendonça *et al.*, 2021; Castro *et al.*, 2023) and in cells within capillary tubes via 360° full rotation tomography (Loconte *et al.*, 2021). The first aim of this experiment using BeauR-eGFP-nsp2 infected cells was to observe whether RO formation events could be observed by cryo-SXT. The second aim was to observe the entire RO network in the cell to determine any connections between DMVs and DMSs which would be important to determine whether these RO morphologies form from the same membranes, are different stages of the same structure, or are completely distinct.

Cellular features in the specimen differentially attenuate the penetration of the soft X-rays depending on their biochemical composition and thickness. In full rotation tomography, this means that each voxel in the reconstructed tomogram has a measured linear absorption coefficient (LAC) value which can be used as a quantitative measure to identify specific structures of interest within the cytoplasm as each component will have a characteristic LAC profile (Do *et al.*, 2015). This quantitative measure can be useful for segmentation if different features are not distinguishable by eye.

Cryo-SXT can be correlated with fluorescence microscopy to specifically label molecules of interest and provide molecular level detail of their location within the cellular ultrastructure. Cryo-preservation compatible fluorescence tools such as live cell dyes or endogenously expressed fluorescent markers can be used and their distribution is imaged before SXT which can compromise the fluorophores. Fluorescence screening can be completed on live cells prior to vitrification or using fluorescence microscopes with cryo-stages after vitrification. At B24, fluorescence screening was completed using a custom cryo-structured illumination microscope (cryo-SIM) made in collaboration with the advanced bioimaging unit, Micron, at the University of Oxford (Gustafsson *et al.*, 2008). The cryo-SIM collected a map of the grid with the location of fluorescent regions of interest. At the fluorescent regions of interest, stacks of relatively high-resolution images (~200 nm depending on the emission wavelength of the fluorophores) were collected through the sample. Then, the maps of the grid taken in the fluorescence and X-ray microscopes were correlated so that the same fluorescent region of interest can be targeted for cryo-SXT. Then, once the tilt series had been collected, to assist with finding fluorescence-labelled structures of interest within the volume of the reconstructed

tomograms, the tomograms could be correlated in 3D to the cryo-SIM stacks. To be able to correlate the SXT and fluorescence data in 3D, MitoTracker live cell mitochondria labels were used because the mitochondria are readily visible in the soft X-ray tomograms so they can then be used as common fiducials between the two techniques. 3D correlation was not applied to the X-ray tomograms collected in this thesis because the RO structures were immediately visible. Therefore, 2D fluorescent maps of the grids were appropriate for positioning the soft-X-ray tomograms and could be more easily collected on the Leica cryoCLEM once it was available.

After cryo-fluorescence screening of vitrified grids, the same samples were loaded into the cryo-SXT TXM. Firstly, brightfield maps of vitrified coordinate grids were collected so that cells of interest could be identified. Then, 2D X-ray mosaics were collected encompassing the cell(s) of interest. These images were overlaid with the fluorescence images of the same cells (2D correlation) to guide the positions at which the X-ray tomograms would be collected (10 μm^2 boxes). Then, at each position, a tilt series of 2D X-ray projections was recorded through the cell at discrete incremental angles around the central axis of rotation encompassing as large a tilt series as possible, typically 121° to 141° depending on the set up, without the imaging beam being obstructed. Cryo-preservation of the samples also helps to delay the radiation damage as the sample is irradiated at each tilt angle. The X-rays that passed through the sample were directly detected by a charged couple device positioned at the focal point of the zone plate. For the 25 nm zone plate, each pixel corresponded to 10 nm^2 of sampled space. A Fresnel zone plate was used to focus the soft X-rays and the width of the outermost ring of the zone plate determines the maximum achievable resolution (at beamline B24 a 25 nm or

40 nm zone plate can be used; Gorelick *et al.*, 2011). The projections at each angle were then aligned and reconstructed using IMOD (version 4.9.2; Mastronarde and Held, 2017).

Typical cryo-SXT samples are adherent cells grown on gold TEM grids that are vitrified by plunge freezing. Thicker samples on grids (>10 µm) are better suited to vitrification via high pressure freezing (HPF). Moreover, alternative sample holders for samples in suspension include thin-walled glass capillary tubes. These samples are compatible at beamline 2.1 of the Advanced Light Source at Lawrence Berkeley National Laboratory in which there is a custom cryo-rotation stage allowing specimen to be rotated through 360° (Le Gros *et al.*, 2014). This full rotation avoids the 'missing wedge' artifact inherent to cells grown on grids where the grid bars block X-rays at the minimum and maximum tilt angles. This means that samples on grids are typically collected from ±65°.

4.2. Results

4.2.1. Cryo-preservation of infected cells on grids

The primary chick kidney (CK) cells were the ideal model to study ROs early in infection because they exhibited BeauR-eGFP-nsp2 signal at the earliest hours post infection (h pi) compared to other cells. This was important to image RO formation events before they became indistinguishable from fully formed ROs. However, the CK cells proved difficult to vitrify on EM grids. It is important to note that the CK cells are primary cells and were generated from chick kidney disaggregation weekly at The Pirbright Institute while the plunge freezing was completed in B24 at Diamond Light Source, so the cells had to be driven on ice for at least an hour before seeding on grids. When, the CK cells were

seeded, plunge-frozen, fluorescence screened, and imaged under soft X-rays, several artifacts were apparent.

Firstly, the CK cells were difficult to plate on grids due to their unpredictable health upon seeding, it was likely that cell viability was lost during transport or because they could not adhere to the TEM grid foil. The cells needed to be seeded at high confluency to retain their health and give enough infection-susceptible cells adhered to the grid. This resulted in densely populated and thick samples which held a mixture of different cell types, dead cells, and tissue debris (Figure 4.1 A). Consequently, when cells were frozen 24-72 h post seeding, there were high levels of crystalline ice contamination on the grids and vitrification within the cells was uneven (Figure 4.1 D-F). Moreover, the cryo-SIM fluorescence screening picked up multiple background fluorescence signals in mock-infected CK cells that were excited by the 488 lasers (Figure 4.1 B). Some fluorescence patterns were obviously debris, as was seen from CK cells and viral stocks in egg allantoic fluid previously and could be confirmed by brightfield or X-ray images of the same area, so could be avoided (Figure 4.1 C). However, other areas of GFP autofluorescence from the CK cells appeared very similar to BeauR-eGFP-nsp2 signal in infected cells. It was important to note the difference in size of the sample holders as moving from 13 mm coverslips or CLEM dishes to 3 mm grids meant that there were fewer cells to screen for fluorescence per sample in the first place. Therefore, at early h pi, the grids were screened for small puncta in a small number of cells, which were easy to mistake for autofluorescence patterns in the CK cells.

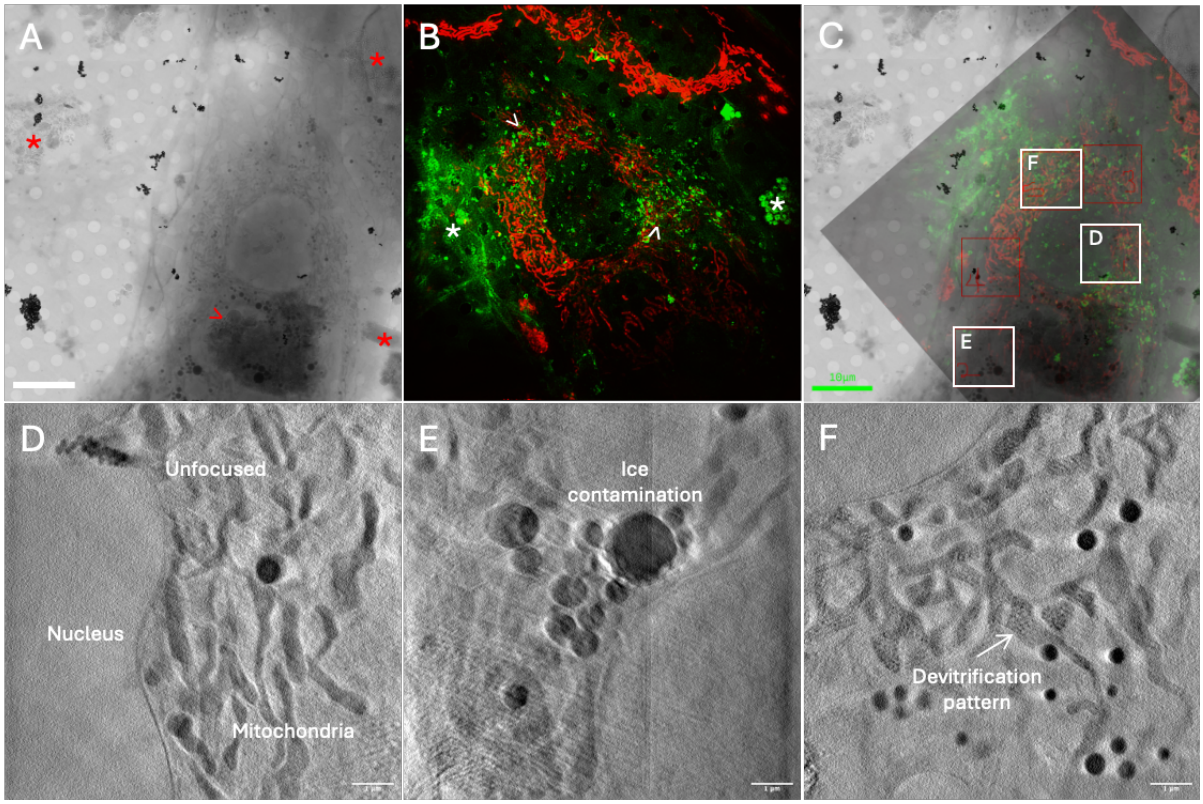


Figure 4. 1 Artifacts in CK cell cryo-preservation.

CK cells were plated on grids for 24-72 h, washed gently to remove dead cells without damaging the grid foil, labelled with Mitotracker FarRed, and plunge frozen with 250 nm Au fiducials. Panel A shows an X-ray mosaic of a plunge frozen CK cell with crystalline ice contamination (red asterisks) and extracellular biological material potentially from a dead cell or unwashed tissue debris from the primary cell preparation (red arrowhead); the scale bar is 10 µm. Panel B shows a cryo-SIM image of the same cell as in panel A with the mitochondria labelled in red and material exhibiting fluorescence when excited by the 488 laser (green). The autofluorescent material appears in extracellular regions (asterisks) and within or on top of the CK cells (arrowheads). Panel C shows the 2D correlation between the X-ray mosaic and the SIM image using the shape of the nuclei and mitochondria; single orthoslices through tomograms are shown in panels D-F (scale bars are 1 µm). Some of the nuclear membrane and mitochondria membrane are resolved while other areas are out of focus, contaminated with ice, or devitrified.

Overall, the CK cell vitrification quality was poor. Therefore, DF1 cells were used as the next best option because they were a relevant cell line, and they supported similar numbers of infected cells to the CK cells from 18 h pi onwards. Therefore, non-time sensitive questions could be addressed in DF1 cells, for example, what is the relationship between DMVs and DMSs in whole cells. Moreover, there would still be the opportunity to image RO formation events as the RO grows over time. BeauR-eGFP-nsp2 was visible in

DF1 cells at 6 h pi, but only in a few cells per coverslip, so it would be more difficult to look at this timepoint in DF1 cells.

The seeding of DF1 cells on grids was easier to control than CK cells because they have a more homogenous population and a predictable replication cycle being immortalised cells. The CK cells were prepared weekly from trypsinisation of chick kidneys so there could be several cell types in each preparation, some of which may not be dividing, and variation between the preparations. The DF1 cells adhered well to grids so after 1 h post seeding the healthy cells had settled, cells that had not adhered were washed away, and more cells were added if needed. Overall, plunge freezing of infected DF1 cells produced better samples with even vitrification and less ice contamination compared to CK cells (Figure 4.2 A). In the cryo-SXT, the mitochondria appeared dense and with the longest visible lengths at an average of 1538 nm (n= 32, standard deviation= 572.9 nm) (Figure 4.2 B-C).

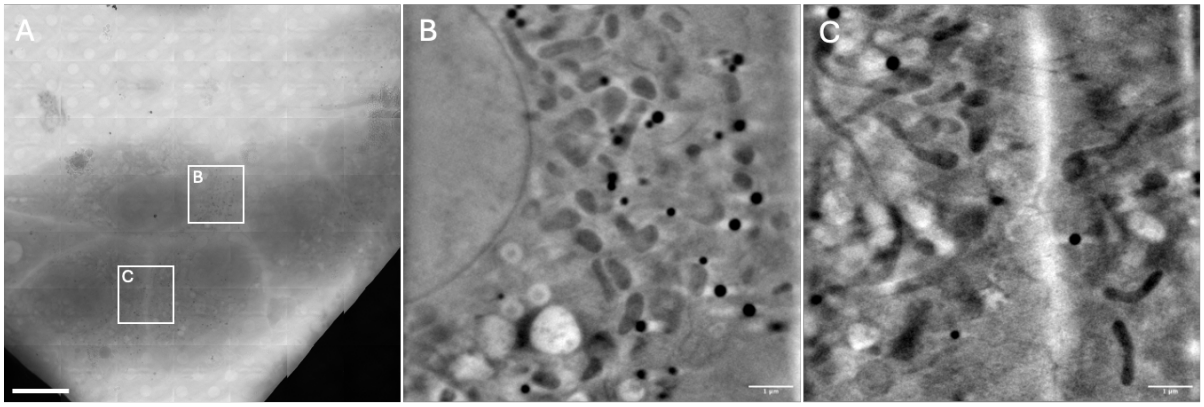


Figure 4. 2 Cryopreservation of DF1 cells.

DF1 cells were seeded on grids and plunge frozen after 24-48 h. Panel A shows a 2D X-ray mosaic of a cluster of six cryo-preserved DF1 cells which have less contamination from ice or sample preparation debris compared to CK cells (Figure 4.1); the scale bar is 10 µm. Panels B and C are single orthoslices through tomograms of uninfected DF1 cells with few ice and devitrification artifacts and clearly focused nucleus and mitochondria membranes and boundaries between two cells; the scale bars are 1 µm.

4.2.2. Cryo-fluorescence microscopy of BeauR-eGFP-nsp2 infected cells on grids

To screen the cryo-preserved grids for infected cells, the cryo-capable Leica cryoCLEM and cryo-SIM at B24 fluorescence microscopes were used. In both cases, brightfield maps of the grids were collected to observe the grid orientation and assess its integrity and ice thickness. In the Leica cryo-CLEM, widefield fluorescence was used to rapidly scan over a grid in live mode. Then, z-stacks were collected at specific regions and then deconvolved using Thunder computational cleaning. Whereas in the cryo-SIM, high power laser-induced fluorescence was used to look at one 64 μm^2 field of view at a time. Then, patterned fluorescence signal was collected at three different angles with 125 nm height increments throughout the cell volume that can computationally be reconstructed into super-resolution fluorescence image stacks.

The appearance of BeauR-eGFP-nsp2 fluorescence under the cryo-SIM was different to the fluorescence seen via confocal microscopy. Looking at later timepoints, the areas of GFP fluorescence appeared as large clouds like in confocal images (Figure 4.3). However, at 6 h pi, small puncta that were obvious in confocal images were less clear in fully hydrated cryo-preserved cells. Plus, as seen in the SIM reconstruction of uninfected cells, some puncta resulted from autofluorescence (Figure 4.1 B). Therefore, the largest patches were prioritised for SXT as the number of GFP-tagged virus-infected cells was limited on the 3 mm TEM grids fixed earlier in infection. It was also observed that healthy cells, which may be more susceptible to infection, might have a higher affinity for

adhering to grid bars compared to the grid foil. Moreover, unlike the DF1 cells, the CK cells were variably susceptible to Mitotracker FarRed labelling so if this was required for correlation to the SXT to find ROs, unambiguously identifying membranes correlating to GFP signal in CK cells would be more difficult.

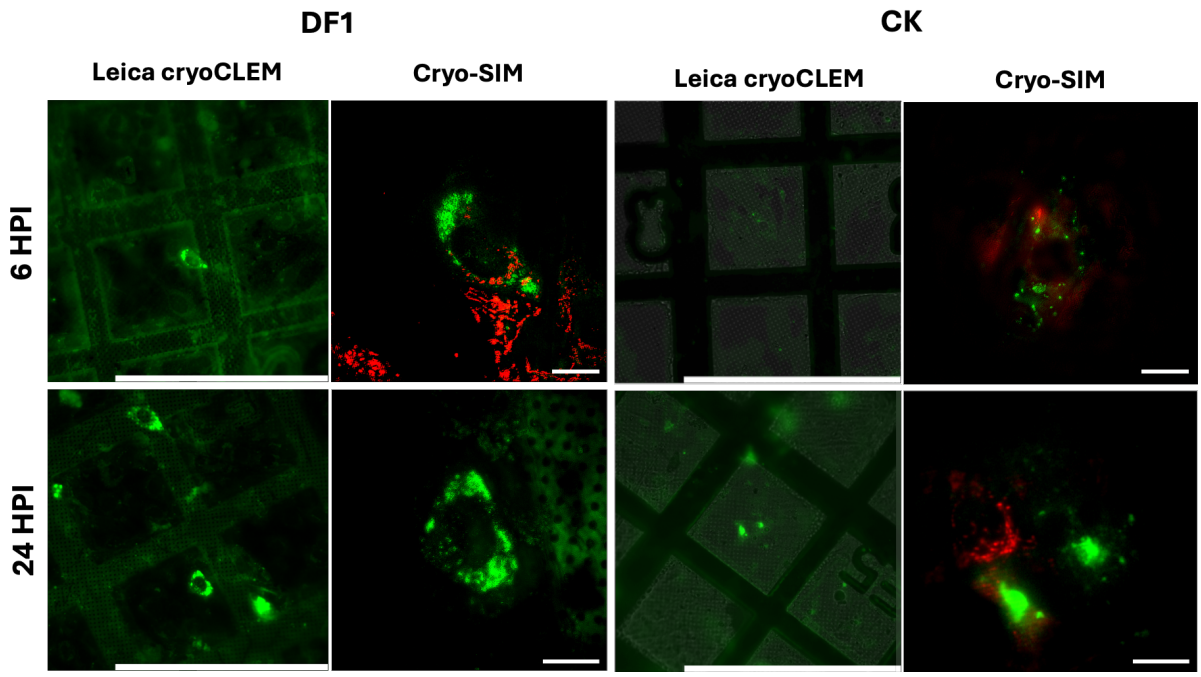


Figure 4. 3 Cryo-fluorescence images of cryopreserved BeauR-eGFP-nsp2 infected cells.

CK or DF1 cells were infected with BeauR-eGFP-nsp2, plunge frozen at 6 or 24 h pi, and imaged on the Leica cryoCLEM or cryo-SIM. Leica cryoCLEM images were computationally cleaned using Leica Thunder and cryo-SIM images were aligned and reconstructed from tri-directional patterned light. Cells prepared for cryo-SIM were also labelled with Mitotracker FarRed (red) in anticipation of using the mitochondrial patterns to correlate the 3D fluorescence stacks with the soft X-ray tomograms collected in the same area. The scale bars for the Leica cryoCLEM images are 200 µm and the scale bars for the cryo-SIM images are 10 µm.

4.2.3. Cryo-soft X-ray tomography of BeauR-eGFP-nsp2 infected in primary CK cells

Although CK cells proved difficult to evenly vitrify, some areas were preserved better than others, and since the CK cells exhibited the earliest signs of RO membranes when infected with BeauR-eGFPnsp2 when compared to other cell lines, they were used to

screen RO formation events in early replication. Even though autofluorescence was observed in the mock-infected cells, some brighter fluorescence patterns were observed in BeauR-eGFP-nsp2 infected CK cells despite fewer events being captured in the limited TEM grid area (Figure 4.4 A, D). It was possible to resolve the double membrane of the nucleus and mitochondrial outer membrane as dark lines however the two bilayers could not be distinguished (Figure 4.4 E). Additionally, there were some spherical cytoplasmic membranes observed with appropriate diameters for DMVs (~250-300 nm) (Knoops *et al.*, 2008; Maier *et al.*, 2013) (Figure 4.4 E-F). However, the double membrane could not be resolved, and the vesicles were not accurately correlated to eGFP-nsp2 fluorescence signal which made examining the RO structures difficult using this method.

Since infection induces membrane proliferation and eventual rounding-up of cells (Jadhav and Kounatidis, 2023), it was thought that the cells with more contrast and noise corresponded to infected cells (Figure 4.4 A). Some of these darker cells also had GFP foci, but the ill-health of the cells exacerbated the sample thickness issue and vitrification was less successful, so no RO membranes were resolved (Figure 4.4 B-C, E-F). This highlighted the heterogenous nature of the CK population and the variability in vitrification across the grid.

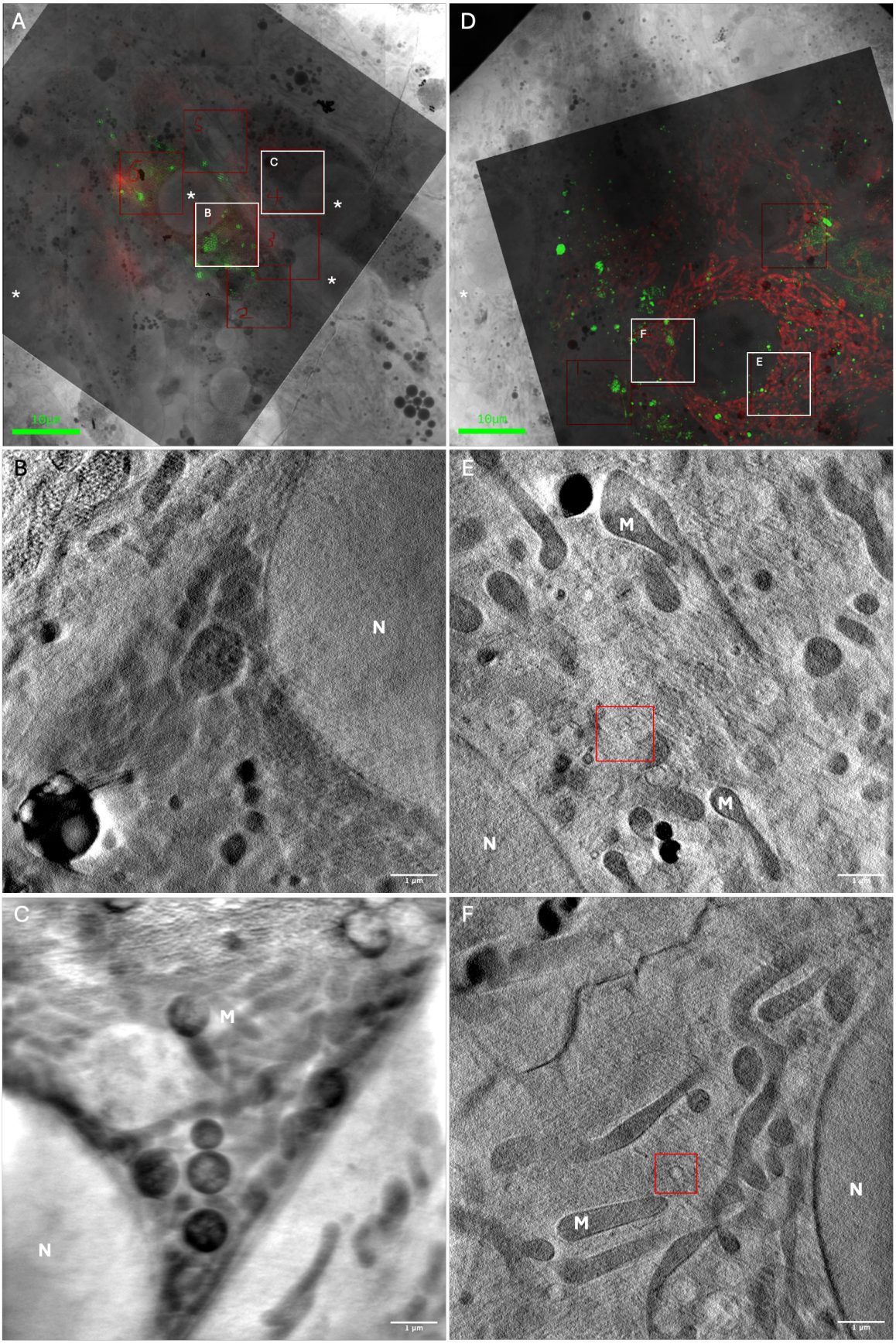


Figure 4. 4 Screening for replication organelle formation events at 6 h pi in CK cells.

CK cells were infected with BeauR-eGFP-nsp2, labelled with Mitotracker FarRed, and plunge frozen with 250 nm fiducials at 6 h pi. The cells were screened for eGFP-nsp2 signal and fluorescence was correlated to X-ray mosaics of the same cells (Panels A and D). Panel A shows 4 cells (nuclei marked with asterisks), with heterogeneous shapes and densities. Panel B shows an orthoslice through a tomogram at a region of GFP fluorescence but devitrification artifacts and a lack of focus prevent any membranes from being resolved. Panel C shows a tomogram through a cell without GFP foci, but appearing dark, like the cell with GFP foci. Once more, the details of the membranes were not resolved. Panel E shows an orthoslice through a tomogram with better focus and some smaller membranes resolved (red box). Panel F shows an orthoslice through a tomogram containing GFP foci with a single spherical membrane structure (red box) with a diameter of ~ 250-300 nm. N, nucleus; M, mitochondria. Between the X-ray mosaic in panels A and D and the reconstruction of the tomograms (panels B, C, E, F), the images are flipped along the x-axis.

The extent of the RO increases throughout infection (Knoops *et al.*, 2008) so there was a greater chance of imaging ROs at 18 h pi or 24 h pi compared to 6h pi. Here, ROs spread throughout the depth of the cell so more focal positions would include RO membranes. Moreover, new ROs may be continually forming so they may have been captured when imaging a large volume throughout the cell. However, this risked any formation intermediates becoming indistinguishable from the mature RO and the cells being in an unhealthier state, rounding, and potentially detaching from the grid foil thus worsening the vitrification quality.

CK cells were cryopreserved at 18 h pi following infection with neat BeauR-eGFP-nsp2. The samples were thicker due to the heterogenous cell population at various stages of their respective cell cycle and dying cells resulting in irregularities in vitrification quality (Figure 4.5 A-B). In some positions, double membrane structures like the nuclear and mitochondrial membranes were resolved as dense single leaflets at this resolution (Figure 4.5 C). In addition, structures with a similar appearance to a patch of DMSs were observed in one tomogram but the resolution was not optimal due to whole cell thickness and poor contrast in the busy cytosol (Figure 4.5 D).

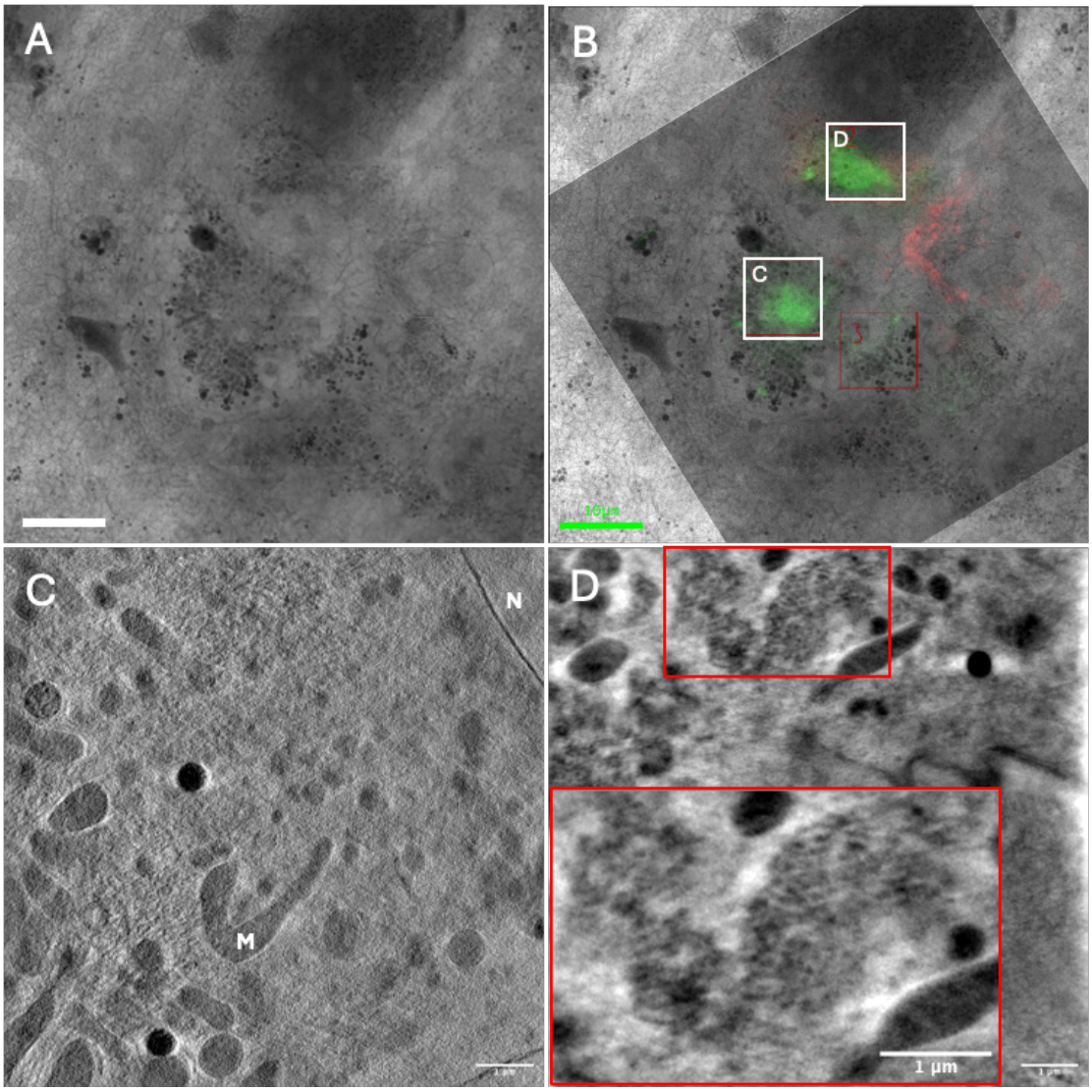


Figure 4. 5 Potential DMS patch in CK cells at 18 h pi.

CK cells were infected with BeauR-eGFP-nsp2 and plunge frozen at 18 h pi. Grids were screened for eGFP-nsp2 fluorescence and images were captured and overlaid with X-ray mosaics (panel A, scale bar 10 μm) of the same cells (panel B). Tomograms were captured in the areas that exhibited eGFP-nsp2 fluorescence across two cells. The detail of the resolved membranes depended on the positions (panel C: M, mitochondria; N, nucleus) but in panel D, an area appearing like DMSs was observed (red box).

4.2.4. Cryo-soft X-ray tomography of BeauR-eGFP-nsp2 infected DF1 cells at 6 h pi

Since the CK cells proved difficult to vitrify, DF1 cells were imaged following infection with BeauR-eGFP-nsp2 to identify ROs under cryogenic conditions. The DF1 cell line has been used previously to study viral infections by cryo-SXT confirming the population can be successfully vitrified (Chichón *et al.*, 2012). Subsequently, the more even vitrification of the cells allowed easier focusing of the X-ray objective onto smaller intracellular membranes.

From the previous fluorescence microscopy experiments, it was shown that at 6 h pi in DF1 cells, the number of cells exhibiting BeauR-eGFP-nsp2 fluorescence was low and foci were discrete. This was observed once more when DF1 cells were infected with BeauR-eGFP-nsp2, vitrified at 6 h pi, and observed under the cryo-SIM. Even fewer infected cells per sample were observed due to the limited area of the grids. When the regions of fluorescent foci were observed by cryo-SXT (Figure 4.6 A), in some areas, spherical vesicles and the endoplasmic reticulum could be resolved (Figure 4.6 B-D). This showed that the DF1 were more promising cells to visualise RO-like structures and ER rearrangements via cryo-SXT compared to the CK cells. The diameters of spherical structures were less than 200 nm so were likely too small to be DMVs which have expected diameters of 250-300 nm (Knoops *et al.*, 2008; Maier *et al.*, 2013) (Figure 4.6 1a-b). They could represent a population of smaller DMVs, but fluorescence foci could not be accurately correlated to these vesicles, and it could not be deciphered whether they had a double membrane.

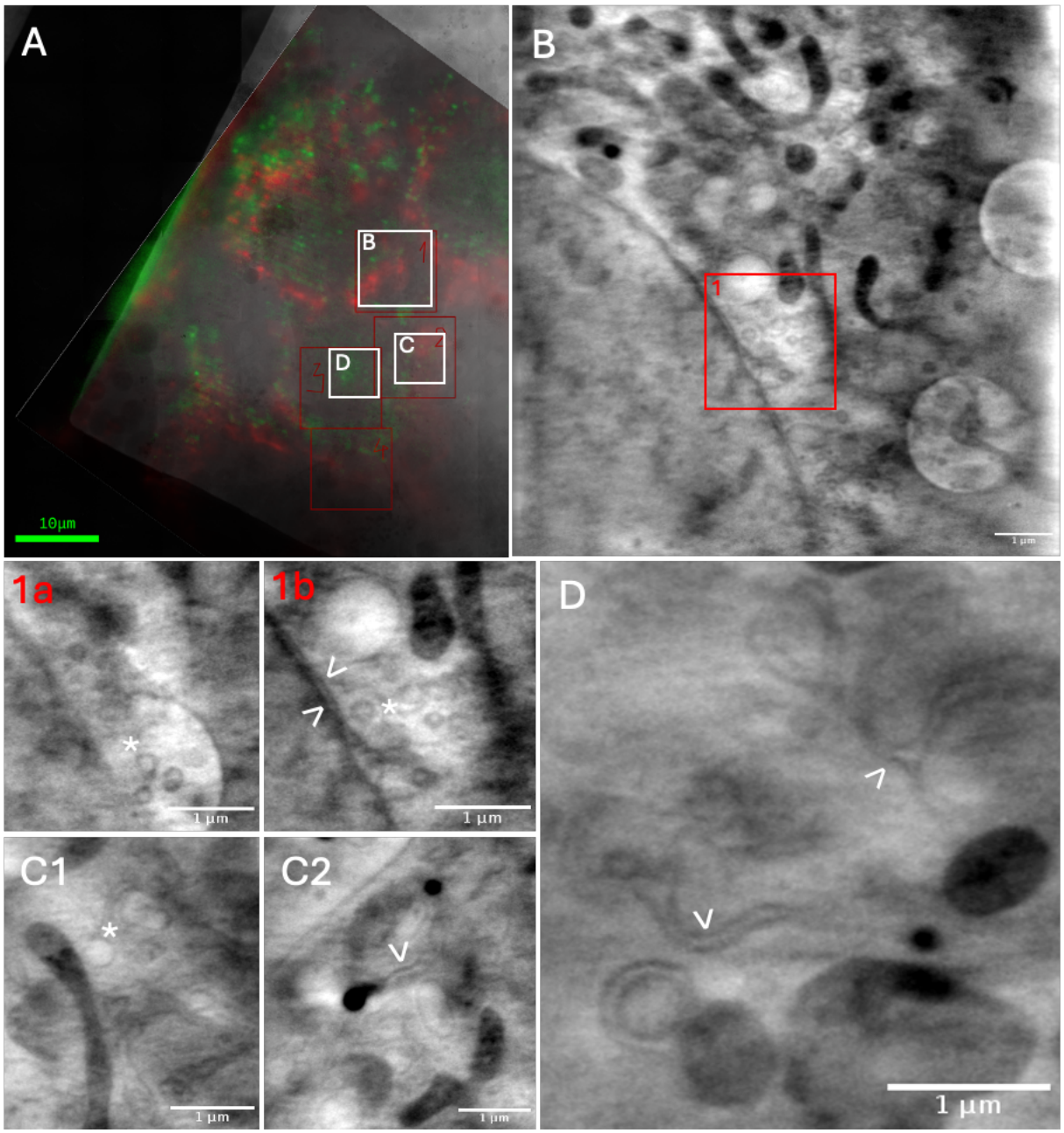


Figure 4. 6 Membrane observations in DF1 cells infected with BeauR-eGFP-nsp2 at 6 h pi.

DF1 cells were infected with BeauR-eGFP-nsp2 and plunge frozen at 6 h pi. Grids were screened for eGFP-nsp2 fluorescence and images were captured and overlaid with X-ray mosaics of the same cells (panel A). Tomograms were captured in the areas that exhibited eGFP-nsp2 fluorescence. In the orthoslice through tomogram B, a small perinuclear patch of spherical vesicles was observed (panel B, box 1). In panels 1a and 1b, two different orthoslices through box 1 are shown with several 100 nm vesicles (asterisks) and the nuclear double membrane resolved (arrowheads). Panels C1 and C2 are two different regions of area C in panel A showing that spherical vesicles (asterisk) and endoplasmic reticulum (arrowhead) can be resolved in DF1 cells. Panel D is a zoomed in region from area D in panel A where the DF1 cell endoplasmic reticulum arrangements could be resolved (arrowheads).

4.2.5. Cryo-soft X-ray tomography of IBV replication organelles in DF1 cells at 24 h pi

Since single membranes, like the ER, were able to be resolved via cryo-SXT in DF1 cells but it was difficult to resolve early RO formation events from small GFP foci at 6 h pi, the RO network was instead investigated in DF1 cells at 24 h pi. Here, the host cells would be better suited to plunge freezing and formation events may still be imaged as the RO network was recorded. At 24 h pi RO membranes were clearly resolved in DF1 cells. In Figure 4.7, three tomograms were collected throughout the cytoplasm of a single cell exhibiting BeauR-eGFP-nsp2 fluorescence (Figure 4.7 A). In each tomogram, spherical vesicles with diameters of 250 – 300 nm were imaged alongside more carbon-dense sections of curved membrane with small (~80 nm) dots tethered along its length (Figure 4.7 B-D). These structures likely correspond to DMVs and DMSs respectively. The DMS-like membranes appear darker than the DMV-like membrane indicating that they absorb more X-rays and have a higher carbon content.

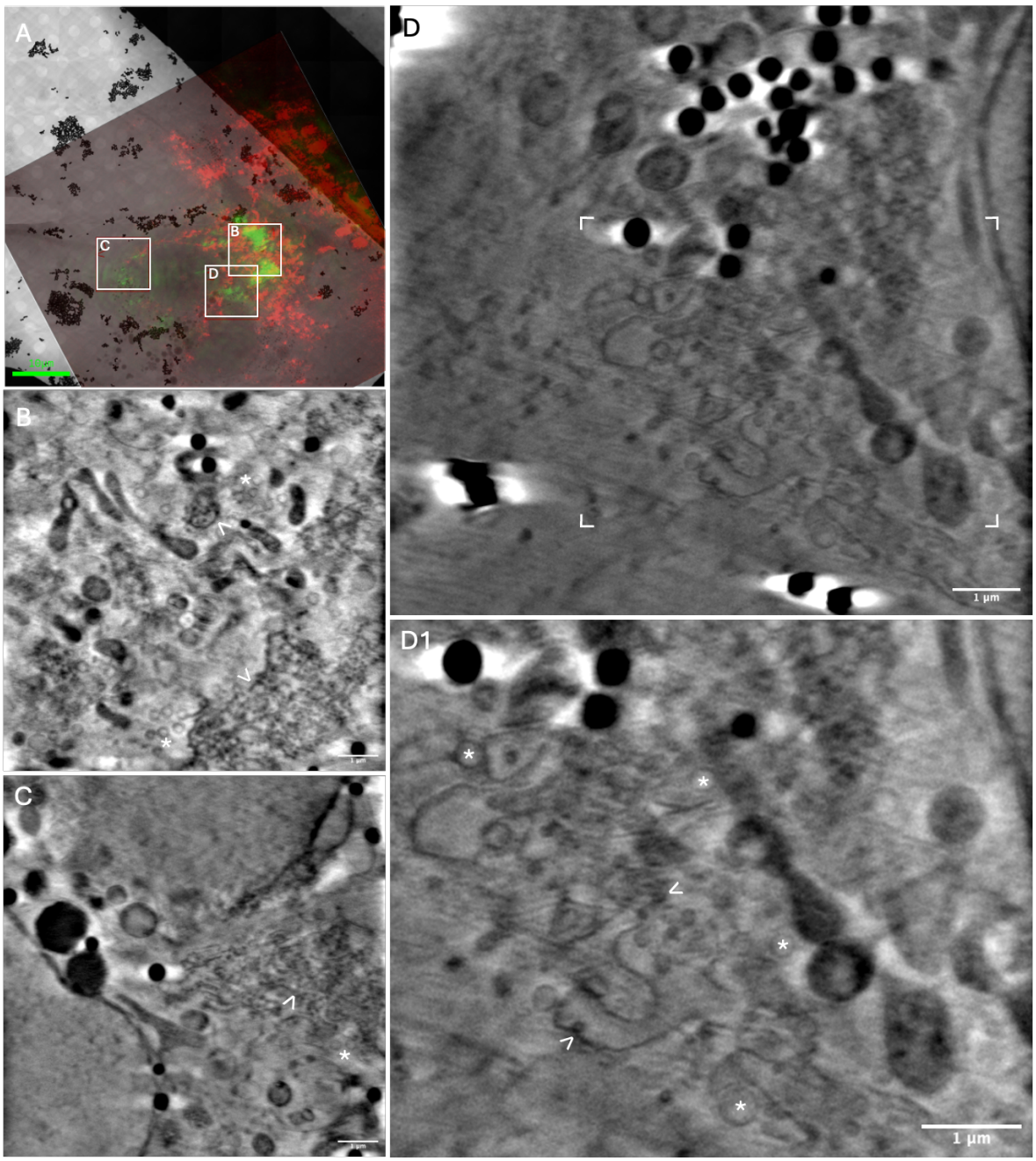


Figure 4. 7 Replication organelles in DF1 cells infected with BeauR-eGFP-nsp2 at 24 h pi.

DF1 cells were infected with BeauR-eGFP-nsp2 and plunge frozen at 24 h pi. Cryo-SIM screening guided tomogram positioning on the X-ray mosaic (panel A). in panels B-D, single orthoslices of the tomograms are shown with DMV-like (asterisks) and DMS-like (arrowheads) membranes. Panel D1 shows a zoom in from the box in panel D with darker DMS-like (arrowheads) and lighter DMV-like (asterisks) membranes.

Similar large networks of vesicular structures, some with diameters consistent with DMVs and DMSs (DMV-like and DMS-like membranes), were also seen in the cytoplasm of infected cells in more detail in further tomograms, however, it was not resolved whether these structures had double membranes (Figure 4.8 A-B; Supplementary movie 1). Each cell and each tomogram had varying levels of detail resolved depending on its location on the grid, its cryopreservation state, and its contents. The mitochondria appeared smaller, with a longest visible length at 621 nm (n= 30, standard deviation= 104 nm), more rounded and less dense than those in uninfected cells (Figure 4.8 C-D). The average longest visible lengths of mitochondria in uninfected cells were 1538 nm (n= 32, standard deviation= 572.9 nm; Figure 4.2 C). DMS-like membranes appeared along sections of zippered ER, in large patches, and were darker than the DMV-like membranes inferring that they are more carbon-dense (Figure 4.8 C-H).

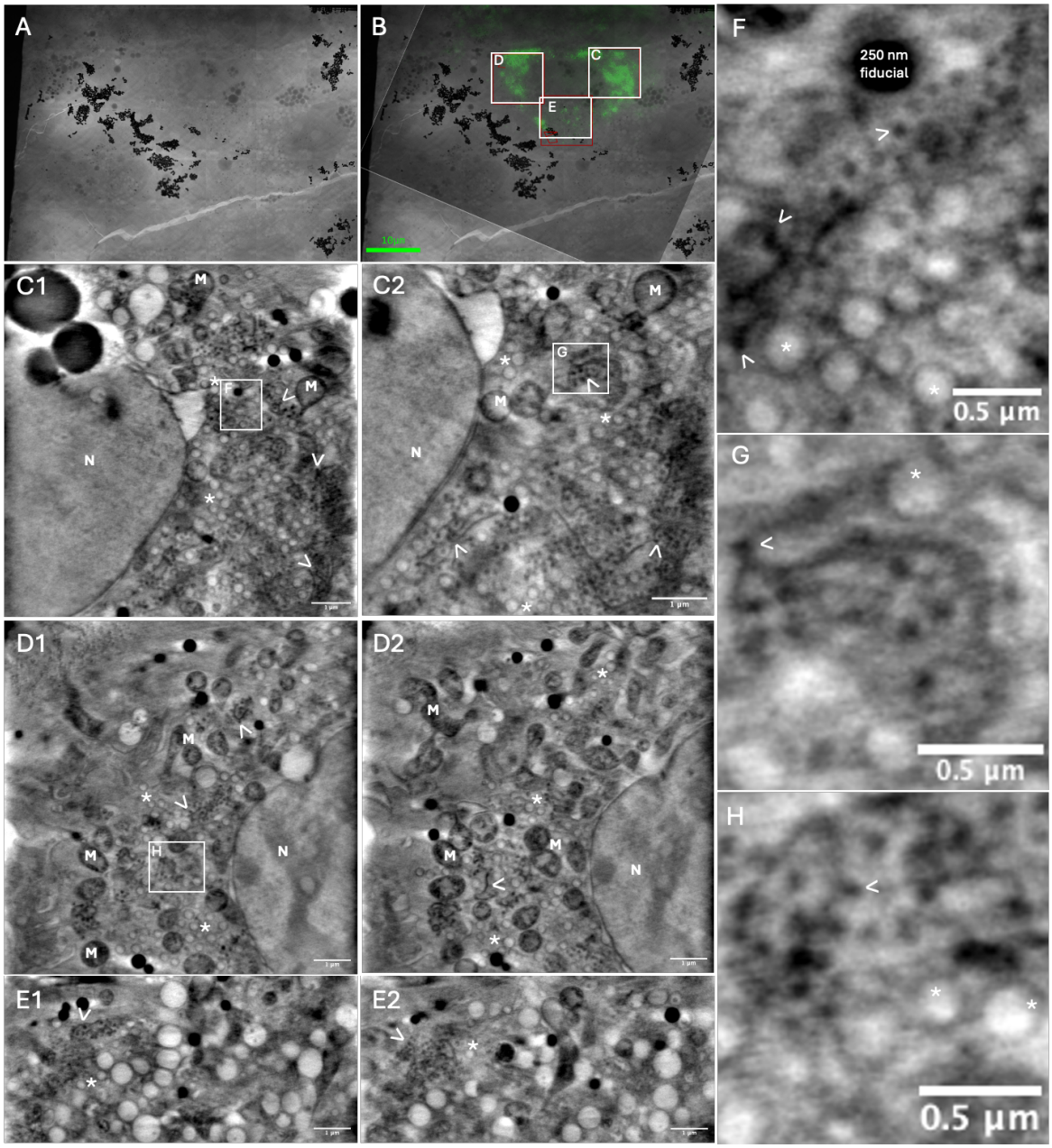


Figure 4. 8 Replication organelles in DF1 cells infected with BeauR-eGFP-nsp2 at 24 h pi.

DF1 cells were infected with BeauR-eGFP-nsp2 and plunge frozen at 24 h pi. Fluorescent regions as observed via cryo-SIM were correlated to the same cell in the X-ray mosaic (panel B). Tomogram positions C-E were collected with two orthoslices shown for each tomogram, and a crop from tomogram E avoiding fiducials and the exterior of the cell. Zoomed-in views of ROs from tomograms C and D are shown in panels F-H; panel F is an orthoslice from box F in panel C1, panel G is an orthoslice from box G in panel C2, panel H is an orthoslice from box H in panel D1. The DMV-like vesicles are marked with asterisks and the DMS-like membranes are marked with arrowheads. N, nucleus; M, mitochondria.

Manual segmentations were completed in IMOD to show the depth of the RO in 3D from the tomogram in Figure 4.8 C (Figure 4.9 A, Supplementary movie 2). 252 DMV-like

vesicles and 424 DMS-like heads in 8 discrete patches of zER were counted in this tomogram which covered approximately one third of the total volume of the infected cell cytoplasm. The DMV-like vesicles were described if they had diameters between 200-300 nm and the DMS-like vesicles were described if they had diameters between 60-80 nm. The tomogram included large clusters of DMV-like vesicles with zER/DMS-like membranes interspersed between the DMV-like vesicles. This cell also exhibited BeauR-eGFP-nsp2 fluorescence and ROs in two further positions (Figure 4.8 B), encompassing most of the cytoplasm so it could be estimated that over 750 DMV-like vesicles and over 1200 DMS-like membranes existed in the cell. The average diameter of the DMV-like vesicles was 251 nm (n= 51, standard deviation = 27.9 nm) and the average diameter of the DMS-like heads was 72.4 nm (n= 56, standard deviation= 8.7 nm) (Figure 4.9 B-C). Furthermore, the average in-focus z-range of the tomogram was 1462 nm (n= 5) so it is possible that further ROs could exist or connect if the full height range of the cell was recorded. Although there were more DMS-like membranes than DMV-like vesicles, the DMV-like vesicles are larger, so they take up a greater overall volume than the DMS-like membranes.

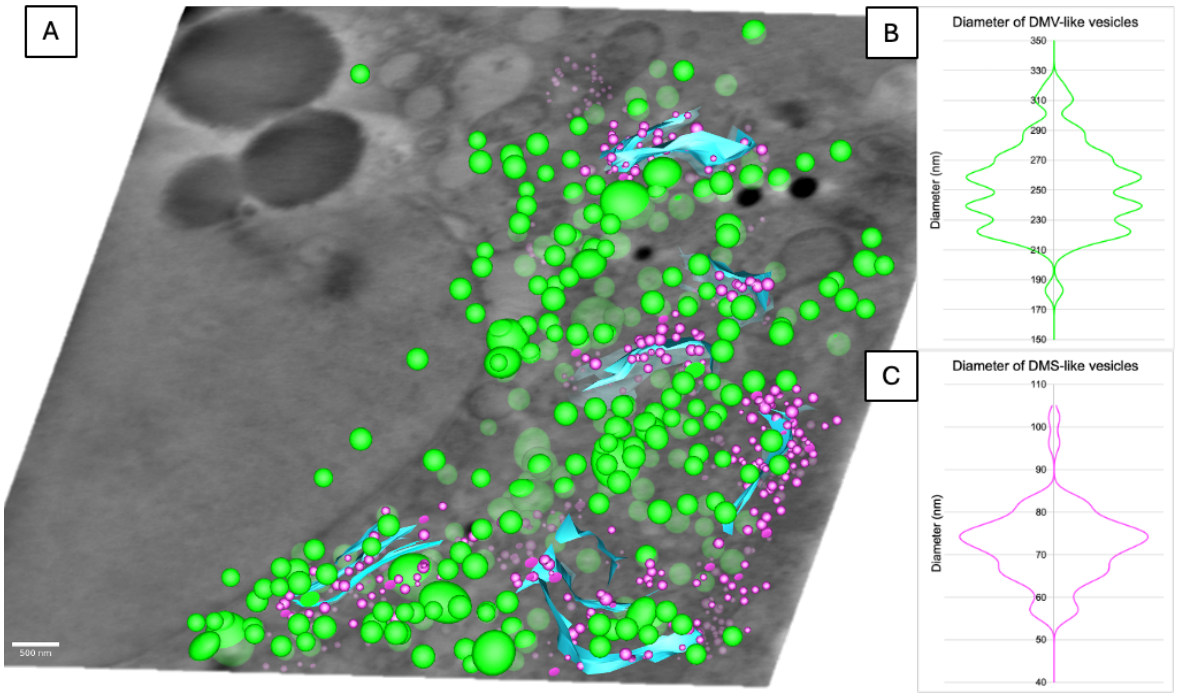


Figure 4. 9 Segmented RO membranes in BeauR-eGFP-nsp2 infected DF1 cells at 24 h pi.

Panel A shows the reconstructed soft X-ray tomogram with RO-like membranes segmented using 3dmod. DMV-like vesicles are labelled in green, zER is labelled in blue, and DMS-like membrane heads are labelled in magenta. Panel B shows a violin plot of the measured diameters of DMV-like vesicles and Panel C shows a violin plot of the measured diameters of DMS-like vesicles. Violin plots were generated in Excel.

The ROs were observed in more detail looking at smaller regions of the tomograms (Figure 4.10 A-H). The DMS-like membranes were darker than the DMV-like vesicles indicating that they had a higher carbon-content within their membranes. The double membranes were not resolved for the DMV-like vesicles or the DMS-like membranes as they are tightly apposed. Furthermore, nascent IBV virions within single membrane vesicles were too difficult to distinguish from other secretory vesicles at this resolution (Figure 4.10 I-J).

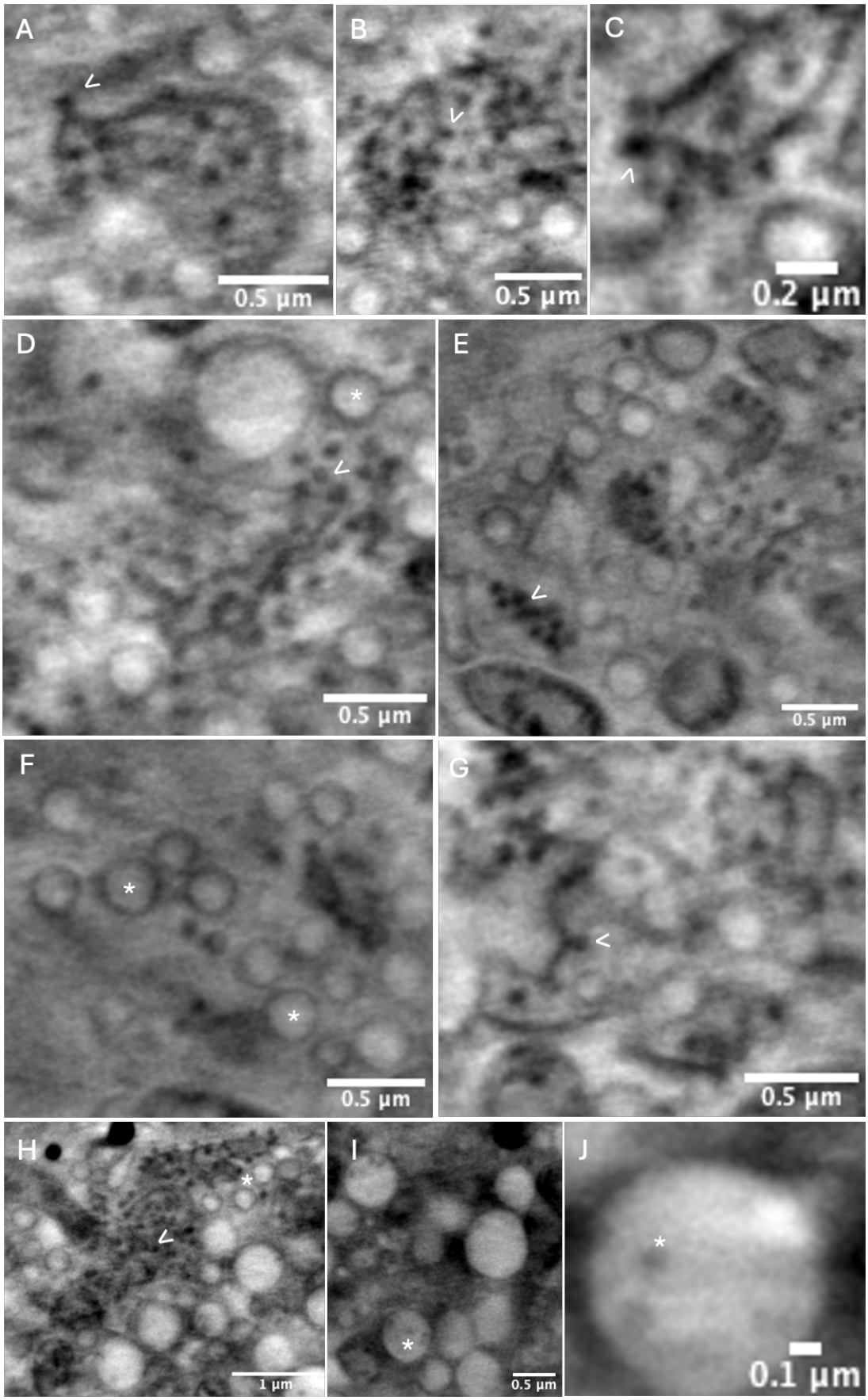


Figure 4. 10 Gallery of ROs taken from the tomograms in Figure 4.8.

After tomogram reconstruction, zoomed in regions of ROs were cropped to measure the sizes of DMSs (arrowheads) and DMV-like vesicles (asterisks) in panels A-H. Panels I and J show a vesicle too large to be a DMV containing ~100 nm diameter dots.

In another tomogram (Figure 4.11 A-C, Supplementary movie 3), the in-focus z-range reached an average of 2525 nm (n= 5). This shows that cryo-SXT can provide a large volume of data to present the cellular context of the object of interest, if it can be resolved at the limited resolution of cryo-SXT. The difference in the mitochondrial morphology between the infected cell and an uninfected cell adjacent to it can be observed in Figure 4.11 B; the mitochondria in the uninfected cell appeared denser. The segmentation shows the (in-focus) RO network throughout the cytoplasm in 3D (Figure 4.11 C, Supplementary movie 4). The cell did not exhibit BeauR-eGFP-nsp2 fluorescence in further positions (Figure 4.11 A), therefore, the RO in this cell was estimated to include 207 DMV-like vesicles and 372 DMS-like heads in 8 discrete patches. Overall, the DMS-like membranes did not seem to be connected to DMV-like vesicles, rather the DMS-like membranes appeared to form from separate membranes to the DMV-like membranes (Figure 4.11 D-F). Then, the number of DMV-like vesicle-ER connectors was not visible at this resolution, but the adjacent DMV-like vesicles did not appear to share an outer membrane or form vesicle packets.

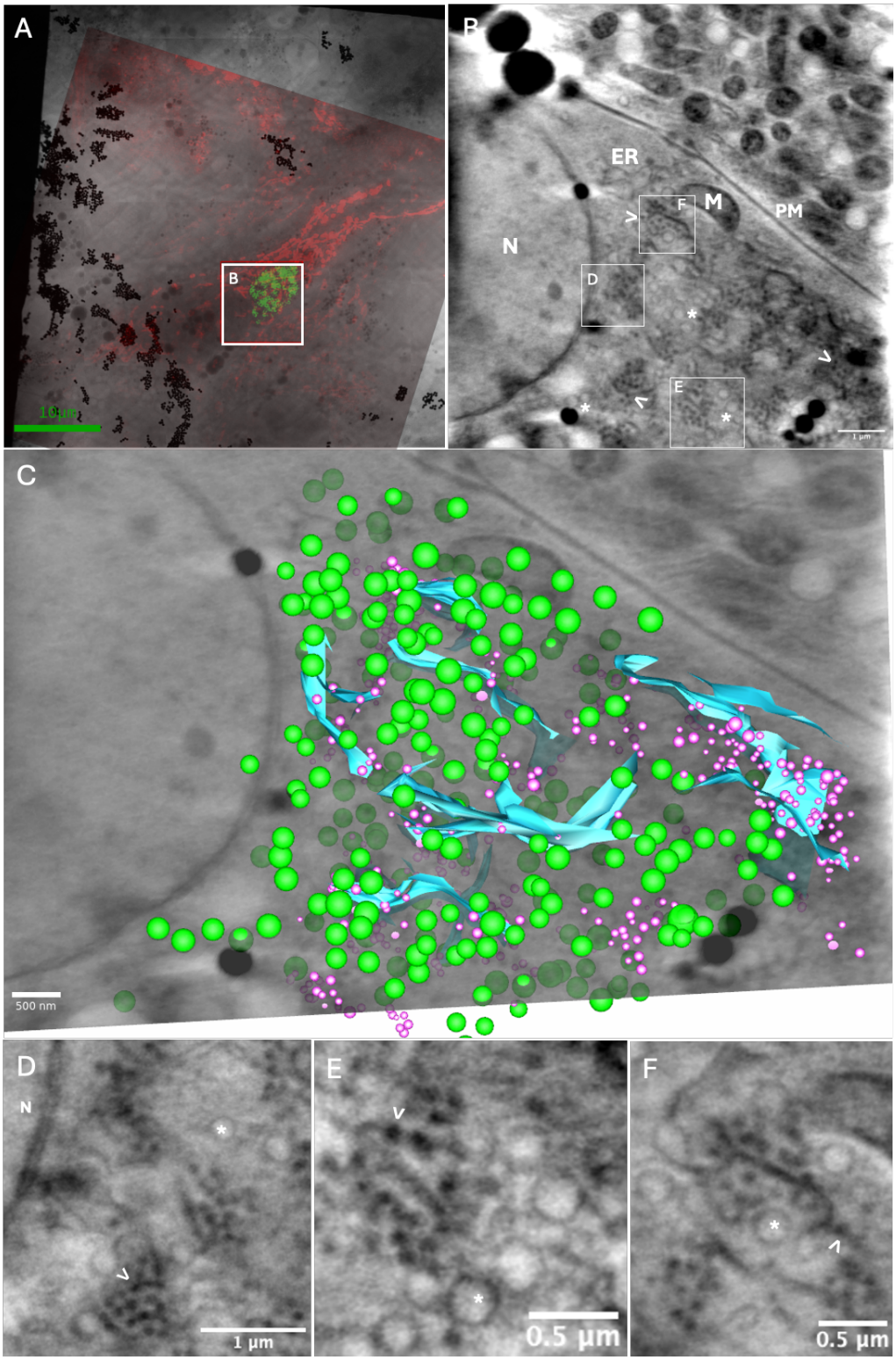


Figure 4. 11 A large depth of field throughout the cells was imaged including ROs.

DF1 cells were infected with BeauR-eGFP-nsp2 and plunge frozen at 24 h pi. A single large GFP patch was observed via cryo-SIM and correlated to the X-ray mosaic of the same cell (panel A). A single tomogram encompassed the entire GFP region (panel B), and the segmentation is shown in panel C with DMV-like vesicles labelled in green, zER labelled in blue, and DMS labelled in magenta. Zoomed-in regions boxed in panel B are shown in panels D-F. The DMV-like vesicles are marked with asterisks and the DMS-like membranes are marked with arrowheads. N, nucleus; M, mitochondria; PM, plasma membrane.

4.3. Discussion

In this chapter, the IBV RO network, including putative DMVs, zER and DMSs, was imaged through a correlative workflow, in whole cells, and under a near-native and hydrated state. This is the first time that CoV DMS-like membranes have been imaged by cryo-SXT. The only other CoV imaged by cryo-SXT so far has been SARS-CoV-2, which have a RO comprising abundant DMVs but with limited numbers of DMSs (Cortese *et al.*, 2020). DMSs are more abundant in IBV infected cells, therefore, it is unsurprising that they were not yet defined by cryo-SXT in SARS-CoV-2 infected cells. The goal was to use the large 3D volumetric data supplied by this technique to image rare events such as RO formation intermediates. Imaging these intermediates could contribute to the understanding of RO biogenesis mechanisms. However, the double membrane of the ROs could not be resolved and membrane budding or wrapping events could not be defined. These experiments also included imaging of CK cells that had been cultured on grids and the first observations of BeauR-eGFP-nsp2 fluorescence in vitreous cells.

The scale of the formation events is unclear but since the double membranes of the ROs were not resolved, it was not possible to describe any membrane budding or wrapping events that could have been potential intermediates in RO formation. Double membranes such as the nuclear membrane and regions of ER were sometimes resolved but appeared less tightly apposed than the double membranes of ROs which span 18-20 nm (Klein *et al., 2020*; Snijder *et al.*, 2020) (Figure 4.6 B,D). Furthermore, connections between ER and RO were not resolved. In these experiments, it was not possible to

reliably observe ROs at 6 h pi or formation events prior to 6 h pi, therefore, questions remain surrounding the RO biogenesis mechanisms are the time course of DMVs and DMSs.

To be able to confirm that the RO structures observed were genuine, more controls are required to be able to make comparisons. Currently, only two tomograms of uninfected DF1 cells (Figure 4.2 B-C) plunge frozen at 48 h post seeding (equivalent to 24 h pi) were used to compare to the infected DF1 cells and the quality of reconstructions from these different samples was variable and made comparisons more difficult. For a complete comparison to infected cells, more tomograms of uninfected cells need to be collected from cells plunge-frozen at the same time as the infected cells and they need to be of the same quality in terms of vitrification, alignment, and reconstruction. Despite using the same plunge-freezing machine and routine, the cells position on the grid would alter its vitrification and ease of tilt series correction and the random dispersal of fiducials would vary tomogram reconstruction quality. Vitrified cell preparations on grids may be able to be made more homogenous using micropatterning and new automated plunge freezing devices such as the Cryogenium from *Linkam Scientific* (Toro-Nahuelpan *et al.*, 2020; Linkam Scientific, 2024). There are further examples of uninfected cells in comparison to virus-infected cells in Doyle *et al.* (2019), Chichón *et al.* (2012), Loconte *et al.* (2021), and Castro *et al.* (2023) which exhibit some cytoplasmic vesicular networks but none with the clustered pattern and uniformity of the DMV-like membranes or with the highly soft X-ray-absorbing and specifically-shaped DMS-like membranes.

Furthermore, for improved fluorescence correlation it would be important to quantify the level of autofluorescence from mock-infected cells observed under each cryo-fluorescence screening microscope for each cell type at each time post freezing. Subsequently, plotting the intensities of autofluorescence to real rIBV signal from meGFP excitation could be used to discern a threshold for real signal and decide which cells and areas in specific cells should be targeted for tilt series collection. This may improve the number of tomograms captured that included ROs but would not improve the throughput of tilt series collection or the heterogeneity of tomograms across different cells or different grids.

Looking at the fully formed IBV RO network at 24 h pi via cryo-SXT, the membrane rearrangements (with distinct patches of DMS-like membranes interspersed with DMV-like vesicles) are comparable to the room temperature EM data for cells fixed from 16 h pi onwards (Maier *et al.*, 2013). The total number of DMV-like vesicles and DMS-like membranes in infected cells has not previously been reported. Here, the number of DMV-like vesicles was estimated to be between 200-250 and the number of DMS-like heads was estimated to be between 370-420 per approximately 50 μm^3 of the RO in the cytoplasm of the infected cell (the field of view of tomograms was 10 μm^2, nuclei/extracellular areas occupied about half of the tomogram, and the average in focus depth of the cytoplasm was 2.1 μm (n= 9)). SARS-CoV-2 viral membrane rearrangements (described as CM/DMVs) has previously been described to occupy 11.8 μm^3 of a cell, with a total volume measured at 1738 ± 458μm^3, from full rotation tomography of infected cells in suspension (Loconte *et al.*, 2021). The CM was shown in contact with three DMVs, described as 'hollowed structures', and mitochondria, but ER networks or paired

membranes were not visible at the available resolution (50 nm) (Loconte *et al.*, 2021). The B24 cryo-SXT had a higher resolution limit (25 nm) so numerous BeauR-eGFP-nsp2 DMV-like vesicles and DMS-like membranes were resolved, and no CM were described. Furthermore, in some cells at 24 h pi, the full cytoplasm labelled for several patches of ROs, and in other cells, the ROs were imaged in a single patch full, as is consistent with the fluorescence data. Therefore, in the cell with a single RO patch (Figure 4.11 A-B), the RO volume was approximately 50 μm^3, and in the cell with several RO patches covering most of the cytoplasm (Figure 4.8 B-E), the RO volume could be estimated to be 150 μm^3. This is much larger than the volume of CM/DMVs reported for the one SARS-CoV-2 infected cell in Loconte *et al.* (2021), however, these are measurements taken from SXT at different resolutions, from different cell types, and from cells on grids compared to cells in suspension, and the RO size varies in across cells as indicated by the fluorescence. To make more comparisons of RO volume, different cell types could be infected to measure whether the RO volume range differs, infection could be synchronised to ensure the volume measurements were of RO at the same stage of infection (Klein *et al.*, 2023), and more timepoints could be tested to measure how the RO develops.

The diameter of the DMS-like heads was estimated to be 72 nm (±8.7 nm) which fits within the range of DMS diameters described in HPF and chemically fixed cells (Maier *et al.*, 2013). Interestingly, the DMS-like membranes appeared as dark dots tethered to dark sections of zER while the DMV-like vesicles were lighter. This shows that the DMS-like membranes and zER absorbed more soft X-rays than the DMV-like vesicles inferring that they have a higher carbon content. This could suggest that the DMS-like membranes and zER are packed with proteins. EM images of DMSs have shown that they have an

electron-dense interior and the double membrane continuous with zER is also darker and more tightly apposed than the DMV double membrane (Maier *et al.*, 2013; Snijder *et al.*, 2020; Cortese *et al.*, 2020). In cryo-ET studies, the DMVs have been shown to contain RNA within their interior, but the double membranes are mostly empty with only a few protein pores (Klein *et al.*, 2020; Wolff *et al.*, 2020). Together, these observations suggest that the DMSs and zER contain proteins which may perform a function for the virus. The voxel density could be given a value to quantify the differential absorption of the soft X-rays by the putative DMSs, zER, and DMVs. Linear absorption coefficient (LAC) values are further measures of X-ray absorbance that can be calculated for full rotation tomography (Do *et al.*, 2015).

Focusing on the IBV DMV-like vesicles observed by cryo-SXT, they had a uniform spherical shape and size with an average diameter of 251 nm (±27.9 nm). The violin plot (Figure 4.9 B) shows the range of diameters of vesicles in the RO membrane region highlighted by the rIBV fluorescence signal. The average diameter of DMV-like vesicles taken from the cryo-SXT agrees with EM observations of DMVs from chemically fixed dehydrated samples, HPF-FS samples, and fully hydrated *in situ* samples (Maier *et al.*, 2013; Snijder *et al.*, 2020; Knoops *et al.*, 2008; Klein *et al.*, 2020). Furthermore, the vesicles seen in the cryo-SXT experiments of SARS-CoV-2 infected cells had diameters of 233 ± 18 nm (Castro *et al.*, 2023) and 366 ± 37 nm (Loconte *et al.*, 2021). In another SARS-CoV-2 cryo-SXT study, Mendonça *et al.* (2021) described one example of perinuclear vesicles with consistent diameters to DMVs.

EM experiments have also suggested that SARS-CoV and SARS-CoV-2 DMVs are interconnected and can make vesicle packets at late timepoints post infection (Knoops *et al.*, 2008; Klein *et al.*, 2020), whereas IBV DMVs usually appear as individual entities, although possibly connected to the ER, interspersed with DMSs (Maier *et al.*, 2013). This might suggest why in cryo-SXT experiments, SARS-CoV-2 induced membranes appear more tightly packed (Castro *et al.*, 2023) compared to the IBV DMV-like vesicles presented in this thesis. SARS-CoV-2 DMVs and dsRNA had also previously been shown to cluster in cages of the intermediate filament vimentin (Cortese *et al*., 2020) but vimentin structures were not identified in another SARS-CoV-2 cryo-SXT study (Castro *et al.*, 2023). It could be tested whether vimentin also encompasses dsRNA and ROs in IBV infected cells as it is suggested to have several roles and arrangements during viral infection (Zhang *et al.*, 2020).

The volume of data provided by cryo-SXT is useful for looking at the cellular context of infection, so this was the focus of the SARS-CoV-2 cryo-SXT experiments. Loconte *et al.* (2021) did show that the volume of the mitochondria and nuclei, and the DNA packing within the nucleus (as measured by LAC value), were not significantly different between mock, 6 h pi and 24 h pi cells. On the other hand, smaller mitochondria, with increased contrast, were described as stressed in SARS-CoV-2 infected cells by Castro *et al.* (2023). The denser appearance suggested that the mitochondrial matrix was condensed and infers dysfunction of the mitochondria. Smaller mitochondria have also described in SARS-CoV-2 infected cells previously (Mendonça *et al.*, 2021; Cortese *et al.*, 2020). Furthermore, aberrant mitochondrial morphologies such as rounding, matrix condensation, and cristae compaction, characterised by increased X-ray absorption, have

been described in several cryo-SXT studies of virus infection (Pérez-Berná *et al.*, 2016; Garriga *et al.*, 2021). Large numbers of mitochondria were not found in the infected cells here. Therefore, measuring their volumes in more samples could provide a better comparison of the host organelles following IBV infection and SARS-CoV-2 infection. The longest visible length of the mitochondria was measured here, and the mitochondria were significantly shorter in the infected cells (622 nm (±104 nm, n=30)) compared to mock-infected cells (1538 nm (±572 nm, n=30)). On the other hand, the quantitative analysis was limited as mitochondria were only measured from two tomograms of uninfected DF1 cells (Figure 4.2 B-C) and six tomograms of infected DF1 cells (Figures 4.7 B-D, 4.8 C-D, 4.11 B) with only 30 mitochondria measured under each condition. To generate a more robust comparison, more mitochondria over more tomograms covering a range of cells would need to be measured. For further comparison, the mitochondrial densities could be quantified using voxel densities or LAC values available from full rotation tomography. The shorter lengths measured in the infected cells infers that the mitochondria were rounder too. IBV has also previously been shown to activate mitochondria-mediated apoptosis pathways in cells and reduce the number of mitochondria in some segments of the oviduct in chickens (Han *et al.*, 2024; Khan *et al.*, 2019). The virus likely needs energy for RNA and protein synthesis so it would be interesting to investigate whether mitochondria are recruited to ROs and determine how the mitochondria may link this to antiviral signalling (Sorouri *et al.*, 2022).

Sufficient numbers of lipid droplets (LDs) were not imaged in the tomograms presented here to draw any conclusions about their role in viral replication. However, LDs have been suggested to be involved in lipid flow to DMVs via nsp6 (Ricciardi *et al.*, 2022). Following

SARS-CoV-2 infection, Loconte *et al.* (2021) also showed that the radius of lipid droplets was significantly larger at 24 h pi compared to mock cells and at 24 h pi compared to 6 h pi. Moreover, LDs have been shown to accumulate in SARS-CoV-2 infected cells (Dias *et al.*, 2020). LDs have also been shown to participate in the replication of other +RNA viruses (Farías *et al.*, 2024). For example, HCV nsps are localised to LD-associated membranes (Miyanari *et al.*, 2007; Shavinskaya *et al.*, 2007), ZIKV hijacks LD biogenesis pathways (Qin *et al.*, 2022), DENV proteins modulate LD levels (Samsa *et al.*, 2009; Zhang *et al.*, 2018; Tang *et al.*, 2014), and PV RO biogenesis is driven by lipids from LDs (Viktorova *et al.*, 2018). Therefore, it would be interesting to investigate the role of LDs in CoV ROs further. LD volume measurements could be completed from further SXT samples or using lipid dyes for measurements by confocal microscopy (García *et al.*, 2020). If the full volume of the object was not included in the tomograms from limited tilt axis tomography on grids, correction factors could be used to account for the 'missing wedge' of data. Otherwise, the capillary sample holders used by Loconte *et al.* (2021) are advantageous as they enabled 360° imaging of the sample so there is no 'missing wedge' of data, meaning volumes can be more accurately measured, and the X-rays are evenly distributed across the sample without X-ray shadowing at low tilt angles (Le Gros *et al.*, 2014). However, this type of sample holder is only currently available at beamline 2.1 of the Advanced Light Source at Lawrence Berkeley National Laboratory (Chen *et al.*, 2022).

Although BeauR-eGFP-nsp2 fluorescence was successful in identifying RO membranes, the titre of the virus was relatively low compared to WT virus, so the number of infected cells, especially on the limited area of the TEM grids and at early timepoints, could be increased. Therefore, different cryo-fluorescence markers could be tested. For example,

Castro *et al.* (2023) used a reporter A549-ACE2 cell line with a fluorescent construct susceptible to cleavage by the SARS-CoV-2 Mpro to identify infected cells (Pahmeier *et al.*, 2021). A similar reporter could be made for IBV to test if the number of fluorescence-positive cells per grid was increased. Furthermore, BeauR-eGFP-nsp2 fluorescence was shown to label RO membranes specifically but was eventually not required for post-imaging identification of ROs so it was essentially used as a more general a marker for infected cells like the reporter cell line.

The CK cells were the best model to identify BeauR-eGFP-nsp2 fluorescence signal at early h pi for the goal of imaging RO formation intermediates before they were indistinguishable from fully formed ROs. However, the primary source of the cells and their heterogeneity made them difficult to successfully vitrify on grids which resulted in several artifacts during the screening and imaging and difficulty focusing the TXM zone plate. Therefore, the rest of the cryo-SXT was completed using DF1 cells which have been used for cryo-SXT of virus infected cells previously (Chichón *et al.*, 2012). Even with the thinner DF1 cells, only rarely were single ER membranes observed when setting the focal point in increments of 0.1-0.5 µm. Therefore, only when the tilt series had been reconstructed into the tomogram did any ROs become visible due to the combined contrast of multiple images of the same area at different tilt angles. Consequently, multiple tomograms were out of focus, and this problem was exacerbated if the cytoplasm of the area of interest was thicker, as is the case for perinuclear regions of membrane proliferation, and as was the case for the CK cells. Successful vitrification of the CK cells could be attempted using HPF rather than plunge freezing (Moor, 1987). HPF has been completed for cells on grids using several techniques including the ‘waffle’

method (Harapin *et al.*, 2015; Kelley *et al.*, 2022). CK samples would still need to be transported from The Pirbright Institute somewhere with this equipment which is likely detrimental to the cell health. Moreover, from experience at B24, HPF samples may also require cryo-FIB milling before cryo-SXT.

Further approaches to image large volumes under cryogenic condition include serial cryo-FIB-SEM (Mendonça *et al.*, 2021) but the practical achievable resolution (10-20 nm) may not reveal more detail of RO formation intermediates due to the low contrast of biological samples. On the other hand, to image more viral replication intermediates, improving the resolution, even if looking in large volumes, may not be successful. To unambiguously identify abundant RO formation intermediates, sub-inhibitory doses of RO inhibitors could be applied to infected cells to test whether ROs were halted in an intermediate form. For example, K22, which interferes with CoV replication membranes (Lundin *et al.*, 2014), and A922500, which inhibits LDs and reduced viral replication (Ricciardi *et al.*, 2022), could be tested. RO formation intermediates could also be observed in infected cells treated with siRNAs to knockdown cellular factors known to be involved in in ROs such as FAM149B1, CCAR2, and ZC3HAV1 (Pahmeier *et al.*, 2023).

The image quality in the tomograms was also dependent on the tilt series alignment and reconstruction for which different parameters could be tested. In the method used here, 250 nm Au fiducials were added to the grids upon plunge freezing so that they could be used for aligning the tilt series since the biological material was often too low contrast to be tracked throughout the images. The fiducials could sit on top of the cells rather than within the cytoplasm or at the membranes of interest. Therefore, lipid droplets were also

used for tracking and techniques to introduce intracellular fiducials have been tested at B24 to aid tomogram alignment. Furthermore, tomograms in which low tilt angles were blocked (by ice or grid bars) were collected with over a shorter tilt series resulting in tomograms with a large missing wedge of data. Positioning the cells in the centre of grid squares using micropatterning can ensure that the maximum tilt series can be collected (Toro-Nahuelpan *et al.*, 2020). This was optimised for HeLa cells plunge frozen 1-5 h post seeding, but did not work when DF1 or CK cells were left in the patterns for up to 24 h as they were infected with virus because the cells outgrew the patterns over this time.

To combine the large volume ultrastructural imaging of cryo-SXT with higher resolution information, several correlated techniques can be used. Cryo-fluorescence microscopy such as cryo-SIM is set up in-line with cryo-SXT at B24 and this technique has been used to study virus infected cells (Kounatidis *et al.*, 2020; Nahas *et al.*, 2022). Although BeauR-eGFP-nsp2 was compatible with this technique, the signal from this fluorophore was difficult to distinguish from background fluorescence using this technique, especially at early timepoints and in the CK cells. Therefore, the larger foci were imaged instead, and they labelled several membranes, as indicated by the room temperature CLEM, because nsp2 might function in several complexes across several locations. The cryo-SIM can provide a higher magnification and super-resolution information that is useful for detailed 3D fluorescence correlation to the soft X-ray tomograms. Here, *eC-CLEM* (Paul-Gilloteaux *et al.*, 2017) was used to correlate the SIM and SXT reconstructions and the mitochondria were used as common fiducials between the two modalities (this was the purpose of the MitoTracker labelling). Where ROs were found, mitochondrial SIM fluorescence was poor (the mitochondria likely decreased in volume throughout

infection) so they were not used for correlation in 3D. Then, once the tomograms were reconstructed, the ROs were obvious so super-resolution fluorescence correlation to the tomograms was not essential. Consequently, after eBIC obtained the Leica cryoCLEM, this microscope was preferably used because it was faster to screen grids, it did not use lasers so a live fluorescence mode could be used, Z-stacks could still provide 3D data, and the magnification and resolution (especially after Leica Thunder computational cleaning) was sufficient to observe the location of fluorescent puncta within the cytoplasm of infected cells. To find small scale ultrastructural changes in the infected cells, such as RO formation events, correlating smaller cryo-SIM super-resolution eGFP-nsp2 foci could be repeated. However, since the double membranes of DMVs or DMSs were not resolved by SXT, it may be unlikely that RO formation intermediates could be described from the images.

Depending on the fluorophore and level of detail required for finding the object of interest, alternative cryo-fluorescence microscopes can be used to for correlation to cryo-SXT. Epi-fluorescence microscopes with cryo-stages have been used (Castro *et al.*, 2023) and cryo-confocal microscopes from Zeiss (Airyscan) and Leica (SP8 or Stellaris) have been used for correlative cryo-SXT (Myllys *et al.*, 2016) or cryo-ET workflows (Feldmüller *et al.*, 2024; Klumpe *et al.*, 2021). Furthermore, fluorescence microscopes have now been developed in-line with SXT at the National Synchrotron Radiation Laboratory (Zhang *et al.*, 2023) and in the SXT100 from SiriusXT (Fahy *et al.*, 2024). X-ray sources with tuneable wavelengths can also be used to detect specific elements (Groen *et al.*, 2021) and X-ray fluorescence can be used to identity metals (Conesa *et al.*, 2020) in-line with SXT.

4.4. Summary

1. *BeauR-eGFP-nsp2 infected DF1 cells were successfully cultured and vitrified on grids*
2. *BeauR-eGFP-nsp2 DMV-like vesicles fill a large volume of the RO and are interspersed with distinct DMS-like membranes*
3. *Imaging RO formation intermediates was unsuccessful at this resolution so in the next experiments ROs would be observed in 3D and under cryogenic conditions but at higher resolution using cryo-ET*

Chapter 5. Cryo-correlative light and electron tomography to observe IBV replication organelles *in situ* under near-native conditions

5.1. Introduction

Positive-sense RNA virus replication organelles have been studied extensively by cryo-ET and STA (de Beijer *et al.,* 2024). Cryo-SXT was able to image the 3D RO ultrastructure in whole cells at a near native state, but RO membrane formation events were not resolved. Therefore, cryo-ET was used next to observe IBV ROs at higher resolution. Following the 2019 pandemic of SARS-CoV-2, all CoV RO cryo-ET and STA so far have been focused on *Betacoronavirus* DMVs and elucidating the minimal structure of the DMV pore (Klein *et al.*, 2020; Zimmerman *et al.*, 2023). Once more, it is important to note that while nsp3, nsp4 and nsp6 have been shown to be involved in DMV formation and that nsp3 and nsp4 are constituents of the pore (Ricciardi *et al.*, 2022; Huang *et al.*, 2024), these experiments were completed expressing these nsps from plasmids, so there will be more components involved when looking at these ROs during *in situ* virus infection (Chen *et al.*, 2024). Plus, although these factors in DMV formation are known, they may not be universal across the CoV family (Doyle *et al.*, 2018), and the mechanisms of the membrane rearrangements have not yet been observed. Furthermore, the DMSs, which are observed across the CoV family (Snijder *et al.*, 2020) but appear more abundant following *Gammacoronavirus* IBV infection (Maier *et al.*, 2013), are yet to be imaged under cryogenic conditions and their function is unknown. Consequently, using the

correlative workflow with BeauR-eGFP-nsp2 infected cells, sites of ROs, including DMVs, zER, and DMSs, were directly targeted for lamella preparation and cryo-ET. The -preserved structure of DMSs at high resolution became a focal question because it had not been observed previously. Simultaneously, RO formation intermediates for DMVs or DMSs could be observed to see whether membrane budding or wrapping events occur. Finally, interactions between DMVs, DMSs, and nascent virion formation could also be revealed.

STA of the DMV pore provided clues to its function in RNA translocation (Wolff *et al.*, 2020; Huang *et al.*, 2024). It has also been hypothesised that the DMSs have a function due to their uniformity, prevalence across the CoVs, and the energy that would be required to induce and retain curvature of a double membrane in different directions. The DMSs are also thought to contain material as the DMS interior is densely stained in room temperature EM samples (Maier *et al.*, 2013; Snijder *et al.*, 2020). Therefore, if high enough resolution STA reconstructions could be obtained for the DMSs, the model could be used to fit crystal or predicted protein structures into the densities, and their stoichiometry, location or binding partners in the DMSs could be identified. Consequently, the function of DMSs could be hypothesised. Identifying the composition of the DMSs would be dependent on the number of particles available to be used for the averaging and the maximum achievable resolution (Nyquist value). This resolution is limited by the image pixel size which is determined by the magnification and the physical pixel size of the camera used for tilt series collection.

Overall, using a correlative approach, the aims of these experiments were to:

1) Investigate the structure of DMSs under cryogenic conditions at high resolution for the first time for any CoV
2) Investigate the protein composition of DMSs to inform functional hypotheses
3) Image IBV DMVs to confirm the presence of pores in *Gammacoronavirus* DMVs
4) Image IBV ROs via cryo-ET to see whether any intermediate steps of RO formation (DMVs or DMSs) could be observed

5.2. Results

5.2.1. Cryo-preservation of infected cells on grids for electron microscopy

DF1 cells on 200 or 300 mesh grids were infected with BeauR-eGFP-nsp2, blotted for 8-10 s depending on cell confluency, and plunge frozen. The grids were loaded onto a Talos Arctica 200 kV system where atlases of the grids were collected (Figure 5.1 A-D). The confluency, thickness, and vitrification quality of the grids were assessed. Atlases that were too dark meant that grids were not be suitable for FIB milling because the topological surface of the cells showing their shape and orientation on the grid foil would not be visible at the milling angle. Furthermore, the cells could be too thick for efficiently milling lamellae using the gallium ion beam on the available cryo-FIB-SEMs. The more visible the shape of the vitrified cell was (the thinner the surface ice layer), the easier it was to accurately position the lamellae. This was particularly important when using beads for correlation as the beads were 1 µm in diameter and if they were under a layer of thick ice, they were not visible in the cryo-FIB-SEM and could not be used for 3D correlation. If the atlas was too light, the sample was too thin, so the cells were too flat (either unhealthy or over-blotted), and when milled, lamellae were too short and fragile with no

surface area for placing tomograms during cryo-ET. DF1 cells had good confluence on the grids and good electron transparency and 200 mesh grids gave greater areas for cell spreading without encountering grid bars (Figure 5.1 A-B). CK cells were also tested but they were difficult to seed and vitrify on grids.

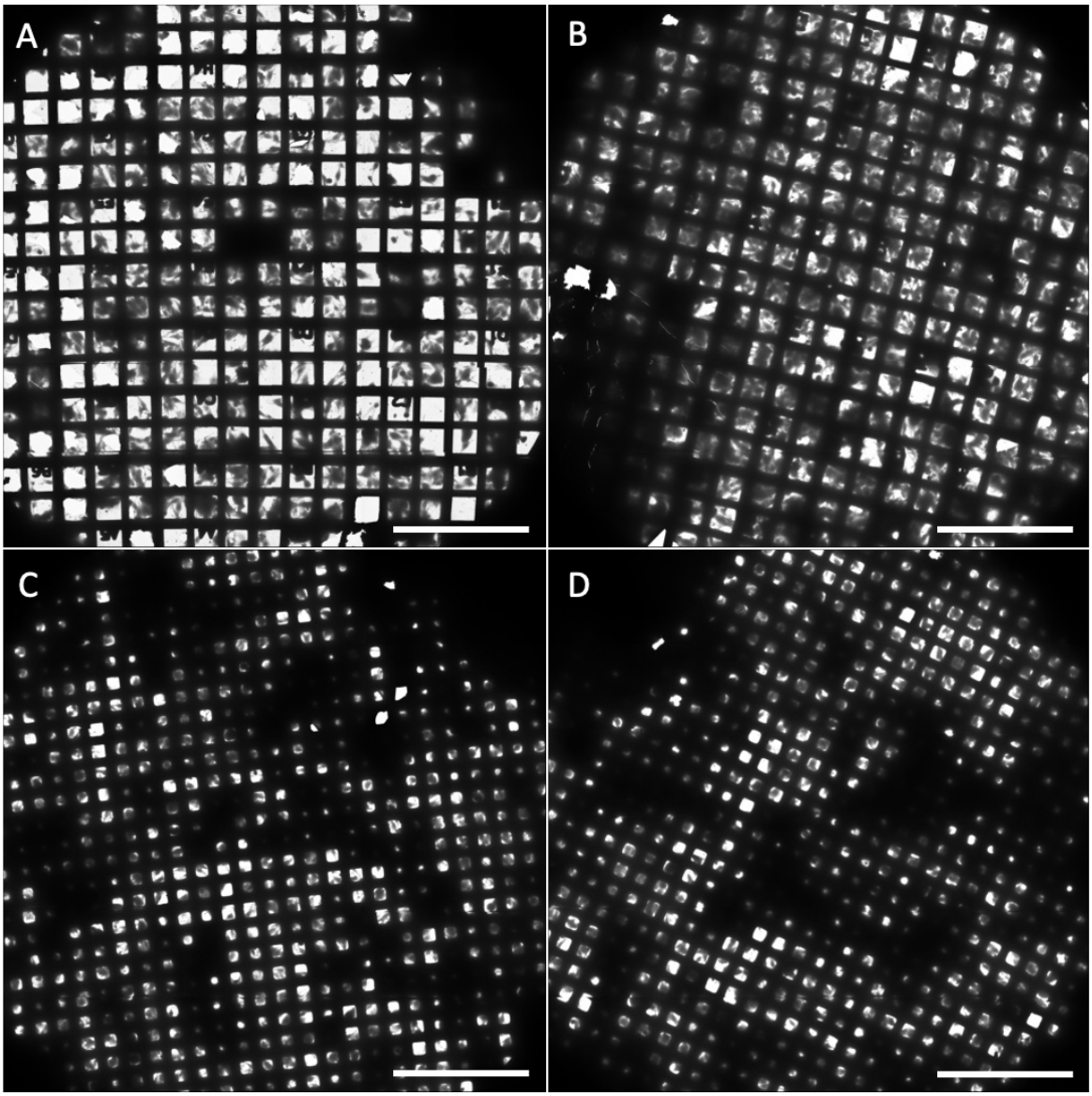


Figure 5. 1 Atlases of DF1 cells on grids.

The confluency of the cells on the grid in panel A was optimal, the atlas in panel B has some thin positions but the bottom left has visible ice cracks where the ice was too thick and cells would be inaccessible. The atlases of 300 mesh grids in panels C and D show some visible cells but more thick areas than the 200 mesh grids. Scale bars are 500 μm.

5.2.2. Cryo-fluorescence mapping of BeauR-eGFP-nsp2 infected DF1 cells

Once the seeding rate and vitrification parameters for grids were confirmed by the atlases, grids were screened for BeauR-eGFP-nsp2 infected cells using the Leica cryoCLEM. At each position the ice thickness was assessed by looking for surface contamination (Figure 5.2 A), cracks (Figure 5.2 B), and pooling of the ice in the corners (Figure 5.2 C-D). These were indications that the ice was too thick, and the position was disregarded. On grids with 1 μm Dynabeads, the image stacks were collected across a z-range including all beads in the field of view in the red and green channels (Figure 5.2 E). Image stacks of cells in millable positions were collected and their positions on a brightfield map of the grid were noted (Figure 5.2 F).

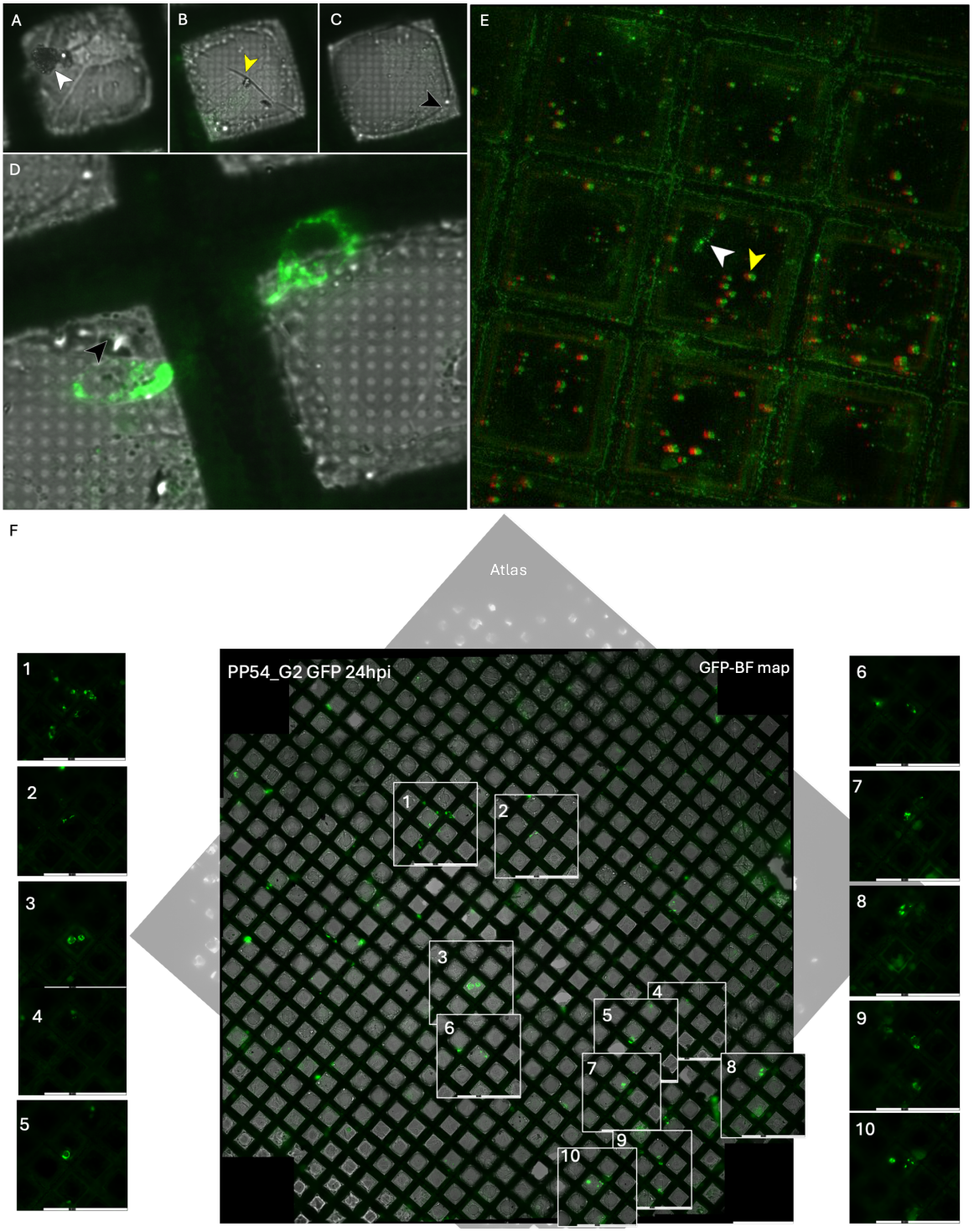


Figure 5. 2 Cryo-fluorescence screening grids for correlative cryo-FIB-SEM.

DF1 cells on grids were infected with BeauR-eGFP-nsp2 and plunge frozen in 10 % glycerol with or without 1 μm Dynabeads. The ice quality of fluorescent areas was assessed (panels A-D; white arrowhead, surface contamination; yellow arrowhead crack; black arrowhead, pooled ice), and fluorescent stacks of cells of interest (and their surrounding beads) were collected (panel E; white arrowhead, eGFP-nsp2; yellow arrowhead, Dynabead visible in red and green channels). The location of each cell of interest was noted on a brightfield map of the grid which could be overlaid with the atlas (panel F).

5.2.3. Fluorescence-guided cryo-focused ion beam (cryo-FIB) milling to generate lamella

Once fluorescent cells had been mapped, the grids were loaded into the Scios cryo-FIB-SEM. The first attempts at correlative milling were completed in two dimensions (X and Y) by overlaying the fluorescence and SEM images of the grid in PowerPoint or ImageJ (Figure 5.3 A-C). If landmarks could be identified in the FIB or SEM images, the *Landmark Correspondences* plugin in ImageJ could be used to correlate them with the fluorescence images (Saalfeld and Tomancák, 2008). Here, the SEM image of the grid square of interest was distorted (Figure 5.3 D) by matching the corners of the grid square in the SEM image to those in the fluorescence image of the same square. The fluorescent image and distorted SEM image were then merged (Figure 5.3 E). Next, this merged image was distorted to fit the FIB angle of the same square using features like surface ice particles visible in the SEM and FIB views. Finally, the distorted fluorescence channel alone was overlaid with the FIB angle view on which the lamella boxes were placed (Figure 5.3 F-G). Once milling had begun, to estimate the location of the fluorescent region of interest, the lamella in the SEM view could be correlated to the fluorescence image at each milling step and the lamella boxes could be adjusted. When the target was further away from the leading edge of the lamella, the boxes were moved up in the FIB image to move the target towards the centre of the lamella. When the target was closer to the leading edge of the lamella, the boxes were moved down in the FIB image to move the target towards the centre of the lamella.

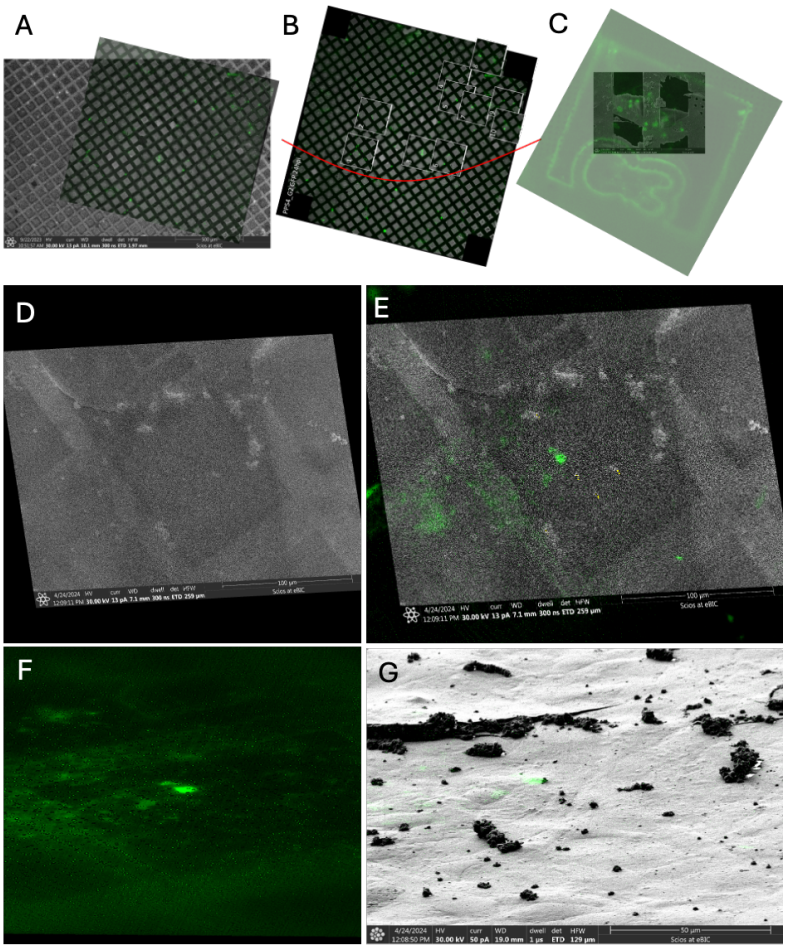


Figure 5. 3 2D correlation of fluorescence data to FIB-SEM.

Cryo-fluorescence and SEM images of the same grid were overlaid in PowerPoint or ImageJ (Panels A-C). Panels D-G show the use of the *Landmark Correspondences* tool in ImageJ to distort and overlay the fluorescence images and assist lamella positioning.

After subsequent tomogram collection, the ROs were observed in 41 % of the 2D correlated lamellae (n= 17). Therefore, the 2D correlation technique did not provide the accuracy in the Z-direction when positioning the milling boxes to retain the fluorescent RO in the lamellae. Consequently, 3D correlation was tested using beads. Here, fluorescent Z-stacks in red and green channels were taken in the region of cells of interest and their surrounding beads using the Leica cryoCLEM. The stacks were imported into the 3D Correlative Toolbox software (Arnold *et al.*, 2016) and resized to fit the scale of the FIB image (Figure 5.4). A flat fluorescence intensity maximum image was outputted next to

the FIB view of the cell of interest with beads visible in both images (as fluorescent puncta in the fluorescence image and as round uniform bumps in the FIB view) were clicked. Once at least three beads were identified manually in both images, beads could be clicked in the fluorescence image and the software would predict their locations in the FIB view in which they could be confirmed or repositioned. Finally, points were clicked on the fluorescence foci of interest and the prediction marked the sites in the FIB view (Figure 5.4). The resulting image was used to place the milling boxes in the FIB software. This approach improved RO detection following tomogram collection to 68 % of lamellae (n = 22).

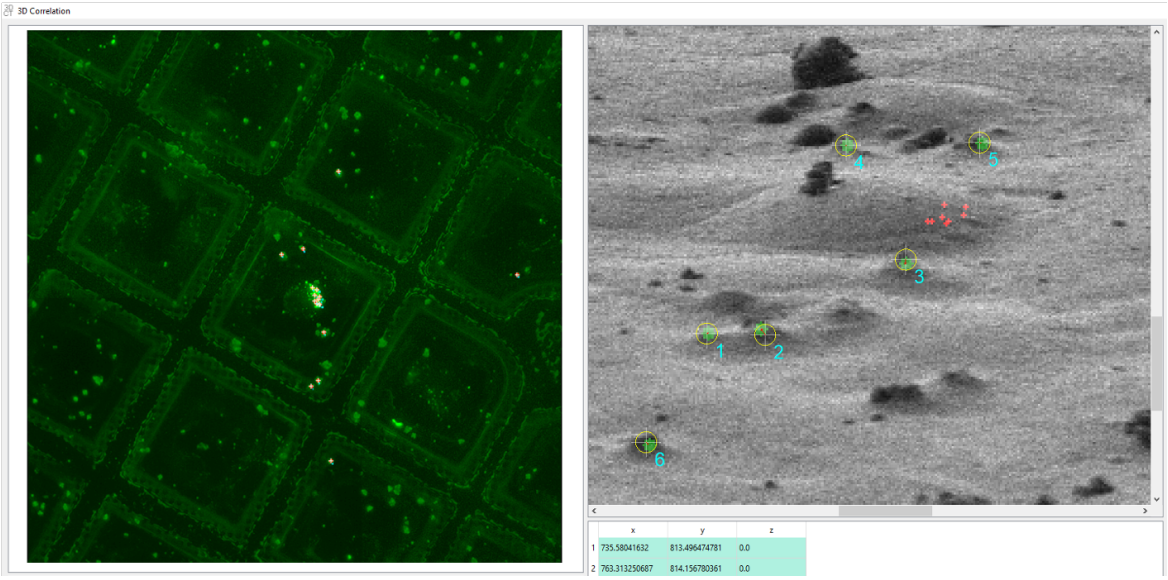


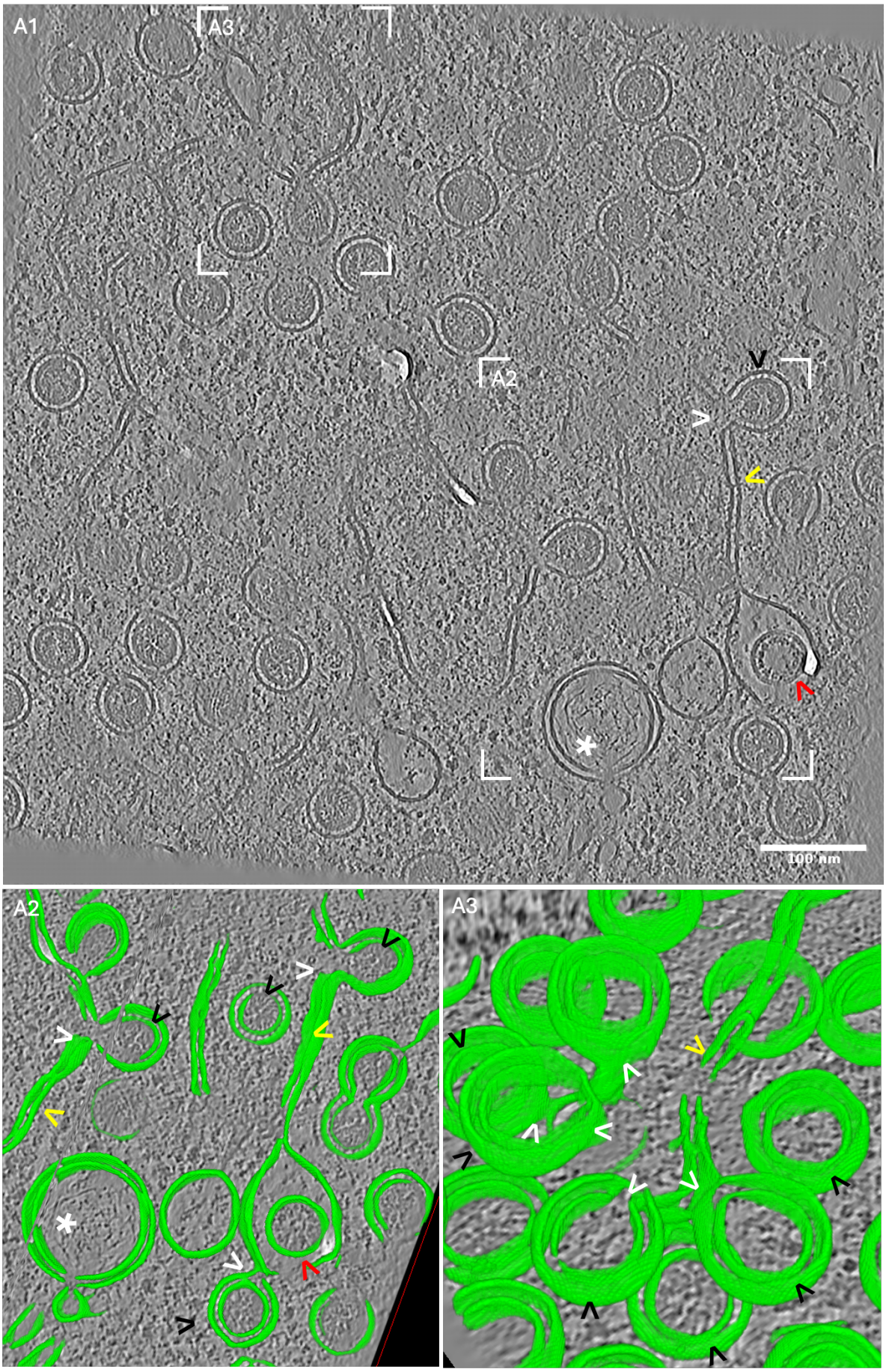
Figure 5. 4 3D correlation of fluorescence data to FIB-SEM.

Cryo-fluorescence Z-stacks of cells of interest and their surrounding beads were captured in red and green channels and the same cell was found in the FIB-SEM. The beads were correlated between the fluorescence and FIB views in the 3D Correlative Toolbox software (Arnold *et al.*, 2016). The correlated image was used to position the milling boxes in the FIB-SEM.

5.2.4. Cryo-electron tomography of BeauR-eGFP-nsp2 fluorescence-guided lamella

5.2.4.1. Cryo-electron tomography of the IBV RO

After milling lamella in a correlative manner, grids were loaded into a Krios for cryo-ET. Points were placed over the surface of the lamella in as many positions as possible without overlap, and tilt series were collected. The automated pipeline available at eBIC was used to align and reconstruct the tilt-series into initial 3D volumes to monitor data quality during collection. This allowed us to identify tomograms with the IBV RO clearly discernible and reprocess them such that we could clearly observe DMSs, zER, DMVs, and virus particles (Figure 5.5, Supplementary movie 5-6). This was the first time that DMSs and zER have been imaged under cryogenic conditions for any CoV. Sections of zippered ER ran into DMS necks that curved into DMS heads (Figure 5.5. A-B). The DMSs were uniform in size, always appeared full of material within their interiors, and were always tethered to zER. Some longer regions of zER appeared without DMSs while large 3D bunches of several DMSs tethered to zER were also observed (Figure 5.5 B2). These observations were all consistent with those from cryo-SXT and room temperature EM of IBV ROs (Maier *et al.*, 2013). Significantly, a striation pattern spanning the zER and DMS double membranes was observed which has not been reported previously (Figure 5.5 A1, B1). Both individual DMVs and clusters of DMVs were also observed in proximity with DMSs (Figure 5.5 A, C). Furthermore, single membrane vesicles were observed containing both single and multiple virions and, interestingly, some were found to share membranes with zER and DMSs (Figure 5.5 A1, A2, B1, C2), which has not been previously described.


A1
A3
A2
100 nm
A2
A3

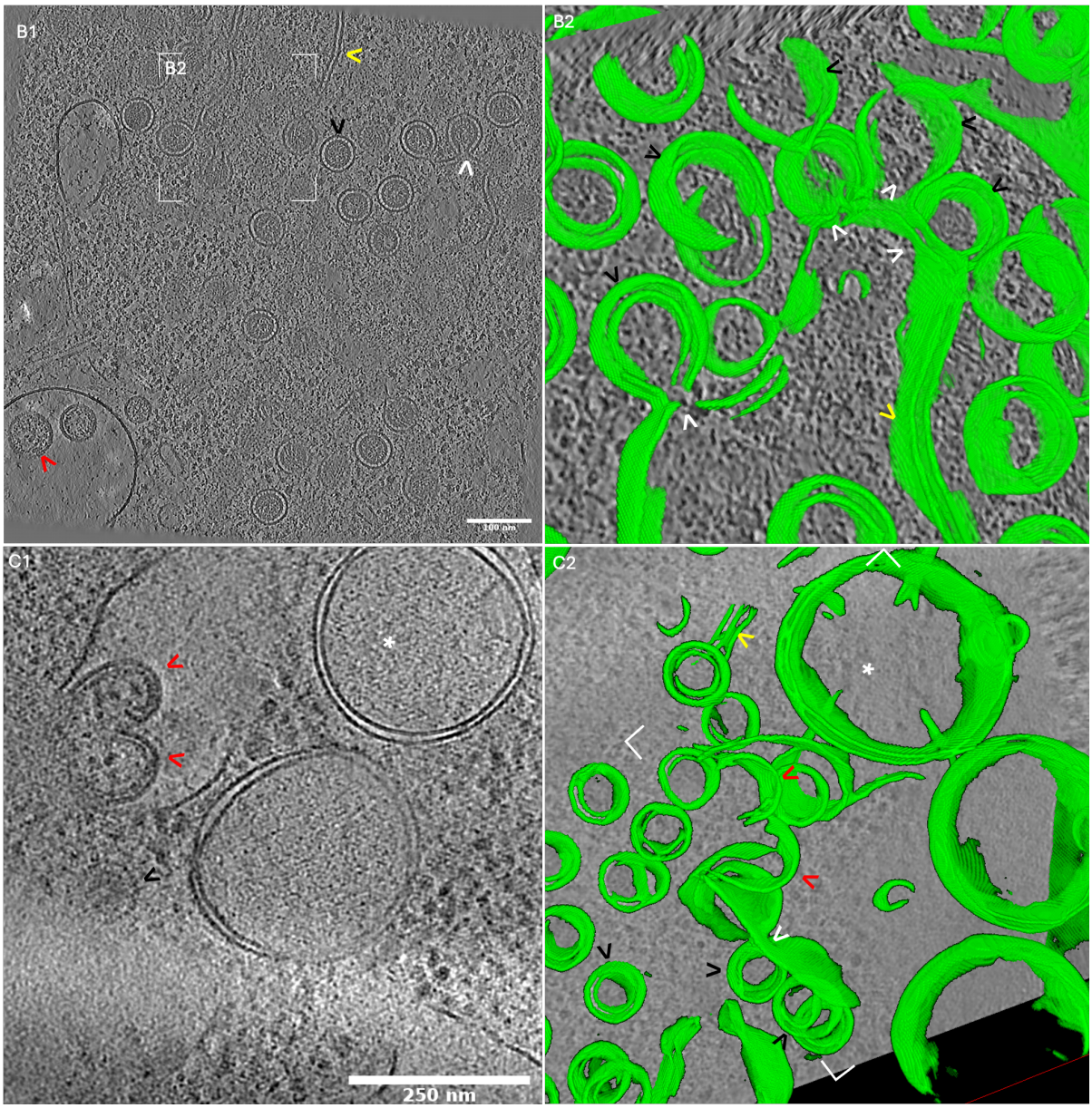


Figure 5. 5 Cryo-ET overview of the IBV RO.

DF1 cells were infected with BeauR-eGFP-nsp2 and plunge frozen at 24 h pi before correlative FIB milling to generate lamella for tomography. Sections of zippered ER (yellow arrowheads) curved into DMS necks (white arrowheads) that rounded into DMS heads with uniform diameters and material within their interior (black arrowheads). Single membrane vesicles were conserved containing virions (red arrowheads) which shared membranes with zER and DMSs. DMVs (asterisks) were observed in proximity with DMSs and virions. Panel A1 is a single slice through a tomogram with two segmented regions shown by boxes A2 and A3. Panel B1 and B2 are two slices through the same tomogram with a segmented region in box B3. Panel C1 is an area of a tomogram segmented in panel C2 with a box marking the same area. Tomograms were reconstructed using AreTomo and denoised using Isonet. Segmentations were completed with MemBrain-seg.

Any connections between DMVs and DMSs were investigated in 3D via membrane segmentation (Supplementary movie 7-8). One example of a balloon-shaped single membrane continuous with the DMV outer membrane was also continuous with a membrane that might be paired with another membrane (Figure 5.6 A-B, white arrowhead). However, it was not clear whether the paired membranes of DMVs were continuous with zER that make the DMSs. In another example the DMV double membrane might be continuous with a zippered double membrane that contained a DMS (Figure 5.6 C-D). Therefore, although DMVs appeared connected to paired ER connectors, only in one tomogram could contacts between DMVs and zER with DMSs be described. In most cases, although in proximity, the DMVs and DMSs appeared to be derived from separate membranes, as is consistent with the cryo-SXT.

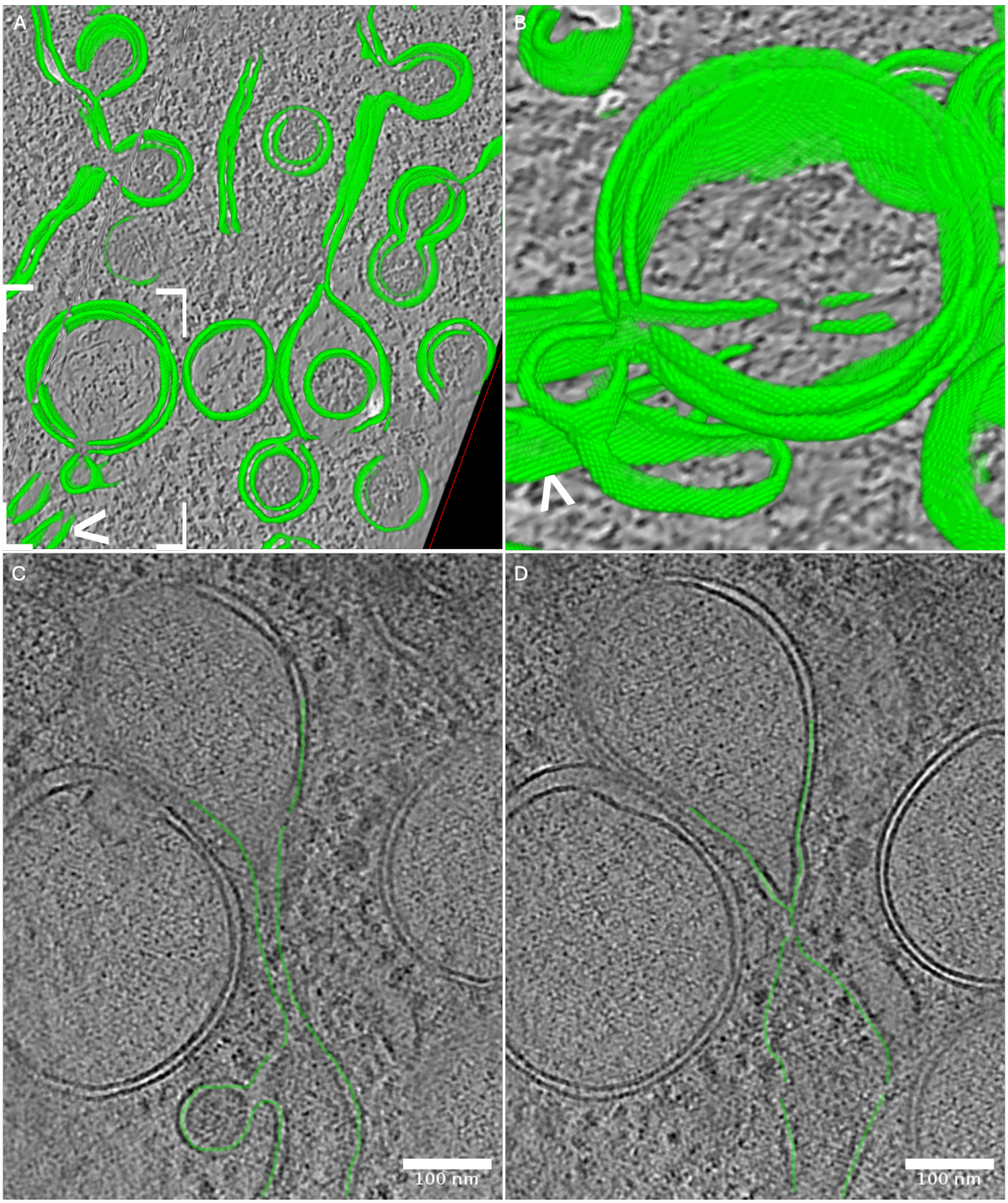


Figure 5. 6 Potential RO membrane connections.

In panels A and B the white arrowheads mark a region of paired membrane, that is not zER, which is continuous with a single membrane vesicle continuous with the DMV outer membrane. In panels C and D the double membrane is marked with a green line and may show a continuous double membrane sheet being used for the DMVs and the DMSs. The double membrane sheet does not appear zippered in the DMV but does appear zippered at the DMS. Tomograms were reconstructed using AreTomo and denoised using Isonet. Segmentations were completed with MemBrain-seg.

5.2.4.2. Cryo-ET of zER and DMSs

The novel observation of the striation pattern between the double membranes of zER and DMSs was examined in greater detail (Figure 5.7 A-C). Each stripe spanned the double membrane and were termed ‘spokes’ in the double membrane of the DMS heads. Analysis revealed that the DMSs were always connected to zER and the widths of zER and DMS double membrane were equal. The average width of the full zippered double membrane in zER and DMSs was 172 Å (± 16.5) (n= 21 Å) and the width of the double membrane lumen was ~80 Å. The average DMS diameter was 85 nm (± 3.1 nm) (n= 64), and the diameter of the inner shell of material was 60.8 nm (± 3.4 nm) (n= 48). Some regions of zER were also straight and over 700 nm long, however, they may also curve into DMSs in different positions in the volume (Figure 5.7 C). In other areas the zER also branched into convoluted membranes (Figure 5.7 D1-3).

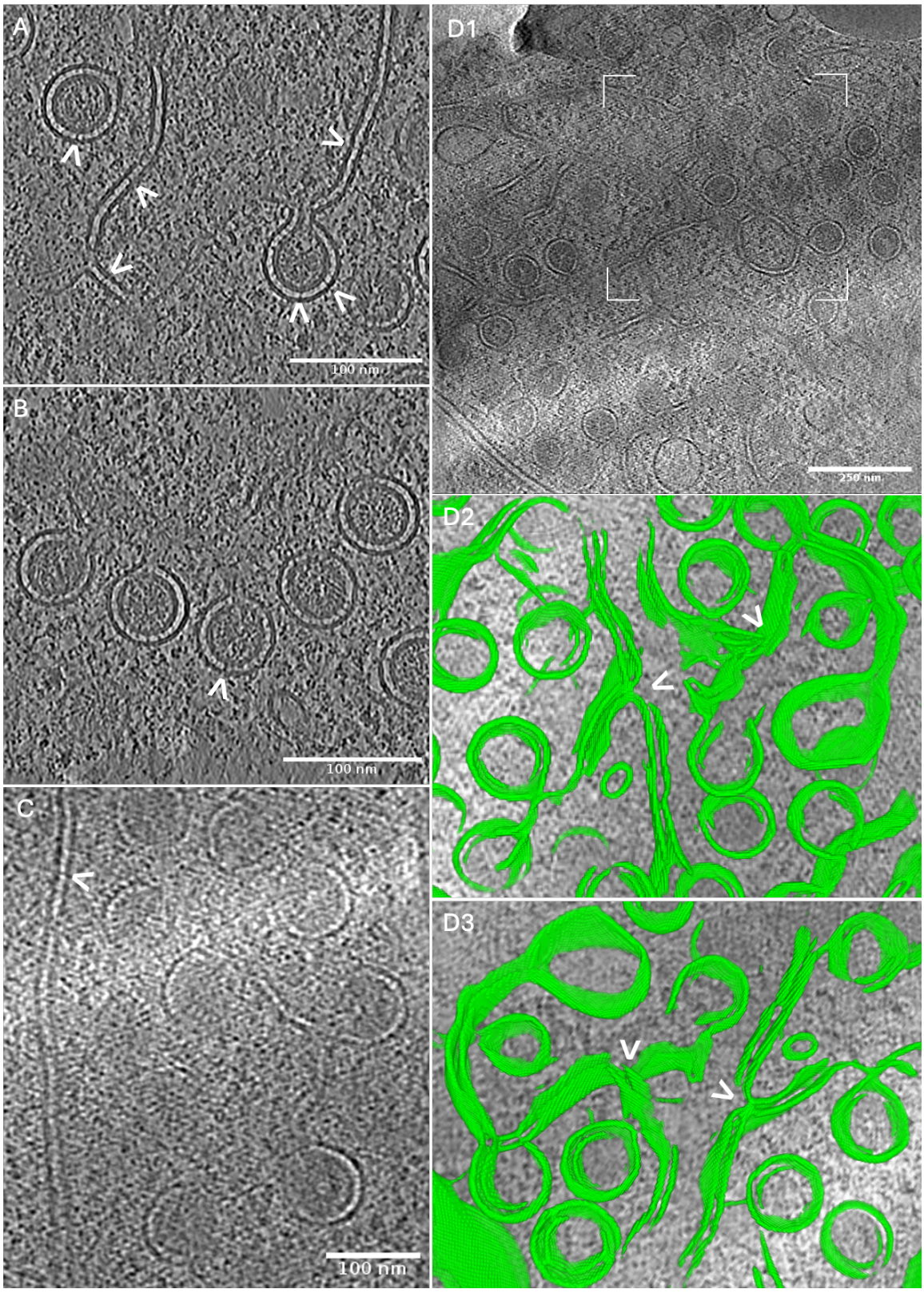


Figure 5. 7 DMS and zER double membranes contain striation patterns and some zER branches.

Tomographic top views of DMS and zER membranes were striated, each stripe spanned the double membrane and together were termed 'spokes' around the DMS heads (panels A-C; white arrowheads). The DMSs were always connected to zER and always contained material but sections of straight zER and branched zER were also observed (tomogram D1, segmentation views D2-D3; white arrowheads). Segmentations were completed with MemBrain-seg.

Interestingly, consistent with earlier observations, the DMS heads appeared to pinch along the zER but did not bud off. The DMSs seem to remain connected to the networks of modified ER and all DMS for which the complete head was visualised contained a neck. Those frames where DMS heads appear alone in the cytoplasm, not bound to zER, are likely bound to zER in a different plane or are bound within the volume that was removed during milling. An example of this is shown in Figure 5.8 A-B.

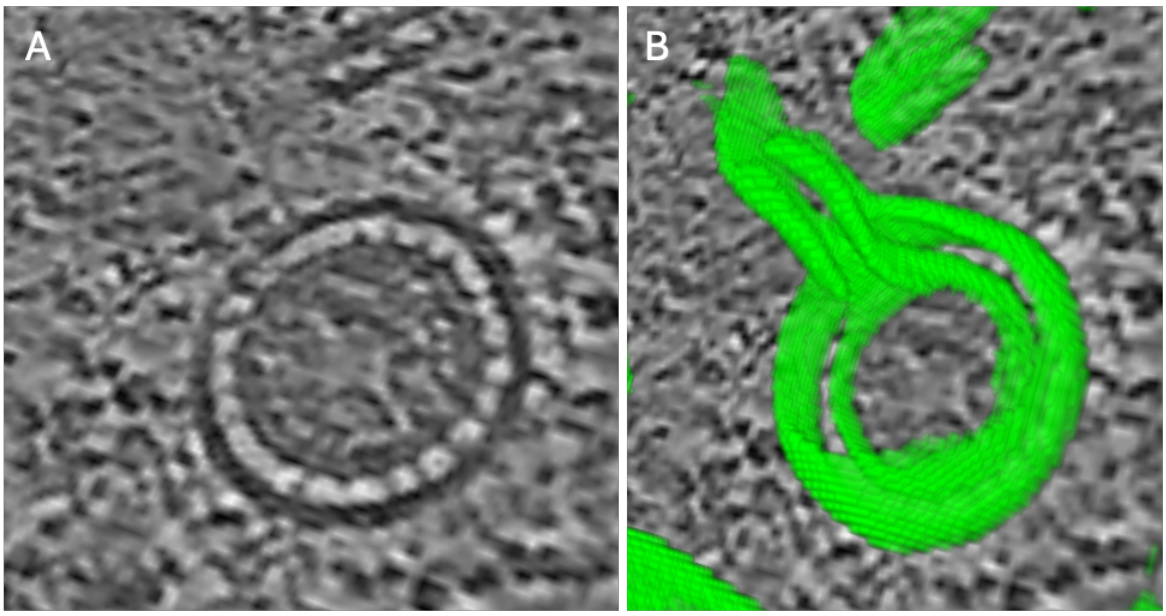


Figure 5. 8 All DMSs are tethered to zER.

Although some DMS appeared as individual structures in the cytoplasm, the segmentations revealed that they were always tethered, at least by their outer membranes sometimes to the regular ER or further zER and DMSs.

5.2.4.3. The DMS 'spokes'

Looking in more detail at the DMSs, the 'spokes' spanning the DMS double membrane appeared to extend into the DMS interior (Figure 5.9 A-F). These extensions appeared continuous with the spokes going through the inner membrane and making a second layer of lines under the inner membrane at an angle to the spokes. Interestingly, these extended densities were not observed either side of the spokes in the zER.

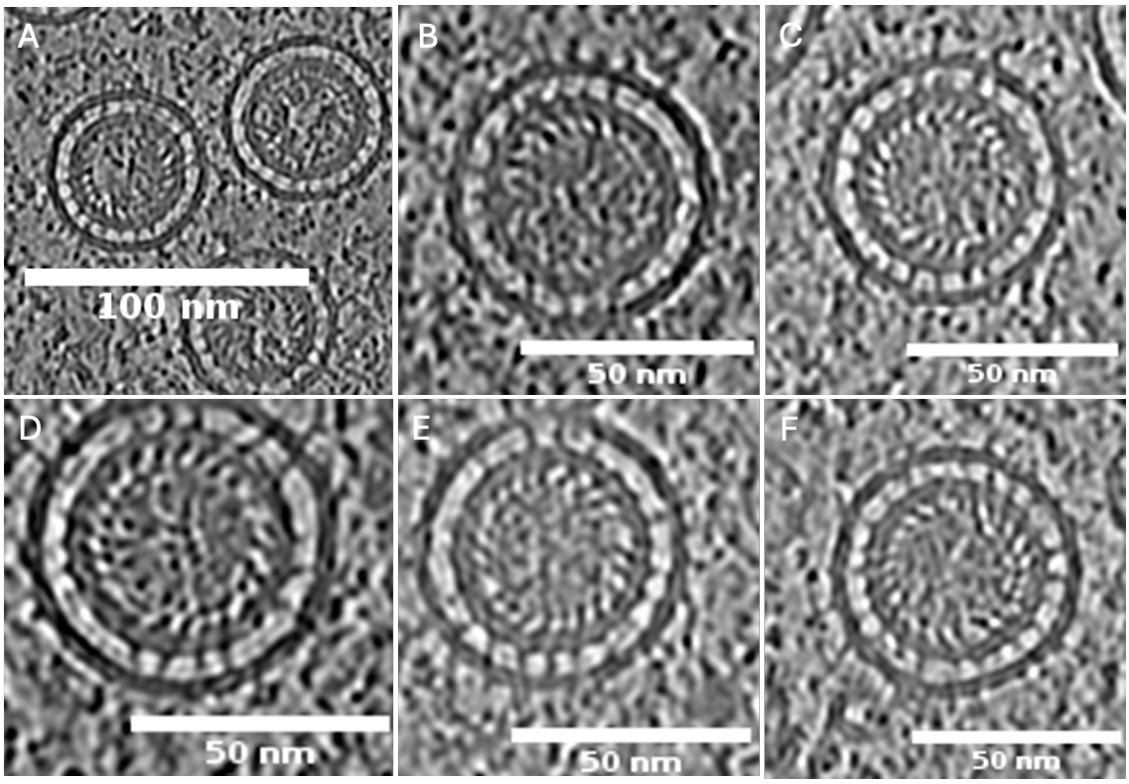


Figure 5. 9 The DMS 'spokes' extend into the DMS interior.

Top views of DMS showed that the 'spokes' which span the double membrane also extend into the interior of the DMS creating a second layer of diagonal stripes within the DMS inner membrane. The DMSs always contained further electron dense material under this second layer filling up the interior.

The axial views of the 'spokes' in the lumen between the outer and inner membranes were observed (Figure 5.10 A-B, Supplementary movie 9). The spokes at the top of the DMS heads appeared equally spaced apart and were arranged in an ordered square grid (Figure 5.10 B-D). The average distance between adjacent spokes was 6 nm (n= 52) and the spokes were not resolved around the full surface area of the DMS double membrane but the average number of visible spokes per DMS head was 68.7 (n= 10) and covered ~ $1/6^{th}$ of the surface area of the full spherular double membrane. The spokes did extend through the inner membrane and into the DMS interior, but they did not appear to stick out of the outer membrane (Figure 5.10 E). Although there were some additional densities on the outer surface of the DMSs, they did not appear continuous with the spokes. Some of the 'tops' and 'bottoms' of DMSs were not resolved primarily because of the missing wedge (Figure 5.10 F). Assuming that the spokes were equally spaced around the whole DMS head then it could be estimated that approximately 400 spokes exist in each DMS (with ~68 spokes counted in $1/6^{th}$ of the DMS surface area).

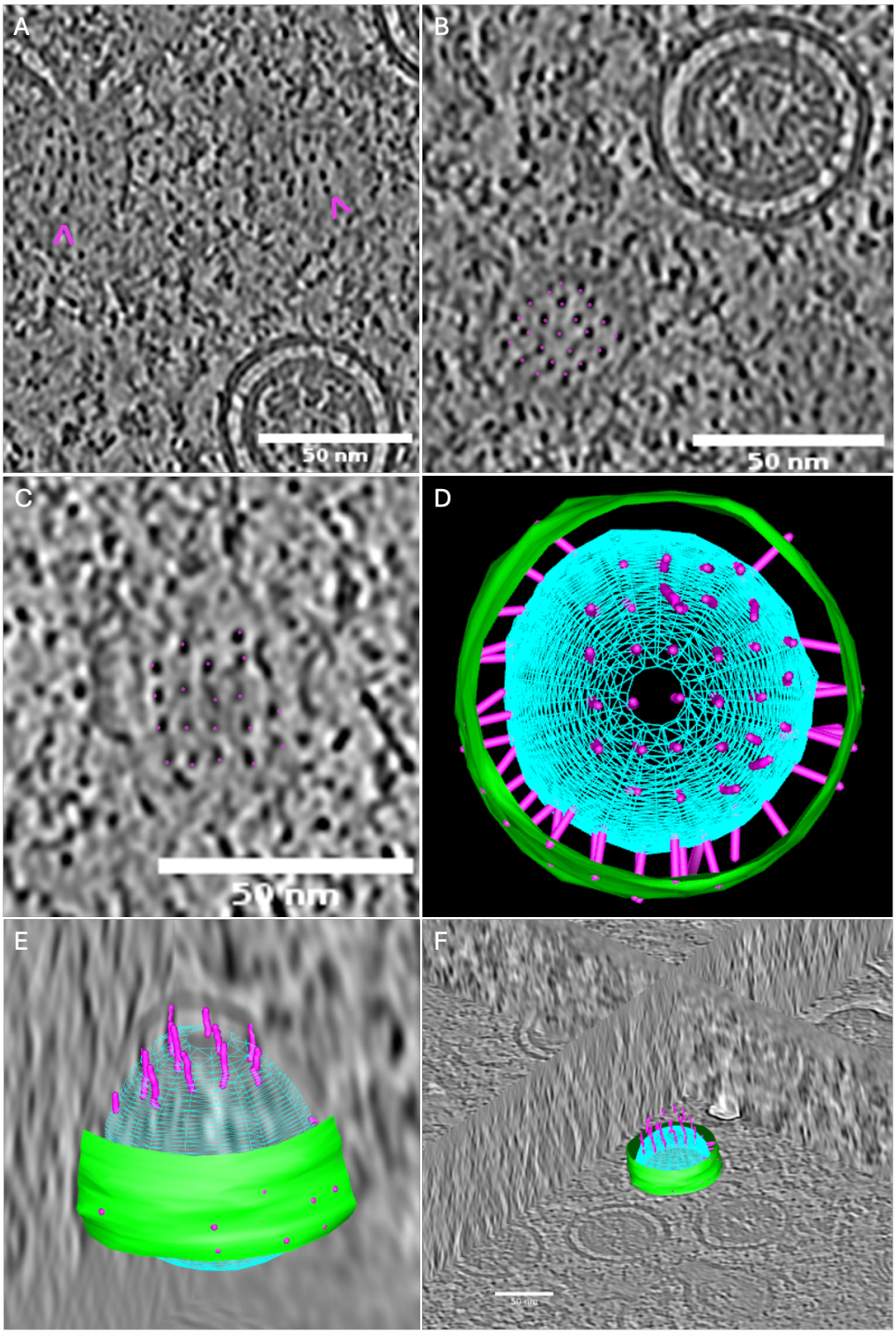


Figure 5. 10 Ordered arrangement of the DMS 'spokes'.

Axial views of the DMS 'spokes' could be observed through the DMS double membrane either at tilted views of the DMS heads (panel A; magenta arrowheads) or at the top of the DMS heads (panel B-C; magenta dots). The segmentation of a DMS head is shown in panels D-F with the outer membrane in green, the inner membrane in cyan with predicted spherical shape shown via the mesh, and the spokes in magenta making a square grid pattern. In the context of the tomogram, the DMS double membrane and spokes were not resolved around the full spherular surface area of the DMS (panel E) and some of the 'tops' and 'bottoms of the DMS were cut off due to the missing wedge (panel F). Segmentations were completed with Imod.

5.2.4.4. The DMS necks

All DMSs observed were found to be tethered to the zER via a neck region. Looking at edge-views of the DMSs with visible necks, the average neck width was 21 nm (± 3.5 nm) (n= 61) (Figure 5.11 A, DMS on the right side of the panel; Figure 5.11 B, DMS in the top left of the panel). However, seven examples of DMSs with thinner necks were imaged where the DMS inner membrane appeared to seal (Figure 5.11 A, left side of the panel) and three examples of DMSs with wider necks were imaged (Figure 5.11 B, centre of the panel) which may be DMS formation intermediates. Moreover, the structure of the membranes at the DMS necks were difficult to resolve so no spokes or crown complex could be described (Figure 5.11 C). Two examples of DMSs with a sealed inner membrane and a 'long' neck at which the outer membrane appeared to be paired to itself were also observed (Figure 5.11 D-F). It was thought that the DMSs with apparently sealed inner membranes could truly be open elsewhere in the volume. However, in the examples of the long neck DMSs with sealed inner membranes, it does not appear that there would be space for a neck of inner membrane between the paired outer membrane. Therefore, ~90 % (n= 68) of the visible necks were open and ~10 % of the DMSs may be sealed or the necks could remain open elsewhere in the volume. Looking at the 'long necks' at this resolution, there were no obvious structures holding the membranes together (Figure 5.11 F).

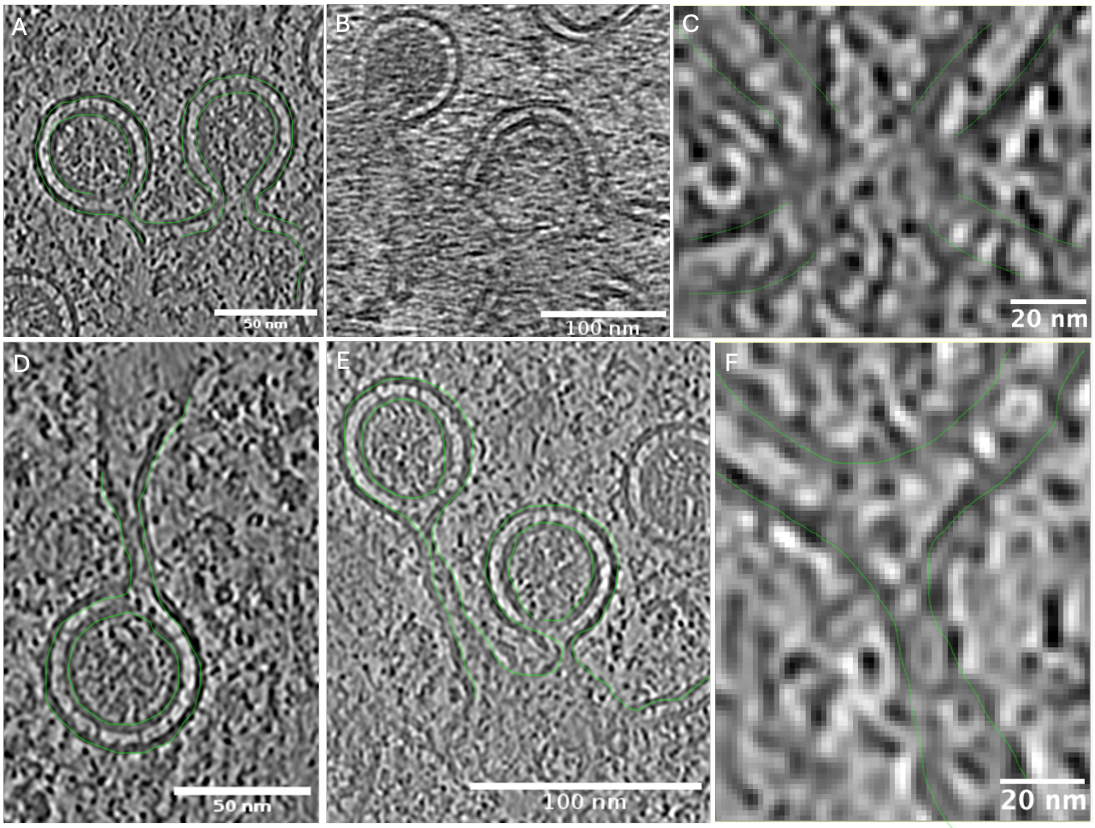


Figure 5. 11 The DMS necks vary in width and length.

Different DMS neck morphologies were observed with the two sides of the neck closer or further apart perhaps dependent on whether there were contents lining the inner membrane (panels A-B). The existence of a specific structure at these regions was not observed (panels C and F). Some of the necks appeared longer than others and the outer membrane became tightly apposed at the base of the DMS (panels D-F).

5.2.4.5. Contents of the DMS and formation intermediates

Following examination of DMSs with wide necks in more detail, potential intermediates in DMS formation were observed (Figure 5.12 A). DMSs were observed with wider or more 'open' necks and their striated membranes were bound by material following the curve of the membranes (Figure 5.12 A-B). Therefore, the straight zER contained the spokes but lacked the angled second layer. Then, when the angled second line appeared, the membrane started to curve. There was also electron-dense cargo bound to the second layer which filled the interior of the curving membrane. Therefore, the components of

the DMSs could be described in three layers from the ‘spokes’ between the two membranes, the ‘second layer’ on the interior of the inner membrane, and the ‘cargo’ bound to the ‘second layer’ in the interior (Figure 5.12 C). The ‘second layer’ appeared at an angle to the ‘spokes’ and the outer bilayer appeared smooth while the inner bilayer appeared ruffled (Figure 5.12 C). These images may support a hypothesis in which the DMSs form via wrapping of zER around ordered cargo that produces a spherule of specific size and interacts with the spokes on what becomes the inner DMS membrane.

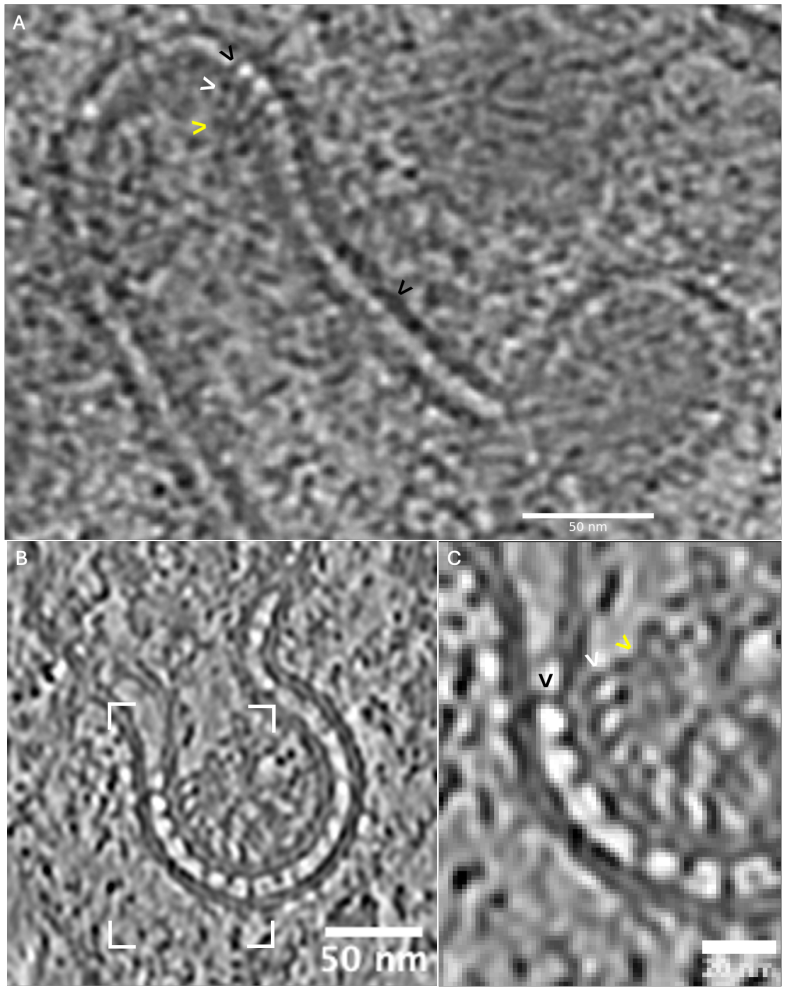


Figure 5. 12 Zippered ER is wrapped around layers of material to form the DMS.

Panel A shows a region of zER wrapping around extra electron-dense material on the inner side of the concaving double membrane to form a DMS. Panel B shows the DMS with an empty open neck and material bound to the inner membrane and filling the contents of the DMS. Panel C shows the three layers of the DMS: the ‘spokes’ (black arrowhead), the ruffled inner membrane, the ‘second layer’ (white arrowhead), and the ‘cargo’ (yellow arrowhead).

The contents appeared to pack around the interior of the inner membrane of the DMSs and in some views an empty spherical space was seen in the centre of the heads (Figure 5.13 A-C). This suggests that the cargo forms a spherical shell.

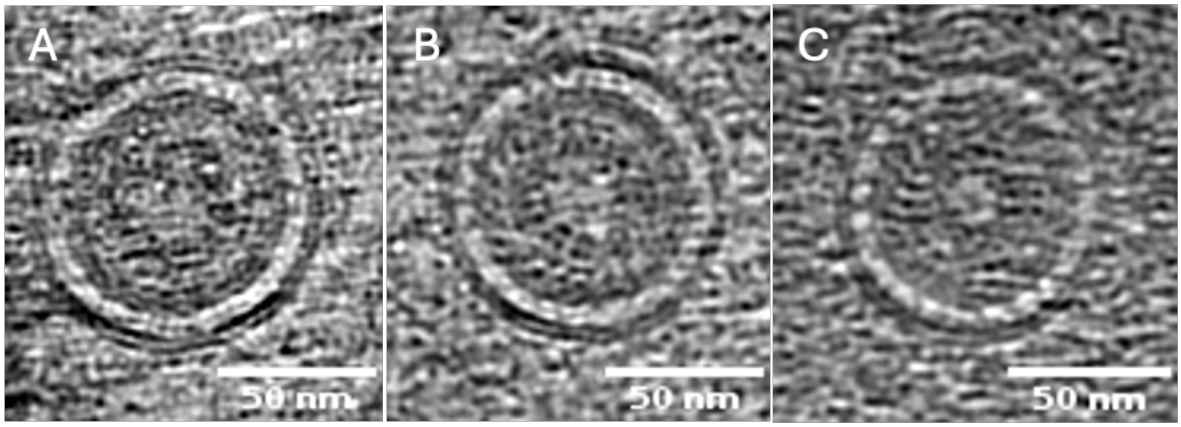


Figure 5. 13 Contents surround the inner membrane of the DMS head.

Through central slices of DMS heads, the contents appeared to pack around the inner spherical membrane surface which did not reach into the centre of the DMSs but left a spherical space in the DMS interior.

5.2.4.6. Stacked membranes were observed in IBV nsp4-GFP transfected cells

To investigate which nsps could be responsible for the DMS spokes, DF1 cells were transfected with plasmids expressing IBV nsp4 fused to GFP. IBV nsp4 was chosen because it is the only IBV TM nsp that was shown to be sufficient to induce membrane rearrangements alone, in the form of paired membranes (Doyle *et al.*, 2018). This observation is specific to IBV nsp4 because nsp4 from other CoVs does not zipper membranes on their own (Angelini *et al.*, 2013). Lamellae were milled in a correlative manner and used for cryo-ET. Overexpression of nsp4 was found to stack and zipper membranes in four tomograms but was not sufficient to form any RO structures; this is consistent with earlier data (Doyle *et al.*, 2018). Interestingly, nsp4-GFP did not appear to

form paired membranes with the same striation pattern seen in zER and DMSs of IBV infected cells. This suggests that additional proteins are involved in spoke formation and membrane curvature. The same rounded and stacked membranes were also observed in IBV infected cells so they could be formed from excess nsp4 or other viral factors (Figure 5.14).

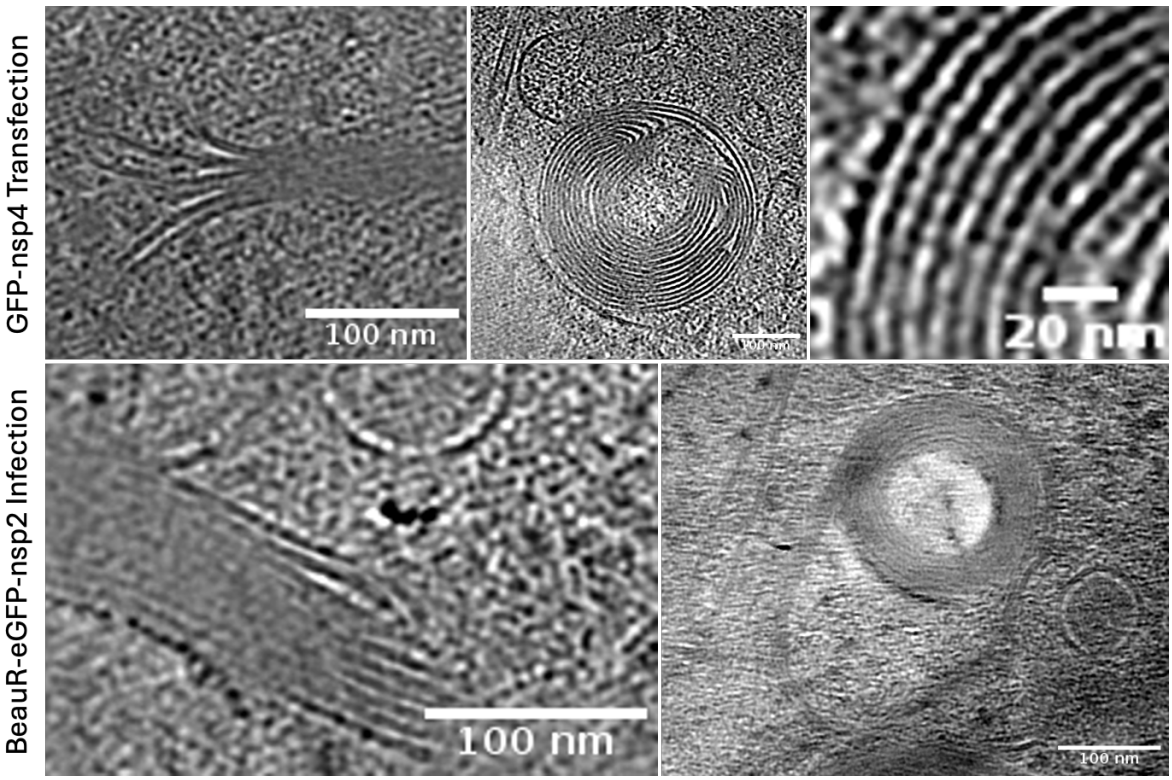


Figure 5. 14 IBV GFP-nsp4 transfection-induced membrane stacking.

Extensively stacked membranes were observed in cells transfected with GFP-NSP4 but striation patterns holding the membranes together were not visible. The membrane stacking events were also seen in infected cells.

5.2.4.7. Cryo-ET of the IBV DMV

Alongside observations of DMSs, the IBV DMVs were also observed under cryogenic conditions for the first time. The DMVs appeared in clusters in the cytoplasm with average diameters of 265 nm (± 36.3 nm) (n= 53) (Figure 5.15 A-K) as is consistent with the cryo-SXT measurements. Despite imaging cells late in infection at 24 h pi, the clustered DMVs did not appear connected via their outer membrane in vesicle packets like those observed in *Betacoronavirus* infected cells and this is consistent with previous work (Maier *et al.*, 2013). However, some connections to the ER were observed (Figure 5.15 B, C and K). The ER appeared continuous with the DMV outer membrane while the inner membrane was a complete sphere. Strand-like patterns were observed in the DMV interior and for the first time for a *Gammacoronavirus*, pores were observed spanning the double membrane (Figure 5.15 E-F). The pores appeared to be randomly and sparsely spread around the double membrane with just 1-3 pores imaged within the DMVs in the lamellae. The DMVs were observed interspersed with DMSs and, unlike the DMSs, the DMVs did not contain spokes spanning their double membrane. DMVs were also observed near virions (Figure 5.15 K).

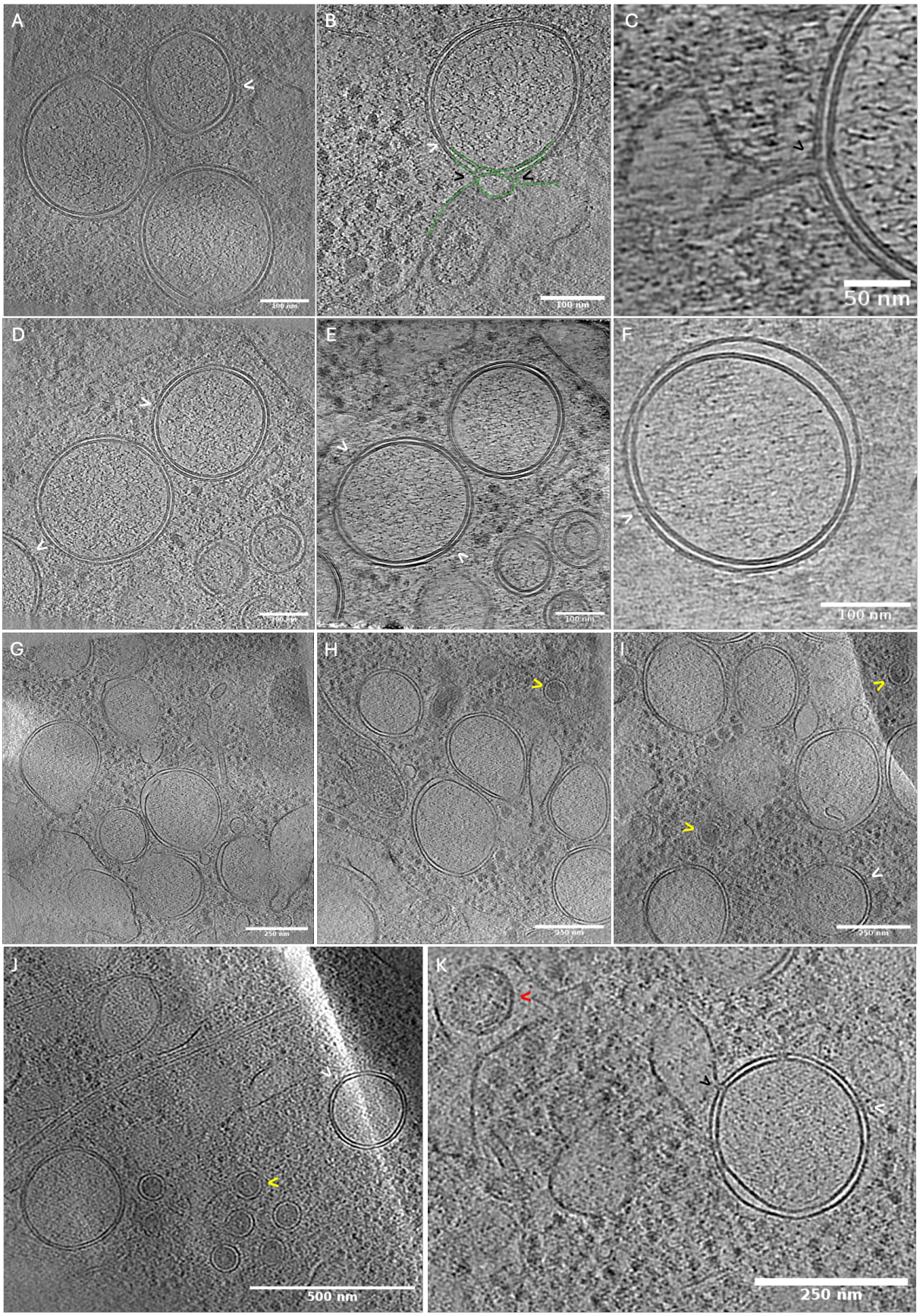


Figure 5. 15 Cryo-ET of the IBV DMV.

Several examples of IBV DMVs were observed clustering in the cytoplasm (panels A, G) with some having connections to the ER (panel B, C and K, black arrowheads and green segmentation). The DMVs contained RNA and double membrane spanning pores (white arrowheads). The DMVs were also interspersed with DMSs (yellow arrowheads; panels H-J) and in proximity with virions (red arrowhead, panel K). Panels A-F were collected at 81000x magnification while the others were collected at 42000x magnification.

Looking at the DMV pores in more detail showed that they had cytosolic crowns (Figure 5.16 A-D). Plus, the DMV pores had associated luminal and cytoplasmic densities which could be N, RNA, or other components of the RTC (Figure 5.16 A, E-H). The pores had a width of ~ 20 nm within the membrane and the cytosolic prongs extended about 10 nm from the DMV outer membrane. In some views, pinching of the double membrane into the pore was observed (Figure 5.16 E and G). Only edge views of the pores were captured.

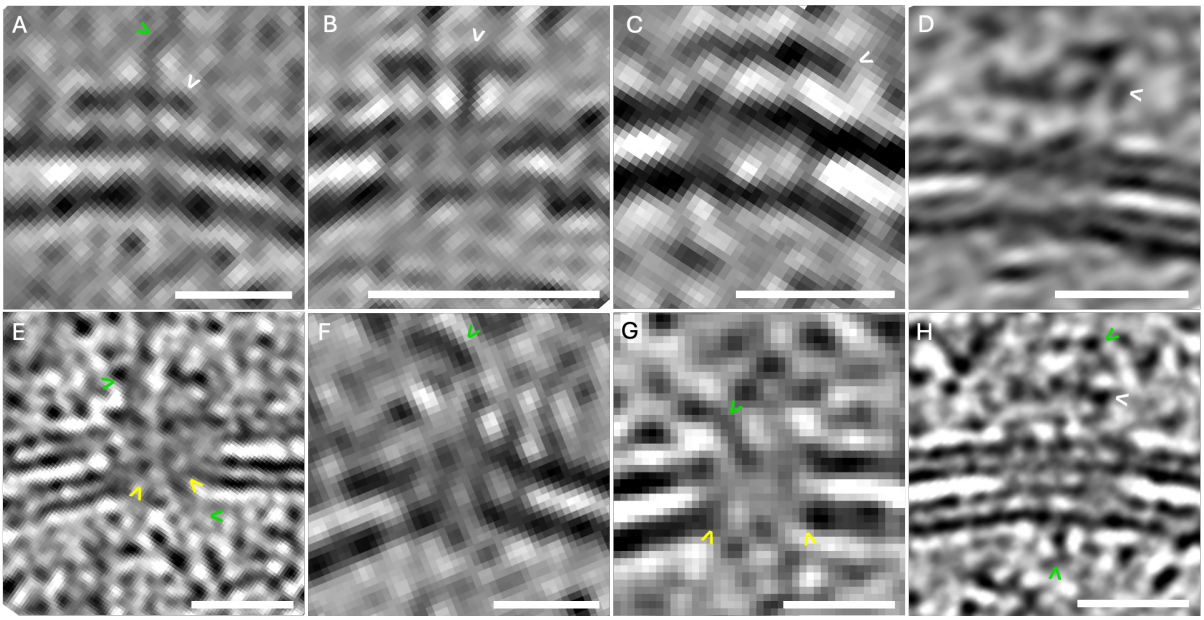


Figure 5. 16 Side views of the IBV DMV pore.

Several examples of the IBV DMV pore were observed. The cytosolic prongs are labelled with white arrowheads, associated luminal and cytosolic densities are labelled with green arrowheads, and double membrane pinching into the pores is labelled with yellow arrowheads. Scale bars are 20 nm.

5.2.4.8. Potential DMV precursors

A few examples (13) of small DMVs with diameters ranging from 90-166 nm were also observed here, which have not been reported for other CoV (Figure 5.17 A-F). These smaller DMVs had less uniformly spaced membranes than the larger DMVs but the same number of pores (between 1 and 3) so, since they were on a smaller vesicle, they appeared to be more closely spaced together than the pores on the large DMVs (Figure 5.17 B, E and F). Importantly, they had no spokes or dense content lining the inner membrane (like DMSs) but in some examples, densities spanning the membrane were observed but they could not be distinguished from the pores (Figure 5.17 F). Also, the small DMVs did appear to contain some tightly packed content in their centres that was different to the overlapping strands observed in the larger DMVs, and different to the organised cargo seen in DMSs. One example of a small DMV also appeared with a single membrane connector (Figure 5.17 B).

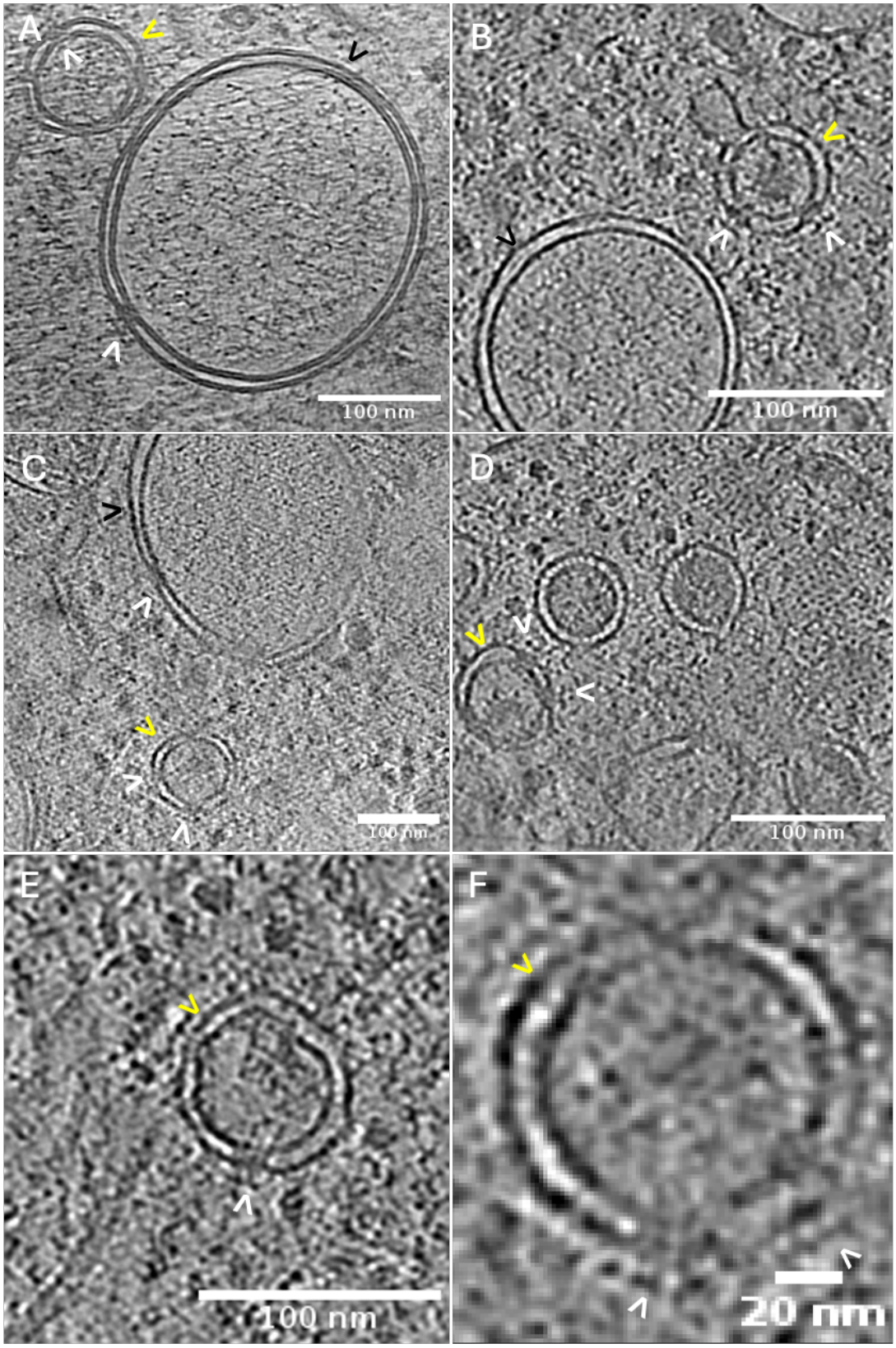


Figure 5. 17 Small DMVs with closely spaced pores.

Small DMVs (yellow arrowheads) were observed in proximity to larger 'regular' DMVs (black arrowheads) in panels A-C. The separation of the two bilayers was more uneven in the small DMVs. Pores were labelled with white arrowheads and appear close together in the small DMVs.

5.2.4.9. DMVs with associated single membrane vesicles and invaginations

A single example of a DMV with evaginated double membrane was observed and about 10 % of all DMVs were observed with round balloon-shaped single membrane vesicles attached at points around their surfaces (Figure 5.18 A-F). The single membrane vesicles were not attached where the pores were, and they did not appear like the connections of the DMV to the ER due to their round shape. Most ER-DMV connectors have been observed as straight paired ER contacting the DMV outer membrane like in Figure 5.15 C, however, the balloon shaped vesicle attached to the DMV in Figure 5.18 C was shown to be continuous with ER (Figure 5.6 B).

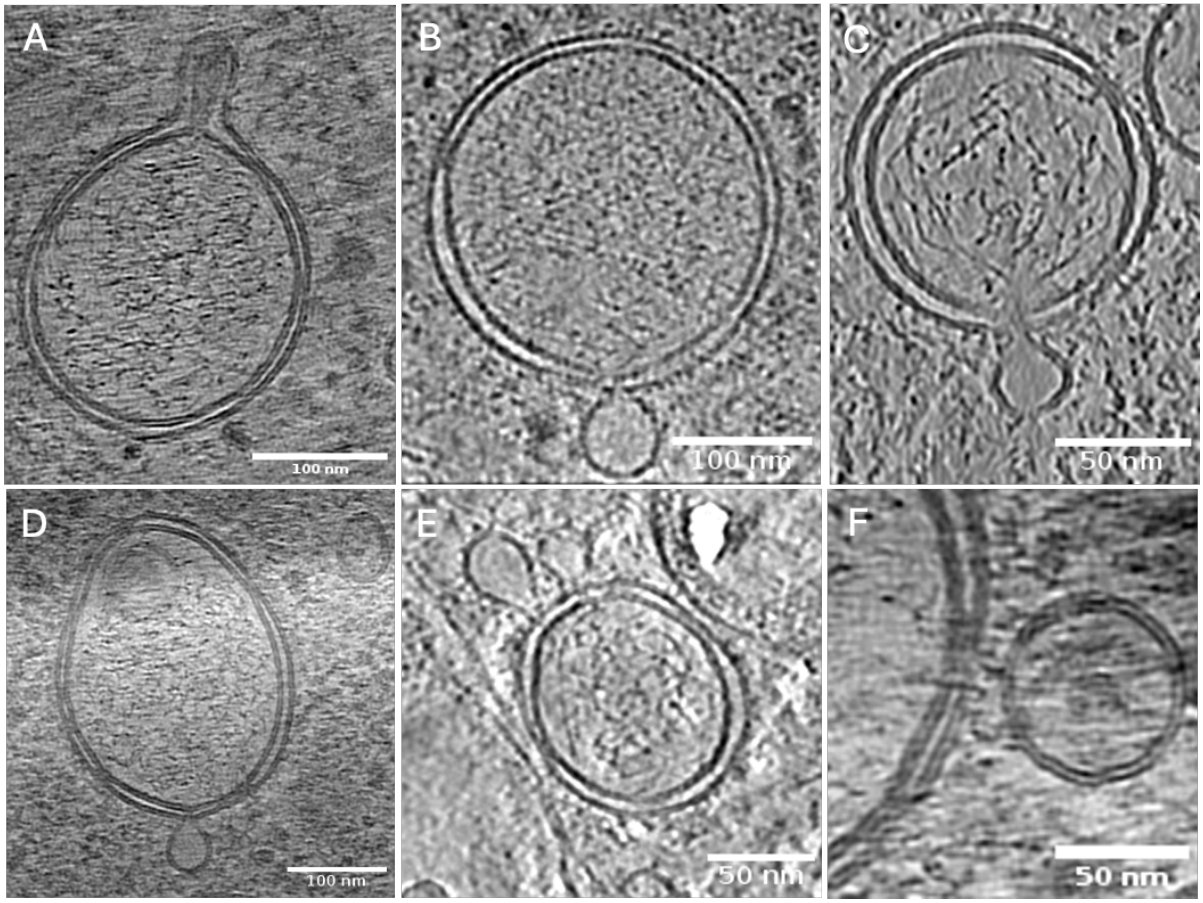


Figure 5. 18 Membrane evaginations were observed attached to DMVs.

One example of a double membrane evagination was observed (panel A) and balloon-shaped single membranes were attached to several DMVs, the pores do not interact with these vesicles as seen in panel B-F.

DMVs with double membrane invaginations were also observed (Figure 5.19 A-H). The invaginations were continuous with both membranes of the DMV, and they did not appear to be the connectors to the ER as the ER connectors were continuous with the DMV membrane outer membrane only. These structures have previously been reported (Zhou *et al.*, 2017; Ulasli *et al.*, 2010) and similar structures have been described as DMV fusion events (Knoops *et al.*, 2008). The invaginations also appeared to be filled with contents and alongside other RO elements and virus budding sites (Figure 5.19 G-H).

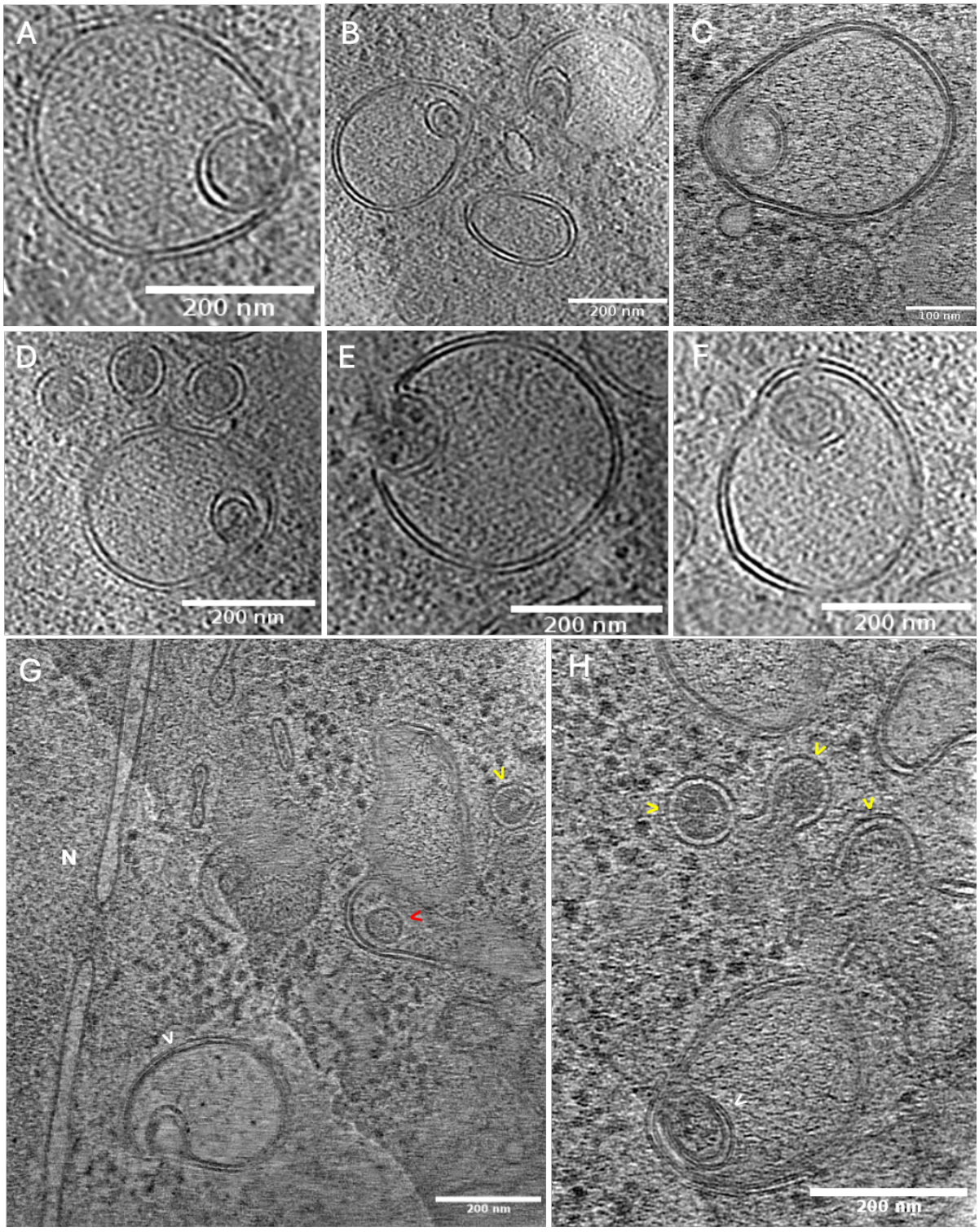


Figure 5. 19 DMVs with double membrane invaginations.

The invaginations appeared continuous with the DMV membrane and filled with electron dense material. In panels G-H DMVs with double membrane invaginations (white arrowheads) were also near virus budding sites (red arrowheads), and DMSs (yellow arrowheads); N, nucleus.

5.2.4.10. Cryo-ET of IBV virions

Alongside the RO observations, the IBV virion structure was also observed under cryogenic conditions for the first time (Figure 5.20 A-C). Spike and the RNP were observed, the membrane envelope had an average diameter of 87.9 nm (± 6.5 nm) (n= 25), and the RNP shell on the inside of the envelope had a diameter of 60 nm (Figure 5.20 A-B). Spike proteins lining up on the interior of single membrane vesicles and budding viruses were also observed (Figure 5.20 C).

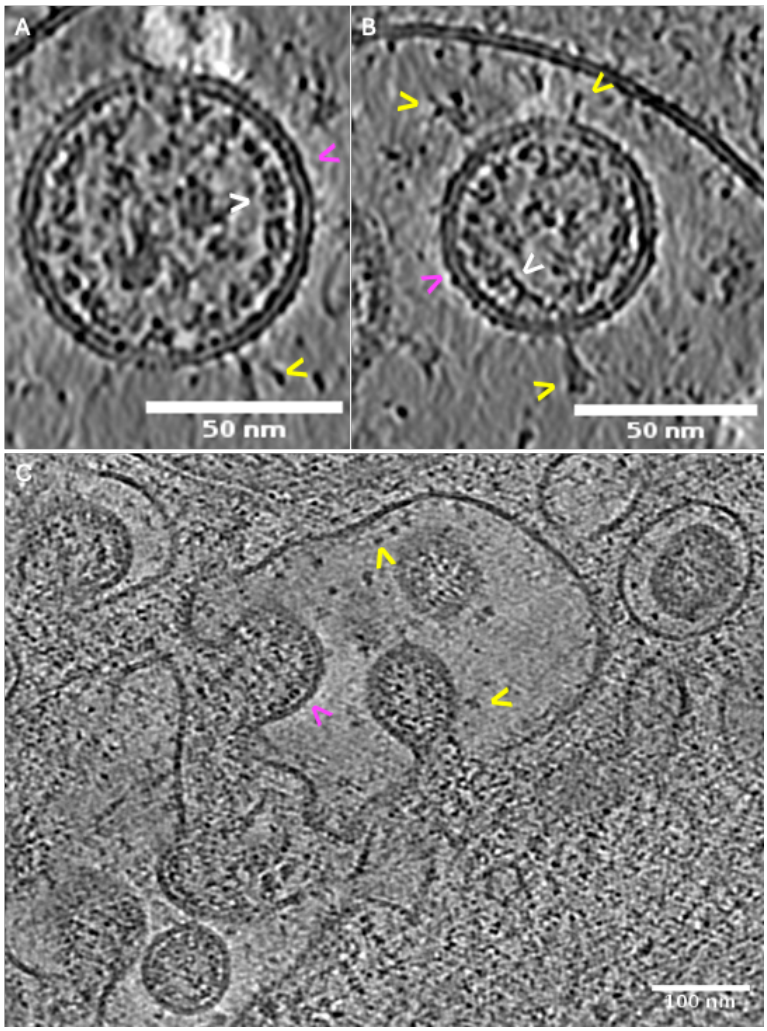


Figure 5. 20 BeauR-eGFP-nsp2 virions.

The envelope (magenta arrowheads), Spike (yellow arrowheads), and ribonucleoprotein (RNP; white arrowheads) and budding events (panel C) were all observed in the fluorescence guided lamellae.

5.2.4.11. Partially degraded DMSs were also observed

Interestingly, partially degraded DMSs were observed in infected cells. The broken DMSs appeared within a single membrane that may potentially be a lysosome (Figure 5.21 A-D). BeauR-eGFP-nsp2 fluorescence guided milling to these areas so this might indicate that GFP-nsp2 is contained within the DMS as is consistent with the room temperature CLEM and cryo-SXT. The interior contents of the DMSs appeared to form assemblies but the dense material could also be unrelated material that has also been delivered into the vesicle.

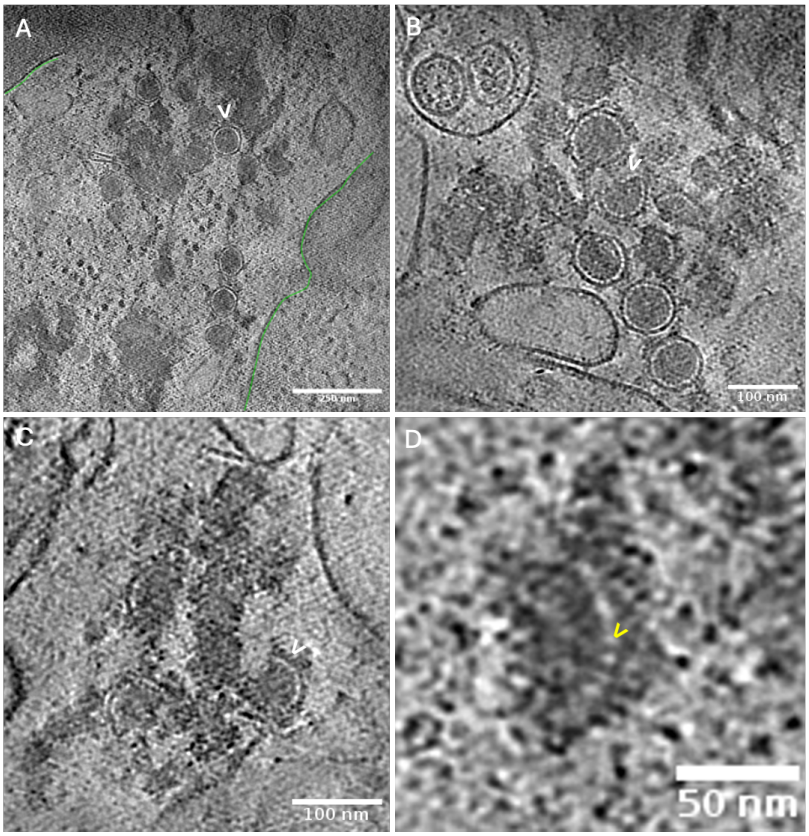


Figure 5. 21 Partially degraded DMS are observed inside single membrane vesicles in multiple tomograms.

The single membrane vesicle is marked with a green line (panel A) and DMS are marked with white arrowheads which appear open with their contents exposed to the lumen of the vesicle (panels B-C). Short sections of zippered double membrane are labelled with yellow arrowheads in panel D.

5.2.5. Subvolume averaging from cryo-electron tomograms

The repeating structure of the DMS double membrane was investigated by STA to try and determine the level of order within the DMS head and see if the structure of the spoke protein could be determined. The IBV DMSs were picked in 34 tomograms using a sphere for each DMS head (Figure 5.22 A). Most tomograms had between 1-10 DMSs but four of the tomograms contained a patch of over 40 DMSs, the total number of DMSs sampled was 266. The spokes were spaced about 60 Å apart and subvolumes were extracted every 40 Å around the surface of each sphere to oversample the surface of the DMS inner membrane and ensure no spokes were missed, later duplicate particles were removed. Euler angles were derived for each subvolume based on where they were extracted from on the sphere's surface, and this allowed the generation of an initial model. This was then used to align and classify the subvolumes at bin 4 (Figure 5.22 B). The best class reached the Nyquist frequency at bin4 and was selected and used as a new reference at bin 2. Using the bin2 reference, the particles were further classified, and their alignment was refined (Figure 5.22 C). At this point duplicate particles were removed, using the minimum inter-particle distance set at 40 Å, leaving 3796 particles which were refined to a resolution of 23 Å (Figure 5.23 A-B, Supplementary movie 10). The ordered structure of DMS was visualised as follows: the spokes sat between the membranes in a square grid pattern with a more electron dense region at the base of the spoke going into the inner membrane. Then, beneath the inner membrane there was a second layer of ordered protein that continued the square grid pattern with a Z-shaped envelope. The Z-shaped proteins lined and curved around the inner surface of the DMS inner membrane at sites

where the spokes were embedded. Below the second layer of Z-shaped proteins, there was a third square grid of proteins, termed the cargo, packed following the curve of the second layer. The absolute handedness of the model could not be resolved. STA of ribosomes was also completed by Dr Daniel Clare to estimate the maximum achievable resolution from the tomograms and from 2512 particles a 12.5 Å model was generated.

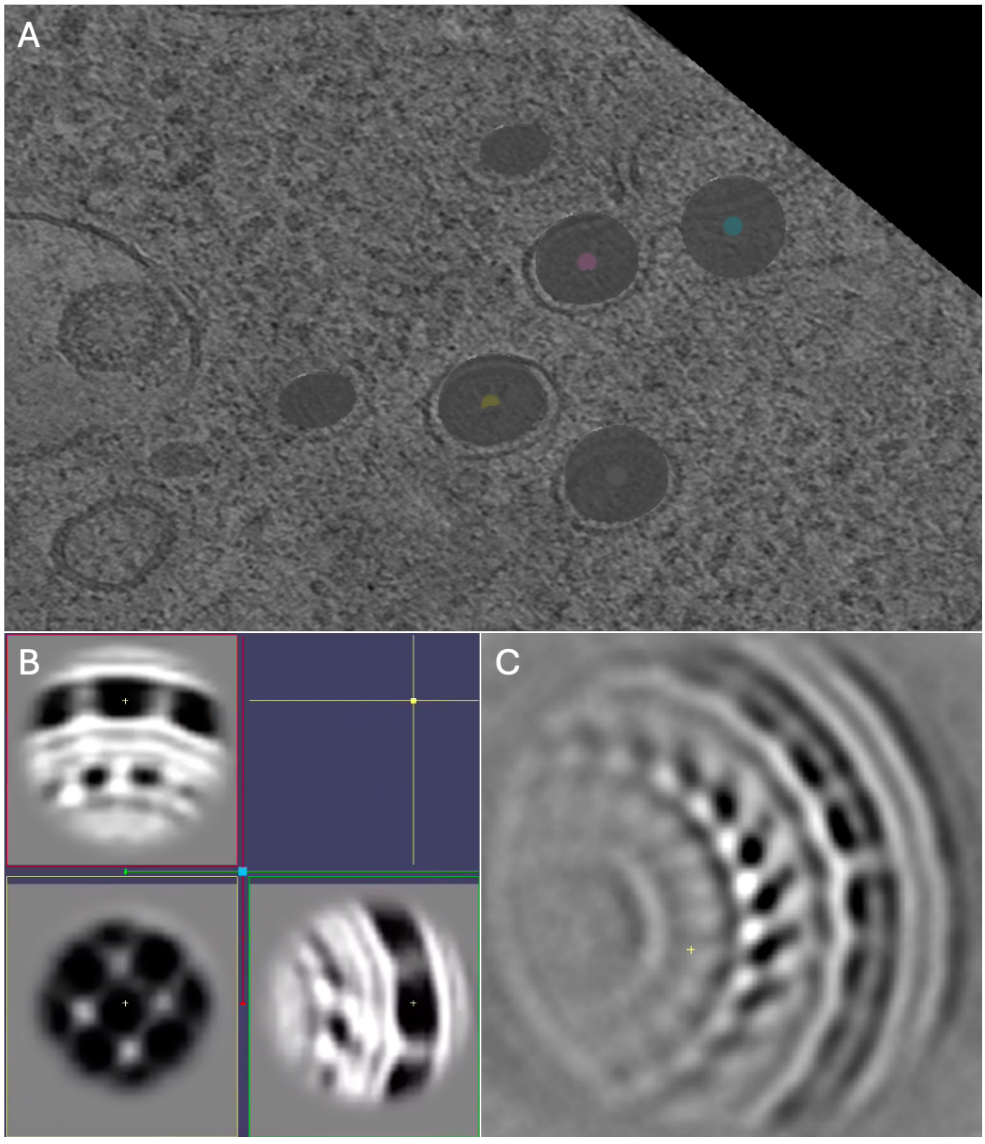


Figure 5. 22 Particle picking strategy (oversampling the surface of spheres) and 3D classification.

Within the Napari GUI of RELION-5, the centre of each DMS head was marked (coloured circles), and the radius was set at the DMS inner membrane, creating a grey sphere in 3D (panel A). These spheres defined the surface for which subvolumes would be extracted around at the set spacing of 40 Å. The subvolumes were classified at bin 4 and the particles from the average of the best class (panel B) were extracted at bin 2 and refined to make a final bin 2 model (panel C).

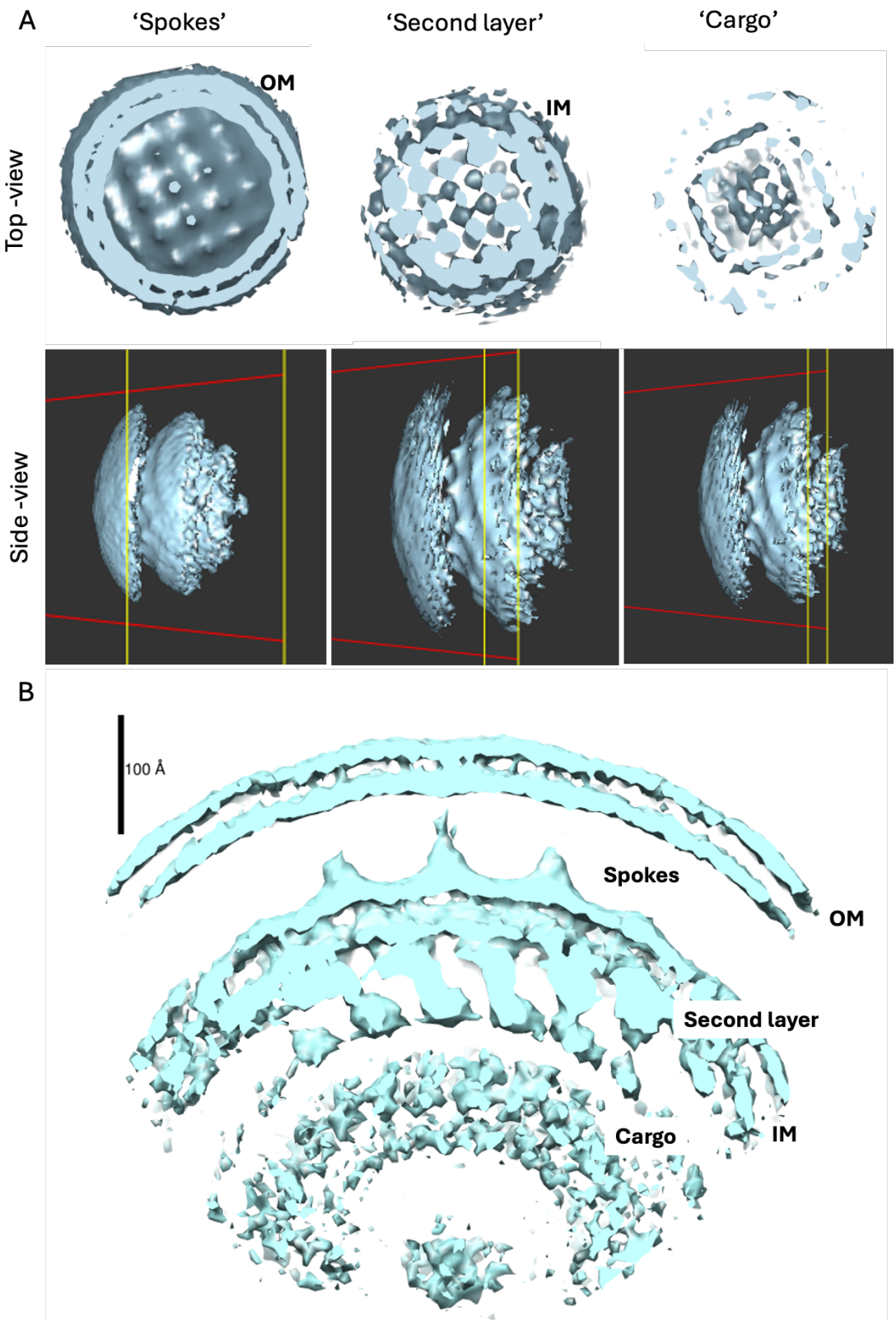


Figure 5. 23 3D modelling of the DMS after STA.

Panel A shows the top-down view of the square grid pattern made by the 'spokes', the 'second layer', and the 'cargo', the yellow lines in the side views show the section of the model depicted in the top-view. Panel B shows the side view of the DMS with three ordered layers: the spokes sit between the outer membrane (OM) and inner membrane (IM), the second layer of Z-shaped proteins line the IM, and the cargo follow the curve of the second layer in the interior of the DMS.

5.3. Discussion

In this chapter, the IBV RO was observed for the first time by cryo-ET. Here, DMVs with pores, DMSs, zER, virus particles, and the membrane network that connects these structures, were visualised. This is significant as it provides a comparison to the cryo-ET structure of *Betacoronavirus* ROs such that we can begin to understand the conservation of the RO across the CoV family as well as provide novel insights. The cryo-ET data also supports that the RO-like structures from the cryo-SXT data were indeed DMVs and DMSs.

The cryo-ET study is limited by the lack of tomograms of uninfected cells as controls. The cytoplasm of the cells is heterogenous with several vesicular structures so large numbers of tomograms encompassing the cytoplasm of the cells would be needed to generate a picture of the uninfected cells. This could be used to show that the RO structures are genuine in the infected cells and not a caveat of infection. Using the rIBV, which was first shown to label sites of nascent viral RNA synthesis (Chapter 3.2.9), for the correlative imaging of the RO membranes provides confidence that these structures are acting in virus replication. Furthermore, it is generally accepted that the CoV RO consists of DMVs, and DMSs tethered to CM-zER and CoV-ROs have been validated in several other studies including Maier *et al.* (2013), Doyle *et al.* (2019), Snijder *et al.* (2020), Loconte *et al.* (2021), and Castro *et al.* (2023). In some of these studies uninfected cells are imaged which do exhibit some cytoplasmic vesicular networks but none with the uniform and clustered organisation of DMVs or the distinct DMSs.

Cryo-ET revealed that the IBV DMVs contain pores with cytosolic prongs. To complete STA, we would need to substantially increase the particle numbers to get an intermediate resolution structure comparable to the MHV pore and the SARS-CoV-2 nsp3-nsp4 minimal pore (Wolff *et al.*, 2020; Huang *et al.*, 2024). Only 52 pores were observed here while 347 particles and ~ 115000 particles were used in the final averages of the pores from Wolff *et al.* (2020) and Huang *et al.* (2024) respectively. Furthermore, the origin of the DMV paired membranes was unclear, only in one example did the DMV double membrane appear to be shared with zER and DMS but the region at which these structures were connected, and the double membrane became zippered with the striation pattern, was not fully resolved (Figure 5.6 C-D). An example of a DMV connected to stacked membranes has been described before, but it did not appear to contain RNA (Klein *et al.*, 2020; supplementary fig. 5). Interestingly, there was a lack of spherical single membrane vesicles in the cryo-electron tomograms suggesting that the spherical vesicles observed by cryo-SXT were indeed DMVs despite the double membrane not being discernible using this technique. Another interesting observation was that although most virus assembly was seen at separate single membranes, two examples of virus budding into membranes that were shared with zER and DMSs were also observed.

Significantly, the proteins holding together the zER and DMS double membranes, termed ‘spokes’, were resolved. Then, by STA, the DMS was shown to hold an ordered array of proteins. When the DMS ‘spokes’ were analysed in more detail it was found that they embed in both membranes and span the lumen of the double membrane with a total length of ~160 Å and a soluble luminal region spanning ~ 65 Å. The spokes appeared in a

square grid pattern spaced 60 Å apart within the lumen of the double membrane. Furthermore, the inner membrane appeared ruffled and within the DMS interior there appeared to be further ordered protein lattices making a 'second layer' beneath the inner membrane and at an angle to the spokes, appearing like a spiral, plus, a third layer of 'cargo' also in a square grid pattern. The third layer of 'cargo' may be part of the second layer but there appeared to be a gap between the two densities. Finally, there may also be an empty space in the centre of the spherule like observed in Figure 5.13.

To improve the resolution of the model, more lamellae would need to be generated by the correlative workflow and more tomograms collected to contribute additional particles to the average. To concentrate the BeauR-eGFP-nsp2 positive cells on grids, it could be attempted to sort the cells expressing the GFP signal and plate these on the grids, like has been done for transfection experiments (Huang *et al.*, 2024), but this may be detrimental to the health of the infected cells. Or the RO membranes could be purified on columns for plating on grids and tomography without FIB milling as has been done previously for DMVs (Huang *et al.*, 2024). Plus, particles from the zER could also be picked using a membrane surface model and averaged to test if the spoke density could be seen at higher resolution. Masking was attempted to reduce the noise in the averages however the masks lost too much of the membrane curvature which the averages were aligning to. More complex mask shapes could be useful to apply to the averages. There are ongoing discussions for the best-practice for fitting SPA, crystal or AlphaFold structures into cryo-ET models. For example, *Coot* (Emsley *et al.*, 2010), *Phenix* (Liebschner *et al.*, 2019) and likelihood-based signal to noise analysis (Read *et al.*, 2023) could be tested for fitting protein structures into higher resolution STA maps.

Several lamellae were also imaged at higher magnification, but they were only correlated in 2D. In addition, these samples also had poor vitrification so did not provide any more information on the DMS at higher resolution. Moreover, fewer DMSs were imaged in each tomogram at this magnification so more lamellae would be required to get as many particles as could be picked from the lower magnification tomograms and this approach could be less practical. The higher magnification cryo-ET could be repeated on new samples alongside the 3D correlative milling routine to increase the chance of a higher resolution DMS structure.

The striation pattern of the spokes visualised on DMSs and zER was entirely novel and has not been seen for any CoVs to date. Significantly, the spokes were not seen on the DMV double membranes as is consistent with cryo-ET of *Betacoronavirus* DMVs (Klein *et al.*, 2020). This suggests that DMVs are likely to form via a different mechanism to DMSs. As DMV formation is known to involve nsp3, nsp4 and nsp6 (Angelini *et al.*, 2013; Oudshoorn *et al.*, 2017; Ricciardi *et al.*, 2022; Zimmerman *et al.*, 2023), these nsps could also be involved in other elements of the RO but in potentially different conformations or complexes.

The identity of the IBV protein or proteins forming zER and DMSs is unknown. It was unclear whether a single protein or a protein complex was required to zipper the two membranes (Figure 5.24 A-C). However, nsp4 was thought to be a likely candidate because IBV nsp4 alone was shown to zipper membranes (Doyle *et al.*, 2018). Therefore, to test the hypothesis that nsp4 was potentially creating the striations, DF1 cells were

transfected with nsp4-GFP and imaged via cryo-ET (Figure 5.14). Although nsp4-GFP expression induced zippered and stacked membranes, agreeing with Doyle *et al.* (2018), zER with clear spokes were not visible, suggesting that the hypothesis may not be true. Therefore, it appears that additional proteins are required to produce the spoke pattern in the DMSs, or the GFP tag was impairing the ability of nsp4 to form these structures. To help understand the composition of DMSs in more detail, the minimal components required for zER and DMS formation need to be identified. This could be done using different IBV deletion mutants, replicons, or transfected nsp expression cassettes. Furthermore, if DMSs were isolated from DMVs and nsp antibodies were available, it would be interesting to perform fluorescence proximity labelling experiments or immunoprecipitation, immunoblotting, and mass spectrometry experiments to determine which nsps were in DMSs (Chen *et al.*, 2024).

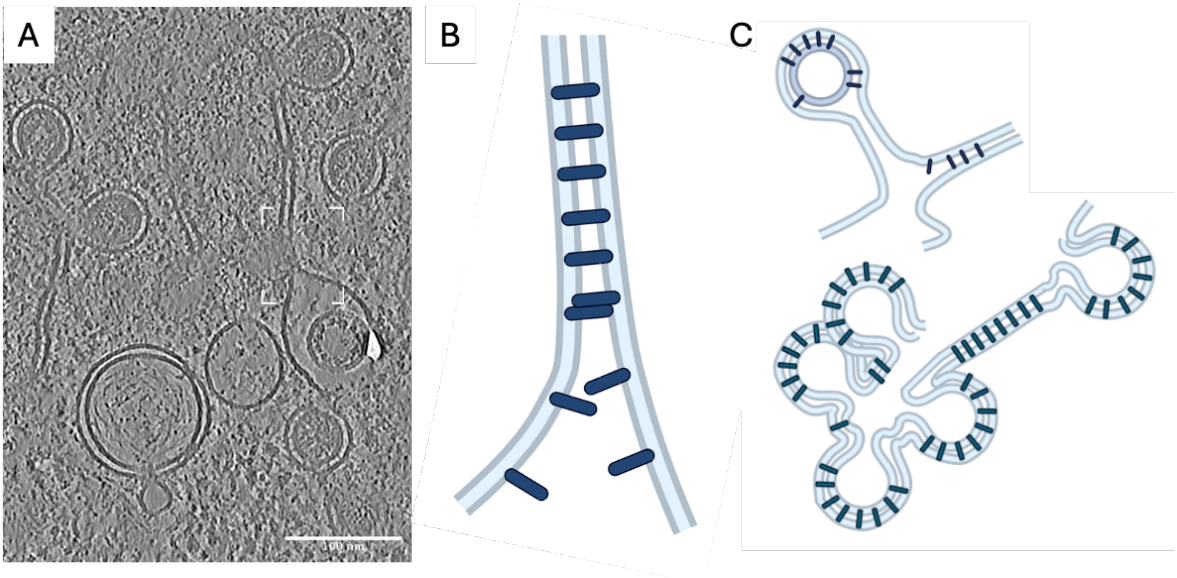


Figure 5. 24 ER zippering mechanisms and DMS schematic.

Panel B shows a schematic of potential ER zippering methods from the boxed region in panel A, Zippering could occur using single double membrane spanning proteins or dimerising proteins on opposite membrane sheets.

Only seven lamellae from nsp4-GFP transfected cells were imaged so more imaging would need to be undertaken to fully understand if there are any additional structures formed with nsp4 alone. SARS-CoV and MHV nsp4 has previously been tagged with enhanced GFP at the C-terminus for IF and IEM experiments, but ROs were not described (Oostra *et al.*, 2007; Hagemeijer *et al.*, 2011). Differential tagging of nsp4 could also be tested because regular GFP was fused to nsp4 so it may cause aggregates unlike monomeric GFP. Tagging nsp4 may also disturb its function in RO structures, this is suggested as other nsp tagging experiments avoid altering nsp4. For example, in GFP tagged SARS-CoV-2 nsp3-nsp4 constructs to study DMV pores, the GFP was tagged at the N-terminus of nsp3 (Huang *et al.*, 2024). It is known that nsp4 forms homomultimers (Manolaridis *et al.*, 2009; Huang *et al.*, 2024) and STA including the long sections of zER, via particle picking using surface membrane models, might help answer how the ER zippers.

Nsp6 is another candidate protein for the spokes. MHV nsp6 was shown to zipper ER via homodimerisation and establish connectors between the ER and DMVs (Ricciardi *et al.* 2022) but this same function has not been observed for IBV nsp6 (Doyle *et al.,* 2018). Moreover, the spoke pattern was not observed in the ER-DMV connectors (Figure 5.15) so the zippering may be a result of luminal loop interactions from nsp6 dimers on parallel membranes rather than via a soluble ectodomain (Ricciardi *et al.*, 2022). Previously, nsp3, nsp4 and nsp6 were concluded to be essential for biogenesis of SARS-CoV DMVs (Angelini *et al.*, 2013) but the addition of MERS-CoV nsp6 to cells expressing nsp3 and nsp4 did not noticeably affect DMV biogenesis (Oudshoorn *et al.*, 2017). On the other hand, addition

of MHV nsp6 to nsp3-nsp4 expressing cells appeared to reconstitute DMVs that more closely resemble those seen under infection (Ricciardi *et al.*, 2022). SARS-CoV nsp6 was also shown to induce single membrane vesicles particularly around microtubule organising centres, which may be used for trafficking parts of the RTC or may be a result of disrupting Golgi trafficking to supply vesicles (Angelini *et al.*, 2013; Hagemeijer *et al.*, 2010; Giansanti *et al.*, 2007; Verheije *et al.*, 2008). Finally, IBV nsp6, even in addition to nsp3 and nsp4, did not reconstitute any RO structures (Doyle *et al.*, 2018). Therefore, nsp6 may have slightly different roles in different CoVs but it appears to be involved in lipid supply, particularly for DMVs.

It may be informative to draw parallels from other +RNA viruses that induce DMSs. However, the only other DMSs that have been observed are from plant viruses that invaginate into the double membrane of chloroplasts and appear more like +RNA virus single membrane invaginated spherules (Li *et al.*, 2016; Jin *et al.*, 2018). The CoV DMSs are unique because they are not invaginated into a vesicle but exist from zER in the cytoplasm. Moreover, the plant viruses have labelled for dsRNA in the DMS interior, and they do not produce DMVs as part of their RO. Therefore, the function of CoV DMSs is expected to be different to these plant virus DMSs.

To investigate the DMS structure in more detail, STA was completed on sections of the DMS membrane with repeating order corresponding to the grid pattern of the spoke proteins and interior contents. There were several STA and particle picking programs that could be applied to this dataset such as *cryoSPARC* (Punjani *et al.*, 2017) and *Vesicle*

Picker (Karimi *et al.*, 2024). *Dynamo* (Scaramuzza and Castaño-Díez, 2021) was also tested for particle picking but *RELION-5* (Burt *et al.*, 2024) was the approach that worked best.

The 3D EM density did not reach a high enough resolution to confirm the handedness and unequivocally fit proteins into the structure. However, it was interesting to hypothesise that nsp4 was the protein forming the spoke. This was partly based on observations of nsp4 in the SARS-CoV-2 nsp3-nsp4 minimal DMV pore (Huang *et al.*, 2023). In their structure, nsp4 was presumed to span the double membrane of the DMV with a flexible TM1 in the outer membrane, an appropriately sized soluble ectodomain in the intermembrane space, TM2-6 in the inner membrane, and the CTD in the DMV lumen (Huang *et al.*, 2024) (Figure 5.25 A). In the intermembrane space, the nsp4 ectodomain interacted with other nsp4 and nsp3 ectodomains, and in the DMV lumen, the nsp4 CTD interacted with other nsp4 CTDs. The topology of nsp4 with a cytoplasmic N-terminus followed by a transmembrane helix, a large luminal domain, and a second transmembrane domain placing the C-terminus back into the cytoplasm was also proposed by Oostra *et al.* (2007). Consequently, the IBV nsp4 structure was predicted using AlphaFold2 (Figure 5.25 A), where it also had a flexible TM1 (Figure 5.25 C), and following the suggested topology, the TM domains were fit into the DMS membranes (Figure 5.25 B). With this fitting, the nsp4 ectodomain could fit the spokes and the CTD could fit electron density in the top half of the Z-shaped proteins in the second layer (Figure 5.25 B-D). Therefore, the nsp4 CTD might interact with another protein to fill the density in the bottom half the Z-shaped protein (Figure 5.25 D-E). Additional densities were sometimes observed either side of spokes in the zER, but they could not be distinguished from background densities in the cytoplasm so it would be interesting to

look in more detail. The predicted grid pattern of nsp4 is shown at different angles in Figure 5.25 panels E-G: panel E shows fitting of the nsp4 CTD to the 'second layer', panel F shows the fitting of the TM2-6 in the inner membrane, and panel G shows the fitting of the nsp4 ectodomains into the spokes. The identity of the remainder of the second layer and the third layer in the DMS are also unknown so other viral or cellular proteins are likely to exist as part of the complex.

There are several limitations of model fitting into low resolution EM density maps. Firstly, without resolving the directionality of alpha helices the handedness of models cannot be determined prior to fitting. Secondly, the model may fit in several orientations. To aid the fitting, a low threshold model could be used to fit into the EM density rather than the higher resolution secondary structure model. This may provide a better idea of the shape of the protein and the space it fills. Furthermore, new likelihood-based model docking software could be tested such as *em_place* (Read *et al.*, 2024).

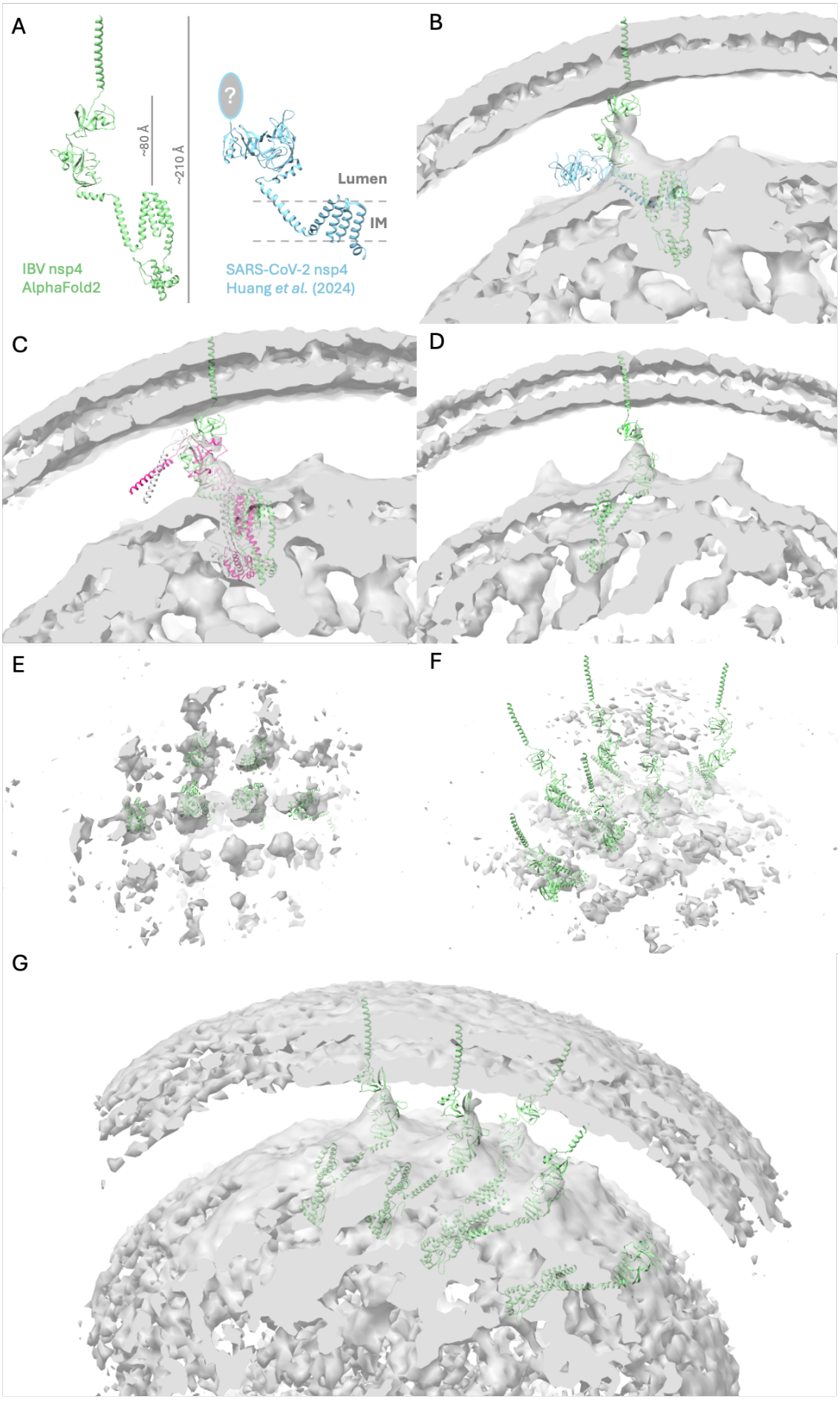

A
~80 Å
~210 Å
IBV nsp4
AlphaFold2
?
Lumen
IM
SARS-CoV-2 nsp4
Huang et al. (2024)
B
C
D
E
F
G

Figure 5. 25 Fitting nsp4 into the model.

Although the model was not high enough resolution to decipher the handedness and identity of the proteins, nsp4 was hypothesised to be a likely target so an AlphaFold2 predicted IBV nsp4 structure was manually docked into the EM density. AlphaFold2 generated several potential conformations for IBV nsp4 and we selected the one that matched out EM density. Panel A shows one of the predicted IBV nsp4 structures next to the SARS-CoV-2 nsp4 structure resolved from the minimal nsp3-nsp4 DMV pore and from this structure the TM1 was not resolved but the ectodomain was in the lumen between the two membranes and TM2-6 were in the inner membrane (IM). In panel B, the two structures were overlaid according to their TM2-6 and fit into the DMS model at the inner membrane so the ectodomains sat in the intermembrane space. Interestingly, this put TM1 of the predicted IBV nsp4 structure in the outer membrane. The flexibility of TM1 is shown in the grey and pink AlphaFold predictions of IBV nsp4 in panel C. Panel D shows an estimated fit of predicted IBV nsp4 into the DMS model with TM1 in the outer membrane, the ectodomain in the intermembrane space, TM2-6 in the inner membrane, and the C-terminal domain (CTD) in one part of the electron density under the inner membrane in the 'second layer'. Panels E-G show the estimated grid pattern of IBV nsp4 in the DMS from the CTD in the 'second layer' (panel E), to the TM2-6 in the inner membrane (panel F), and the ectodomain in the 'spokes' (panel G).

As nsp4 alone is not enough to explain all the EM density, the DMS must contain several proteins. Nsp3 and nsp4 have a close relationship and it is known, for example, that DMV formation is dependent on nsp3-nsp4 cleavage (Oudshoorn *et al.*, 2017; Zimmerman *et al.*, 2023; Huang *et al.*, 2024). Paired membranes are formed by cleavage deficient nsp3-nsp4 cassettes so the pre-cleavage construct may have alternative conformations and interactions that zipper membranes. Subsequently, it has been suggested that upon cleavage, nsp3-nsp4 constructs snap into pores and bend membranes into a double membrane (Huang *et al.*, 2024). Interestingly, nsp3 did appear to label MERS-CoV DMSs/CM via IEM (Snijder *et al.*, 2020). However, from the STA there are no appropriate densities to account for nsp3 as the spoke or for nsp3 as the interior of the DMS with nsp4 as the spoke.

Overall, nsp4 could also adopt a completely different conformation to how it was observed in the minimal DMV pore. The nsps are dynamic and can adopt several different conformations, even within the same complex, and have multiple binding partners. This is observed in the crowns at the spherule necks of FHV (Tan *et al.*, 2022) and CHIKV (Zhan *et al.*, 2023) where the same nsp has multiple copies with different conformations. Although these viruses encode fewer nsps so they must act as multifunctional proteins with different conformations, the RTC of CoVs is also likely to exist in different conformations as it performs different stages of RNA synthesis. Currently, not enough is known about the arrangement of the CoV RTC within the cell or how this changes to achieve different functions. Since all nsps have also been confirmed to organise at some stage at the RTC, alongside host factors (V'kovski *et al.*, 2019), several other binding partners could exist effecting the confirmation of nsps. *In silico*, the RTC has been modelled into a complex with a mass greater than 2 MDa (Perry *et al.*, 2021). The conformational states and interactions are also likely to be time sensitive based on the polyprotein cleavage and membrane dynamics. Potential protein candidates that may form complexes in the DMSs include nsp2 homotypic interactions and heterotypic interactions with nsp3 and nsp6 (Hagemeijer *et al.*, 2011). Nsp4 and nsp3 are also known to form membrane rearrangements in conjugation with their cleavage (Oudshoorn *et al.*, 2017; Zimmerman *et al.*, 2023). Nsp5 is the main protease so will have several interacting partners while Nsp6 is another candidate for interactions at DMSs since it is membrane bound. Nsp3 has also been shown to interact with structural proteins E and N (Álvarez *et al*. 2020; Li *et al.*, 2023) but further experiments are required to test why these proteins may interact at these membranes.

Although the spoke proteins could not be identified, the structures did provide novel insights into DMS biogenesis. The zER and DMSs both had the striation pattern of spoke proteins between the two membranes, but only the DMSs (and their formation intermediates with curving double membranes) were associated with the second layer and cargo protein. DMSs have also always been observed with electron density in their interiors in earlier data (Maier *et al.*, 2013; Snijder *et al.*, 2020). This suggests a mechanism by which the double membrane wraps around a protein shell, rather than the membranes being curved first, and then filled. In this hypothesis, the DMSs with wider necks would represent an earlier stage in DMS formation, and as the second layer of Z-shaped proteins and the cargo bind to the spokes and oligomerise, the membrane is wrapped around the protein shell, and the neck closes to form a uniformly sized head. In a few cases, the protein shell and the inner membrane could also fully seal and form the long neck DMSs observed in this thesis or the 'closed DMSs' previously reported for IBV and MERS-CoV (Snijder *et al.*, 2020). Of the fully reconstructed DMSs, Snijder *et al.* (2020) reported that ~80% of MERS-CoV DMSs were sealed (n= 54) and ~50 % of IBV DMSs were sealed (n= 39) but here, only ~10 % of IBV DMSs were sealed (n= 68). The necks appeared to be obviously closed where the neck was long (the membranes were paired without space for a channel of inner membrane), but the sealed DMS with shorter necks could be a misinterpretation due to missing data in Z. The DMSs shown in Figure 5.13 also appear to show a protein shell lining the inner membrane and space in the centre of the shells that could correspond to the channel that connects the spherule interior to the cytoplasm, as has been described for the majority of 'open' DMSs. For example, the first EM of the IBV DMS imaged regions of electron density lining the curved inner membrane opposite the open neck (Maier *et al.*, 2013). Furthermore, only some sections of zER had

well resolved spokes and the most obvious ordered arrangement of the spokes into a square grid was seen at the top of the DMS heads. It could be that interaction with the second layer and cargo bring the components into the correct arrangement.

To test these hypotheses and whether the contents of the DMS were made of a single protein or a complex of proteins that curve the double membrane via a stepwise assembly, it would be useful to perform cryo-ET and STA on more examples of the partially formed DMSs. The timeframe of DMS wrapping may be fast so looking at several timepoints post infection to try and compare 'earlier' and 'later' DMSs may not be as useful as just looking at large patches in which formation events are likely to be continuously happening. For example, the room temperature CLEM of BeauR-eGFP-nsp2 showed a few formed DMSs at 6 h pi and abundant DMSs at 18 h pi. Finding formation intermediates could also be achieved by enforcing a defect in spherule assembly via the loss or inhibition of a critical viral or cellular protein. However, proteins specific to DMS formation have not yet been elucidated. It is known that IBV nsp3, nsp4, and nsp6, alone or in combination have not been sufficient to recapitulate any RO structures so further viral or host factors must be required (Doyle *et al.,* 2018). Expression of various combinations of nsps may not recapitulate DMSs if they are only produced under infection conditions, for example if an antiviral protein was involved. Various antiviral compounds that target RNA synthesis could be added to infected cells to test whether the appearance of DMS was altered. Replication of specific strains of IBV is also temperature sensitive (Keep *et al.*, 2020) so infecting cells at different temperatures may also alter RO appearance.

The formation of other +RNA virus single membrane spherules is known to be associated with nsps involved at the spherule crown complexes. This has been shown for BMV (Schwartz *et al.*, 2002), FHV (Zhan *et al.*, 2022), CHIKV (Tan *et al.*, 2022), and Flaviviruses DENV (Cerikan *et al.*, 2020), classical swine fever (CSF) (Cheng *et al.*, 2023), and (TBEV) (Dahmane *et al.*, 2024). However, the CoV DMS does not appear to have a protein structure at the neck, and they have a unique function, so they are likely to form differently. TBEV spherules also appear to be shaped by a protein coat that establishes the curve of the membrane as well as the pressure from replicating RNA (Dahmane *et al.*, 2024). Additionally, for CSF spherules, a vimentin cage has also been shown to line the inner membrane of the spherule via interactions to viral NS5A (Cheng *et al.*, 2023). Vimentin was also shown to colocalise with dsRNA clusters in SARS-CoV-2 infected cells via IF microscopy (Castro *et al.*, 2023) so it may also be involved with shaping CoV ROs, but perhaps not DMSs specifically.

There are several other mechanisms by which proteins bend membranes into spherical shapes. For example, scaffold proteins, such as BAR domain proteins, can sit on the inside or outside of the curving membrane, or membrane proteins can embed into membranes and oligomerise. Furthermore, cytoskeleton proteins can push membranes from one side to induce positive curvature on the opposite side, or they could push sections of membrane together at the vesicle neck to form a bud (Collins *et al.*, 2011). In most cases, membrane curvature is induced to form spherical vesicles that bud off or form the curved membranes at the ends of an extended filopodia or stacked ER, mitochondrial cristae or chloroplast thylakoids (Jarsch *et al.*, 2016). The CoV DMSs are spherical, but do not bud off so it is unknown how the membranes can be curved in such a way but be held pinched

at the necks and maintained within the network of zER/CM. One example of interactions that hold bud-shaped membranes in-place include tetraspanin proteins at the yeast plasma membrane which counteract membrane curvature applied by BAR domain proteins to maintain the membrane furrows at the neck of the curved membrane and prevent closure of the bud (Haase *et al.*, 2023). Tetraspanins are also involved in the intracellular trafficking of viruses so it could be speculated that they could hold the DMS neck in-place but their involvement in the CoV RO has not been investigated (Florin and Lang, 2018). Membrane biophysics could also be tested *in silico* using molecular dynamics and lattice-based simulations of predicted proteins involved in the RO membranes. For example, *in silico* studies have previously been used to investigate the remodelling of membranes by CHIKV (Laurent *et al.*, 2022), the SARS-CoV-2 E protein (Yang *et al.*, 2022), nsp3 and nsp4 interactions (Hensel, 2022), and SARS-CoV-2 virions (Yu *et al.*, 2021). However, the composition of the DMSs would need to be known before these tests could be conducted. Overall, the membrane may well bend around a cargo, but it is then not clear how the neck is maintained, especially considering there is no current evidence for a cap or crown complex.

Another example of membrane wrapping around a protein shell can be taken from the envelopment of viral capsids. For example, Human Immunodeficiency Virus (HIV) Gag polyprotein lattices curve membranes at budding sites (Carlson *et al.*, 2008) and Herpesviruses have icosahedral capsids that bud into membranes, via tegument proteins, to obtain their envelope (Nahas *et al.*, 2022). The capsids of enveloped +RNA viruses such as Togaviruses also have an icosahedral structure while Flaviviruses appear more like CoVs in which the nucleocapsid N binds RNA to make the RNP. Arterivirus virions have

also been described as having a ‘double-layered chain of nucleocapsid proteins bundled into a hollow ball’ (Spilman *et al.*, 2009) that may make an icosahedral shell (Wieringa *et al.*, 2004). The CoV RNP has a diameter of 14-16 nm which form a structure like beads on a string that pack into helices (Macnaughton *et al.*, 1978; Davies *et al.*, 1981). SPA of SARS-CoV, FCoV and MHV virions also revealed that the RNPs were arranged into an oblique lattice with a unit cell of 6 nm by 7.5 nm and an interior angle of ~100° (Figure 5.26 A-C) (Neuman *et al.*, 2006). Furthermore, from purified MHV RNPs, the distance between repeating strands of globular subunits was 7 nm (Figure 5.26 D-G) (Gui *et al.*, 2017). Interestingly, these paracrystalline arrays of RNP densities appear like the grid pattern of the second layer of Z-shaped proteins of the DMS (Figure 5.26 J-K). This grid pattern could also be described as an oblique lattice with a unit cell of 6 nm by 7 nm (Figure 5.26 I). Furthermore, the compacted intertwined assembly of the purified RNP (Figure 5.26 G (right)) might resemble the interior of disrupted DMSs (Figure 5.26 H). This suggests that N could be lining the interior of the DMS inner membrane. However, it is unknown why N would exist at DMSs. It could be speculated that N sequesters specific RNA in DMSs that is not packaged into nascent virions. Furthermore, N has been shown to label MERS-CoV DMSs via IEM (Snijder *et al.*, 2020).

Although the helical filamentous RNP structure has also been described for IBV (Saikatendu *et al.*, 2007), the organisation of individual N proteins with RNA has not been deciphered. It is known that N CTDs dimerise (Chen *et al.*, 2007), and helical packing can occur in the presence (Bárcena *et al.*, 2009) or absence (Saikatendu *et al.*, 2007) of RNA. Plus, RNPs in SARS-CoV-2 virions may organise each linked RNP subunit into higher order assemblies such as stacks with preferred orientation, tetrahedrons, and hexons (Klein *et*

al., 2020; Yao *et al.*, 2020). Moreover, N interacts in the RTC, so it is likely to be at RO membranes (V'kovski *et al.*, 2019), but it may not be at DMSs specifically. If N did exist in the second layer of Z-shaped proteins, this may not fit with the hypothesis that nsp4 makes the spokes and the nsp4 CTD makes up the top half of the Z-shape, unless N made up the bottom half of the Z-shaped proteins which follow the same grid pattern as the top half. However, for the nsps, N is currently only reported to interact with nsp3 (Hurst *et al.*, 2013; Cong *et al.*, 2020). N is also not required for the formation of spherical virus-like particles (VLPs), so it is not expected to be able to induce spherical membrane rearrangements alone (Vennema *et al.*, 1996).

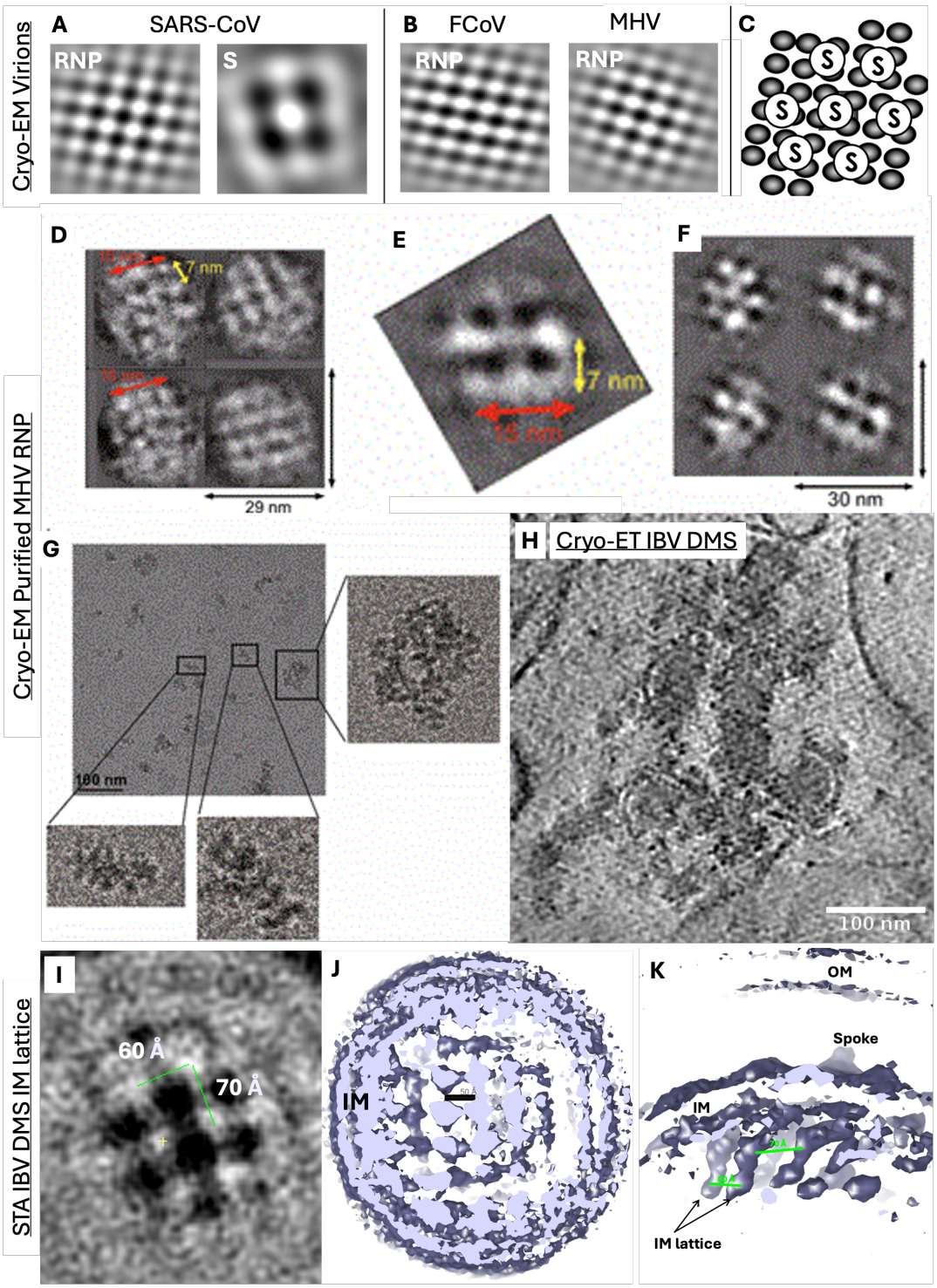


Figure 5. 26 Organisation of N in virions compared to the DMS model.

A-C) Cryo-EM of CoV virions show that S proteins sit in register with four RNP densities that make an oblique lattice with a unit cell of 6 nm by 7.5 nm (modified from Neuman *et al.*, 2006). D-G) Cryo-EM of purified MHV RNPs were shown to make compact intertwined assemblies and helical filaments a width of 15 nm with globular densities spaced 7 nm apart (Modified from Gui *et al.*, 2017). H) Cryo-ET of disrupted DMSs in BeauR-eGFP-nsp2 infected cells. I-J) STA of the lattice layer lining the inner leaflet of the DMS double membrane making an oblique lattice in the axial views with a unit cell of approximately 6 nm by 7 nm. K) STA model showing the edge view of repeating parallel strands of the Z-shaped proteins that make the second lattice layer of the DMSs with 60 Å and 70 Å measurements between adjacent globular domains.

N does interact with M, and it is thought that the spherical shape of virus particles is primarily controlled by M (Neuman *et al.*, 2011; Vennema *et al.*, 1996; Boscarino *et al.*, 2008). Therefore, although there would be no known function for M in DMSs, it was speculated that M could be involved in shaping DMS membranes. Other viral membrane proteins also induce highly curved convex membranes such as the HIV-1 Gag polyprotein (Carlson *et al.*, 2008), the Influenza A M1 protein (Dahmani *et al.*, 2019), and EAV GP5 and M protein heterodimers (Snijder *et al.*, 2003). Furthermore, M forms a lattice like those observed in axial views of the DMSs (Figure 5.27) (Neuman *et al.*, 2011). M has been described as spaced at ~ 6.5 nm apart (Bárcena *et al.*, 2009) or 4 to 5 nm apart in a loosely ordered oblique lattice (Neuman *et al.*, 2011). These lengths could fit with those observed in axial views of the second layer of Z-shaped proteins or the third layer of cargo proteins in the DMSs (Figure 5.27). Furthermore, M homodimers were shown to exist in two forms within the envelope, termed M_{LONG} and $M_{COMPACT}$, and edge views of M_{LONG}, with a distinct tilt relative to the membrane, might resemble edge views of the top half of the second layer of Z-shaped proteins in the DMSs (Neuman *et al.*, 2011) (Figure 5.27). Presence of N was also shown to be important for formation of M_{LONG}, or make up part of the density, in virions (Neuman *et al.*, 2011) so they could exist together in the DMSs. The interactions and affinity of M from different CoVs may also vary for example TGEV M adopts an N-endo/C-ecto topology, so this could also be considered for fitting M into the DMS (Risco *et al.*, 1995). On the other hand, M was not labelled at MERS-CoV DMSs by IEM (Snijder *et al.*, 2020) and there is no known function of N and M in DMSs.

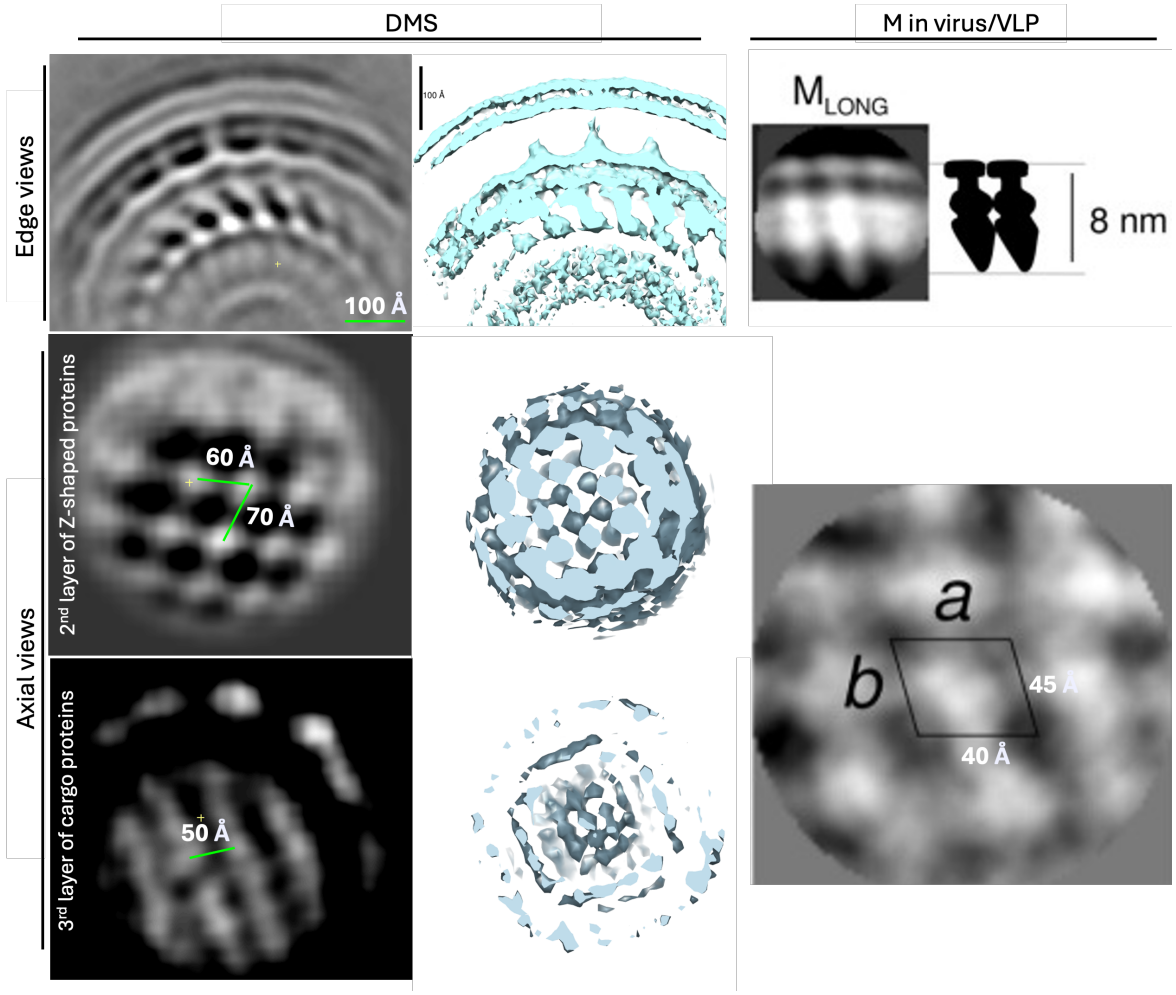


Figure 5. 27 The DMS interior lattices compared to the M lattice.

Edge views of the DMS second layer of Z-shaped proteins have similarities to M_{LONG} proteins described from 2D averaging of CoV virions and virus-like particles (VLPs) reconstituted from E,M, and N expression (Neuman *et al.*, 2011). For example, both densities are endodomains tethered beneath a membrane leaflet, both endodomains sit at an angle to the membrane, both endodomains have two globular densities spanning approximately 8 nm, and both structures are observed in the presence of other proteins such as N for M_{LONG}. Axial views of M make a rough oblique lattice that appears slightly smaller than the lattice made by the 2nd layer of Z-shaped proteins in the DMS and may be more-like the 3rd layer of cargo proteins.

Neuman *et al.* (2011) estimated that each M_{LONG} dimer curved the membrane by 5°. Whereas, in the DMSs, roughly 22 densities in the second layer of Z-shaped proteins surrounded the circumference of the inner DMS membrane inducing a membrane curvature of ~ 16°. The inner shell of the DMS was on average 60.8 nm (n= 48) and the virion including the envelope was on average 87.9 nm (n= 25), so it makes sense that the

DMSs could be more extensively packed with a greater membrane curvature. Therefore, it could be speculated that excess of M and N might produce DMSs, but this does not explain the double membrane or spokes.

Although nsp4, N and M have been speculated here to exist in the DMSs because they have been observed to produce similar structures previously, this does not answer what the densities in the DMS are or why this structure would form. The first step to determine whether N or M existed at DMSs could be to test for their colocalisation with BeauR-eGFP-nsp2 by IF microscopy. E may also play a role in the conformation of M as mutations in E can produce aberrant virus particles (Fischer *et al.*, 1998) and E has previously labelled at 'tubular bodies' similar to CM in MHV infected cells (Ulasli *et al.*, 2010) so the role of E with M in shaping membranes warrants further studies. However, the components are likely to be nsps, so the minimal nsps required to form DMSs will be interesting to investigate. The stoichiometry of the DMS contents could then be investigated by purifying the soluble components and testing if they have different oligomerisation states via perfluoro-octanoic acid (PFO)-PAGE (Neuman *et al.*, 2008). Further STA of the DMS layered lattices would allow clearer counting of the number of proteins in each layer and a better comparison to the putative virion M and RNP lattice ratios. It could also be postulated that the interior contents of the DMSs include sequestered cellular proteins. This may explain why the DMSs exist in different numbers for different CoV, if they have different mechanisms to control the antiviral response from their hosts.

IBV DMVs have also been imaged here by cryo-ET for the first time, allowing for comparison to DMVs from *Betacoronaviruses* SARS-CoV-2 and MHV (Klein *et al.*, 2020; Wolff *et al.*, 2020). Interestingly, the IBV DMVs appear highly comparable to DMVs produced by SARS-CoV-2 and MHV, with average diameters of 265 nm and RNA strands within their interior. The size is comparable to the vesicles observed in the cryo-SXT (251 nm) and the strand pattern has previously been described as viral RNA which lack additional electron densities that could correspond to the RTC (Knoops *et al.*, 2008; Gopal *et al.*, 2012; Klein *et al.*, 2020). Significantly, IBV DMVs were also observed to contain double membrane spanning protein pores with cytosolic prongs. Furthermore, some of the pores had additional luminal and cytoplasmic electron densities that could correspond to RNA, N, or other elements of the RTC. As most DMVs were larger than the thickness of lamellae, it was not visible whether they always remained connected the ER, and any connectors were also not resolved in the cryo-SXT. Nevertheless, the IBV DMVs appeared to be less interconnected than SARS-CoV and SARS-CoV-2 DMVs which have previously been shown to share an outer membrane or exist in vesicle packets (Knoops *et al.*, 2008; Klein *et al.*, 2020). This agrees with the cryo-SXT and room temperature EM of IBV DMVs (Maier *et al.*, 2013). For all CoV the DMVs have been observed to be interspersed with CM/zER and DMSs and the possibility of DMVs and DMSs being related structures has been raised. Significantly however, data here clearly demonstrate that in comparison to the DMSs, the DMV double membrane lumen appears empty while the DMS double membrane is held together by the striation pattern of spokes. This is consistent with chemically fixed samples where DMV membranes separate from one another and are only pinched together at a few points, presumably where the pores are located. However, the zER and DMS membranes always remain tightly paired. This

observation is also supported by the SXT data since the zER and DMSs appear much darker than the DMVs. Together, this strongly indicates that the DMVs and DMSs form from different membranes via different mechanisms.

The IBV DMVs were also shown to contain double membrane spanning pores with cytosolic prongs as described for MHV (Wolff *et al.*, 2020). The pores have only previously been described by cryo-ET for *Betacoronaviruses*. However, all CoV DMVs imaged via room temperature EM have points where the double membranes pinch which are consistent with pores. There were also extra electron densities observed tethered to the IBV pores (Figure 5.16) that could correspond to other components of the RTC, the RNP, or RNA strands as described for MHV (Wolff, 2022). It is now also known that the active *Alphacoronavirus* HCoV-229E replicase involving nsp7, nsp8, nsp9, nsp12, and nsp13 is located inside DMVs and nascent viral mRNA transcripts exit the DMVs via pores lined with nsp4 (Chen *et al.*, 2024). Unfortunately, only 52 IBV DMV pores could be picked from 30 tomograms containing DMVs, so there were insufficient particles for STA. To be able to make a detailed comparison between IBV DMV pores and those formed by MHV or the SARS-CoV-2 nsp3-4 minimal pore, additional data would need to be collected. This could be used to confirm the presence of IBV nsp3 and nsp4 at the DMV pore and look for the presence of RNA, N, and the RdRp nsp12 at the pore and suggest a mechanism of RNA translocation.

Several examples of smaller DMVs were also imaged. They contained the same number of pores as were visible in the larger DMVs (~3) and since they were within a smaller surface area, they appeared closer together. One hypothesis could be that the smaller

DMVs are precursors to the larger DMVs and the pores form first before viral RNA synthesis expands the lumen. Here, nsp3-nsp4 constructs could line membranes before cleavage and pore formation which simultaneously bends the membrane making the double membrane (Huang *et al.*, 2024). Then, as RNA synthesis begins, nsp6 could filter lipids to accommodate the growing membrane via connectors to the ER while blocking ER proteins from entering the DMVs (Ricciardi *et al.*, 2022). Arterivirus DMVs are smaller like these small CoV DMVs described, but they have smaller genomes (Wolff, 2022). It is known that genome template length determines the size of single membrane spherules of other +RNA viruses (Kallio *et al.*, 2013). Furthermore, it has been demonstrated that the energy required to bend CHIKV spherule membranes was less than the energy generated by RNA polymerisation (Laurent *et al.*, 2022). Therefore, it is feasible that RNA filling the vesicle can result in expansion and bending of RO membranes. Interestingly, the smaller IBV DMVs had non-uniform double membrane lumens and resembled minimal DMVs produced by transfection of SARS-CoV-2 nsp3-4 constructs (Zimmerman *et al.*, 2023; Huang *et al.*, 2024). This supports the hypothesis that the smaller DMVs imaged in this thesis could be DMVs at early stages in formation, before the peak of RNA synthesis, because in the DMVs produced by nsp3-nsp4 transfection, there is no RNA synthesis, so the DMVs are not filled with RNA, and the DMVs do not expand. Some densities were observed inside the smaller DMVs, but they did not resemble the RNA strands imaged in larger DMVs. It would be interesting to investigate, for example by EM-ISH (Gosert *et al.*, 2002), whether all DMVs contained all RNA or if negative and positive sense RNA transcripts were separated.

5.4. Summary

1. *The IBV RO was imaged by cryo-ET for the first time using a correlative workflow*
2. *The zER and DMSs double membranes were observed to be held together by densities that span the double membrane and the DMSs appear to form via zER wrapping around a protein shell*
3. *STA was performed on DMSs to show that the DMS interior contains ordered and layered lattices of proteins*
4. *Small DMVs were observed alongside larger DMVs suggesting a potential mechanism for DMV formation*

Chapter 6. Final Discussion

The aim of this thesis was to understand the organisation of the IBV RO and characterise the membrane structures formed *in situ* during virus infection. To achieve this, fluorescent recombinant viruses were generated, confirmed to label RO membranes, and used for correlative fluorescence and 3D ultrastructural analysis in cryogenically preserved cells. Consequently, the RO was efficiently targeted and preserved in a near native state. One element of the CoV RO, the DMVs, is better understood than the DMSs tethered to zER, and has been extensively imaged *in situ* under cryogenic conditions especially following the advent of SARS-CoV-2. DMVs are now known to be the sites of viral RNA synthesis, and their biogenesis involving pores formed by nsp3 and nsp4, and nsp6, is beginning to be understood (Snijder *et al.*, 2020; Angelini *et al.*, 2013; Oudshoorn *et al.*, 2017; Ricciardi *et al.*, 2022; Zimmermann *et al.*, 2023; Huang *et al.*, 2024). However, mechanisms of DMV formation, apart from paired membranes, have remained elusive. Furthermore, previous experiments have been completed using the *Betacoronaviruses* MHV, SARS-CoV, and SARS-CoV-2, and their nsps. Interestingly, these viruses do not appear to produce extensive amounts of zER and DMSs like another *Betacoronavirus*, MERS-CoV (Snijder *et al.*, 2020), or the *Gammacoronavirus* IBV (Maier *et al.*, 2013), and the *Deltacoronavirus*, PDCoV (Doyle *et al.*, 2019). Therefore, although all CoV produce DMSs to some extent, this RO element has been understudied, and little is known about its biogenesis and function.

Recombinant viruses, based on the BeauR strain of IBV, were generated containing meGFP, mCherry, and TC tags fused to the N-terminus of nsp2 (Chapter 3.2). BeauR-eGFP-nsp2 was taken forward for correlative imaging because this virus produced the highest number of visibly infected cells at the earliest timepoints by fluorescence microscopy. Moreover, addition of the tag did not significantly affect viral RNA synthesis up to 12 h pi. Subsequently, BeauR-eGFP-nsp2 fluorescence was shown to localise with known markers for viral RNA synthesis, via IF microscopy, and ROs equivalent to those observed in cells following infection with WT BeauR, via CLEM using live cell fluorescence microscopy and resin section EM.

BeauR-eGFP-nsp2 was first analysed in vitreous cells by cryo-SXT (Chapter 4.2). The large 3D volume and near-native state imaging provided by this technique were advantageous for studying rare ultrastructural events (Harkiolaki *et al.*, 2018). Cryo-SXT has been used to image SARS-CoV-2 infected cells previously, and a few examples of DMVs have been described (Mendonça *et al.*, 2021; Loconte *et al.*, 2021; Castro *et al.*, 2023). However, the first cryo-SXT images of DMSs are presented here, alongside abundant putative DMVs which fill most of the RO volume. The difference in soft X-ray absorption between the DMV and DMS membranes was apparent and suggested that the DMS and zER contain additional carbon dense material such as proteins. Although it was possible to look for ROs prior to 6 h pi via CLEM of infected cells in larger dishes, with the goal of imaging RO formation events before they became indistinguishable from fully formed ROs, the smaller size of the TEM grids meant that very few infected cells could be found at 6 h pi. Furthermore, the fluorescence imaging under cryogenic conditions required optimisation to confidently detect smaller fluorescent foci at 6 h pi and earlier. Eventually, later

timepoints were imaged as RO formation events should be continually occurring as the RO grows, although they may be more difficult to distinguish. Different fluorophores could be tested, or different cryo-fluorescence microscopes could have also been tested for the 6 h pi and earlier timepoints. Overall, the tightly apposed double membranes of the RO could not be resolved using this technique so RO formation intermediates could not be described.

Next, using cryo-ET, high resolution near-native state tomograms of the IBV RO were imaged for the first time (Chapter 5.2). Here, the double lipid bilayer of DMVs and DMSs were resolved and the protein complexes within the membranes were imaged. Furthermore, although smaller 3D volumes were imaged, later h pi were imaged, and most DMVs and DMSs appeared fully formed, several examples of RO formation intermediates were captured. Finally, the repeating structures observed in the DMS were subjected to STA to reveal the organisation of DMSs in more detail. This concluded the correlative multiscale analysis of the IBV RO (Figure 6.1).

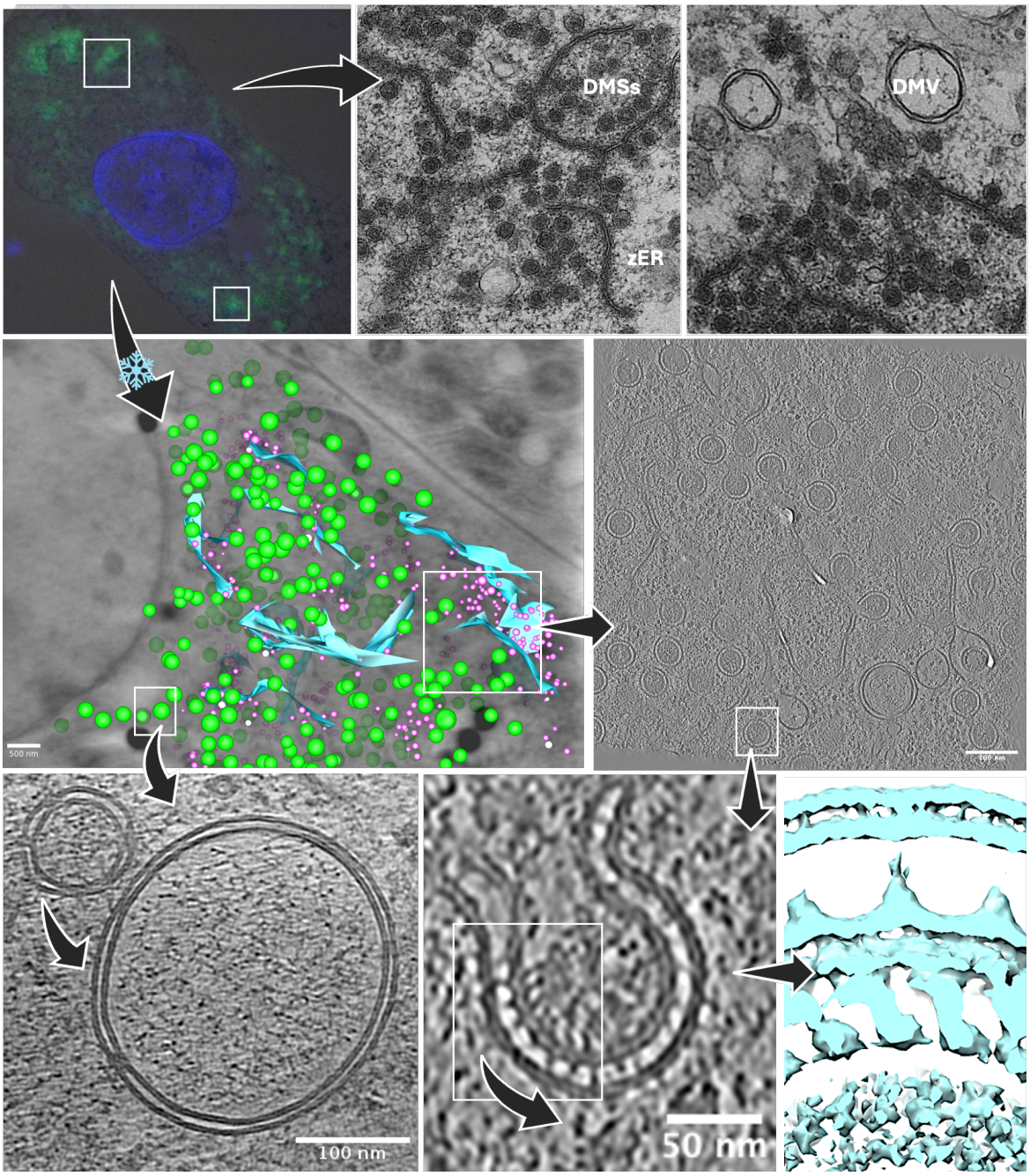


Figure 6. 1 Correlative imaging of the IBV RO over multiple scales with unprecedented detail.

The nsp2-eGFP rIBV was generated and confirmed to label ROs by room temperature CLEM before being imaged in vitreous cells by cryo-SXT and cryo-ET. Here, the IBV RO was imaged over large volumes and to unprecedented levels of detail revealing potential DMV and DMS biogenesis mechanisms and, via STA, ordered protein lattices within the DMSs.

6.1. Novel insights into IBV DMVs

Firstly, IBV DMVs were observed to contain double membrane spanning pores with cytosolic prongs (Chapter 5.2). These pore structures were expected as positions in which the DMV double membranes compress in standard EM images have been shown previously (Knoops *et al.*, 2008; Maier *et al.*, 2013). Moreover, the DMV pore has been observed for MHV and SARS-CoV-2 and the cytosolic prongs were determined to consist of nsp3 (Wolff *et al.*, 2020). Subsequently, the DMV pore was shown to have minimal constituents of nsp3 and nsp4 (Zimmerman *et al.*, 2023). Interestingly, extra electron densities were observed proximal to the pores that could correspond to other elements of the RTC such as N and the RdRp, as well as densities appearing like strands which could be RNA, and this has been shown in DMV pores from other whole viruses (Wolff *et al.*, 2020; Wolff, 2022). Recently, the active viral replicase involving nsp7, nsp8, nsp9, nsp12, and nsp13 has also been shown to localise in the interior of DMVs in *Alphacoronavirus* HCoV-229E infected cells (Chen *et al.*, 2024). This positions viral mRNA synthesis in the DMV lumen and the nascent transcripts then exit via the nsp4-lined pore. Subsequently, links between RNA synthesis and packaging into nascent virions have been suggested as N is known to interact with nsp3 on the cytosolic side of the pores (Hurst *et al.*, 2013; Ni *et al.*, 2023), the packaging signal on genomic RNAs interact with N (Kuo *et al.*, 2016), then N interacts with M which is embedded in membranes (Kuo and Masters, 2002). Some DMVs also had multiple balloon-shaped single membrane vesicles attached to their surface which could appear like vesicles to transport material to/from DMVs, or they could be part of the connectors to the ER.

Furthermore, alongside the majority of IBV DMVs with similar sizes to those observed for other CoV (250-300 nm; Knoops *et al.*, 2008; Klein *et al.*, 2020; Tabata *et al.*, 2021; Cortese *et al.*, 2020) (Chapter 4), small DMVs with diameters of 90-166 nm were also observed (Chapter 5). This smaller population of DMVs has not been described previously in CoV infected cells. Interestingly, they had similar diameters to DMVs formed by cells transfected with nsp3-nsp4 constructs (with an average diameter of 104 nm; Zimmermann *et al.*, 2023). Moreover, there appeared to be a defined number of pores per DMV and there were a similar number of visible pores in the small and large DMVs. This suggests that the pores, at least containing nsp3-4, and the DMV form simultaneously before RNA synthesis begins. This is supported by observations that cleavage-deficient nsp3-nsp4 form paired membranes but not DMVs (Oudshoorn *et al.*, 2017). Whereas ectodomain interactions have been observed for cleaved nsp3 and nsp4 that may drive the curvature of the membrane into a double membrane at the pore, thus creating a DMV, before the onset of RNA synthesis then expands the DMV lumen (Huang *et al.*, 2024). It has also been shown that the size of the CHIKV spherule RO is controlled by the RNA content and the energy released by RNA polymerisation (Laurent *et al.*, 2022). This is important because it implies that CoV RNA polymerisation could supply sufficient energy to expand the membranes of the DMVs.

6.2. Novel insights into DMSs

Significantly, the presence of proteins spanning the double membrane of DMSs and zER were observed for the first time. These proteins were termed ‘spokes’ and appeared to form an ordered arrangement on the DMSs. The spokes were speculated to be nsp4

(Chapter 5.3) since IBV nsp4 is known to zipper membranes and nsp4 has been shown to span double membranes with an appropriately sized ectodomain to fit the STA density (Doyle *et al.*, 2018; Huang *et al.*, 2024). Furthermore, the STA revealed layered protein lattices within the DMS interior. Unfortunately, the identity of these proteins was not elucidated. Although it was interesting to suggest the presence of N, and 'long' forms of M in the DMSs, since they have been observed to form similar lattices in virus particles previously (Neuman *et al.*, 2006; Neuman *et al.*, 2011), there would be no known function for these proteins in DMSs. Furthermore, IEM labelling of MERS-CoV infected cells did suggest that nsp3 and N localise to DMSs/CM but M and S were not present at these structures. Overall, the components of the DMSs remain elusive (Snijder *et al.*, 2020). Therefore, elucidating the viral or cellular proteins required to make DMS is a high priority for future experiments.

DMS formation intermediates were also imaged. These structures supported a hypothesis by which the zER is wrapped around a shell of protein which forms inside the interior of the DMS. The DMS heads were all uniform in size suggesting that there was a controlled stoichiometry for the protein lattices making up the DMS interior shell. Furthermore, 90 % of the visible DMS necks appeared to be held with a uniform channel connecting the DMS interior to the cytoplasm (n= 61, average width= 21 nm (± 3.5 nm)). Therefore, 10 % (n= 7) of the DMSs appeared to have a sealed inner membrane but it could not be determined if the channel was in fact open elsewhere in the volume but not imaged due to the milling or the missing wedge. Larger proportions of sealed DMSs from MERS-CoV and IBV infected cells have been reported previously (Snijder *et al.*, 2020) but the missing wedge was not considered during this analysis and the function of DMS sealed or open

remains unknown. Here, we saw that the DMS contents appear like ordered protein lattices and there was no observation of RNA molecules. Interestingly, there were no structures resolved at the DMS necks like the crowns observed for CHIKV and FHV single membrane spherules, which are also known to have functions in RNA synthesis (Tan *et al.*, 2022; Zhan *et al.*, 2023; Ertel *et al.*, 2017).

CM and zER have distinct appearances but are considered to be functionally analogous as both structures are tethered with DMSs. These structures are also prevalent across the CoV family and it has been highlighted that the DMS are highly regular. The STA completed in this thesis emphasise the ordered arrangement of the DMSs, so it would appear that they have a specific function. Although, the function of CoV DMSs remains elusive. It has been postulated by others that DMSs are intermediate stages in DMV biogenesis that do not progress fully. However, the cryo-SXT and cryo-ET presented here indicate that the DMVs and DMSs are formed from different double membranes; the zER and DMS have proteins spanning the double membrane, while the DMVs appear to only be held together by the transmembrane pores. CM/zER/DMSs have also been suggested to be stress-induced cubic membranes formed by protein accumulation (Oudshoorn *et al.*, 2017; Deng *et al.*, 2010) and CoVs have been described to induce ER stress (Jiao *et al.*, 2023; Movaqar *et al.*, 2021; Liang *et al.*, 2022). However, although the DMSs were shown to contain packed proteins, the contents appeared highly ordered, once more suggesting that they might have a specific function. Moreover, although CM appear less ordered, highly branching, and label for abundant nsps late in infection (such as nsp2, nsp3, nsp4, nsp5, and nsp8) (Snijder *et al.*, 2020; Ulasli *et al.*, 2010; Knoops *et al.*, 2008; de Wilde *et*

al., 2013), SARS-CoV infection produces CM as early as 3 h pi (Knoops *et al.*, 2008), supporting the hypothesis that the CM/DMS are not aberrant membrane aggregates.

6.3. Future work

To identify the components of the DMSs, several further experiments could be completed. To determine whether any structural proteins were localised in the DMSs, IF imaging could be completed in BeauR-eGFP-nsp2 infected cells to determine if any of the labels colocalised with any of the eGFP-nsp2 signal which is known to mark DMVs and DMSs. Furthermore, structural protein antibody labelling in BeauR-eGFP-nsp2 infected cells could also be completed following treatment of cells with low concentrations of Digitonin, which can only permeabilise the plasma membrane and not intracellular membranes (Doyle *et al.*, 2021), to observe whether any structural protein labelling was lost or re-localised relative to eGFP-nsp2 signal. This could determine if any structural proteins were concealed within intracellular membranes. However, since the DMSs are RO membranes, they are expected to contain nsps. Therefore, further experiments to elucidate the minimal nsps required to recapitulate DMSs could be undertaken. For example, using replicons or transfection of cells with different cassettes of nsps such as nsp3-4 and combinations with nsp5-16. Nevertheless, the components could be viral or cellular but only expressed and structured into DMSs upon virus infection. For example, it could be speculated that the contents of the DMSs are cellular antiviral proteins which it is advantageous for the virus to sequester using viral protein-induced zER. This may explain why the DMSs appear in different numbers for different CoVs if they each utilise different mechanisms to control the antiviral response.

For IEM or on-section labelling of HPF-FS infected cells, there are no suitable IBV nsp antibodies. The current available antibodies label nsp12, which does not localise to ROs (Doyle *et al.*, 2021), and nsp5, which appears diffuse and will be associated with sites of translation rather than RNA synthesis. There are antibodies for the structural proteins, but the components are thought to be nsps since the DMSs are part of the RO. Labelling proteins with gold beads coupled to antibodies have been adapted for use in cryo-ET (Ertel *et al.*, 2017). However, for more precise labelling, smaller protein tags can be fused to the protein of interest which are subsequently tagged with gold beads (Unchwaniwala *et al.*, 2020). Gold beads can produce artefacts as they can heavily scatter electrons (Fernandez *et al.*, 2016) so DNA origami signposts are a new technique for labelling proteins of interest (Silvester *et al.*, 2021). Furthermore, addition of a small domain to a protein of interest, that is recognisable in STA, can be used to identify the protein using comparison to the WT average of the structure (Wolff *et al.*, 2020). Additionally, novel labelling techniques include radiation-sensitive tags that create a gas bubble upon exposure to electron that can guide the user to the location of the protein in the cryo-tomogram (CZI, 2020). These tags may facilitate the identification of further macromolecules associated with ROs. With the current IF data, quantitative and statistical analysis of colocalisation between rIBV fluorescence and markers for RNA replication could be completed to define how accurately the nsp2-tagged fluorophores localise at replication sites. Interestingly, different strains of IBV also appear to produce varying amounts of DMSs. For example, few DMSs have been observed in cells following IBV M41 infection, but they are abundant in cells infected with recombinant M41

containing the BeauR pp1ab (the nsps) (Dr Helena Maier, personal communication). Therefore, BeauR nsps could be swapped into M41 until DMSs were recovered.

The DMVs are known to be the primary if not only sites of RNA synthesis (Snijder *et al.*, 2020) and they were observed to fill a large volume of IBV infected cells by cryo-SXT, while the DMSs were interspersed between them. Our findings support that the DMSs are not involved in RNA synthesis, but this does not help explain why DMSs exist across the CoV family, and they have been observed in small numbers early in infection before growing into larger networks. Moreover, although the active viral replicase appears to be located inside DMVs and mRNAs are then exported via the nsp4-lined pore (Chen *et al.*, 2024), questions remain surrounding the population of RNA molecules within the DMVs and how positive and negative sense transcripts may be synthesised, translocated, and packaged. RNA probes could be developed to label specific RNA sequences and imaged via EM-ISH to determine their location (Gosert *et al.*, 2002). The hypothesis that the DMVs grow as they are filled with RNA can also be challenged. It is known that the nsp3-4 transfection DMVs lacking RNA synthesis are smaller than DMVs formed following virus infection, and a smaller population of DMVs were observed in IBV infected cells, but it would be interesting to test whether attenuating viral RNA synthesis at some point altered the size of DMVs.

To be able to image more RO intermediate structures, replication inhibitors such as K22 (Ricciardi *et al.*, 2022), siRNA knockdown of RO-associated host proteins, or IBV strains with temperature-sensitive replication could all be tested to see if ROs were arrested in an intermediate state. Alternatively, new techniques could be applied to the BeauR-

eGFP-nsp2 tool to increase the chance of successfully imaging early ROs. For example, one limitation of the tool was autofluorescence in uninfected cells. To address this in the future, quantitative measurements could be taken to compare fluorescence intensity between mock and infected cells and find a threshold to discern real signal. Furthermore, higher resolution fluorescence and higher levels of correlation (onto the lamella or in 3D to the SXT) could have identified single RO formation events earlier in infection, for example using a cryo-confocal microscope. Also, alternative tags could be tested such as mNeonGreen, StayGold, or SunTag (Shaner *et al.*, 2013; Hirano *et al.*, 2022; Tanenbaum *et al.*, 2014). Furthermore, cryo-FIB-SEM instruments with integrated fluorescence (such as Thermo Fisher Scientific Arctis or Delmic METEOR attachment) or cryo-confocal fluorescence imaging (such as with Zeiss Airyscan or Leica STELLARIS cryo) could be used. Cryo-SIM data could also be correlated to lamellae in 2D using beads around the lamellae. Furthermore, if smaller (and earlier) rIBV fluorescence foci could be accurately imaged via cryo-fluorescence microscopy, correlation to SXT data in 3D could be improved by using additional fluorescent fiducials and organelle dyes such as for lipid droplet dyes. Different methods of mapping fluorescence signal to ET data have also been proposed (Kukulski *et al.*, 2011). Plus, as used in this thesis, bead-based techniques for high precision correlation and 3D targeting have now become widely used (Allegretti *et al.*, 2020; Klumpe *et al.*, 2021; Bieber *et al.*, 2022). Overall, the number of infected cells was a limiting factor for imaging rIBV infected cells, therefore several other techniques could be used to concentrate the cells or membranes of interest onto grids. For example, since TwinStrep-GFP tagged SARS-CoV-2 nsp3-4 constructs were known to form DMVs, they could be purified by streptavidin affinity chromatography and seeded on grids (Huang *et al.*, 2024). So far, a method to separate DMVs and DMSs has not been devised

but if the DMSs contained a unique component, it could be used to purify these membranes onto grids for ET without milling. Fluorescence-activated cell sorting (FACS) was also used for cells transfected with TwinStrep-GFP tagged SARS-CoV-2 nsp3-4, so only cells exhibiting GFP fluorescence were seeded on grids (Huang *et al.*, 2024). This may not be compatible with the BeauR-eGFP-nsp2 tool because the infected cells may be unlikely to re-adhere to grids, but it could be interesting to try this for cells at earlier h pi. Otherwise, FACs would be a useful tool for sorting cells transfected with fluorescence tagged nsp constructs onto grids if the nsp constituents of the DMSs were known.

Concentrating the purified DMSs on grids or transfection for overexpression of factors that induce DMSs, assuming these could all be elucidated and that the DMSs could be recapitulated outside of infection conditions, could provide a larger data set of particles to push the STA resolution. Combining this with automated milling and improved fluorescence targeting could also increase the numbers of particles to be averaged and may improve the homogeneity of particles picked across different lamellae. Increasing the dataset with DMSs imaged at higher magnification would also contribute to determining the composition of DMSs.

The lack of uninfected cell controls for CLEM, cryo-SXT and cryo-FIB and cryo-ET could also be addressed in further experiments to emphasise that the RO structures are not a caveat of infection but are functioning in virus replication as is generally accepted (Snijder *et al.,* 2020). Examples of ultrastructural images of uninfected cell cytoplasm can be found in other publications such as: Doyle *et al.* (2019), Chichón *et al.* (2012), Loconte *et al.* (2021), and Castro *et al.* (2023), and the EM data bank (EMDB) (Iudin *et al.*, 2023).

Correlating cryo-SXT and cryo-ET from the same sample is a new challenge. Samples on grids for cryo-SXT typically have shorter blot times (Nahas *et al.*, 2022) compared to samples prepared for cryo-ET (Wolff *et al.*, 2020; Lai, 2023). For cryo-SXT, it is thought that the shorter blot time will retain the shape of the cells, and reduce any mechanical stress imposed, such that the native state and full volume of the cell is preserved. A continuous vitreous ice layer can also help equalise the X-ray dose given at each tilt angle. However, in cryo-FIB-SEM for cryo-ET, it is often important to be able to observe the topology of the cells under a thinner layer of ice. If SXT is completed on thinner samples, depending on the exposure time required to generate enough contrast to observe the ultrastructure of interest, the sample can devitrify because of the exposure to X-rays. Novel correlative light, electron and X-ray microscopy (CLEXM) techniques are being investigated. So far, these techniques have been used to begin to investigate SARS-CoV-2 entry (Groen *et al.*, 2024). Moreover, collaborations between SiriusXT and Tescan are developing the SXT100, with in-line fluorescence microscopy and SXT, to be compatible with the Amber cryo-FIB-SEM and Coral software for preparation of lamellae for cryo-ET from the same sample imaged by SXT (SiriusXT, 2024). To achieve this, they used a universal sample holder, and early results indicated that the final lamellae were not damaged by the SXT. Varying the X-ray dose required to image the ultrastructure of interest by SXT (to suit the sample size, composition, and thickness) may affect the quality of the final lamellae used for cryo-ET. Further SXT experiments would also improve the robustness of statistics comparing mitochondria size and numbers between uninfected and infected cells.

6.4 Conclusion

In summary, the structure of the IBV RO has been studied using a correlative workflow over multiple scales and in cryogenically preserved cells. The correlative workflow employed a fluorescent recombinant virus to directly label RO membranes for *in situ* ultrastructural interrogation. DMV- and DMS-like structures were observed over large volumes in vitreous infected cells by cryo-SXT. Furthermore, the DMSs were imaged using cryo-ET for the first time. The preservation of the macromolecular components using these techniques revealed that proteins span the double membrane of zER and DMSs, indicating that they are distinct from DMVs, and that the DMSs contain layered protein lattices. The highly ordered structure of the DMSs highlights that they may have a specific function. Consequently, further experiments are required to elucidate the components of the DMS which may provide important clues to their roles in viral replication. RO biogenesis hypotheses were also suggested by the observations. The DMSs were suggested to form via wrapping of zER around a uniform protein shell binding in the interior of the DMSs. Then, DMV and pore formation were suggested to be simultaneous before RNA synthesis fills the vesicle lumen and the DMV grows. These findings, alongside the correlative imaging tools and workflow, will aid future studies into the composition and function of CoV ROs, in particular DMSs, and ultimately contribute to a wider understanding of +RNA virus replication.

Chapter 7. Bibliography

Aktepe, T.E. *et al.* (2017) 'The Host Protein Reticulon 3.1A Is Utilized by Flaviviruses to Facilitate Membrane Remodelling', *Cell Reports*, 21(6), pp. 1639–1654. Available at: https://doi.org/10.1016/j.celrep.2017.10.055.

Al-Amoudi, A. *et al.* (2004) 'Cryo-electron microscopy of vitreous sections', *The EMBO Journal*, 23(18), pp. 3583–3588. Available at: https://doi.org/10.1038/sj.emboj.7600366.

Allegretti, M. *et al.* (2020) 'In-cell architecture of the nuclear pore and snapshots of its turnover', *Nature*, 586(7831), pp. 796–800. Available at: https://doi.org/10.1038/s41586-020-2670-5.

Almeida, J.D. and Tyrrell, D.A.J. (1967) 'The Morphology of Three Previously Uncharacterized Human Respiratory Viruses that Grow in Organ Culture', *Journal of General Virology*, 1(2), pp. 175–178. Available at: https://doi.org/10.1099/0022-1317-1-2-175.

Alonso-Caplen, F.V. *et al.* (1984) 'Replication and morphogenesis of avian coronavirus in Vero cells and their inhibition by monensin', *Virus Research*, 1(2), pp. 153–167. Available at: https://doi.org/10.1016/0168-1702(84)90070-4.

Álvarez, E. *et al.* (2010) 'The envelope protein of severe acute respiratory syndrome coronavirus interacts with the non-structural protein 3 and is ubiquitinated', *Virology*, 402(2), pp. 281–291. Available at: https://doi.org/10.1016/j.virol.2010.03.015.

Angeletti, S. et al. (2020) 'COVID-2019: The role of the nsp2 and nsp3 in its pathogenesis', Journal of Medical Virology, 92(6), pp. 584–588. Available at: https://doi.org/10.1002/jmv.25719.

Angelini, M.M. *et al.* (2013) 'Severe Acute Respiratory Syndrome Coronavirus Nonstructural Proteins 3, 4, and 6 Induce Double-Membrane Vesicles', *mBio*, 4(4), p. 10.1128/mbio.00524-13. Available at: https://doi.org/10.1128/mbio.00524-13.

Armesto, M. *et al.* (2012) 'Coronavirus Reverse Genetics', in *Reverse Genetics of RNA Viruses*. John Wiley & Sons, Ltd, pp. 25–63. Available at: https://doi.org/10.1002/9781118405338.ch2.

Arnold, J. *et al.* (2016) 'Site-Specific Cryo-focused Ion Beam Sample Preparation Guided by 3D Correlative Microscopy', *Biophysical Journal*, 110(4), pp. 860–869. Available at: https://doi.org/10.1016/j.bpj.2015.10.053.

Ávila-Pérez, G. *et al.* (2022) 'Architecture of torovirus replicative organelles', *Molecular Microbiology*, 117(4), pp. 837–850. Available at: https://doi.org/10.1111/mmi.14875.

Ávila-Pérez, G., Rejas, M.T. and Rodríguez, D. (2016) 'Ultrastructural characterization of membranous torovirus replication factories', *Cellular Microbiology*, 18(12), pp. 1691–1708. Available at: https://doi.org/10.1111/cmi.12620.

Bank, R.P.D. (no date) *RCSB PDB - 7F52: Crystal Structure of IBV Nsp2*. Available at: https://www.rcsb.org/structure/7F52 (Accessed: 15 September 2024).

Bárcena, M. *et al.* (2009) 'Cryo-electron tomography of mouse hepatitis virus: Insights into the structure of the coronavirion', *Proceedings of the National Academy of Sciences*, 106(2), pp. 582–587. Available at: https://doi.org/10.1073/pnas.0805270106.

Barnard, T.R. *et al.* (2021) 'Molecular Determinants of Flavivirus Virion Assembly', *Trends in Biochemical Sciences*, 46(5), pp. 378–390. Available at: https://doi.org/10.1016/j.tibs.2020.12.007.

Baudoux, P. *et al.* (1998) 'Coronavirus Pseudoparticles Formed with Recombinant M and E Proteins Induce Alpha Interferon Synthesis by Leukocytes', *Journal of Virology*, 72(11), pp. 8636–8643. Available at: https://doi.org/10.1128/jvi.72.11.8636-8643.1998.

Bäuerlein, F.J.B. and Baumeister, W. (2021) 'Towards Visual Proteomics at High Resolution', *Journal of Molecular Biology*, 433(20), p. 167187. Available at: https://doi.org/10.1016/j.jmb.2021.167187.

Beachboard, D.C., Anderson-Daniels, J.M. and Denison, M.R. (2015) 'Mutations across Murine Hepatitis Virus nsp4 Alter Virus Fitness and Membrane Modifications', *Journal of Virology*, 89(4), pp. 2080–2089. Available at: https://doi.org/10.1128/jvi.02776-14.

de Beijer, N.L., Snijder, E.J. and Bárcena, M. (2024) 'A Cool Look at Positive-Strand RNA Virus Replication Organelles: New Insights from Cryo–Electron Microscopy', *Annual Review of Biochemistry*, 93(Volume 93, 2024), pp. 163–187. Available at: https://doi.org/10.1146/annurev-biochem-052521-115736.

Belov, G.A. *et al.* (2012) 'Complex Dynamic Development of Poliovirus Membranous Replication Complexes', *Journal of Virology*, 86(1), pp. 302–312. Available at: https://doi.org/10.1128/jvi.05937-11.

Bennett, R. and IJpelaar, J. (2005) 'Updated Estimates of the Costs Associated with Thirty Four Endemic Livestock Diseases in Great Britain: A Note', *Journal of Agricultural Economics*, 56(1), pp. 135–144. Available at: https://doi.org/10.1111/j.1477-9552.2005.tb00126.x.

Bentley, K. *et al.* (2013) 'Identification of a Noncanonically Transcribed Subgenomic mRNA of Infectious Bronchitis Virus and Other Gammacoronaviruses', *Journal of Virology*, 87(4), pp. 2128–2136. Available at: https://doi.org/10.1128/jvi.02967-12.

Bentley, K., Armesto, M. and Britton, P. (2013) 'Infectious Bronchitis Virus as a Vector for the Expression of Heterologous Genes', *PLoS ONE*, 8(6), p. e67875. Available at: https://doi.org/10.1371/journal.pone.0067875.

Bepler, T. *et al.* (2020) 'Topaz-Denoise: general deep denoising models for cryoEM and cryoET', *Nature Communications*, 11(1), p. 5208. Available at: https://doi.org/10.1038/s41467-020-18952-1.

Berger, C. *et al.* (2023) 'Cryo-electron tomography on focused ion beam lamellae transforms structural cell biology', *Nature Methods*, 20(4), pp. 499–511. Available at: https://doi.org/10.1038/s41592-023-01783-5.

Berry, D.M. *et al.* (1964) 'The structure of infectious bronchitis virus', *Virology*, 23(3), pp. 403–407. Available at: https://doi.org/10.1016/0042-6822(64)90263-6.

Bessa, L.M. *et al.* (2022) 'The intrinsically disordered SARS-CoV-2 nucleoprotein in dynamic complex with its viral partner nsp3a', *Science Advances*, 8(3), p. eabm4034. Available at: https://doi.org/10.1126/sciadv.abm4034.

Bhatt, P.R. et al. (2021) 'Structural basis of ribosomal frameshifting during translation of the SARS-CoV-2 RNA genome', Science, 372(6548), pp. 1306–1313. Available at: https://doi.org/10.1126/science.abf3546.

Bickerton, E. *et al.* (2018) 'The S2 Subunit of Infectious Bronchitis Virus Beaudette Is a Determinant of Cellular Tropism', *Journal of Virology*, 92(19), p. 10.1128/jvi.01044-18. Available at: https://doi.org/10.1128/jvi.01044-18.

Bickerton, E., Keep, S.M. and Britton, P. (2017) 'Reverse Genetics System for the Avian Coronavirus Infectious Bronchitis Virus', in D.R. Perez (ed.) *Reverse Genetics of RNA Viruses: Methods and Protocols*. New York, NY: Springer, pp. 83–102. Available at: https://doi.org/10.1007/978-1-4939-6964-7_6.

Bieber, A. *et al.* (2022) 'In situ structural analysis reveals membrane shape transitions during autophagosome formation', *Proceedings of the National Academy of Sciences*, 119(39), p. e2209823119. Available at: https://doi.org/10.1073/pnas.2209823119.

Bienz, K. *et al.* (1992) 'Structural and functional characterization of the poliovirus replication complex', *Journal of Virology*, 66(5), pp. 2740–2747. Available at: https://doi.org/10.1128/jvi.66.5.2740-2747.1992.

Bílý, T. *et al.* (2015) 'Electron Tomography Analysis of Tick-Borne Encephalitis Virus Infection in Human Neurons', *Scientific Reports*, 5(1), p. 10745. Available at: https://doi.org/10.1038/srep10745.

Binns, M.M. *et al.* (1986) 'Nucleotide sequence encoding the membrane protein of the IBV strain 6/82.', *Nucleic Acids Research*, 14(13), p. 5558.

den Boon, J.A. *et al.* (2024) 'Positive-strand RNA virus genome replication organelles: structure, assembly, control', *Trends in Genetics*, 40(8), pp. 681–693. Available at: https://doi.org/10.1016/j.tig.2024.04.003.

den Boon, J.A. and Ahlquist, P. (2010) 'Organelle-Like Membrane Compartmentalization of Positive-Strand RNA Virus Replication Factories', *Annual Review of Microbiology*, 64(Volume 64, 2010), pp. 241–256. Available at: https://doi.org/10.1146/annurev.micro.112408.134012.

Boscarino, J.A. *et al.* (2008) 'Envelope Protein Palmitoylations Are Crucial for Murine Coronavirus Assembly', *Journal of Virology*, 82(6), pp. 2989–2999. Available at: https://doi.org/10.1128/jvi.01906-07.

Bouvet, M. *et al.* (2010) 'In Vitro Reconstitution of SARS-Coronavirus mRNA Cap Methylation', *PLOS Pathogens*, 6(4), p. e1000863. Available at: https://doi.org/10.1371/journal.ppat.1000863.

Bouwman, K.M. et al. (2020) 'Three Amino Acid Changes in Avian Coronavirus Spike Protein Allow Binding to Kidney Tissue', Journal of Virology, 94(2), p. 10.1128/jvi.01363-19. Available at: https://doi.org/10.1128/jvi.01363-19.

Brierley, I., Digard, P. and Inglis, S.C. (1989) 'Characterization of an efficient coronavirus ribosomal frameshifting signal: Requirement for an RNA pseudoknot', Cell, 57(4), pp. 537–547. Available at: https://doi.org/10.1016/0092-8674(89)90124-4.

Brierley, I., Jenner, A.J. and Inglis, S.C. (1992) 'Mutational analysis of the "slippery-sequence" component of a coronavirus ribosomal frameshifting signal', *Journal of Molecular Biology*, 227(2), pp. 463–479. Available at: https://doi.org/10.1016/0022-2836(92)90901-U.

Britton, P. *et al.* (1996) 'Expression of bacteriophage T7 RNA polymerase in avian and mammalian cells by a recombinant fowlpox virus', *Journal of General Virology*, 77(5), pp. 963–967. Available at: https://doi.org/10.1099/0022-1317-77-5-963.

Britton, P. *et al.* (2005) 'Generation of a recombinant avian coronavirus infectious bronchitis virus using transient dominant selection', *Journal of Virological Methods*, 123(2), pp. 203–211. Available at: https://doi.org/10.1016/j.jviromet.2004.09.017.

Broekkamp, C.L., Weemaes, A.J. and Van Rossum, J.M. (1975) 'Does fenfluramine act via norfenfluramine', *The Journal of pharmacy and pharmacology*, 27(2), pp. 129–130. Available at: https://doi.org/10.1111/j.2042-7158.1975.tb09421.x.

von Brunn, A. *et al.* (2007) 'Analysis of Intraviral Protein-Protein Interactions of the SARS Coronavirus ORFeome', *PLOS ONE*, 2(5), p. e459. Available at: https://doi.org/10.1371/journal.pone.0000459.

Buchholz, T.-O. *et al.* (2018) 'Cryo-CARE: Content-Aware Image Restoration for Cryo-Transmission Electron Microscopy Data'. arXiv. Available at: https://doi.org/10.48550/arXiv.1810.05420.

Burkard, C. *et al.* (2014) 'Coronavirus Cell Entry Occurs through the Endo-/Lysosomal Pathway in a Proteolysis-Dependent Manner', *PLOS Pathogens*, 10(11), p. e1004502. Available at: https://doi.org/10.1371/journal.ppat.1004502.

Burt, A. *et al.* (2024) 'An image processing pipeline for electron cryo-tomography in RELION-5'. bioRxiv, p. 2024.04.26.591129. Available at: https://doi.org/10.1101/2024.04.26.591129.

Bykov, Y.S. *et al.* (2016) 'Correlative light and electron microscopy methods for the study of virus–cell interactions', *FEBS Letters*, 590(13), pp. 1877–1895. Available at: https://doi.org/10.1002/1873-3468.12153.

Cabantous, S., Terwilliger, T.C. and Waldo, G.S. (2005) 'Protein tagging and detection with engineered self-assembling fragments of green fluorescent protein', *Nature Biotechnology*, 23(1), pp. 102–107. Available at: https://doi.org/10.1038/nbt1044.

Cao, X. *et al.* (2015) 'Morphogenesis of Endoplasmic Reticulum Membrane-Invaginated Vesicles during Beet Black Scorch Virus Infection: Role of Auxiliary Replication Protein and New Implications of Three-Dimensional Architecture', *Journal of Virology*, 89(12), pp. 6184–6195. Available at: https://doi.org/10.1128/jvi.00401-15.

Carbajo-Lozoya, J. *et al.* (2014) 'Human coronavirus NL63 replication is cyclophilin A-dependent and inhibited by non-immunosuppressive cyclosporine A-derivatives including Alisporivir', *Virus Research*, 184, pp. 44–53. Available at: https://doi.org/10.1016/j.virusres.2014.02.010.

Carlson, L.-A. *et al.* (2008) 'Three-Dimensional Analysis of Budding Sites and Released Virus Suggests a Revised Model for HIV-1 Morphogenesis', *Cell Host & Microbe*, 4(6), pp. 592–599. Available at: https://doi.org/10.1016/j.chom.2008.10.013.

Casais, R. *et al.* (2001) 'Reverse Genetics System for the Avian Coronavirus Infectious Bronchitis Virus', *Journal of Virology*, 75(24), pp. 12359–12369. Available at: https://doi.org/10.1128/jvi.75.24.12359-12369.2001.

Casais, R. *et al.* (2003) 'Recombinant Avian Infectious Bronchitis Virus Expressing a Heterologous Spike Gene Demonstrates that the Spike Protein Is a Determinant of Cell Tropism', *Journal of Virology*, 77(16), pp. 9084–9089. Available at: https://doi.org/10.1128/jvi.77.16.9084-9089.2003.

Castaño-Rodriguez, C. *et al.* (2018) 'Role of Severe Acute Respiratory Syndrome Coronavirus Viroporins E, 3a, and 8a in Replication and Pathogenesis', *mBio*, 9(3), p. 10.1128/mbio.02325-17. Available at: https://doi.org/10.1128/mbio.02325-17.

Castro, V. *et al.* (2023) 'Three-Dimensional Remodeling of SARS-CoV2-Infected Cells Revealed by Cryogenic Soft X-ray Tomography', *ACS Nano*, 17(22), pp. 22708–22721. Available at: https://doi.org/10.1021/acsnano.3c07265.

Cavanagh, D. (2007) 'Coronavirus avian infectious bronchitis virus', *Veterinary Research*, 38(2), pp. 281–297. Available at: https://doi.org/10.1051/vetres:2006055.

Cavanagh, D (1997) *NS. Infectious bronchitis. In: Calnek BW BH, Beard CW, McDougald LR, Saif YM, editor. Diseases of Poultry, 10th Edn. Iowa: Iowa State Univeristy Press; 1997. p. 511-26.*

Cerikan, B. *et al.* (2020) 'A Non-Replicative Role of the 3' Terminal Sequence of the Dengue Virus Genome in Membranous Replication Organelle Formation', *Cell Reports*, 32(1). Available at: https://doi.org/10.1016/j.celrep.2020.107859.

Cesaro, T. and Michiels, T. (2021) 'Inhibition of PKR by Viruses', *Frontiers in Microbiology*, 12. Available at: https://doi.org/10.3389/fmicb.2021.757238.

Chan Zuckerberg Initiative (CZI) (2020) *Clonable In-situ Label for High-resolution Cellular Imaging.* Available at: https://chanzuckerberg.com/science/programs-resources/imaging/frontiers/clonable-in-situ-label-for-high-resolution-cellular-imaging/ (Accessed: 9 December 2024).

Chang, C. *et al.* (2013) 'Transient Oligomerization of the SARS-CoV N Protein – Implication for Virus Ribonucleoprotein Packaging', *PLOS ONE*, 8(5), p. e65045. Available at: https://doi.org/10.1371/journal.pone.0065045.

Chen, A. *et al.* (2024) 'A coronaviral pore-replicase complex links RNA synthesis and export from double-membrane vesicles', *Science Advances*, 10(45), p. eadq9580. Available at: https://doi.org/10.1126/sciadv.adq9580.

Chen, C.-Y. *et al.* (2007) 'Structure of the SARS Coronavirus Nucleocapsid Protein RNA-binding Dimerization Domain Suggests a Mechanism for Helical Packaging of Viral RNA', *Journal of Molecular Biology*, 368(4), pp. 1075–1086. Available at: https://doi.org/10.1016/j.jmb.2007.02.069.

Chen, Y. *et al.* (2009) 'Functional screen reveals SARS coronavirus nonstructural protein nsp14 as a novel cap N7 methyltransferase', *Proceedings of the National Academy of Sciences*, 106(9), pp. 3484–3489. Available at: https://doi.org/10.1073/pnas.0808790106.

Chichón, F.J. *et al.* (2012) 'Cryo X-ray nano-tomography of vaccinia virus infected cells', *Journal of Structural Biology*, 177(2), pp. 202–211. Available at: https://doi.org/10.1016/j.jsb.2011.12.001.

Chua, E.Y.D. *et al.* (2022) 'Better, Faster, Cheaper: Recent Advances in Cryo–Electron Microscopy', *Annual Review of Biochemistry*, 91(Volume 91, 2022), pp. 1–32. Available at: https://doi.org/10.1146/annurev-biochem-032620-110705.

Clementz, M.A. *et al.* (2008) 'Mutation in murine coronavirus replication protein nsp4 alters assembly of double membrane vesicles', *Virology*, 375(1), pp. 118–129. Available at: https://doi.org/10.1016/j.virol.2008.01.018.

Cohen, J.R., Lin, L.D. and Machamer, C.E. (2011) 'Identification of a Golgi Complex-Targeting Signal in the Cytoplasmic Tail of the Severe Acute Respiratory Syndrome Coronavirus Envelope Protein', *Journal of Virology*, 85(12), pp. 5794–5803. Available at: https://doi.org/10.1128/jvi.00060-11.

Collins, A. *et al.* (2011) 'Structural Organization of the Actin Cytoskeleton at Sites of Clathrin-Mediated Endocytosis', *Current Biology*, 21(14), pp. 1167–1175. Available at: https://doi.org/10.1016/j.cub.2011.05.048.

Conesa, J.J. *et al.* (2020) 'Unambiguous Intracellular Localization and Quantification of a Potent Iridium Anticancer Compound by Correlative 3D Cryo X-Ray Imaging', *Angewandte Chemie International Edition*, 59(3), pp. 1270–1278. Available at: https://doi.org/10.1002/anie.201911510.

Cong, Y. *et al.* (2020) 'Nucleocapsid Protein Recruitment to Replication-Transcription Complexes Plays a Crucial Role in Coronaviral Life Cycle', *Journal of Virology*, 94(4), p. 10.1128/jvi.01925-19. Available at: https://doi.org/10.1128/jvi.01925-19.

Cook, J.K.A., Jackwood, M. and Jones, R.C. (2012) 'The long view: 40 years of infectious bronchitis research', *Avian Pathology*, 41(3), pp. 239–250. Available at: https://doi.org/10.1080/03079457.2012.680432.

Cornillez-Ty, C.T. *et al.* (2009) 'Severe Acute Respiratory Syndrome Coronavirus Nonstructural Protein 2 Interacts with a Host Protein Complex Involved in Mitochondrial Biogenesis and Intracellular Signaling', *Journal of Virology*, 83(19), pp. 10314–10318. Available at: https://doi.org/10.1128/jvi.00842-09.

Corse, E. and Machamer, C.E. (2000) 'Infectious Bronchitis Virus E Protein Is Targeted to the Golgi Complex and Directs Release of Virus-Like Particles', *Journal of Virology*, 74(9), pp. 4319–4326. Available at: https://doi.org/10.1128/jvi.74.9.4319-4326.2000.

Corse, E. and Machamer, C.E. (2002) 'The Cytoplasmic Tail of Infectious Bronchitis Virus E Protein Directs Golgi Targeting', *Journal of Virology*, 76(3), pp. 1273–1284. Available at: https://doi.org/10.1128/jvi.76.3.1273-1284.2002.

Corse, E. and Machamer, C.E. (2003) 'The cytoplasmic tails of infectious bronchitis virus E and M proteins mediate their interaction', *Virology*, 312(1), pp. 25–34. Available at: https://doi.org/10.1016/S0042-6822(03)00175-2.

Cortese, M. *et al.* (2017) 'Ultrastructural Characterization of Zika Virus Replication Factories', *Cell Reports*, 18(9), pp. 2113–2123. Available at: https://doi.org/10.1016/j.celrep.2017.02.014.

Cortese, M. *et al.* (2020) 'Integrative Imaging Reveals SARS-CoV-2-Induced Reshaping of Subcellular Morphologies', *Cell Host & Microbe*, 28(6), pp. 853-866.e5. Available at: https://doi.org/10.1016/j.chom.2020.11.003.

Cottam, E.M. *et al.* (2011) 'Coronavirus nsp6 proteins generate autophagosomes from the endoplasmic reticulum via an omegasome intermediate', *Autophagy*, 7(11), pp. 1335–1347. Available at: https://doi.org/10.4161/auto.7.11.16642.

Cuconati, A., Molla, A. and Wimmer, E. (1998) 'Brefeldin A Inhibits Cell-Free, De Novo Synthesis of Poliovirus', *Journal of Virology*, 72(8), pp. 6456–6464. Available at: https://doi.org/10.1128/jvi.72.8.6456-6464.1998.

Dahmane, S. *et al.* (2022) 'Membrane-assisted assembly and selective secretory autophagy of enteroviruses', *Nature Communications*, 13(1), p. 5986. Available at: https://doi.org/10.1038/s41467-022-33483-7.

Dahmani, I., Ludwig, K. and Chiantia, S. (2019) 'Influenza A matrix protein M1 induces lipid membrane deformation via protein multimerization', *Bioscience Reports*, 39(8), p. BSR20191024. Available at: https://doi.org/10.1042/BSR20191024.

Danev, R., Yanagisawa, H. and Kikkawa, M. (2019) 'Cryo-Electron Microscopy Methodology: Current Aspects and Future Directions', *Trends in Biochemical Sciences*, 44(10), pp. 837–848. Available at: https://doi.org/10.1016/j.tibs.2019.04.008.

Darbyshire, J.H. *et al.* (1979) 'Taxonomic studies on strains of avian infectious bronchitis virus using neutralisation tests in tracheal organ cultures', *Archives of Virology*, 61(3), pp. 227–238. Available at: https://doi.org/10.1007/BF01318057.

Davies, H.A., Dourmashkin, R.R. and Macnaughton, M.R. (1981) 'Ribonucleoprotein of Avian Infectious Bronchitis Virus', *Journal of General Virology*, 53(1), pp. 67–74. Available at: https://doi.org/10.1099/0022-1317-53-1-67.

DeDiego, M.L. *et al.* (2007) 'A Severe Acute Respiratory Syndrome Coronavirus That Lacks the E Gene Is Attenuated In Vitro and In Vivo', *Journal of Virology*, 81(4), pp. 1701–1713. Available at: https://doi.org/10.1128/jvi.01467-06.

Delputte, P.L. *et al.* (2004) 'Effect of virus-specific antibodies on attachment, internalization and infection of porcine reproductive and respiratory syndrome virus in primary macrophages', *Veterinary Immunology and Immunopathology*, 102(3), pp. 179–188. Available at: https://doi.org/10.1016/j.vetimm.2004.09.007.

Deng, H. *et al.* (2024) 'Viral replication organelles: the highly complex and programmed replication machinery', *Frontiers in Microbiology*, 15. Available at: https://doi.org/10.3389/fmicb.2024.1450060.

Denison, M.R. *et al.* (2004) 'Cleavage between Replicase Proteins p28 and p65 of Mouse Hepatitis Virus Is Not Required for Virus Replication', *Journal of Virology*, 78(11), pp. 5957–5965. Available at: https://doi.org/10.1128/jvi.78.11.5957-5965.2004.

Diaz, A. and Wang, X. (2014) 'Bromovirus-induced remodeling of host membranes during viral RNA replication', *Current Opinion in Virology*, 9, pp. 104–110. Available at: https://doi.org/10.1016/j.coviro.2014.09.018.

Dinan, A.M. *et al.* (2019) 'Comparative Analysis of Gene Expression in Virulent and Attenuated Strains of Infectious Bronchitis Virus at Subcodon Resolution', *Journal of Virology*, 93(18), p. 10.1128/jvi.00714-19. Available at: https://doi.org/10.1128/jvi.00714-19.

Do, M. *et al.* (2015) 'Imaging and characterizing cells using tomography', *Archives of Biochemistry and Biophysics*, 581, pp. 111–121. Available at: https://doi.org/10.1016/j.abb.2015.01.011.

Doerflinger, S.Y. *et al.* (2017) 'Membrane alterations induced by nonstructural proteins of human norovirus', *PLOS Pathogens*, 13(10), p. e1006705. Available at: https://doi.org/10.1371/journal.ppat.1006705.

Dolan, K.A. *et al.* (2022) 'Structure of SARS-CoV-2 M protein in lipid nanodiscs', *eLife*. Edited by O. Pornillos and S.L. Sawyer, 11, p. e81702. Available at: https://doi.org/10.7554/eLife.81702.

Doyle, N. *et al.* (2018) 'Infectious Bronchitis Virus Nonstructural Protein 4 Alone Induces Membrane Pairing', *Viruses*, 10(9), p. 477. Available at: https://doi.org/10.3390/v10090477.

Doyle, N. *et al.* (2019) 'The Porcine Deltacoronavirus Replication Organelle Comprises Double-Membrane Vesicles and Zippered Endoplasmic Reticulum with Double-Membrane Spherules', *Viruses*, 11(11), p. 1030. Available at: https://doi.org/10.3390/v11111030.

Doyle, N. *et al.* (2021) 'Coronavirus RNA Synthesis Takes Place within Membrane-Bound Sites', *Viruses*, 13(12), p. 2540. Available at: https://doi.org/10.3390/v13122540.

Doyle, N. *et al.* (2024) 'A novel optimized pre-embedding antibody-labelling correlative light electron microscopy technique', *Access Microbiology*, 6(2), p. 000750.v3. Available at: https://doi.org/10.1099/acmi.0.000750.v3.

Doyle, N. and Hawes, P.C. (2020) 'Preparation of Cultured Cells Using High-Pressure Freezing and Freeze Substitution for Subsequent 2D or 3D Visualization in the Transmission Electron Microscope', in H.J. Maier and E. Bickerton (eds) *Coronaviruses: Methods and Protocols*. New York, NY: Springer US, pp. 263–275. Available at: https://doi.org/10.1007/978-1-0716-0900-2_19.

Du, X. *et al.* (2018) 'Replicase-mediated shielding of the poliovirus replicative double-stranded RNA to avoid recognition by MDA5', *Journal of General Virology*, 99(9), pp. 1199–1209. Available at: https://doi.org/10.1099/jgv.0.001111.

Dubochet, J. *et al.* (1988) 'Cryo-electron microscopy of vitrified specimens', *Quarterly Reviews of Biophysics*, 21(2), pp. 129–228. Available at: https://doi.org/10.1017/S0033583500004297.

Dubois-Dalcq, M., Holmes, K.V. and Rentier, B. (1984) 'Assembly of Coronaviridae', in M. Dubois-Dalcq, K.V. Holmes, and B. Rentier (eds) *Assembly of Enveloped RNA Viruses*. Vienna: Springer, pp. 100–119. Available at: https://doi.org/10.1007/978-3-7091-8756-2_7.

Dunoyer, P. *et al.* (2002) 'Intracellular Localization of the Peanut Clump Virus Replication Complex in Tobacco BY-2 Protoplasts Containing Green Fluorescent Protein-Labeled Endoplasmic Reticulum or Golgi Apparatus', *Journal of Virology*, 76(2), pp. 865–874. Available at: https://doi.org/10.1128/jvi.76.2.865-874.2002.

Egger, D. *et al.* (2000) 'Formation of the Poliovirus Replication Complex Requires Coupled Viral Translation, Vesicle Production, and Viral RNA Synthesis', *Journal of Virology*, 74(14), pp. 6570–6580. Available at: https://doi.org/10.1128/jvi.74.14.6570-6580.2000.

Egger, D. *et al.* (2002) 'Expression of Hepatitis C Virus Proteins Induces Distinct Membrane Alterations Including a Candidate Viral Replication Complex', *Journal of*

Virology, 76(12), pp. 5974–5984. Available at: https://doi.org/10.1128/jvi.76.12.5974-5984.2002.

Egloff, M.-P. *et al.* (2004) 'The severe acute respiratory syndrome-coronavirus replicative protein nsp9 is a single-stranded RNA-binding subunit unique in the RNA virus world', *Proceedings of the National Academy of Sciences*, 101(11), pp. 3792–3796. Available at: https://doi.org/10.1073/pnas.0307877101.

Emsley, P. *et al.* (2010) 'Features and development of Coot', *Acta Crystallographica Section D: Biological Crystallography*, 66(4), pp. 486–501. Available at: https://doi.org/10.1107/S0907444910007493.

Erickson, H.P. *et al.* (1997) 'Measurement and compensation of defocusing and aberrations by Fourier processing of electron micrographs', *Philosophical Transactions of the Royal Society of London. B, Biological Sciences*, 261(837), pp. 105–118. Available at: https://doi.org/10.1098/rstb.1971.0040.

Eriksson, K.K. *et al.* (2008) 'Mouse Hepatitis Virus Liver Pathology Is Dependent on ADP-Ribose-1"-Phosphatase, a Viral Function Conserved in the Alpha-Like Supergroup', *Journal of Virology*, 82(24), pp. 12325–12334. Available at: https://doi.org/10.1128/jvi.02082-08.

Ertel, K.J. *et al.* (2017) 'Cryo-electron tomography reveals novel features of a viral RNA replication compartment', *eLife*. Edited by W.I. Sundquist, 6, p. e25940. Available at: https://doi.org/10.7554/eLife.25940.

Esnault, E. *et al.* (2011) 'A novel chicken lung epithelial cell line: Characterization and response to low pathogenicity avian influenza virus', *Virus Research*, 159(1), pp. 32–42. Available at: https://doi.org/10.1016/j.virusres.2011.04.022.

Everest, H. *et al.* (2022) 'Known Cellular and Receptor Interactions of Animal and Human Coronaviruses: A Review', *Viruses*, 14(2), p. 351. Available at: https://doi.org/10.3390/v14020351.

Fahy, K. *et al.* (2021) 'Compact Cell Imaging Device (CoCID) provides insights into the cellular origins of viral infections', *Journal of Physics: Photonics*, 3(3), p. 031002. Available at: https://doi.org/10.1088/2515-7647/abfc5a.

Fan, H. *et al.* (2005) 'The Nucleocapsid Protein of Coronavirus Infectious Bronchitis Virus: Crystal Structure of Its N-Terminal Domain and Multimerization Properties', *Structure*, 13(12), pp. 1859–1868. Available at: https://doi.org/10.1016/j.str.2005.08.021.

Feldmüller, M. *et al.* (2024) 'Stepwise assembly and release of Tc toxins from Yersinia entomophaga', *Nature Microbiology*, 9(2), pp. 405–420. Available at: https://doi.org/10.1038/s41564-024-01611-2.

Fernandez, J.-J. *et al.* (2016) 'Removing Contamination-Induced Reconstruction Artifacts from Cryo-electron Tomograms', *Biophysical Journal*, 110(4), pp. 850–859. Available at: https://doi.org/10.1016/j.bpj.2015.10.043.

Fernández de Castro, I. *et al.* (2017) 'Three-dimensional imaging of the intracellular assembly of a functional viral RNA replicase complex', *Journal of Cell Science*. Edited by A. Ewald, 130(1), pp. 260–268. Available at: https://doi.org/10.1242/jcs.181586.

Ferraris, P. *et al.* (2013) 'Sequential biogenesis of host cell membrane rearrangements induced by hepatitis C virus infection', *Cellular and Molecular Life Sciences*, 70(7), pp. 1297–1306. Available at: https://doi.org/10.1007/s00018-012-1213-0.

Finkel, Y. *et al.* (2021) 'The coding capacity of SARS-CoV-2', *Nature*, 589(7840), pp. 125–130. Available at: https://doi.org/10.1038/s41586-020-2739-1.

Fischer, F. *et al.* (1998) 'Analysis of Constructed E Gene Mutants of Mouse Hepatitis Virus Confirms a Pivotal Role for E Protein in Coronavirus Assembly', *Journal of Virology*, 72(10), pp. 7885–7894. Available at: https://doi.org/10.1128/jvi.72.10.7885-7894.1998.

Florin, L. and Lang, T. (2018) 'Tetraspanin Assemblies in Virus Infection', *Frontiers in Immunology*, 9, p. 1140. Available at: https://doi.org/10.3389/fimmu.2018.01140.

Fontana, J. *et al.* (2010) 'Three-dimensional structure of Rubella virus factories', *Virology*, 405(2), pp. 579–591. Available at: https://doi.org/10.1016/j.virol.2010.06.043.

Freeman, M.C. *et al.* (2014) 'Coronavirus Replicase-Reporter Fusions Provide Quantitative Analysis of Replication and Replication Complex Formation', *Journal of Virology*, 88(10), pp. 5319–5327. Available at: https://doi.org/10.1128/jvi.00021-14.

Frolova, E.I. *et al.* (2010) 'Functional Sindbis Virus Replicative Complexes Are Formed at the Plasma Membrane', *Journal of Virology*, 84(22), pp. 11679–11695. Available at: https://doi.org/10.1128/jvi.01441-10.

Gadlage, M.J. *et al.* (2010) 'Murine Hepatitis Virus Nonstructural Protein 4 Regulates Virus-Induced Membrane Modifications and Replication Complex Function', *Journal of Virology*, 84(1), pp. 280–290. Available at: https://doi.org/10.1128/jvi.01772-09.

Gadlage, M.J., Graham, R.L. and Denison, M.R. (2008) 'Murine Coronaviruses Encoding nsp2 at Different Genomic Loci Have Altered Replication, Protein Expression, and Localization', *Journal of Virology*, 82(23), pp. 11964–11969. Available at: https://doi.org/10.1128/jvi.01126-07.

Gaifas, L., Timmins, J. and Gutsche, I. (2023) 'blik: an extensible napari plugin for cryo-ET data visualisation, annotation and analysis'. bioRxiv, p. 2023.12.05.570263. Available at: https://doi.org/10.1101/2023.12.05.570263.

Gallagher, T.M. and Buchmeier, M.J. (2001) 'Coronavirus Spike Proteins in Viral Entry and Pathogenesis', *Virology*, 279(2), pp. 371–374. Available at: https://doi.org/10.1006/viro.2000.0757.

Gao, B. *et al.* (2021) 'Inhibition of anti-viral stress granule formation by coronavirus endoribonuclease nsp15 ensures efficient virus replication', *PLOS Pathogens*, 17(2), p. e1008690. Available at: https://doi.org/10.1371/journal.ppat.1008690.

Garriga, D. *et al.* (2021) 'Imaging of Virus-Infected Cells with Soft X-ray Tomography', *Viruses*, 13(11), p. 2109. Available at: https://doi.org/10.3390/v13112109.

Gautier, A. *et al.* (2008) 'An Engineered Protein Tag for Multiprotein Labeling in Living Cells', *Chemistry & Biology*, 15(2), pp. 128–136. Available at: https://doi.org/10.1016/j.chembiol.2008.01.007.

Gazina, E.V. *et al.* (2002) 'Differential Requirements for COPI Coats in Formation of Replication Complexes among Three Genera of Picornaviridae', *Journal of Virology*, 76(21), pp. 11113–11122. Available at: https://doi.org/10.1128/jvi.76.21.11113-11122.2002.

Ghosh, S. *et al.* (2020) 'β-Coronaviruses Use Lysosomes for Egress Instead of the Biosynthetic Secretory Pathway', *Cell*, 183(6), pp. 1520-1535.e14. Available at: https://doi.org/10.1016/j.cell.2020.10.039.

Giansanti, M.G., Belloni, G. and Gatti, M. (2007) 'Rab11 Is Required for Membrane Trafficking and Actomyosin Ring Constriction in Meiotic Cytokinesis of Drosophila Males',

Molecular Biology of the Cell, 18(12), pp. 5034–5047. Available at: https://doi.org/10.1091/mbc.e07-05-0415.

Gias, E. *et al.* (2008) 'Purification of human respiratory syncytial virus by ultracentrifugation in iodixanol density gradient', *Journal of Virological Methods*, 147(2), pp. 328–332. Available at: https://doi.org/10.1016/j.jviromet.2007.09.013.

Gillespie, L.K. *et al.* (2010) 'The Endoplasmic Reticulum Provides the Membrane Platform for Biogenesis of the Flavivirus Replication Complex', *Journal of Virology*, 84(20), pp. 10438–10447. Available at: https://doi.org/10.1128/jvi.00986-10.

Godeke, G.-J. *et al.* (2000) 'Assembly of Spikes into Coronavirus Particles Is Mediated by the Carboxy-Terminal Domain of the Spike Protein', *Journal of Virology*, 74(3), pp. 1566–1571. Available at: https://doi.org/10.1128/jvi.74.3.1566-1571.2000.

Goldsmith, C.S. *et al.* (no date) 'Ultrastructural Characterization of SARS Coronavirus - Volume 10, Number 2—February 2004 - Emerging Infectious Diseases journal - CDC'. Available at: https://doi.org/10.3201/eid1002.030913.

Gómez-Aix, C. *et al.* (2015) 'Melon necrotic spot virus Replication Occurs in Association with Altered Mitochondria', *Molecular Plant-Microbe Interactions®*, 28(4), pp. 387–397. Available at: https://doi.org/10.1094/MPMI-09-14-0274-R.

Gopal, A. *et al.* (2012) 'Visualizing large RNA molecules in solution', *RNA*, 18(2), pp. 284–299. Available at: https://doi.org/10.1261/rna.027557.111.

Gordon, D.E. et al. (2020) 'A SARS-CoV-2 protein interaction map reveals targets for drug repurposing', Nature, 583(7816), pp. 459–468. Available at: https://doi.org/10.1038/s41586-020-2286-9.

Gorelick, S. *et al.* (2011) 'High-efficiency Fresnel zone plates for hard X-rays by 100 keV e-beam lithography and electroplating', *Journal of Synchrotron Radiation*, 18(3), pp. 442–446. Available at: https://doi.org/10.1107/S0909049511002366.

Gorkhali, R. *et al.* (2021a) 'Structure and Function of Major SARS-CoV-2 and SARS-CoV Proteins', *Bioinformatics and Biology Insights*, 15, p. 11779322211025876. Available at: https://doi.org/10.1177/11779322211025876.

Gorkhali, R. *et al.* (2021b) 'Structure and Function of Major SARS-CoV-2 and SARS-CoV Proteins', *Bioinformatics and Biology Insights*, 15, p. 11779322211025876. Available at: https://doi.org/10.1177/11779322211025876.

Gosert, R. *et al.* (2002) 'RNA Replication of Mouse Hepatitis Virus Takes Place at Double-Membrane Vesicles', *Journal of Virology*, 76(8), pp. 3697–3708. Available at: https://doi.org/10.1128/jvi.76.8.3697-3708.2002.

Gosert, R. *et al.* (2003) 'Identification of the Hepatitis C Virus RNA Replication Complex in Huh-7 Cells Harboring Subgenomic Replicons', *Journal of Virology*, 77(9), pp. 5487–5492. Available at: https://doi.org/10.1128/jvi.77.9.5487-5492.2003.

Graham, R.L. *et al.* (2005) 'The nsp2 Replicase Proteins of Murine Hepatitis Virus and Severe Acute Respiratory Syndrome Coronavirus Are Dispensable for Viral Replication', *Journal of Virology*, 79(21), pp. 13399–13411. Available at: https://doi.org/10.1128/jvi.79.21.13399-13411.2005.

Graham, R.L. and Denison, M.R. (2006) 'Replication of Murine Hepatitis Virus Is Regulated by Papain-Like Proteinase 1 Processing of Nonstructural Proteins 1, 2, and 3', *Journal of Virology*, 80(23), pp. 11610–11620. Available at: https://doi.org/10.1128/jvi.01428-06.

van der Grein, S.G. *et al.* (2022) 'The encephalomyocarditis virus Leader promotes the release of virions inside extracellular vesicles via the induction of secretory autophagy', *Nature Communications*, 13(1), p. 3625. Available at: https://doi.org/10.1038/s41467-022-31181-y.

Grimley, P.M., Berezesky, I.K. and Friedman, R.M. (1968) 'Cytoplasmic Structures Associated with an Arbovirus Infection: Loci of Viral Ribonucleic Acid Synthesis', *Journal of Virology*, 2(11), pp. 1326–1338. Available at: https://doi.org/10.1128/jvi.2.11.1326-1338.1968.

Groen, J. *et al.* (2024) 'Multimodal and correlative imaging approaches to study early stages of SARS-CoV 2 infection', *BIO Web of Conferences*, 129, p. 13004. Available at: https://doi.org/10.1051/bioconf/202412913004.

Gui, M. *et al.* (2017) 'Electron microscopy studies of the coronavirus ribonucleoprotein complex', *Protein & Cell*, 8(3), pp. 219–224. Available at: https://doi.org/10.1007/s13238-016-0352-8.

Gulyaeva, A.A. and Gorbalenya, A.E. (2021) 'A nidovirus perspective on SARS-CoV-2', *Biochemical and Biophysical Research Communications*, 538, pp. 24–34. Available at: https://doi.org/10.1016/j.bbrc.2020.11.015.

Gupta, M. et al. (2021) 'CryoEM and AI reveal a structure of SARS-CoV-2 Nsp2, a multifunctional protein involved in key host processes'. bioRxiv, p. 2021.05.10.443524. Available at: https://doi.org/10.1101/2021.05.10.443524.

Gustafsson, M.G.L. *et al.* (2008) 'Three-Dimensional Resolution Doubling in Wide-Field Fluorescence Microscopy by Structured Illumination', *Biophysical Journal*, 94(12), pp. 4957–4970. Available at: https://doi.org/10.1529/biophysj.107.120345.

de Haan, C.A.M. *et al.* (1999) 'Mapping of the Coronavirus Membrane Protein Domains Involved in Interaction with the Spike Protein', *Journal of Virology*, 73(9), pp. 7441–7452. Available at: https://doi.org/10.1128/jvi.73.9.7441-7452.1999.

de Haan, C.A.M. *et al.* (2004) 'Cleavage Inhibition of the Murine Coronavirus Spike Protein by a Furin-Like Enzyme Affects Cell-Cell but Not Virus-Cell Fusion', *Journal of Virology*, 78(11), pp. 6048–6054. Available at: https://doi.org/10.1128/JVI.78.11.6048-6054.2004.

de Haan, C.A.M., Molinari, M. and Reggiori, F. (2010) 'Autophagy-independent LC3 function in vesicular traffic', *Autophagy*, 6(7), pp. 994–996. Available at: https://doi.org/10.4161/auto.6.7.13309.

Haase, D. *et al.* (2023) 'Tetraspanner-based nanodomains modulate BAR domain-induced membrane curvature', *EMBO reports*, 24(12), p. e57232. Available at: https://doi.org/10.15252/embr.202357232.

Hagemeijer, M.C. *et al.* (2010) 'Dynamics of Coronavirus Replication-Transcription Complexes', *Journal of Virology*, 84(4), pp. 2134–2149. Available at: https://doi.org/10.1128/jvi.01716-09.

Hagemeijer, M.C. *et al.* (2011) 'Mobility and Interactions of Coronavirus Nonstructural Protein 4', *Journal of Virology*, 85(9), pp. 4572–4577. Available at: https://doi.org/10.1128/jvi.00042-11.

Hagemeijer, M.C. *et al.* (2012) 'Visualizing Coronavirus RNA Synthesis in Time by Using Click Chemistry', *Journal of Virology*, 86(10), pp. 5808–5816. Available at: https://doi.org/10.1128/jvi.07207-11.

Hagemeijer, M.C. *et al.* (2014) 'Membrane rearrangements mediated by coronavirus nonstructural proteins 3 and 4', *Virology*, 458–459, pp. 125–135. Available at: https://doi.org/10.1016/j.virol.2014.04.027.

Hagen, W.J.H., Wan, W. and Briggs, J.A.G. (2017) 'Implementation of a cryo-electron tomography tilt-scheme optimized for high resolution subtomogram averaging', *Journal of Structural Biology*, 197(2), pp. 191–198. Available at: https://doi.org/10.1016/j.jsb.2016.06.007.

Han, X., Huang, Y. and Hao, J. (2024) 'Avian Coronavirus Infectious Bronchitis Virus Activates Mitochondria-Mediated Apoptosis Pathway and Affects Viral Replication by Inducing Reactive Oxygen Species Production in Chicken HD11 Cells', *Biology*, 13(7), p. 491. Available at: https://doi.org/10.3390/biology13070491.

Harak, C. and Lohmann, V. (2015) 'Ultrastructure of the replication sites of positive-strand RNA viruses', *Virology*, 479–480, pp. 418–433. Available at: https://doi.org/10.1016/j.virol.2015.02.029.

Harapin, J. *et al.* (2015) 'Structural analysis of multicellular organisms with cryo-electron tomography', *Nature Methods*, 12(7), pp. 634–636. Available at: https://doi.org/10.1038/nmeth.3401.

Harkiolaki, M. *et al.* (2018) 'Cryo-soft X-ray tomography: using soft X-rays to explore the ultrastructure of whole cells', *Emerging Topics in Life Sciences*. Edited by M. Ubbink and A. Perrakis, 2(1), pp. 81–92. Available at: https://doi.org/10.1042/ETLS20170086.

Hartenian, E. *et al.* (2020) 'The molecular virology of coronaviruses', *Journal of Biological Chemistry*, 295(37), pp. 12910–12934. Available at: https://doi.org/10.1074/jbc.REV120.013930.

Heinze, C. *et al.* (2004) 'Pelargonium necrotic spot virus: a new member of the genus Tombusvirus', *Archives of Virology*, 149(8), pp. 1527–1539. Available at: https://doi.org/10.1007/s00705-004-0319-6.

van Hemert, M.J., van den Worm, S.H.E., *et al.* (2008) 'SARS-Coronavirus Replication/Transcription Complexes Are Membrane-Protected and Need a Host Factor for Activity In Vitro', *PLOS Pathogens*, 4(5), p. e1000054. Available at: https://doi.org/10.1371/journal.ppat.1000054.

van Hemert, M.J., de Wilde, A.H., *et al.* (2008) 'The in Vitro RNA Synthesizing Activity of the Isolated Arterivirus Replication/Transcription Complex Is Dependent on a Host Factor *', *Journal of Biological Chemistry*, 283(24), pp. 16525–16536. Available at: https://doi.org/10.1074/jbc.M708136200.

Hengel, S. *et al.* (2013) 'Reverse Genetics of RNA Viruses: Applications and Perspectives', in, pp. 289–317. Available at: https://doi.org/10.1002/9781118405338.ch10.

Hensel, Z. (2022) 'Predicted binding interface between coronavirus nsp3 and nsp4'. bioRxiv, p. 2022.03.05.483145. Available at: https://doi.org/10.1101/2022.03.05.483145.

Himly, M. *et al.* (1998) 'The DF-1 Chicken Fibroblast Cell Line: Transformation Induced by Diverse Oncogenes and Cell Death Resulting from Infection by Avian Leukosis Viruses', *Virology*, 248(2), pp. 295–304. Available at: https://doi.org/10.1006/viro.1998.9290.

Hirano, M. *et al.* (2022) 'A highly photostable and bright green fluorescent protein', *Nature Biotechnology*, 40(7), pp. 1132–1142. Available at: https://doi.org/10.1038/s41587-022-01278-2.

Hodgson, T. *et al.* (2004) 'Recombinant Infectious Bronchitis Coronavirus Beaudette with the Spike Protein Gene of the Pathogenic M41 Strain Remains Attenuated but Induces Protective Immunity', *Journal of Virology*, 78(24), pp. 13804–13811. Available at: https://doi.org/10.1128/jvi.78.24.13804-13811.2004.

van der Hoeven, B. *et al.* (2016) 'Biogenesis and architecture of arterivirus replication organelles', *Virus Research*, 220, pp. 70–90. Available at: https://doi.org/10.1016/j.virusres.2016.04.001.

Hoffmann, C. *et al.* (2010) 'Fluorescent labeling of tetracysteine-tagged proteins in intact cells', *Nature Protocols*, 5(10), pp. 1666–1677. Available at: https://doi.org/10.1038/nprot.2010.129.

Hogue, B.G. and Machamer, C.E. (2007) 'Coronavirus Structural Proteins and Virus Assembly', in *Nidoviruses*. John Wiley & Sons, Ltd, pp. 179–200. Available at: https://doi.org/10.1128/9781555815790.ch12.

Horstmann, A. *et al.* (2024) 'A service-based approach to cryoEM facility processing pipelines at eBIC', *Acta Crystallographica Section D: Structural Biology*, 80(3), pp. 174–180. Available at: https://doi.org/10.1107/S2059798324000986.

Huang, Q. *et al.* (2004) 'Structure of the N-terminal RNA-binding domain of the SARS CoV nucleocapsid protein', *Biochemistry*, 43(20), pp. 6059–6063. Available at: https://doi.org/10.1021/bi036155b.

Huang, Y. *et al.* (2024) 'Molecular architecture of coronavirus double-membrane vesicle pore complex', *Nature*, pp. 1–8. Available at: https://doi.org/10.1038/s41586-024-07817-y.

Hurst, K.R., Koetzner, C.A. and Masters, P.S. (2013) 'Characterization of a Critical Interaction between the Coronavirus Nucleocapsid Protein and Nonstructural Protein 3 of the Viral Replicase-Transcriptase Complex', *Journal of Virology*, 87(16), pp. 9159–9172. Available at: https://doi.org/10.1128/jvi.01275-13.

Hyde, J.L. *et al.* (2009) 'Mouse Norovirus Replication Is Associated with Virus-Induced Vesicle Clusters Originating from Membranes Derived from the Secretory Pathway',

Journal of Virology, 83(19), pp. 9709–9719. Available at: https://doi.org/10.1128/jvi.00600-09.

Irigoyen, N. *et al.* (2016) 'High-Resolution Analysis of Coronavirus Gene Expression by RNA Sequencing and Ribosome Profiling', *PLOS Pathogens*, 12(2), p. e1005473. Available at: https://doi.org/10.1371/journal.ppat.1005473.

Iudin, A. *et al.* (2023) 'EMPIAR: the Electron Microscopy Public Image Archive', *Nucleic Acids Research*, 51(D1), pp. D1503–D1511. Available at: https://doi.org/10.1093/nar/gkac1062.

Jackwood, M.W. and de Wit, S. (2013) 'Infectious Bronchitis', in *Diseases of Poultry*. John Wiley & Sons, Ltd, pp. 139–159. Available at: https://doi.org/10.1002/9781119421481.ch4.

Jadhav, A.C. and Kounatidis, I. (2023) 'Correlative Cryo-imaging Using Soft X-Ray Tomography for the Study of Virus Biology in Cells and Tissues', in S. Vijayakrishnan, Y. Jiu, and J.R. Harris (eds) *Virus Infected Cells*. Cham: Springer International Publishing, pp. 169–196. Available at: https://doi.org/10.1007/978-3-031-40086-5_6.

Jarsch, I.K., Daste, F. and Gallop, J.L. (2016) 'Membrane curvature in cell biology: An integration of molecular mechanisms', *The Journal of cell biology*, 214(4), pp. 375–387. Available at: https://doi.org/10.1083/jcb.201604003.

Jayaram, H. *et al.* (2006) 'X-Ray Structures of the N- and C-Terminal Domains of a Coronavirus Nucleocapsid Protein: Implications for Nucleocapsid Formation', *Journal of Virology*, 80(13), pp. 6612–6620. Available at: https://doi.org/10.1128/jvi.00157-06.

Jiao, P. *et al.* (2023) 'SARS-CoV-2 nonstructural protein 6 triggers endoplasmic reticulum stress-induced autophagy to degrade STING1', *Autophagy*, 19(12), pp. 3113–3131. Available at: https://doi.org/10.1080/15548627.2023.2238579.

Jimenez-Guardeño, J.M. *et al.* (2015) 'Identification of the Mechanisms Causing Reversion to Virulence in an Attenuated SARS-CoV for the Design of a Genetically Stable Vaccine', *PLOS Pathogens*, 11(10), p. e1005215. Available at: https://doi.org/10.1371/journal.ppat.1005215.

Jin, X. *et al.* (2018) 'Three-Dimensional Analysis of Chloroplast Structures Associated with Virus Infection', *Plant Physiology*, 176(1), pp. 282–294. Available at: https://doi.org/10.1104/pp.17.00871.

Jin, Z. *et al.* (2020) 'Structure of Mpro from SARS-CoV-2 and discovery of its inhibitors', *Nature*, 582(7811), pp. 289–293. Available at: https://doi.org/10.1038/s41586-020-2223-y.

Jones, R. *et al.* (2021) 'Capping pores of alphavirus nsP1 gate membranous viral replication factories', *Nature*, 589(7843), pp. 615–619. Available at: https://doi.org/10.1038/s41586-020-3036-8.

Jones, R. *et al.* (2023) 'Structural basis and dynamics of Chikungunya alphavirus RNA capping by nsP1 capping pores', *Proceedings of the National Academy of Sciences*, 120(12), p. e2213934120. Available at: https://doi.org/10.1073/pnas.2213934120.

Jonkman, J. et al. (2020) 'Tutorial: guidance for quantitative confocal microscopy', Nature Protocols, 15(5), pp. 1585–1611. Available at: https://doi.org/10.1038/s41596-020-0313-9.

Kallio, K. *et al.* (2013) 'Template RNA Length Determines the Size of Replication Complex Spherules for Semliki Forest Virus', *Journal of Virology*, 87(16), pp. 9125–9134. Available at: https://doi.org/10.1128/jvi.00660-13.

Kandela, I.K., Bleher, R. and Albrecht, R.M. (2008) 'Immunolabeling for Correlative Light and Electron Microscopy on Ultrathin Cryosections', *Microscopy and Microanalysis*, 14(2), pp. 159–165. Available at: https://doi.org/10.1017/S1431927608080239.

Kanjanahaluethai, A. *et al.* (2007) 'Membrane topology of murine coronavirus replicase nonstructural protein 3', *Virology*, 361(2), pp. 391–401. Available at: https://doi.org/10.1016/j.virol.2006.12.009.

Karimi, R., Coupland, C.E. and Rubinstein, J.L. (2024) 'Vesicle Picker: A tool for efficient identification of membrane protein complexes in vesicles', *Journal of Structural Biology*, 216(4), p. 108148. Available at: https://doi.org/10.1016/j.jsb.2024.108148.

Keane, S.C. and Giedroc, D.P. (2013) 'Solution Structure of Mouse Hepatitis Virus (MHV) nsp3a and Determinants of the Interaction with MHV Nucleocapsid (N) Protein', *Journal of Virology*, 87(6), pp. 3502–3515. Available at: https://doi.org/10.1128/jvi.03112-12.

Keep, S. *et al.* (2018) 'The ADRP domain from a virulent strain of infectious bronchitis virus is not sufficient to confer a pathogenic phenotype to the attenuated Beaudette strain', *Journal of General Virology*, 99(8), pp. 1097–1102. Available at: https://doi.org/10.1099/jgv.0.001098.

Keep, S., Sives, S., *et al.* (2020) 'Limited Cross-Protection against Infectious Bronchitis Provided by Recombinant Infectious Bronchitis Viruses Expressing Heterologous Spike Glycoproteins', *Vaccines*, 8(2), p. 330. Available at: https://doi.org/10.3390/vaccines8020330.

Keep, S., Oade, M.S., *et al.* (2020) 'Multiple novel non-canonically transcribed sub-genomic mRNAs produced by avian coronavirus infectious bronchitis virus', *Journal of General Virology*, 101(10), pp. 1103–1118. Available at: https://doi.org/10.1099/jgv.0.001474.

Keep, S., Stevenson-Leggett, P., *et al.* (2020) 'Temperature Sensitivity: A Potential Method for the Generation of Vaccines against the Avian Coronavirus Infectious Bronchitis Virus', *Viruses*, 12(7), p. 754. Available at: https://doi.org/10.3390/v12070754.

Keep, S.M., Bickerton, E. and Britton, P. (2015) 'Transient Dominant Selection for the Modification and Generation of Recombinant Infectious Bronchitis Coronaviruses', in H.J. Maier, E. Bickerton, and P. Britton (eds) *Coronaviruses: Methods and Protocols*. New York, NY: Springer, pp. 115–133. Available at: https://doi.org/10.1007/978-1-4939-2438-7_12.

Kelley, K. *et al.* (2022) 'Waffle Method: A general and flexible approach for improving throughput in FIB-milling', *Nature Communications*, 13(1), p. 1857. Available at: https://doi.org/10.1038/s41467-022-29501-3.

Khan, S., Roberts, J. and Wu, S.-B. (2019) 'Genes involved in mitochondrial biogenesis and function may not show synchronised responses to mitochondria in shell gland of laying chickens under infectious bronchitis virus challenge', *BMC Molecular and Cell Biology*, 20, p. 3. Available at: https://doi.org/10.1186/s12860-019-0190-7.

Kikkert, M. *et al.* (1999) 'Tomato Spotted Wilt Virus Particle Morphogenesis in Plant Cells', *Journal of Virology*, 73(3), pp. 2288–2297. Available at: https://doi.org/10.1128/jvi.73.3.2288-2297.1999.

Klatte, N., Shields, D.C. and Agoni, C. (2022) 'Modelling the Transitioning of SARS-CoV-2 nsp3 and nsp4 Lumenal Regions towards a More Stable State on Complex Formation', *International Journal of Molecular Sciences*, 24(1), p. 720. Available at: https://doi.org/10.3390/ijms24010720.

Klein, S. *et al.* (2020) 'SARS-CoV-2 structure and replication characterized by in situ cryo-electron tomography', *Nature Communications*, 11(1), p. 5885. Available at: https://doi.org/10.1038/s41467-020-19619-7.

Klein, S. *et al.* (2023) 'IFITM3 blocks influenza virus entry by sorting lipids and stabilizing hemifusion', *Cell Host & Microbe*, 31(4), pp. 616-633.e20. Available at: https://doi.org/10.1016/j.chom.2023.03.005.

Klumpe, S. *et al.* (2021) 'A modular platform for automated cryo-FIB workflows', *eLife*. Edited by A.T. Brunger, R.W. Aldrich, and B. Carragher, 10, p. e70506. Available at: https://doi.org/10.7554/eLife.70506.

Klumperman, J. *et al.* (1994) 'Coronavirus M proteins accumulate in the Golgi complex beyond the site of virion budding', *Journal of Virology*, 68(10), pp. 6523–6534. Available at: https://doi.org/10.1128/jvi.68.10.6523-6534.1994.

Knoops, K. *et al.* (2008) 'SARS-Coronavirus Replication Is Supported by a Reticulovesicular Network of Modified Endoplasmic Reticulum', *PLOS Biology*, 6(9), p. e226. Available at: https://doi.org/10.1371/journal.pbio.0060226.

Knoops, K. *et al.* (2012) 'Ultrastructural Characterization of Arterivirus Replication Structures: Reshaping the Endoplasmic Reticulum To Accommodate Viral RNA Synthesis', *Journal of Virology*, 86(5), pp. 2474–2487. Available at: https://doi.org/10.1128/JVI.06677-11.

Kopek, B.G. *et al.* (2007) 'Three-Dimensional Analysis of a Viral RNA Replication Complex Reveals a Virus-Induced Mini-Organelle', *PLOS Biology*, 5(9), p. e220. Available at: https://doi.org/10.1371/journal.pbio.0050220.

Kopek, B.G. *et al.* (2010) 'Nodavirus-induced membrane rearrangement in replication complex assembly requires replicase protein a, RNA templates, and polymerase activity', *Journal of Virology*, 84(24), pp. 12492–12503. Available at: https://doi.org/10.1128/JVI.01495-10.

Korneeva, N. et al. (2023) 'SARS-CoV-2 viral protein Nsp2 stimulates translation under normal and hypoxic conditions', Virology Journal, 20(1), p. 55. Available at: https://doi.org/10.1186/s12985-023-02021-2.

Kovalev, N. *et al.* (2016) 'Role of Viral RNA and Co-opted Cellular ESCRT-I and ESCRT-III Factors in Formation of Tombusvirus Spherules Harboring the Tombusvirus Replicase', *Journal of Virology*, 90(7), pp. 3611–3626. Available at: https://doi.org/10.1128/jvi.02775-15.

Kremer, J.R., Mastronarde, D.N. and McIntosh, J.R. (1996) 'Computer Visualization of Three-Dimensional Image Data Using IMOD', *Journal of Structural Biology*, 116(1), pp. 71–76. Available at: https://doi.org/10.1006/jsbi.1996.0013.

Kubo, H., Yamada, Y.K. and Taguchi, F. (1994) 'Localization of neutralizing epitopes and the receptor-binding site within the amino-terminal 330 amino acids of the murine coronavirus spike protein', *Journal of Virology*, 68(9), pp. 5403–5410. Available at: https://doi.org/10.1128/jvi.68.9.5403-5410.1994.

Kukulski, W. *et al.* (2011) 'Correlated fluorescence and 3D electron microscopy with high sensitivity and spatial precision', *Journal of Cell Biology*, 192(1), pp. 111–119. Available at: https://doi.org/10.1083/jcb.201009037.

Kuo, L. *et al.* (2016) 'Analyses of Coronavirus Assembly Interactions with Interspecies Membrane and Nucleocapsid Protein Chimeras', *Journal of Virology*, 90(9), pp. 4357–4368. Available at: https://doi.org/10.1128/jvi.03212-15.

Kuo, L. and Masters, P.S. (2002) 'Genetic Evidence for a Structural Interaction between the Carboxy Termini of the Membrane and Nucleocapsid Proteins of Mouse Hepatitis Virus', *Journal of Virology*, 76(10), pp. 4987–4999. Available at: https://doi.org/10.1128/jvi.76.10.4987-4999.2002.

Kounatidis, I. *et al.* (2020) '3D Correlative Cryo-Structured Illumination Fluorescence and Soft X-ray Microscopy Elucidates Reovirus Intracellular Release Pathway', *Cell*, 182(2), pp. 515-530.e17. Available at: https://doi.org/10.1016/j.cell.2020.05.051.

Lai, P.Y.A. (2023) *Using light and electron microscopy to understand the replication of aphthoviruses*. University of Oxford. Available at:

https://ora.ox.ac.uk/objects/uuid:14c553e6-bd83-4761-a7a4-d42a0beccf9e (Accessed: 9 December 2024).

Lambert, T.J. (2019) 'FPbase: a community-editable fluorescent protein database', *Nature Methods*, 16(4), pp. 277–278. Available at: https://doi.org/10.1038/s41592-019-0352-8.

Lamm, L. et al. (2022) 'MemBrain: A deep learning-aided pipeline for detection of membrane proteins in Cryo-electron tomograms', Computer Methods and Programs in Biomedicine, 224, p. 106990. Available at: https://doi.org/10.1016/j.cmpb.2022.106990.

Lamm, L. *et al.* (2024) 'MemBrain v2: an end-to-end tool for the analysis of membranes in cryo-electron tomography'. bioRxiv, p. 2024.01.05.574336. Available at: https://doi.org/10.1101/2024.01.05.574336.

Laurent, T. *et al.* (2022) 'Architecture of the chikungunya virus replication organelle', *eLife*. Edited by G. Zanetti and V. Malhotra, 11, p. e83042. Available at: https://doi.org/10.7554/eLife.83042.

Le Gros, M.A. *et al.* (2014) 'Biological soft X-ray tomography on beamline 2.1 at the Advanced Light Source', *Journal of Synchrotron Radiation*, 21(6), pp. 1370–1377. Available at: https://doi.org/10.1107/S1600577514015033.

Lee, J.Y. *et al.* (2022) 'Absolute quantitation of individual SARS-CoV-2 RNA molecules provides a new paradigm for infection dynamics and variant differences', *eLife*. Edited by M.P. Davenport, 11, p. e74153. Available at: https://doi.org/10.7554/eLife.74153.

Lei, J., Kusov, Y. and Hilgenfeld, R. (2018) 'Nsp3 of coronaviruses: Structures and functions of a large multi-domain protein', *Antiviral Research*, 149, pp. 58–74. Available at: https://doi.org/10.1016/j.antiviral.2017.11.001.

Li, P. *et al.* (2023) 'Nsp3-N interactions are critical for SARS-CoV-2 fitness and virulence', *Proceedings of the National Academy of Sciences*, 120(31), p. e2305674120. Available at: https://doi.org/10.1073/pnas.2305674120.

Li, S. *et al.* (2020) 'Regulation of the ER Stress Response by the Ion Channel Activity of the Infectious Bronchitis Coronavirus Envelope Protein Modulates Virion Release, Apoptosis, Viral Fitness, and Pathogenesis', *Frontiers in Microbiology*, 10. Available at: https://doi.org/10.3389/fmicb.2019.03022.

Li, Y. *et al.* (2016) 'The altered photosynthetic machinery during compatible virus infection', *Current Opinion in Virology*, 17, pp. 19–24. Available at: https://doi.org/10.1016/j.coviro.2015.11.002.

Liang, H. *et al.* (2022) 'Coronavirus Usurps the Autophagy-Lysosome Pathway and Induces Membranes Rearrangement for Infection and Pathogenesis', *Frontiers in Microbiology*, 13. Available at: https://doi.org/10.3389/fmicb.2022.846543.

Liang, J.Q. *et al.* (2019) 'N-Linked glycosylation of the membrane protein ectodomain regulates infectious bronchitis virus-induced ER stress response, apoptosis and pathogenesis', *Virology*, 531, pp. 48–56. Available at: https://doi.org/10.1016/j.virol.2019.02.017.

Liao, Y. *et al.* (2004) 'Expression of SARS-coronavirus envelope protein in *Escherichia coli* cells alters membrane permeability', *Biochemical and Biophysical Research Communications*, 325(1), pp. 374–380. Available at: https://doi.org/10.1016/j.bbrc.2004.10.050.

Liebschner, D. *et al.* (2019) 'Macromolecular structure determination using X-rays, neutrons and electrons: recent developments in Phenix', *Acta Crystallographica Section D: Structural Biology*, 75(10), pp. 861–877. Available at: https://doi.org/10.1107/S2059798319011471.

Limpens, R.W.A.L. *et al.* (2011) 'The Transformation of Enterovirus Replication Structures: a Three-Dimensional Study of Single- and Double-Membrane Compartments', *mBio*, 2(5), p. 10.1128/mbio.00166-11. Available at: https://doi.org/10.1128/mbio.00166-11.

Lin, D.H. and Hoelz, A. (2019) 'The Structure of the Nuclear Pore Complex (An Update)', *Annual Review of Biochemistry*, 88(Volume 88, 2019), pp. 725–783. Available at: https://doi.org/10.1146/annurev-biochem-062917-011901.

Linkam Scientific (2024) Cryogenium. Available at: https://www.linkam.co.uk/cryogenium (Accessed: 17 April 2025).

Liu, Y.-T. *et al.* (2022) 'Isotropic reconstruction for electron tomography with deep learning', *Nature Communications*, 13(1), p. 6482. Available at: https://doi.org/10.1038/s41467-022-33957-8.

Loconte, V., Chen, J.-H., Cortese, M., Ekman, A., Le Gros, M.A., *et al.* (2021) 'Using soft X-ray tomography for rapid whole-cell quantitative imaging of SARS-CoV-2-infected cells', *Cell Reports Methods*, 1(7), p. 100117. Available at: https://doi.org/10.1016/j.crmeth.2021.100117.

Lohmann, V. *et al.* (1999) 'Replication of Subgenomic Hepatitis C Virus RNAs in a Hepatoma Cell Line', *Science*, 285(5424), pp. 110–113. Available at: https://doi.org/10.1126/science.285.5424.110.

Lokhman, E., Rai, S. and Matthews, W. (2020) 'The Preparation of Chicken Kidney Cell Cultures for Virus Propagation', in H.J. Maier and E. Bickerton (eds) *Coronaviruses: Methods and Protocols*. New York, NY: Springer US, pp. 89–95. Available at: https://doi.org/10.1007/978-1-0716-0900-2_7.

Lontok, E., Corse, E. and Machamer, C.E. (2004) 'Intracellular Targeting Signals Contribute to Localization of Coronavirus Spike Proteins near the Virus Assembly Site', *Journal of*

Virology, 78(11), pp. 5913–5922. Available at: https://doi.org/10.1128/jvi.78.11.5913-5922.2004.

Lopez, L.A. *et al.* (2008) 'Importance of Conserved Cysteine Residues in the Coronavirus Envelope Protein', *Journal of Virology*, 82(6), pp. 3000–3010. Available at: https://doi.org/10.1128/jvi.01914-07.

Los, G.V. *et al.* (2008) 'HaloTag: A Novel Protein Labeling Technology for Cell Imaging and Protein Analysis', *ACS Chemical Biology*, 3(6), pp. 373–382. Available at: https://doi.org/10.1021/cb800025k.

Lou, Z. and Rao, Z. (2022) 'The Life of SARS-CoV-2 Inside Cells: Replication–Transcription Complex Assembly and Function', *Annual Review of Biochemistry*, 91(Volume 91, 2022), pp. 381–401. Available at: https://doi.org/10.1146/annurev-biochem-052521-115653.

Luini, A. *et al.* (2008) 'Morphogenesis of post-Golgi transport carriers', *Histochemistry and Cell Biology*, 129(2), pp. 153–161. Available at: https://doi.org/10.1007/s00418-007-0365-8.

Lundin, A. *et al.* (2014) 'Targeting Membrane-Bound Viral RNA Synthesis Reveals Potent Inhibition of Diverse Coronaviruses Including the Middle East Respiratory Syndrome Virus', *PLOS Pathogens*, 10(5), p. e1004166. Available at: https://doi.org/10.1371/journal.ppat.1004166.

Luo, C. *et al.* (2004) 'Nucleocapsid protein of SARS coronavirus tightly binds to human cyclophilin A', *Biochemical and Biophysical Research Communications*, 321(3), pp. 557–565. Available at: https://doi.org/10.1016/j.bbrc.2004.07.003.

Luytjes, W. *et al.* (1988) 'Sequence of mouse hepatitis virus A59 mRNA 2: Indications for RNA recombination between coronaviruses and influenza C virus', *Virology*, 166(2), pp. 415–422. Available at: https://doi.org/10.1016/0042-6822(88)90512-0.

Lyle, J.M. *et al.* (2002) 'Visualization and Functional Analysis of RNA-Dependent RNA Polymerase Lattices', *Science*, 296(5576), pp. 2218–2222. Available at: https://doi.org/10.1126/science.1070585.

Macnaughton, M.R., Davies, H.A. and Nermut, M.V. (1978) 'Ribonucleoprotein-like Structures from Coronavirus Particles', *Journal of General Virology*, 39(3), pp. 545–549. Available at: https://doi.org/10.1099/0022-1317-39-3-545.

Maeda, J. *et al.* (2001) 'Membrane topology of coronavirus E protein', *Virology*, 281(2), pp. 163–169. Available at: https://doi.org/10.1006/viro.2001.0818.

Maier, H.J., Hawes, P.C., *et al.* (2013) 'Infectious Bronchitis Virus Generates Spherules from Zippered Endoplasmic Reticulum Membranes', *mBio*, 4(5), p. 10.1128/mbio.00801-13. Available at: https://doi.org/10.1128/mbio.00801-13.

Maier, H.J., Cottam, E.M., *et al.* (2013) 'Visualizing the autophagy pathway in avian cells and its application to studying infectious bronchitis virus', *Autophagy*, 9(4), pp. 496–509. Available at: https://doi.org/10.4161/auto.23465.

Malone, B. *et al.* (2022) 'Structures and functions of coronavirus replication–transcription complexes and their relevance for SARS-CoV-2 drug design', *Nature Reviews Molecular Cell Biology*, 23(1), pp. 21–39. Available at: https://doi.org/10.1038/s41580-021-00432-z.

Manolaridis, I. *et al.* (2009) 'Structure of the C-terminal domain of nsp4 from feline coronavirus', *Acta Crystallographica Section D: Biological Crystallography*, 65(8), pp. 839–846. Available at: https://doi.org/10.1107/S0907444909018253.

Masters, P.S. (2006) 'The Molecular Biology of Coronaviruses', in *Advances in Virus Research*. Academic Press, pp. 193–292. Available at: https://doi.org/10.1016/S0065-3527(06)66005-3.

Mastronarde, D.N. and Held, S.R. (2017) 'Automated tilt series alignment and tomographic reconstruction in IMOD', *Journal of Structural Biology*, 197(2), pp. 102–113. Available at: https://doi.org/10.1016/j.jsb.2016.07.011.

Matsuyama, S. and Taguchi, F. (2009) 'Two-Step Conformational Changes in a Coronavirus Envelope Glycoprotein Mediated by Receptor Binding and Proteolysis', *Journal of Virology*, 83(21), pp. 11133–11141. Available at: https://doi.org/10.1128/jvi.00959-09.

Matthijs, M.G.R. *et al.* (2003) 'Ability of Massachusetts-type infectious bronchitis virus to increase colibacillosis susceptibility incommercial broilers: A comparison between vaccine and virulent field virus', *Avian Pathology*, 32(5), pp. 473–481. Available at: https://doi.org/10.1080/0307945031000154062.

McBride, C.E., Li, J. and Machamer, C.E. (2007) 'The Cytoplasmic Tail of the Severe Acute Respiratory Syndrome Coronavirus Spike Protein Contains a Novel Endoplasmic Reticulum Retrieval Signal That Binds COPI and Promotes Interaction with Membrane Protein', *Journal of Virology*, 81(5), pp. 2418–2428. Available at: https://doi.org/10.1128/jvi.02146-06.

McClenaghan, C. *et al.* (2020) 'Coronavirus Proteins as Ion Channels: Current and Potential Research', *Frontiers in Immunology*, 11. Available at: https://doi.org/10.3389/fimmu.2020.573339.

McDonald, K. (2007) 'Cryopreparation Methods for Electron Microscopy of Selected Model Systems', in *Methods in Cell Biology*. Academic Press (Cellular Electron Microscopy), pp. 23–56. Available at: https://doi.org/10.1016/S0091-679X(06)79002-1.

Meir, R. *et al.* (2004) 'Identification of a Novel Nephropathogenic Infectious Bronchitis Virus in Israel', *Avian Diseases*, 48(3), pp. 635–641. Available at: https://doi.org/10.1637/7107.

Melia, C.E. *et al.* (2017) 'Escaping Host Factor PI4KB Inhibition: Enterovirus Genomic RNA Replication in the Absence of Replication Organelles', *Cell Reports*, 21(3), pp. 587–599. Available at: https://doi.org/10.1016/j.celrep.2017.09.068.

Melia, C.E. *et al.* (2018) 'The Origin, Dynamic Morphology, and PI4P-Independent Formation of Encephalomyocarditis Virus Replication Organelles', *mBio*, 9(2), p. 10.1128/mbio.00420-18. Available at: https://doi.org/10.1128/mbio.00420-18.

Mendonça, L. *et al.* (2021) 'Correlative multi-scale cryo-imaging unveils SARS-CoV-2 assembly and egress', *Nature Communications*, 12(1), p. 4629. Available at: https://doi.org/10.1038/s41467-021-24887-y.

Mielanczyk, L. *et al.* (2014) 'Closer to the native state. Critical evaluation of cryo-techniques for Transmission Electron Microscopy: preparation of biological samples', *Folia Histochemica et Cytobiologica*, 52(1), pp. 1–17. Available at: https://doi.org/10.5603/FHC.2014.0001.

Mielech, A.M. *et al.* (2014) 'Nidovirus papain-like proteases: Multifunctional enzymes with protease, deubiquitinating and deISGylating activities', *Virus Research*, 194, pp. 184–190. Available at: https://doi.org/10.1016/j.virusres.2014.01.025.

Miguel, B., Pharr, G.T. and Wang, C. (2002) 'The role of feline aminopeptidase N as a receptor for infectious bronchitis virus', Archives of Virology, 147(11), pp. 2047–2056. Available at: https://doi.org/10.1007/s00705-002-0888-1.

Milewska, A. *et al.* (2020) 'Visualizing Coronavirus Entry into Cells', in H.J. Maier and E. Bickerton (eds) *Coronaviruses: Methods and Protocols*. New York, NY: Springer US, pp. 241–261. Available at: https://doi.org/10.1007/978-1-0716-0900-2_18.

Miller, S. and Krijnse-Locker, J. (2008) 'Modification of intracellular membrane structures for virus replication', *Nature Reviews Microbiology*, 6(5), pp. 363–374. Available at: https://doi.org/10.1038/nrmicro1890.

Millet, J.K. *et al.* (2016) 'A camel-derived MERS-CoV with a variant spike protein cleavage site and distinct fusion activation properties', *Emerging Microbes & Infections*, 5(1), pp. 1–9. Available at: https://doi.org/10.1038/emi.2016.125.

Ming, Z. *et al.* (2021) 'Crystal Structure of IBV Nsp2'. Available at: https://www.rcsb.org/structure/7F52 (Accessed: 9 August 2024).

Minskaia, E. *et al.* (2006) 'Discovery of an RNA virus 3'→5' exoribonuclease that is critically involved in coronavirus RNA synthesis', *Proceedings of the National Academy of Sciences*, 103(13), pp. 5108–5113. Available at: https://doi.org/10.1073/pnas.0508200103.

Miorin, L. *et al.* (2013) 'Three-Dimensional Architecture of Tick-Borne Encephalitis Virus Replication Sites and Trafficking of the Replicated RNA', *Journal of Virology*, 87(11), pp. 6469–6481. Available at: https://doi.org/10.1128/jvi.03456-12.

Möbius, W. and Posthuma, G. (2019) 'Sugar and ice: Immunoelectron microscopy using cryosections according to the Tokuyasu method', *Tissue and Cell*, 57, pp. 90–102. Available at: https://doi.org/10.1016/j.tice.2018.08.010.

Moor, H. (1987) 'Theory and Practice of High Pressure Freezing', in R.A. Steinbrecht and K. Zierold (eds) *Cryotechniques in Biological Electron Microscopy*. Berlin, Heidelberg: Springer, pp. 175–191. Available at: https://doi.org/10.1007/978-3-642-72815-0_8.

Movaqar, A. *et al.* (no date) 'Coronaviruses construct an interconnection way with ERAD and autophagy', *Future Microbiology*, 16(14), pp. 1135–1151. Available at: https://doi.org/10.2217/fmb-2021-0044.

Müller, C. *et al.* (2018) 'Inhibition of Cytosolic Phospholipase A2α Impairs an Early Step of Coronavirus Replication in Cell Culture', *Journal of Virology*, 92(4), p. 10.1128/jvi.01463-17. Available at: https://doi.org/10.1128/jvi.01463-17.

Myllys, M. *et al.* (2016) 'Herpes simplex virus 1 induces egress channels through marginalized host chromatin', *Scientific Reports*, 6(1), p. 28844. Available at: https://doi.org/10.1038/srep28844.

Nahas, K.L. *et al.* (2022) 'Near-native state imaging by cryo-soft-X-ray tomography reveals remodelling of multiple cellular organelles during HSV-1 infection', *PLOS Pathogens*, 18(7), p. e1010629. Available at: https://doi.org/10.1371/journal.ppat.1010629.

Netherton, C.L. and Wileman, T. (2011) 'Virus factories, double membrane vesicles and viroplasm generated in animal cells', *Current Opinion in Virology*, 1(5), pp. 381–387. Available at: https://doi.org/10.1016/j.coviro.2011.09.008.

Neufeldt, C.J. *et al.* (2016) 'The Hepatitis C Virus-Induced Membranous Web and Associated Nuclear Transport Machinery Limit Access of Pattern Recognition Receptors to Viral Replication Sites', *PLOS Pathogens*, 12(2), p. e1005428. Available at: https://doi.org/10.1371/journal.ppat.1005428.

Neufeldt, C.J. *et al.* (2019) 'ER-shaping atlastin proteins act as central hubs to promote flavivirus replication and virion assembly', *Nature Microbiology*, 4(12), pp. 2416–2429. Available at: https://doi.org/10.1038/s41564-019-0586-3.

Neufeldt, C.J. and Cortese, M. (2022) 'Membrane architects: how positive-strand RNA viruses restructure the cell', *Journal of General Virology*, 103(8), p. 001773. Available at: https://doi.org/10.1099/jgv.0.001773.

Neuman, B.W. *et al.* (2006) 'Supramolecular Architecture of Severe Acute Respiratory Syndrome Coronavirus Revealed by Electron Cryomicroscopy', *Journal of Virology*, 80(16), pp. 7918–7928. Available at: https://doi.org/10.1128/jvi.00645-06.

Neuman, B.W. *et al.* (2011) 'A structural analysis of M protein in coronavirus assembly and morphology', *Journal of Structural Biology*, 174(1), pp. 11–22. Available at: https://doi.org/10.1016/j.jsb.2010.11.021.

Neuman, B.W. *et al.* (2014) 'Atlas of coronavirus replicase structure', *Virus Research*, 194, p. 49. Available at: https://doi.org/10.1016/j.virusres.2013.12.004.

Neuman, B.W. (2016) 'Bioinformatics and functional analyses of coronavirus nonstructural proteins involved in the formation of replicative organelles', *Antiviral Research*, 135, pp. 97–107. Available at: https://doi.org/10.1016/j.antiviral.2016.10.005.

Neupane, K. et al. (2021) 'Structural dynamics of single SARS-CoV-2 pseudoknot molecules reveal topologically distinct conformers', Nature Communications, 12(1), p. 4749. Available at: https://doi.org/10.1038/s41467-021-25085-6.

Newbould, S.A. (1989) 'Studies of the reversal of the mammalian transformed phenotyp'. Available at: https://ethos.bl.uk/OrderDetails.do?uin=uk.bl.ethos.237073 (Accessed: 15 September 2024).

Nguyen-Dinh, V. and Herker, E. (2021) 'Ultrastructural Features of Membranous Replication Organelles Induced by Positive-Stranded RNA Viruses', *Cells*, 10(9), p. 2407. Available at: https://doi.org/10.3390/cells10092407.

Ni, X. *et al.* (2023) 'Structural insights into ribonucleoprotein dissociation by nucleocapsid protein interacting with non-structural protein 3 in SARS-CoV-2', *Communications Biology*, 6(1), pp. 1–12. Available at: https://doi.org/10.1038/s42003-023-04570-2.

Nieto-Torres, J.L. *et al.* (2014) 'Severe Acute Respiratory Syndrome Coronavirus Envelope Protein Ion Channel Activity Promotes Virus Fitness and Pathogenesis', *PLOS Pathogens*, 10(5), p. e1004077. Available at: https://doi.org/10.1371/journal.ppat.1004077.

Nishikiori, M. *et al.* (2022) 'Crowning Touches in Positive-Strand RNA Virus Genome Replication Complex Structure and Function', *Annual Review of Virology*, 9(Volume 9, 2022), pp. 193–212. Available at: https://doi.org/10.1146/annurev-virology-092920-021307.

Nugent, C.I. *et al.* (1999) 'Functional Coupling between Replication and Packaging of Poliovirus Replicon RNA', *Journal of Virology*, 73(1), pp. 427–435. Available at: https://doi.org/10.1128/jvi.73.1.427-435.1999.

Ojha, N.K. *et al.* (2021) 'Interplay of the ubiquitin proteasome system and the innate immune response is essential for the replication of infectious bronchitis virus', *Archives of Virology*, 166(8), pp. 2173–2185. Available at: https://doi.org/10.1007/s00705-021-05073-3.

Oostra, M. *et al.* (2007) 'Localization and Membrane Topology of Coronavirus Nonstructural Protein 4: Involvement of the Early Secretory Pathway in Replication',

Journal of Virology, 81(22), pp. 12323–12336. Available at: https://doi.org/10.1128/jvi.01506-07.

Oostra, M. *et al.* (2008) 'Topology and Membrane Anchoring of the Coronavirus Replication Complex: Not All Hydrophobic Domains of nsp3 and nsp6 Are Membrane Spanning', *Journal of Virology*, 82(24), pp. 12392–12405. Available at: https://doi.org/10.1128/jvi.01219-08.

Otón, J. *et al.* (2017) 'XTEND: Extending the depth of field in cryo soft X-ray tomography', *Scientific Reports*, 7(1), p. 45808. Available at: https://doi.org/10.1038/srep45808.

Oudshoorn, D. *et al.* (2017) 'Expression and Cleavage of Middle East Respiratory Syndrome Coronavirus nsp3-4 Polyprotein Induce the Formation of Double-Membrane Vesicles That Mimic Those Associated with Coronaviral RNA Replication', *mBio*, 8(6), p. 10.1128/mbio.01658-17. Available at: https://doi.org/10.1128/mbio.01658-17.

Pahmeier, F. *et al.* (2023) 'Identification of host dependency factors involved in SARS-CoV-2 replication organelle formation through proteomics and ultrastructural analysis', *Journal of Virology*, 97(11), pp. e00878-23. Available at: https://doi.org/10.1128/jvi.00878-23.

Pan, J. *et al.* (2008) 'Genome-Wide Analysis of Protein-Protein Interactions and Involvement of Viral Proteins in SARS-CoV Replication', *PLOS ONE*, 3(10), p. e3299. Available at: https://doi.org/10.1371/journal.pone.0003299.

Parsons, L.M. *et al.* (2019) 'Glycosylation of the viral attachment protein of avian coronavirus is essential for host cell and receptor binding', *Journal of Biological Chemistry*, 294(19), pp. 7797–7809. Available at: https://doi.org/10.1074/jbc.RA119.007532.

Parthasarathy, K. *et al.* (2012) 'Expression and purification of coronavirus envelope proteins using a modified β-barrel construct', *Protein Expression and Purification*, 85(1), pp. 133–141. Available at: https://doi.org/10.1016/j.pep.2012.07.005.

Paul, D. and Bartenschlager, R. (2013) 'Architecture and biogenesis of plus-strand RNA virus replication factories', *World Journal of Virology*, 2(2), pp. 32–48. Available at: https://doi.org/10.5501/wjv.v2.i2.32.

Paul-Gilloteaux, P. *et al.* (2017) 'eC-CLEM: flexible multidimensional registration software for correlative microscopies', *Nature Methods*, 14(2), pp. 102–103. Available at: https://doi.org/10.1038/nmeth.4170.

Pedersen, K.W. *et al.* (1999) 'Open reading frame 1a-encoded subunits of the arterivirus replicase induce endoplasmic reticulum-derived double-membrane vesicles which carry the viral replication complex', *Journal of Virology*, 73(3), pp. 2016–2026. Available at: https://doi.org/10.1128/JVI.73.3.2016-2026.1999.

Peng, S. *et al.* (2022) 'Current Knowledge on Infectious Bronchitis Virus Non-structural Proteins: The Bearer for Achieving Immune Evasion Function', *Frontiers in Veterinary Science*, 9. Available at: https://doi.org/10.3389/fvets.2022.820625.

Pérez-Berná, A.J. *et al.* (2016) 'Structural Changes In Cells Imaged by Soft X-ray Cryo-Tomography During Hepatitis C Virus Infection', *ACS Nano*, 10(7), pp. 6597–6611. Available at: https://doi.org/10.1021/acsnano.6b01374.

Perlman, S. and Netland, J. (2009) 'Coronaviruses post-SARS: update on replication and pathogenesis', *Nature Reviews Microbiology*, 7(6), pp. 439–450. Available at: https://doi.org/10.1038/nrmicro2147.

Perry, J.K. *et al.* (2021) 'An atomistic model of the coronavirus replication-transcription complex as a hexamer assembled around nsp15', *Journal of Biological Chemistry*, 297(4). Available at: https://doi.org/10.1016/j.jbc.2021.101218.

Pettersen, E.F. *et al.* (2021) 'UCSF ChimeraX: Structure visualization for researchers, educators, and developers', *Protein Science*, 30(1), pp. 70–82. Available at: https://doi.org/10.1002/pro.3943.

Phillips, J.E. *et al.* (2012) 'Changes in nonstructural protein 3 are associated with attenuation in avian coronavirus infectious bronchitis virus', *Virus Genes*, 44(1), pp. 63–74. Available at: https://doi.org/10.1007/s11262-011-0668-7.

Phillips, M.A. *et al.* (2020) 'CryoSIM: super-resolution 3D structured illumination cryogenic fluorescence microscopy for correlated ultrastructural imaging', *Optica*, 7(7), pp. 802–812. Available at: https://doi.org/10.1364/OPTICA.393203.

Plant, E.P. et al. (2010) 'Achieving a Golden Mean: Mechanisms by Which Coronaviruses Ensure Synthesis of the Correct Stoichiometric Ratios of Viral Proteins', Journal of Virology, 84(9), pp. 4330–4340. Available at: https://doi.org/10.1128/jvi.02480-09.

Posthuma, C.C. *et al.* (2008) 'Formation of the Arterivirus Replication/Transcription Complex: a Key Role for Nonstructural Protein 3 in the Remodeling of Intracellular Membranes', *Journal of Virology*, 82(9), pp. 4480–4491. Available at: https://doi.org/10.1128/jvi.02756-07.

Prentice, E. *et al.* (2004) 'Coronavirus Replication Complex Formation Utilizes Components of Cellular Autophagy *', *Journal of Biological Chemistry*, 279(11), pp. 10136–10141. Available at: https://doi.org/10.1074/jbc.M306124200.

Prod'homme, D. *et al.* (2001) 'Detection and Subcellular Localization of the Turnip Yellow Mosaic Virus 66K Replication Protein in Infected Cells', *Virology*, 281(1), pp. 88–101. Available at: https://doi.org/10.1006/viro.2000.0769.

Promkuntod, N. et al. (2014) 'Mapping of the receptor-binding domain and amino acids critical for attachment in the spike protein of avian coronavirus infectious bronchitis virus', Virology, 448, pp. 26–32. Available at: https://doi.org/10.1016/j.virol.2013.09.018.

Punjani, A. *et al.* (2017) 'cryoSPARC: algorithms for rapid unsupervised cryo-EM structure determination', *Nature Methods*, 14(3), pp. 290–296. Available at: https://doi.org/10.1038/nmeth.4169.

Pyle, E., Hutchings, J. and Zanetti, G. (2022) 'Strategies for picking membrane-associated particles within subtomogram averaging workflows', *Faraday Discussions*, 240(0), pp. 101–113. Available at: https://doi.org/10.1039/D2FD00022A.

Raamsman, M.J.B. *et al.* (2000) 'Characterization of the Coronavirus Mouse Hepatitis Virus Strain A59 Small Membrane Protein E', *Journal of Virology*, 74(5), pp. 2333–2342. Available at: https://doi.org/10.1128/jvi.74.5.2333-2342.2000.

Rajah, M.M. *et al.* (2022) 'The Mechanism and Consequences of SARS-CoV-2 Spike-Mediated Fusion and Syncytia Formation', *Journal of Molecular Biology*, 434(6), p. 167280. Available at: https://doi.org/10.1016/j.jmb.2021.167280.

Ramos, F.D. et al. (2004) 'Programmed −1 ribosomal frameshifting in the SARS coronavirus', Biochemical Society Transactions, 32(6), pp. 1081–1083. Available at: https://doi.org/10.1042/BST0321081.

Read, R.J. *et al.* (2023) 'Likelihood-based signal and noise analysis for docking of models into cryo-EM maps', *Acta Crystallographica Section D: Structural Biology*, 79(4), pp. 271–280. Available at: https://doi.org/10.1107/S2059798323001596.

Read, R.J. et al. (2024) 'Likelihood-based interactive local docking into cryo-EM maps in ChimeraX', Acta Crystallographica Section D: Structural Biology, 80(8), pp. 588–598. Available at: https://doi.org/10.1107/S2059798324006776.

Rehwinkel, J. and Gack, M.U. (2020) 'RIG-I-like receptors: their regulation and roles in RNA sensing', *Nature Reviews Immunology*, 20(9), pp. 537–551. Available at: https://doi.org/10.1038/s41577-020-0288-3.

Reiss, S. *et al.* (2011) 'Recruitment and Activation of a Lipid Kinase by Hepatitis C Virus NS5A Is Essential for Integrity of the Membranous Replication Compartment', *Cell Host & Microbe*, 9(1), pp. 32–45. Available at: https://doi.org/10.1016/j.chom.2010.12.002.

Ricciardi, S. *et al.* (2022) 'The role of NSP6 in the biogenesis of the SARS-CoV-2 replication organelle', *Nature*, 606(7915), pp. 761–768. Available at: https://doi.org/10.1038/s41586-022-04835-6.

Rigort, A. *et al.* (2010) 'Micromachining tools and correlative approaches for cellular cryo-electron tomography', *Journal of Structural Biology*, 172(2), pp. 169–179. Available at: https://doi.org/10.1016/j.jsb.2010.02.011.

Risco, C. *et al.* (1995) 'Membrane protein molecules of transmissible gastroenteritis coronavirus also expose the carboxy-terminal region on the external surface of the

virion', *Journal of Virology*, 69(9), pp. 5269–5277. Available at: https://doi.org/10.1128/jvi.69.9.5269-5277.1995.

Rochon, D. *et al.* (2014) 'The p33 auxiliary replicase protein of Cucumber necrosis virus targets peroxisomes and infection induces *de novo* peroxisome formation from the endoplasmic reticulum', *Virology*, 452–453, pp. 133–142. Available at: https://doi.org/10.1016/j.virol.2013.12.035.

Rohou, A. and Grigorieff, N. (2015) 'CTFFIND4: Fast and accurate defocus estimation from electron micrographs', *Journal of Structural Biology*, 192(2), pp. 216–221. Available at: https://doi.org/10.1016/j.jsb.2015.08.008.

Romei, M.G. and Boxer, S.G. (2019) 'Split Green Fluorescent Proteins: Scope, Limitations, and Outlook', *Annual Review of Biophysics*, 48(Volume 48, 2019), pp. 19–44. Available at: https://doi.org/10.1146/annurev-biophys-051013-022846.

Romero-Brey, I. *et al.* (2012) 'Three-Dimensional Architecture and Biogenesis of Membrane Structures Associated with Hepatitis C Virus Replication', *PLOS Pathogens*, 8(12), p. e1003056. Available at: https://doi.org/10.1371/journal.ppat.1003056.

Romero-Brey, I. and Bartenschlager, R. (2014) 'Membranous Replication Factories Induced by Plus-Strand RNA Viruses', *Viruses*, 6(7), pp. 2826–2857. Available at: https://doi.org/10.3390/v6072826.

Ruch, T.R. and Machamer, C.E. (2011) 'The Hydrophobic Domain of Infectious Bronchitis Virus E Protein Alters the Host Secretory Pathway and Is Important for Release of Infectious Virus', *Journal of Virology*, 85(2), pp. 675–685. Available at: https://doi.org/10.1128/jvi.01570-10.

Ruch, T.R. and Machamer, C.E. (2012) 'A Single Polar Residue and Distinct Membrane Topologies Impact the Function of the Infectious Bronchitis Coronavirus E Protein', *PLOS Pathogens*, 8(5), p. e1002674. Available at: https://doi.org/10.1371/journal.ppat.1002674.

Russell, M.R.G. *et al.* (2017) '3D correlative light and electron microscopy of cultured cells using serial blockface scanning electron microscopy', *Journal of Cell Science*. Edited by A. Ewald, 130(1), pp. 278–291. Available at: https://doi.org/10.1242/jcs.188433.

Saalfeld, S. and Tomančák, P. (2008) 'Automatic landmark correspondence detection for ImageJ'. Available at: https://www.semanticscholar.org/paper/Automatic-landmark-correspondence-detection-for-Saalfeld-Toman%C4%8D%C3%A1k/2775a50b33ae83cd064bb31c17005f80a0eb4d7a (Accessed: 9 December 2024).

Saikatendu, K.S. *et al.* (2007) 'Ribonucleocapsid Formation of Severe Acute Respiratory Syndrome Coronavirus through Molecular Action of the N-Terminal Domain of N Protein', *Journal of Virology*, 81(8), pp. 3913–3921. Available at: https://doi.org/10.1128/jvi.02236-06.

Sainz, Bruno *et al.* (2005) 'The Aromatic Domain of the Coronavirus Class I Viral Fusion Protein Induces Membrane Permeabilization: Putative Role during Viral Entry', *Biochemistry*, 44(3), pp. 947–958. Available at: https://doi.org/10.1021/bi048515g.

Sakai, Y. *et al.* (2017) 'Two-amino acids change in the nsp4 of SARS coronavirus abolishes viral replication', *Virology*, 510, pp. 165–174. Available at: https://doi.org/10.1016/j.virol.2017.07.019.

Salanueva, I.J., Carrascosa, J.L. and Risco, C. (1999) 'Structural Maturation of the Transmissible Gastroenteritis Coronavirus', *Journal of Virology*, 73(10), pp. 7952–7964. Available at: https://doi.org/10.1128/jvi.73.10.7952-7964.1999.

Saraste, J. *et al.* (2022) 'Evidence for the role of Rab11-positive recycling endosomes as intermediates in coronavirus egress from epithelial cells', *Histochemistry and Cell Biology*, 158(3), pp. 241–251. Available at: https://doi.org/10.1007/s00418-022-02115-y.

Saraste, J. and Prydz, K. (2021) 'Assembly and Cellular Exit of Coronaviruses: Hijacking an Unconventional Secretory Pathway from the Pre-Golgi Intermediate Compartment via the Golgi Ribbon to the Extracellular Space', *Cells*, 10(3), p. 503. Available at: https://doi.org/10.3390/cells10030503.

Sawicki, S.G. and Sawicki, D.L. (1995) 'Coronaviruses use Discontinuous Extension for Synthesis of Subgenome-Length Negative Strands', in P.J. Talbot and G.A. Levy (eds)

Corona- and Related Viruses: Current Concepts in Molecular Biology and Pathogenesis. Boston, MA: Springer US, pp. 499–506. Available at: https://doi.org/10.1007/978-1-4615-1899-0_79.

Scaramuzza, S. and Castaño-Díez, D. (2021) 'Step-by-step guide to efficient subtomogram averaging of virus-like particles with Dynamo', *PLOS Biology*, 19(8), p. e3001318. Available at: https://doi.org/10.1371/journal.pbio.3001318.

van der Schaar, H.M. *et al.* (2016) 'Illuminating the Sites of Enterovirus Replication in Living Cells by Using a Split-GFP-Tagged Viral Protein', *mSphere*, 1(4), pp. e00104-16. Available at: https://doi.org/10.1128/mSphere.00104-16.

Schalk, A.F. *et al.* (1931) 'An Apparently New Respiratory Disease of Baby Chicks', *J. Amer. Vet. Med. Ass*, 78, pp. 413–423.

Scheres, S.H.W. (2012) 'RELION: Implementation of a Bayesian approach to cryo-EM structure determination', *Journal of Structural Biology*, 180(3), pp. 519–530. Available at: https://doi.org/10.1016/j.jsb.2012.09.006.

Schindelin, J. *et al.* (2012) 'Fiji: an open-source platform for biological-image analysis', *Nature Methods*, 9(7), pp. 676–682. Available at: https://doi.org/10.1038/nmeth.2019.

Schiøtz, O.H. *et al.* (2024) 'Serial Lift-Out: sampling the molecular anatomy of whole organisms', *Nature Methods*, 21(9), pp. 1684–1692. Available at: https://doi.org/10.1038/s41592-023-02113-5.

Schroeder, S. *et al.* (2021) 'Functional comparison of MERS-coronavirus lineages reveals increased replicative fitness of the recombinant lineage 5', *Nature Communications*, 12(1), p. 5324. Available at: https://doi.org/10.1038/s41467-021-25519-1.

Schwartz, M. *et al.* (2002) 'A Positive-Strand RNA Virus Replication Complex Parallels Form and Function of Retrovirus Capsids', *Molecular Cell*, 9(3), pp. 505–514. Available at: https://doi.org/10.1016/S1097-2765(02)00474-4.

Schwartz, M. *et al.* (2004) 'Alternate, virus-induced membrane rearrangements support positive-strand RNA virus genome replication', *Proceedings of the National Academy of Sciences*, 101(31), pp. 11263–11268. Available at: https://doi.org/10.1073/pnas.0404157101.

Scutigliani, E.M. and Kikkert, M. (2017) 'Interaction of the innate immune system with positive-strand RNA virus replication organelles', *Cytokine & Growth Factor Reviews*, 37, pp. 17–27. Available at: https://doi.org/10.1016/j.cytogfr.2017.05.007.

Serrano, P. *et al.* (2007a) 'Nuclear Magnetic Resonance Structure of the N-Terminal Domain of Nonstructural Protein 3 from the Severe Acute Respiratory Syndrome

Coronavirus', *Journal of Virology*, 81(21), pp. 12049–12060. Available at: https://doi.org/10.1128/jvi.00969-07.

Serrano, P. *et al.* (2007b) 'Nuclear Magnetic Resonance Structure of the N-Terminal Domain of Nonstructural Protein 3 from the Severe Acute Respiratory Syndrome Coronavirus', *Journal of Virology*, 81(21), pp. 12049–12060. Available at: https://doi.org/10.1128/jvi.00969-07.

Shaner, N.C. *et al.* (2013) 'A bright monomeric green fluorescent protein derived from Branchiostoma lanceolatum', *Nature Methods*, 10(5), pp. 407–409. Available at: https://doi.org/10.1038/nmeth.2413.

Shang, J. et al. (2018) 'Cryo-EM structure of infectious bronchitis coronavirus spike protein reveals structural and functional evolution of coronavirus spike proteins', PLOS Pathogens, 14(4), p. e1007009. Available at: https://doi.org/10.1371/journal.ppat.1007009.

Signer, J. *et al.* (2020) 'In vitro virucidal activity of Echinaforce®, an Echinacea purpurea preparation, against coronaviruses, including common cold coronavirus 229E and SARS-CoV-2', *Virology Journal*, 17(1), p. 136. Available at: https://doi.org/10.1186/s12985-020-01401-2.

Silvester, E. *et al.* (2021) 'DNA origami signposts for identifying proteins on cell membranes by electron cryotomography', *Cell*, 184(4), pp. 1110-1121.e16. Available at: https://doi.org/10.1016/j.cell.2021.01.033.

SiriusXT (2024) 'SiriusXT and TESCAN demonstrate a cryo correlative light, x-ray and electron microscopy workflow!' SiriusXT – Cell Structure Imaging. Available at: https://siriusxt.com/library/news/siriusxt-and-tescan-demonstrate-a-cryo-correlative-light-x-ray-and-electron-microscopy-workflow/ (Accessed: 9 December 2024).

Snijder, E.J. *et al.* (2001) 'Non-structural proteins 2 and 3 interact to modify host cell membranes during the formation of the arterivirus replication complex', *Journal of General Virology*, 82(5), pp. 985–994. Available at: https://doi.org/10.1099/0022-1317-82-5-985.

Snijder, E.J. *et al.* (2006) 'Ultrastructure and Origin of Membrane Vesicles Associated with the Severe Acute Respiratory Syndrome Coronavirus Replication Complex', *Journal of Virology*, 80(12), pp. 5927–5940. Available at: https://doi.org/10.1128/JVI.02501-05.

Snijder, E.J. *et al.* (2020) 'A unifying structural and functional model of the coronavirus replication organelle: Tracking down RNA synthesis', *PLOS Biology*, 18(6), p. e3000715. Available at: https://doi.org/10.1371/journal.pbio.3000715.

Snijder, E.J., Dobbe, J.C. and Spaan, W.J.M. (2003) 'Heterodimerization of the Two Major Envelope Proteins Is Essential for Arterivirus Infectivity', *Journal of Virology*, 77(1), pp. 97–104. Available at: https://doi.org/10.1128/jvi.77.1.97-104.2003.

Sola, I. et al. (2015) 'Continuous and Discontinuous RNA Synthesis in Coronaviruses', Annual Review of Virology, 2(Volume 2, 2015), pp. 265–288. Available at: https://doi.org/10.1146/annurev-virology-100114-055218.

Sosinsky, G.E. *et al.* (2008) 'The combination of chemical fixation procedures with high pressure freezing and freeze substitution preserves highly labile tissue ultrastructure for electron tomography applications', *Journal of Structural Biology*, 161(3), pp. 359–371. Available at: https://doi.org/10.1016/j.jsb.2007.09.002.

Spilman, M.S. *et al.* (2009) 'Cryo-electron tomography of porcine reproductive and respiratory syndrome virus: organization of the nucleocapsid', *Journal of General Virology*, 90(3), pp. 527–535. Available at: https://doi.org/10.1099/vir.0.007674-0.

Spuul, P. *et al.* (2010) 'Phosphatidylinositol 3-Kinase-, Actin-, and Microtubule-Dependent Transport of Semliki Forest Virus Replication Complexes from the Plasma Membrane to Modified Lysosomes', *Journal of Virology*, 84(15), pp. 7543–7557. Available at: https://doi.org/10.1128/jvi.00477-10.

Spuul, P. *et al.* (2011) 'Assembly of Alphavirus Replication Complexes from RNA and Protein Components in a Novel trans-Replication System in Mammalian Cells', *Journal of Virology*, 85(10), pp. 4739–4751. Available at: https://doi.org/10.1128/jvi.00085-11.

Stern, D.F. and Sefton, B.M. (1982) 'Coronavirus proteins: structure and function of the oligosaccharides of the avian infectious bronchitis virus glycoproteins', *Journal of Virology*, 44(3), pp. 804–812. Available at: https://doi.org/10.1128/jvi.44.3.804-812.1982.

Stevenson-Leggett, P. *et al.* (2021) 'Analysis of the avian coronavirus spike protein reveals heterogeneity in the glycans present', *Journal of General Virology*, 102(8), p. 001642. Available at: https://doi.org/10.1099/jgv.0.001642.

Stodola, J.K. *et al.* (2018) 'The OC43 human coronavirus envelope protein is critical for infectious virus production and propagation in neuronal cells and is a determinant of neurovirulence and CNS pathology', *Virology*, 515, pp. 134–149. Available at: https://doi.org/10.1016/j.virol.2017.12.023.

Stok, J.E., Vega Quiroz, M.E. and van der Veen, A.G. (2020) 'Self RNA Sensing by RIG-I–like Receptors in Viral Infection and Sterile Inflammation', *The Journal of Immunology*, 205(4), pp. 883–891. Available at: https://doi.org/10.4049/jimmunol.2000488.

Subissi, L. *et al.* (2014) 'SARS-CoV ORF1b-encoded nonstructural proteins 12–16: Replicative enzymes as antiviral targets', *Antiviral Research*, 101, pp. 122–130. Available at: https://doi.org/10.1016/j.antiviral.2013.11.006.

Suhy, D.A., Giddings, T.H. and Kirkegaard, K. (2000) 'Remodeling the Endoplasmic Reticulum by Poliovirus Infection and by Individual Viral Proteins: an Autophagy-Like Origin for Virus-Induced Vesicles', *Journal of Virology*, 74(19), pp. 8953–8965. Available at: https://doi.org/10.1128/jvi.74.19.8953-8965.2000.

Sun, L. *et al.* (2014) 'The P2 of heat yellow mosaic virus rearranges the endoplasmic reticulum and recruits other viral proteins into replication-associated inclusion bodies', *Molecular Plant Pathology*, 15(5), pp. 466–478. Available at: https://doi.org/10.1111/mpp.12109.

Surya, W., Li, Y. and Torres, J. (2018) 'Structural model of the SARS coronavirus E channel in LMPG micelles', *Biochimica et Biophysica Acta (BBA) - Biomembranes*, 1860(6), pp. 1309–1317. Available at: https://doi.org/10.1016/j.bbamem.2018.02.017.

Swift, A.M. and Machamer, C.E. (1991) 'A Golgi retention signal in a membrane-spanning domain of coronavirus E1 protein.', *Journal of Cell Biology*, 115(1), pp. 19–30. Available at: https://doi.org/10.1083/jcb.115.1.19.

Tabata, K. *et al.* (2021) 'Convergent use of phosphatidic acid for hepatitis C virus and SARS-CoV-2 replication organelle formation', *Nature Communications*, 12(1), p. 7276. Available at: https://doi.org/10.1038/s41467-021-27511-1.

Tan, Y.B. *et al.* (2022) 'Molecular architecture of the Chikungunya virus replication complex', *Science Advances*, 8(48), p. eadd2536. Available at: https://doi.org/10.1126/sciadv.add2536.

Tanenbaum, M.E. *et al.* (2014) 'A protein tagging system for signal amplification in gene expression and fluorescence imaging', *Cell*, 159(3), pp. 635–646. Available at: https://doi.org/10.1016/j.cell.2014.09.039.

Tegunov, D. and Cramer, P. (2019) 'Real-time cryo-electron microscopy data preprocessing with Warp', *Nature Methods*, 16(11), pp. 1146–1152. Available at: https://doi.org/10.1038/s41592-019-0580-y.

Tolonen, N. *et al.* (2001) 'Vaccinia Virus DNA Replication Occurs in Endoplasmic Reticulum-enclosed Cytoplasmic Mini-Nuclei', *Molecular Biology of the Cell*, 12(7), pp. 2031–2046. Available at: https://doi.org/10.1091/mbc.12.7.2031.

Tooze, S.A., Tooze, J. and Warren, G. (1988) 'Site of addition of N-acetyl-galactosamine to the E1 glycoprotein of mouse hepatitis virus-A59.', *Journal of Cell Biology*, 106(5), pp. 1475–1487. Available at: https://doi.org/10.1083/jcb.106.5.1475.

Toro-Nahuelpan, M. *et al.* (2020) 'Tailoring cryo-electron microscopy grids by photo-micropatterning for in-cell structural studies', *Nature Methods*, 17(1), pp. 50–54. Available at: https://doi.org/10.1038/s41592-019-0630-5.

Torres, J. *et al.* (2005) 'The Transmembrane Oligomers of Coronavirus Protein E', *Biophysical Journal*, 88(2), pp. 1283–1290. Available at: https://doi.org/10.1529/biophysj.104.051730.

Tseng, Y.-T. *et al.* (2014) 'SARS-CoV envelope protein palmitoylation or nucleocapid association is not required for promoting virus-like particle production', *Journal of Biomedical Science*, 21(1), p. 34. Available at: https://doi.org/10.1186/1423-0127-21-34.

Ulasli, M. *et al.* (2010) 'Qualitative and quantitative ultrastructural analysis of the membrane rearrangements induced by coronavirus', *Cellular Microbiology*, 12(6), pp. 844–861. Available at: https://doi.org/10.1111/j.1462-5822.2010.01437.x.

Unchwaniwala, N. *et al.* (2020) 'Subdomain cryo-EM structure of nodaviral replication protein A crown complex provides mechanistic insights into RNA genome replication', *Proceedings of the National Academy of Sciences*, 117(31), pp. 18680–18691. Available at: https://doi.org/10.1073/pnas.2006165117.

Vennema, H. *et al.* (1991) 'Enhancement of the vaccinia virus/phage T7 RNA polymerase expression system using encephalomyocarditis virus 5'-untranslated region sequences', *Gene*, 108(2), pp. 201–209. Available at: https://doi.org/10.1016/0378-1119(91)90435-E.

Vennema, H. *et al.* (1996) 'Nucleocapsid-independent assembly of coronavirus-like particles by co-expression of viral envelope protein genes.', *The EMBO Journal*, 15(8), pp. 2020–2028. Available at: https://doi.org/10.1002/j.1460-2075.1996.tb00553.x.

Verheije, M.H. *et al.* (2008) 'Mouse Hepatitis Coronavirus RNA Replication Depends on GBF1-Mediated ARF1 Activation', *PLOS Pathogens*, 4(6), p. e1000088. Available at: https://doi.org/10.1371/journal.ppat.1000088.

Viktorova, E.G. *et al.* (2018) 'Phospholipid synthesis fueled by lipid droplets drives the structural development of poliovirus replication organelles', *PLOS Pathogens*, 14(8), p. e1007280. Available at: https://doi.org/10.1371/journal.ppat.1007280.

Villa, E. *et al.* (2013) 'Opening windows into the cell: focused-ion-beam milling for cryo-electron tomography', *Current Opinion in Structural Biology*, 23(5), pp. 771–777. Available at: https://doi.org/10.1016/j.sbi.2013.08.006.

V'kovski, P. *et al.* (2019) 'Determination of host proteins composing the microenvironment of coronavirus replicase complexes by proximity-labeling', *eLife*. Edited by K. Kirkegaard and I. Dikic, 8, p. e42037. Available at: https://doi.org/10.7554/eLife.42037.

V'kovski, P. *et al.* (2021) 'Coronavirus biology and replication: implications for SARS-CoV-2', *Nature Reviews Microbiology*, 19(3), pp. 155–170. Available at: https://doi.org/10.1038/s41579-020-00468-6.

Wan, J. *et al.* (2015) 'Ultrastructural Characterization of Turnip Mosaic Virus-Induced Cellular Rearrangements Reveals Membrane-Bound Viral Particles Accumulating in

Vacuoles', *Journal of Virology*, 89(24), pp. 12441–12456. Available at: https://doi.org/10.1128/jvi.02138-15.

Wang, J. *et al.* (2009) 'Interaction of the Coronavirus Infectious Bronchitis Virus Membrane Protein with β-Actin and Its Implication in Virion Assembly and Budding', *PLOS ONE*, 4(3), p. e4908. Available at: https://doi.org/10.1371/journal.pone.0004908.

Wang, K., Xie, S. and Sun, B. (2011) 'Viral proteins function as ion channels', *Biochimica et Biophysica Acta (BBA) - Biomembranes*, 1808(2), pp. 510–515. Available at: https://doi.org/10.1016/j.bbamem.2010.05.006.

Wang, X. *et al.* (2021) 'Three-dimensional reconstruction and comparison of vacuolar membranes in response to viral infection', *Journal of Integrative Plant Biology*, 63(2), pp. 353–364. Available at: https://doi.org/10.1111/jipb.13027.

Webb, I. *et al.* (2022) 'The Genetic Stability, Replication Kinetics and Cytopathogenicity of Recombinant Avian Coronaviruses with a T16A or an A26F Mutation within the E Protein Is Cell-Type Dependent', *Viruses*, 14(8), p. 1784. Available at: https://doi.org/10.3390/v14081784.

Welsch, S. *et al.* (2009) 'Composition and Three-Dimensional Architecture of the Dengue Virus Replication and Assembly Sites', *Cell Host & Microbe*, 5(4), pp. 365–375. Available at: https://doi.org/10.1016/j.chom.2009.03.007.

Westerbeck, J.W. and Machamer, C.E. (2015) 'A Coronavirus E Protein Is Present in Two Distinct Pools with Different Effects on Assembly and the Secretory Pathway', *Journal of Virology*, 89(18), pp. 9313–9323. Available at: https://doi.org/10.1128/jvi.01237-15.

Westerbeck, J.W. and Machamer, C.E. (2019) 'The Infectious Bronchitis Coronavirus Envelope Protein Alters Golgi pH To Protect the Spike Protein and Promote the Release of Infectious Virus', *Journal of Virology*, 93(11), p. 10.1128/jvi.00015-19. Available at: https://doi.org/10.1128/jvi.00015-19.

Wieringa, R. *et al.* (2004) 'Structural Protein Requirements in Equine Arteritis Virus Assembly', *Journal of Virology*, 78(23), pp. 13019–13027. Available at: https://doi.org/10.1128/jvi.78.23.13019-13027.2004.

de Wilde, A.H. *et al.* (2013) 'MERS-coronavirus replication induces severe in vitro cytopathology and is strongly inhibited by cyclosporin A or interferon-α treatment', *Journal of General Virology*, 94(8), pp. 1749–1760. Available at: https://doi.org/10.1099/vir.0.052910-0.

de Wilde, A.H. *et al.* (2018) 'Host Factors in Coronavirus Replication', in R.A. Tripp and S.M. Tompkins (eds) *Roles of Host Gene and Non-coding RNA Expression in Virus Infection*. Cham: Springer International Publishing, pp. 1–42. Available at: https://doi.org/10.1007/82_2017_25.

Wilson, L., Gage, P. and Ewart, G. (2006) 'Hexamethylene amiloride blocks E protein ion channels and inhibits coronavirus replication', *Virology*, 353(2), pp. 294–306. Available at: https://doi.org/10.1016/j.virol.2006.05.028.

Winey, M. *et al.* (2014) 'Conventional transmission electron microscopy', *Molecular Biology of the Cell*, 25(3), pp. 319–323. Available at: https://doi.org/10.1091/mbc.e12-12-0863.

Winter, C., Herrler, G. and Neumann, U. (2008) 'Infection of the tracheal epithelium by infectious bronchitis virus is sialic acid dependent', Microbes and Infection, 10(4), pp. 367–373. Available at: https://doi.org/10.1016/j.micinf.2007.12.009.

Wolff, G., Limpens, R.W.A.L., *et al.* (2020) 'A molecular pore spans the double membrane of the coronavirus replication organelle', *Science*, 369(6509), pp. 1395–1398. Available at: https://doi.org/10.1126/science.abd3629.

Wolff, G., Melia, C.E., *et al.* (2020) 'Double-Membrane Vesicles as Platforms for Viral Replication', *Trends in Microbiology*, 28(12), pp. 1022–1033. Available at: https://doi.org/10.1016/j.tim.2020.05.009.

Wolff, G. (2022) *Cellular cryo-tomography of nidovirus replication organelles*. Leiden University. Available at: https://hdl.handle.net/1887/3421526 (Accessed: 16 September 2024).

Wölk, B. *et al.* (2008) 'A Dynamic View of Hepatitis C Virus Replication Complexes', *Journal of Virology*, 82(21), pp. 10519–10531. Available at: https://doi.org/10.1128/jvi.00640-08.

Wolter, H. (1952) 'Verallgemeinerte Schwarzschildsche Spiegelsysteme streifender Reflexion als Optiken für Röntgenstrahlen', *Annalen der Physik*, 445(4–5), pp. 286–295. Available at: https://doi.org/10.1002/andp.19524450410.

World Health Organisation (WHO) (2020) *Statement on the second meeting of the International Health Regulations (2005) Emergency Committee regarding the outbreak of novel coronavirus (2019-nCoV)*. Available at: https://www.who.int/news/item/30-01-2020-statement-on-the-second-meeting-of-the-international-health-regulations-(2005)-emergency-committee-regarding-the-outbreak-of-novel-coronavirus-(2019-ncov) (Accessed: 8 September 2024).

Xu, K. and Nagy, P.D. (2014) 'Expanding use of multi-origin subcellular membranes by positive-strand RNA viruses during replication', *Current Opinion in Virology*, 9, pp. 119–126. Available at: https://doi.org/10.1016/j.coviro.2014.09.015.

Xu, L.H. *et al.* (2011) '*Coronavirus* Infection Induces DNA Replication Stress Partly through Interaction of Its Nonstructural Protein 13 with the p125 Subunit of DNA Polymerase δ', *Journal of Biological Chemistry*, 286(45), pp. 39546–39559. Available at: https://doi.org/10.1074/jbc.M111.242206.

Yamada, Y. and Liu, D.X. (2009) 'Proteolytic Activation of the Spike Protein at a Novel RRRR/S Motif Is Implicated in Furin-Dependent Entry, Syncytium Formation, and Infectivity of Coronavirus Infectious Bronchitis Virus in Cultured Cells', *Journal of Virology*, 83(17), pp. 8744–8758. Available at: https://doi.org/10.1128/jvi.00613-09.

Yang, H. *et al.* (2005) 'Design of Wide-Spectrum Inhibitors Targeting Coronavirus Main Proteases', *PLOS Biology*, 3(10), p. e324. Available at: https://doi.org/10.1371/journal.pbio.0030324.

Yang, H. and Rao, Z. (2021) 'Structural biology of SARS-CoV-2 and implications for therapeutic development', *Nature Reviews Microbiology*, 19(11), pp. 685–700. Available at: https://doi.org/10.1038/s41579-021-00630-8.

Yang, R. *et al.* (2022) 'Refinement of SARS-CoV-2 envelope protein structure in a native-like environment by molecular dynamics simulations', *Frontiers in Molecular Biosciences*, 9. Available at: https://doi.org/10.3389/fmolb.2022.1027223.

Yang, T. *et al.* (2009) 'The Protective Immune Response against Infectious Bronchitis Virus Induced by Multi-Epitope Based Peptide Vaccines', *Bioscience, Biotechnology, and Biochemistry*, 73(7), pp. 1500–1504. Available at: https://doi.org/10.1271/bbb.80864.

Yang, Z. *et al.* (2024) 'Interaction between host G3BP and viral nucleocapsid protein regulates SARS-CoV-2 replication and pathogenicity', *Cell Reports*, 43(3), p. 113965. Available at: https://doi.org/10.1016/j.celrep.2024.113965.

Yao, H. *et al.* (2020) 'Molecular Architecture of the SARS-CoV-2 Virus', *Cell*, 183(3), pp. 730-738.e13. Available at: https://doi.org/10.1016/j.cell.2020.09.018.

You, R. et al. (2023) 'Identification and Comparison of the Sialic Acid-Binding Domain Characteristics of Avian Coronavirus Infectious Bronchitis Virus Spike Protein', Journal of Virology, 97(5), pp. e00489-23. Available at: https://doi.org/10.1128/jvi.00489-23.

Yu, A. *et al.* (2021) 'A multiscale coarse-grained model of the SARS-CoV-2 virion', *Biophysical Journal*, 120(6), pp. 1097–1104. Available at: https://doi.org/10.1016/j.bpj.2020.10.048.

Yu, K. *et al.* (2012) 'Purification, crystallization and preliminary X-ray analysis of nonstructural protein 2 (nsp2) from avian infectious bronchitis virus', *Acta Crystallographica Section F: Structural Biology and Crystallization Communications*, 68(6), pp. 716–719. Available at: https://doi.org/10.1107/S1744309112018623.

Yu, L. *et al.* (2017) 'The papain-like protease of avian infectious bronchitis virus has deubiquitinating activity', *Archives of Virology*, 162(7), pp. 1943–1950. Available at: https://doi.org/10.1007/s00705-017-3328-y.

Yuan, Q. *et al.* (2006) 'Biochemical evidence for the presence of mixed membrane topologies of the severe acute respiratory syndrome coronavirus envelope protein

expressed in mammalian cells', *FEBS Letters*, 580(13), pp. 3192–3200. Available at: https://doi.org/10.1016/j.febslet.2006.04.076.

Zhan, H. *et al.* (2023) 'Nodavirus RNA replication crown architecture reveals proto-crown precursor and viral protein A conformational switching', *Proceedings of the National Academy of Sciences*, 120(5), p. e2217412120. Available at: https://doi.org/10.1073/pnas.2217412120.

Zhang, K. *et al.* (2021) 'Structural insights into viral RNA capping and plasma membrane targeting by Chikungunya virus nonstructural protein 1', *Cell host & microbe*, 29(5), pp. 757-764.e3. Available at: https://doi.org/10.1016/j.chom.2021.02.018.

Zhang, P. (2019) 'Advances in cryo-electron tomography and subtomogram averaging and classification', *Current Opinion in Structural Biology*, 58, pp. 249–258. Available at: https://doi.org/10.1016/j.sbi.2019.05.021.

Zhang, W. *et al.* (2018) 'An integrated analysis of membrane remodeling during porcine reproductive and respiratory syndrome virus replication and assembly', *PLOS ONE*, 13(7), p. e0200919. Available at: https://doi.org/10.1371/journal.pone.0200919.

Zhang, X. *et al.* (2020) 'Evaluation of the reproductive system development and egg-laying performance of hens infected with TW I-type infectious bronchitis virus', *Veterinary Research*, 51(1), p. 95. Available at: https://doi.org/10.1186/s13567-020-00819-4.

Zhang, Y., Buckles, E. and Whittaker, G.R. (2012) 'Expression of the C-type lectins DC-SIGN or L-SIGN alters host cell susceptibility for the avian coronavirus, infectious bronchitis virus', Veterinary Microbiology, 157(3), pp. 285–293. Available at: https://doi.org/10.1016/j.vetmic.2012.01.011.

Zhao, J. *et al.* (2021) 'Coronavirus Endoribonuclease Ensures Efficient Viral Replication and Prevents Protein Kinase R Activation', *Journal of Virology*, 95(7), p. 10.1128/jvi.02103-20. Available at: https://doi.org/10.1128/jvi.02103-20.

Zheng, S. *et al.* (2022) 'AreTomo: An integrated software package for automated marker-free, motion-corrected cryo-electron tomographic alignment and reconstruction', *Journal of Structural Biology: X*, 6, p. 100068. Available at: https://doi.org/10.1016/j.yjsbx.2022.100068.

Zheng, S.Q. *et al.* (2017) 'MotionCor2: anisotropic correction of beam-induced motion for improved cryo-electron microscopy', *Nature Methods*, 14(4), pp. 331–332. Available at: https://doi.org/10.1038/nmeth.4193.

Zheng, Y.-X. et al. (2021) 'Nsp2 has the potential to be a drug target revealed by global identification of SARS-CoV-2 Nsp2-interacting proteins', Acta Biochimica et Biophysica Sinica, 53(9), pp. 1134–1141. Available at: https://doi.org/10.1093/abbs/gmab088.

Zhou, S. *et al.* (2023) 'SARS-CoV-2 E protein: Pathogenesis and potential therapeutic development', *Biomedicine & Pharmacotherapy*, 159, p. 114242. Available at: https://doi.org/10.1016/j.biopha.2023.114242.

Zhou, X. *et al.* (2017) 'Ultrastructural Characterization of Membrane Rearrangements Induced by Porcine Epidemic Diarrhea Virus Infection', *Viruses*, 9(9), p. 251. Available at: https://doi.org/10.3390/v9090251.

Ziebuhr, J., Snijder, E.J. and Gorbalenya, A.E. (2000) 'Virus-encoded proteinases and proteolytic processing in the Nidovirales', *Journal of General Virology*, 81(4), pp. 853–879. Available at: https://doi.org/10.1099/0022-1317-81-4-853.

Ziebuhr, J., Thiel, V. and Gorbalenya, A.E. (2001) 'The Autocatalytic Release of a Putative RNA Virus Transcription Factor from Its Polyprotein Precursor Involves Two Paralogous Papain-like Proteases That Cleave the Same Peptide Bond *', *Journal of Biological Chemistry*, 276(35), pp. 33220–33232. Available at: https://doi.org/10.1074/jbc.M104097200.

Zimmermann, L. *et al.* (2022) 'SARS-CoV-2 nsp3-4 suffice to form a pore shaping replication organelles'. bioRxiv, p. 2022.10.21.513196. Available at: https://doi.org/10.1101/2022.10.21.513196.

Zimmermann, L. *et al.* (2023) 'SARS-CoV-2 nsp3 and nsp4 are minimal constituents of a pore spanning replication organelle', *Nature Communications*, 14(1), p. 7894. Available at: https://doi.org/10.1038/s41467-023-43666-5.

Zivanov, J. *et al.* (2022) 'A Bayesian approach to single-particle electron cryo-tomography in RELION-4.0', *eLife*. Edited by E.H. Egelman, V. Dötsch, and A. Bartesaghi, 11, p. e83724. Available at: https://doi.org/10.7554/eLife.83724.

Zou, L. et al. (2022) 'The SARS-CoV-2 protein NSP2 impairs the silencing capacity of the human 4EHP-GIGYF2 complex', iScience, 25(7), p. 104646. Available at: https://doi.org/10.1016/j.isci.2022.104646.

Zúñiga, S. *et al.* (2007) 'Coronavirus nucleocapsid protein is an RNA chaperone', *Virology*, 357(2), pp. 215–227. Available at: https://doi.org/10.1016/j.virol.2006.07.046.

Zúñiga, S. *et al.* (2010) 'Coronavirus Nucleocapsid Protein Facilitates Template Switching and Is Required for Efficient Transcription', *Journal of Virology*, 84(4), pp. 2169–2175. Available at: https://doi.org/10.1128/jvi.02011-09.

Zuo, J. *et al.* (2021) 'The mechanism of antigen-presentation of avian bone marrowed dendritic cells suppressed by infectious bronchitis virus', *Genomics*, 113(4), pp. 1719–1732. Available at: https://doi.org/10.1016/j.ygeno.2021.04.027.

Chapter 8. Appendix

8.1 Tagged nsp2 viruses

3 ala spacer between tag and nsp2, included n-term ala for tetracysteine to generate kozak consensus

mEGFP-nsp2 (1340):

AATTGTCGACGCTACCTAGTGTCCAGCGTCCTACGGGCGTCGTGGCTGGTTCGAGTGCGAGGAACCTCTGGTTCATCTAG
CGGTAGGCGGGTGTGTGGAAGTAGCACTTCAGACGT***ACCGGT***TCTGTTGTGTGAAATACGGGGTCACCTCCCCCCACATAC
CTCTAAGGGCTTTTGAGCCTAGCGTTGGGCTACGTTCTCGCATAAGGTCGGCTATACGACGTTTGTAGGGGGTAGTGCCAA
ACAACCCCTGAGGTGACAGGTTCTGGTGGTGTTTAGTGAGCAGACATACAATAGACAGTGACAAC**ATG**

GTGAGCAAGGGCGAGGAGCTGTTCACCGGGGTGGTGCCCATCCTGGTCGAGCTGGACGGC
GACGTAAACGGCCACAAGTTCAGCGTGTCCGGCGAGGGCGAGGGCGATGCCACCTACGGC
AAGCTGACCCTGAAGTTCATCTGCACCACCGGCAAGCTGCCCGTGCCCTGGCCCACCCTC
GTGACCACCCTGACCTACGGCGTGCAGTGCTTCAGCCGCTACCCCGACCACATGAAGCAG
CACGACTTCTTCAAGTCCGCCATGCCCGAAGGCTACGTCCAGGAGCGCACCATCTTCTTT
AAGGACGACGGCAACTACAAGACCCGCGCCGAGGTGAAGTTCGAGGGCGACACCCTGGTG
AACCGCATCGAGCTGAAGGGCATCGACTTCAAGGAGGACGGCAACATCCTGGGGCACAAG
CTGGAGTACAACTACAACAGCCACAACGTCTATATCATGGCCGACAAGCAGAAGAACGGC
ATCAAGGTGAACTTCAAGATCCGCCACAACATCGAGGACGGCAGCGTGCAGCTCGCCGAC
CACTACCAGCAGAACACCCCCATCGGCGACGGCCCCGTGCTGCTGCCCGACAACCACTAC
CTGAGCACCCAGTCCAAACTGAGCAAAGACCCCAACGAGAAGCGCGATCACATGGTCCTG
CTGGAGTTCGTGACCGCCGCCGGGATCACTCTCGGCATGGACGAGCTGTACAAG
GCAGCTGCC

GCTTCAAGCCTAAAACAGGGAGTATCTCCCAAACCACGGGATGTCATTCTTGTGTCCAAAGACATCCCTGAACAACTTTGT
GACGCTTTGTTTTTCTATACGTCACATAACCCTAAGGATTACGCTGATGCTTTTGCAGTTAGGCAGAAGTTTGACCGTAGT
CTCCAGACTGGGAAACAGTTCAAATTTGAAACTGTGTGTGGTCTCTTCCTCTTGAAGGGAGTTGACAAAATAACACCTGGC
GTCCCAGCAAAAGTTTTAAAAGCCACTTCTAAGTTGGCAGATTTAGAAGACATCTTTGTCGACAATT

mCherry-nsp2 (1330):

AATTGTCGACGCTACCTAGTGTCCAGCGTCCTACGGGCGTCGTGGCTGGTTCGAGTGCGAGGAACCTCTGGTTCATCTAG
CGGTAGGCGGGTGTGTGGAAGTAGCACTTCAGACGT***ACCGGT***TCTGTTGTGTGAAATACGGGGTCACCTCCCCCCACATAC
CTCTAAGGGCTTTTGAGCCTAGCGTTGGGCTACGTTCTCGCATAAGGTCGGCTATACGACGTTTGTAGGGGGTAGTGCCAA
ACAACCCCTGAGGTGACAGGTTCTGGTGGTGTTTAGTGAGCAGACATACAATAGACAGTGACAAC**ATG**

GTGAGCAAGGGCGAGGAGG ATAACATGGC CATCATCAAG GAGTTCATGC
GCTTCAAGGT GCACATGGAGGGCTCCGTGA ACGGCCACGA GTTCGAGATC
GAGGGCGAGG GTGAGGGCCG CCCCTACGAGGGCACCCAGA CCGCCAAGCT
GAAGGTGACC AAGGGTGGCC CCCTGCCCTT CGCCTGGGACATCCTGTCCC
CTCAGTTCAT GTACGGCTCC AAGGCCTACG TGAAGCACCC
CGCCGACATCCCCGACTACT TGAAGCTGTC CTTCCCCGAG GGCTTCAAGT
GGGAGCGCGT GATGAACTTCGAGGACGGCG GCGTGGTGAC CGTGACCCAG
GACTCCTCCC TGCAGGACGG CGAGTTCATCTACAAGGTGA AGCTGCGCGG
CACCAACTTC CCCTCCGACG GCCCCGTAAT GCAGAAGAAGACCATGGGCT
GGGAGGCCTC CTCCGAGCGG ATGTACCCCG AGGACGGCGC
CCTGAAGGGCGAGATCAAGC AGAGGCTGAA GCTGAAGGAC GGCGGCCACT
ACGACGCTGA GGTCAAGACCACCTACAAGG CCAAGAAGCC CGTGCAGCTG

CCCGGCGCCT ACAACGTCAA CATCAAGTTGGACATCACCT CCCACAACGA
GGACTACACC ATCGTGGAAC AGTACGAACG CGCCGAGGGCCGCCACTCCA
CCGGCGGCAT GGACGAGCTG TACAAG GCAGCTGCC

GCTTCAAGCCTAAAACAGGGAGTATCTCCCAAACCACGGGATGTCATTCTTGTGTCCAAAGACATCCCTGAACAACTTTGT
GACGCTTTGTTTTTCTATACGTCACATAACCCTAAGGATTACGCTGATGCTTTTGCAGTTAGGCAGAAGTTTGACCGTAGT
CTCCAGACTGGGAAACAGTTCAAATTTGAAACTGTGTGTGGTCTCTTCCTCTTGAAGGGAGTTGACAAAATAACACCTGGC
GTCCCAGCAAAAGTTTTAAAAGCCACTTCTAAGTTGGCAGATTTAGAAGACATCTTTGTCGACAATT

tetra-cysteine-nsp2 (650):

AATTGTCGACGCTACCTAGTGTCCAGCGTCCTACGGGCGTCGTGGCTGGTTCGAGTGCGAGGAACCTCTGGTTCATCTAG
CGGTAGGCGGGTGTGTGGAAGTAGCACTTCAGACGT***ACCGGT***TCTGTTGTGTGAAATACGGGGTCACCTCCCCCCACATAC
CTCTAAGGGCTTTTGAGCCTAGCGTTGGGCTACGTTCTCGCATAAGGTCGGCTATACGACGTTTGTAGGGGGTAGTGCCAA
ACAACCCCTGAGGTGACAGGTTCTGGTGGTGTTTAGTGAGCAGACATACAATAGACAGTGACAAC**ATG**

GCA TGTTGCCCTGGCTGTTGC GCAGCTGCC

GCTTCAAGCCTAAAACAGGGAGTATCTCCCAAACCACGGGATGTCATTCTTGTGTCCAAAGACATCCCTGAACAACTTTGT
GACGCTTTGTTTTTCTATACGTCACATAACCCTAAGGATTACGCTGATGCTTTTGCAGTTAGGCAGAAGTTTGACCGTAGT
CTCCAGACTGGGAAACAGTTCAAATTTGAAACTGTGTGTGGTCTCTTCCTCTTGAAGGGAGTTGACAAAATAACACCTGGC
GTCCCAGCAAAAGTTTTAAAAGCCACTTCTAAGTTGGCAGATTTAGAAGACATCTTTGTCGACAATT

SNAP-nsp2 (1170):

AATTGTCGACGCTACCTAGTGTCCAGCGTCCTACGGGCGTCGTGGCTGGTTCGAGTGCGAGGAACCTCTGGTTCATCTAG
CGGTAGGCGGGTGTGTGGAAGTAGCACTTCAGACGT***ACCGGT***TCTGTTGTGTGAAATACGGGGTCACCTCCCCCCACATAC
CTCTAAGGGCTTTTGAGCCTAGCGTTGGGCTACGTTCTCGCATAAGGTCGGCTATACGACGTTTGTAGGGGGTAGTGCCAA
ACAACCCCTGAGGTGACAGGTTCTGGTGGTGTTTAGTGAGCAGACATACAATAGACAGTGACAAC**ATG**

GACAAAGACTGCGAAATGAAGCGCACCACCCTGGATAGCCCTCTGGGCAAGCTGGAACTG
TCTGGGTGCGAACAGGGCCTGCACCGTATCATCTTCCTGGGCAAAGGAACATCTGCCGCC
GACGCCGTGGAAGTGCCTGCCCCAGCCGCCGTGCTGGGCGGACCAGAGCCACTGATGCAG
GCCACCGCCTGGCTCAACGCCTACTTTCACCAGCCTGAGGCCATCGAGGAGTTCCCTGTG
CCAGCCCTGCACCACCCAGTGTTCCAGCAGGAGAGCTTTACCCGCCAGGTGCTGTGGAAA
CTGCTGAAAGTGGTGAAGTTCGGAGAGGTCATCAGCTACAGCCACCTGGCCGCCCTGGCC
GGCAATCCCGCCGCCACCGCCGCCGTGAAAACCGCCCTGAGCGGAAATCCCGTGCCCATT
CTGATCCCCTGCCACCGGGTGGTGCAGGGCGACCTGGACGTGGGGGGCTACGAGGGCGGG
CTCGCCGTGAAAGAGTGGCTGCTGGCCCACGAGGGCCACAGACTGGGCAAGCCTGGGCTG
GGT GCAGCTGCC

GCTTCAAGCCTAAAACAGGGAGTATCTCCCAAACCACGGGATGTCATTCTTGTGTCCAAAGACATCCCTGAACAACTTTGT
GACGCTTTGTTTTTCTATACGTCACATAACCCTAAGGATTACGCTGATGCTTTTGCAGTTAGGCAGAAGTTTGACCGTAGT
CTCCAGACTGGGAAACAGTTCAAATTTGAAACTGTGTGTGGTCTCTTCCTCTTGAAGGGAGTTGACAAAATAACACCTGGC
GTCCCAGCAAAAGTTTTAAAAGCCACTTCTAAGTTGGCAGATTTAGAAGACATCTTTGTCGACAATT

Reading frame and SalI cut sites checked

8.2 Supplementary movies

Supplementary movie 1: Cryo-SXT of IBV RO 1

Supplementary movie 2: Cryo-SXT of IBV RO 1 and segmentation

Supplementary movie 3: Cryo-SXT of IBV RO 2

Supplementary movie 4: Cryo-SXT of IBV RO 2 and segmentation

Supplementary movie 5: Cryo-ET of IBV RO 1

Supplementary movie 6: Cryo-ET of IBV RO 2

Supplementary movie 7: Cryo-ET of IBV RO 1 and segmentation

Supplementary movie 8: Cryo-ET of IBV RO 2 and segmentation

Supplementary movie 9: Cryo-ET of IBV DMS spokes

Supplementary movie 10: STA model of the IBV double membrane